Characterization of the thermodynamic phase of mid-base and low-base clouds over the Arctic and the Southern Ocean

Zur Erlangung des akademischen Grades eines
DOKTORS DER NATURWISSENSCHAFTEN
von der KIT-Fakultät für Physik des
Karlsruher Instituts für Technologie (KIT)

genehmigte

DISSERTATION

von

M.Sc. Barbara Magdalena Dietel
aus Forchheim

Tag der mündlichen Prüfung:	08.12.2023
Referent:	Prof. Dr. Corinna Hoose
Korreferent:	Prof. Dr. Jan Cermak

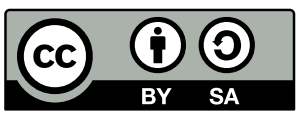

Preface

The PhD candidate confirms that the research presented in this thesis contains significant scientific contributions by herself. Parts of the results of this dissertation have been submitted for publication to „Atmospheric Chemistry and Physics“ on 12 October 2023 in:

Dietel, B., O. Sourdeval, and C. Hoose, 2023: Characterisation of low-base and mid-base clouds and their thermodynamic phase over the Southern and Arctic Ocean. *EGUsphere [preprint]*, 1–38, https://egusphere.copernicus.org/preprints/2023/egusphere-2023-2281/

Major parts of Chapter. 5, and parts of the Sections 2.3, 3.1-3.2, and 4.1 have been submitted as part of the above mentioned paper (Dietel et al., 2023). All analyses in Dietel et al. (2023) were performed by the candidate, but collocated CAMS reanalysis were provided by Prof. Dr. Odran Sourdeval. The paper manuscript was written by the candidate with advice from Prof. Dr. Corinna Hoose and Prof. Dr. Odran Sourdeval. The investigation of the cloud phase over sea ice with the DYAMOND ICON-SAP 5km coupled Winter data, presented in Sec. 7.4 has been performed by Sarah Paratoni as part of her Bachelor thesis (Paratoni, 2023) supervised by the candidate, Dr. Lena Frey, and Prof. Dr. Corinna Hoose.
All other analyses were solely performed by the candidate.
The candidate confirms that appropriate credit has been given within the thesis where reference has been made to the work of others. This copy has been supplied on the understanding that this is copyright material and that no quotation from the thesis may be published without proper acknowledgment.

Abstract

Clouds cover large areas of the Earth and influence the Earth's radiation budget. Biases in the representation of clouds and their phase can lead to radiative biases in model representations, which further impacts for example surface temperature. Such radiative biases over the Southern Ocean have been shown for a long time and are still present in the most recent versions of many climate models. Also the Arctic Ocean shows biases in the representation of clouds in climate and weather models.

To improve the understanding of the cloud phase, i.e. the partitioning of liquid and ice in clouds, over these regions this thesis provides a comprehensive analysis of a two-year mainly satellite-based dataset. A high occurrence frequency of low-level clouds of 21.5 % over the Arctic Ocean and of 25.6 % over the Southern Ocean is found, but clouds spanning the mid-level range (mid-low-level, high-mid-low-level, mid-level, high-mid-level) sum up to a total frequency of approximately 15 %. All investigated cloud types show a rather high frequency of mixed-phase clouds ($\geq$ 24 %), but only low-level, mid-level, and mid-low-level clouds occur as liquid, ice, and mixed-phase cloud and make a major contribution to the cloud type frequency in the mixed-phase temperature regime. Low-level clouds show the highest liquid fraction within a vertical cloud column followed by mid-level clouds. Clouds over the Southern Ocean show higher liquid fractions for cloud top temperatures lower than $-10\,^{\circ}$C, while for higher temperatures, the liquid fraction is higher over the Arctic Ocean. Furthermore, local minima of the liquid fraction are found at temperatures of about $-15\,^{\circ}$C and $-5\,^{\circ}$C. Processes of dendritic growth and secondary ice production are discussed as possible reasons. The liquid fraction is higher in low-level clouds over sea ice compared to the open ocean in both hemispheres. A weaker signal is seen in mid-level and mid-low-level clouds. Aerosol reanalysis exhibit lower sea salt mixing ratios over sea ice, where sea salt is interpreted as a proxy for sea spray in this thesis. High sea salt mixing ratios also correlate with decreasing liquid fraction especially in low-level level clouds, while mid-level clouds show the strongest correlation with dust, which is probably related to the long-range aerosol transport. The highest shortwave cloud radiative effects are shown by high-mid-low-level and mid-low-level clouds over the Southern Ocean. Mostly, mixed-phase clouds show higher shortwave cloud radiative effects than ice or liquid clouds. All investigated cloud types show net negative cloud radiative effects. Low-level clouds contribute most to the shortwave cloud radiative effect followed by mid-low-level clouds due to higher cloud type occurrences.

To investigate the importance of the factors temperature, sea ice cover, sea salt, and dust for the cloud phase determination in mid-level, low-level, and mid-low-level clouds, an explainable machine learning method is used. Sea salt seems to decrease the liquid fraction especially in low-level clouds, while

mid-level clouds are more affected by transported aerosols like dust. The spatial distributions of the different influences show that sea ice cover seems to prevent the release of sea salt aerosol, and strong westerly winds may prevent the pole-ward transport of dust over the Southern Ocean, leading to a strong meridional gradient with more liquid clouds at high latitudes over the Southern Ocean due to less ice nucleating particles (INPs). Over the Arctic Ocean, the spatial distribution is more influenced by the distribution of land surfaces.

The observational results on cloud frequencies, cloud phase and the influence of sea ice is compared with simulation output from the ICOsahedra Nonhydrostatic model (ICON). Strongest biases are found in the frequency of mid-level and high-mid-level clouds with an underestimation in the model by factors between 4.5 and 7.8 in the respective summer-hemispheres. The liquid fraction in low-level and mid-level clouds is underestimated in simulations compared to observations especially for low cloud top temperatures, while it is overestimated for high cloud top temperatures, suggesting a glaciation at too high temperatures in the simulations. Contrary, the liquid fraction of mid-low-level and high-mid-low-level clouds is generally overestimated in models.

The consideration of the INP distribution, which is influenced by sea ice cover and strong wind, in models may be a possibility to improve the representation of cloud phase.

Zusammenfassung

Wolken bedecken einen Großteil der Erde und beeinflussen ihre Strahlungsbilanz. Systematische Fehler in der Repräsentation von Wolken und deren Phase können zu Strahlungsfehlern in Modellen führen, was sich beispielsweise wiederum auf die Oberflächentemperaturen auswirken kann. Solche Strahlungsfehler werden seit langem über dem Südlichen Ozean nachgewiesen und sind auch in den neusten Versionen vieler Klimamodelle vorhanden. Auch der Arktische Ozean zeigt Fehler in der Repräsentation von Wolken in Klima- und Wettermodellen.

Um das Verständnis der Wolkenphase, das heißt die Aufteilung von Flüssigkeit und Eis in Wolken, in diesen Regionen zu verbessern, zeigt diese Arbeit eine umfassende Analyse eines zweijährigen, hauptsächlich satellitengestützten Datensatzes. Auf Basis der Höhen von Wolkenunterkante und -oberkante werden die Wolken in die Kategorien L (low-level), M (mid-level), H (high-level), ML (mid-low-level), HM (high-mid-level), HML (high-mid-low-level) eingeteilt. Ein häufiges Vorkommen von niedrigen Wolken (L) von 21 % über dem Arktischen Ozean und von 25.6 % über dem Südlichen Ozean wurde gefunden, aber auch Wolken die mittlere Höhen abdecken (ML, HML, M, HM) summieren sich zu einen Gesamthäufigkeit von ungefähr 15 %. Alle untersuchten Wolkenarten zeigen relativ häufiges Auftreten von Mischphasenwolken (≥24 %), aber nur Wolken der Kategorien L, M und ML kommen als Flüssig-, Eis-, und Mischphasenwolken vor und tragen einen Großteil zu der Häufigkeit von Wolken im Mischphasentemperaturbereich bei. Niedrige Wolken (L) zeigen die höchsten Flüssiganteile innerhalb einer vertikalen Wolkensäule, gefolgt von mittelhohen (M) Wolken. Wolken über dem Südlichen Ozean zeigen höhere Flüssiganteile für Wolkenoberseitentemperaturen niedriger als −10 °C, während der Flüssiganteil für höhere Temperaturen über dem Arktischen Ozean größer ist. Außerdem werden lokale Minimas des Flüssiganteils bei Temperaturen von ca. −15 °C und −5 °C gefunden. Prozesse wie dendritisches Wachstum und Sekundäreisbildung werden als mögliche Ursachen diskutiert. Der Flüssiganteil ist in beiden Hemisphären in niedrigen Wolken (L) über Meereis größer als über dem offenen Meer. Ein schwächeres Signal wird in Wolken der Kategorien M und ML gesehen. Aerosolreanalysen zeigen niedrigere Meersalzmischungsverhältnisse über Meereis, wobei in dieser Arbeit Meersalz als Indikator für Meeresgischt verwendet wird. Außerdem korrelieren hohe Meersalzmischungsverhältnisse besonders in iedrigen Wolken (L) mit abnehmenden Flüssiganteilen, während mittelhohe Wolken (M) eine starke Korrelation mit Staub zeigen, was wahrscheinlich mit dem großräumigen Aerosoltransport zusammenhängt. Die größten kurzwelligen Wolkenstrahlungseffekte werden in Wolken der Kategorien HM und ML über dem Südlichen Ozean gezeigt. Meistens zeigen Mischphasenwolken größere kurzwellige Wolkenstrahlungseffekte als Eis- oder Flüssigwolken. Alle untersuchten Wolkentypen zeigen negative Nettowolkenstrahlungsef-

fekte. Niedrige Wolken (L) tragen am meisten zu den kurzwelligen Wolkenstrahlungseffekten bei, gefolgt von ML Wolken, da diese Wolkenarten häufiger auftreten.

Um die Bedeutung der Faktoren, Temperatur, Meereisbedeckung, Meersalz und Staub für die Wolkenphase in Wolken der Kategorien M, L, und ML zu untersuchen wird eine erklärbare Methode des maschinellen Lernens verwendet. Meersalz scheint den Flüssiganteil besonders in niedrigen Wolken (L) zu verringern, während mittelhohe Wolken (M) stärker durch transportiere Aerosole wie Staub beeinflusst werden. Die räumliche Verteilung von den verschiedenen Einflüssen zeigt, dass Meereisbedeckung die Freisetzung von Meersalzaerosolen zu verhindern scheint und starke Westwinde den polwärtigen Transport von Staub über dem südlichen Ozean verhindern können, was zu einem starken meridionalen Gradienten mit flüssigeren Wolken in höheren Breiten über dem Südlichen Ozean durch weniger Eisnukleationspartikel (ice nucleating particles, INPs) führt. Über dem Arktischen Ozean ist die räumliche Verteilung stärker durch die Landverteilung beeinflusst.

Die Beobachtungsergebnisse zu Wolkenhäufigkeiten, Wolkenphasen und dem Einfluss von Meereis werden mit Simulationsergebnissen des nicht-hydrostatischen icosahedrischen (ICOsahedral Nonhydrostatic, ICON) Modells verglichen. Die größten Fehler sind in der Häufigkeit von Wolken der Kategorien M und HM mit einer Unterschätzung im Modell um Faktoren zwischen 4.5 und 7.8 in den entsprechenden Sommerhemisphären zu finden. Der Flüssiganteil in Wolken der Kategorie L und M wird im Modell im Vergleich zu Beobachtungen, insbesondere für niedrige Wolkenoberkantentemperaturen unterschätzt, während es für hohe Wolkenoberkantentemperaturen überschätzt wird, was auf eine Vereisung bei zu hohen Temperaturen in den Simulationen hinweist. Im Gegensatz dazu wird der Flüssiganteil in Wolken der Kategorie ML und HML in Modellen generell überschätzt. Die Berücksichtigung der INP-Verteilung in Modellen, die durch Meereisbedeckung und starke Winde beeinflusst wird, könnte eine Möglichkeit sein, die Darstellung der Wolkenphase zu verbessern.

Contents

1 Introduction **1**

2 Background **5**

2.1 Cloud microphysics 5

2.1.1 Droplet formation 5

2.1.2 Primary ice formation 6

2.1.3 Secondary ice formation 8

2.1.4 Cloud particle interactions 9

2.1.5 Cloud particle interaction with radiation 10

2.2 Characteristics of the Arctic and the Southern Ocean regions 12

2.2.1 Atmospheric and oceanic conditions 13

2.2.2 Ice nucleating particles over polar oceans 17

2.3 Clouds over the Arctic and the Southern Ocean and related radiative biases . . . 19

2.3.1 Arctic clouds 20

2.3.2 Clouds over the Southern Ocean 21

2.3.3 Radiative biases in models 22

2.3.4 Summary 25

3 Data **27**

3.1 Region and time 27

3.2 Observational data and reanalysis 28

3.2.1 Cloud phase categorization from DARDAR 29

3.2.2 Sea ice concentration from DMSP 32

3.2.3 Aerosol mixing ratios from CAMS reanalysis 32

3.2.4 Cloud radiative effects from 2B-FLXHR-LIDAR 33

3.3 Model data from different DYAMOND ICON runs 34

3.3.1 ICON-NWP Summer 2.5 35

3.3.2 ICON-NWP Winter 2.5 35

3.3.3 Coupled ICON-SAP Winter 5 36

4 Methodology **37**

4.1 Observations 37

4.1.1 Collocating datasets and preprocessing . . . 38
4.1.2 Cloud type classification . . . 38
4.1.3 Phase analysis by calculating the liquid fraction . . . 39
4.1.4 Sea ice concentration . . . 40
4.1.5 CAMS aerosol reanalysis . . . 41
4.1.6 Horizontal and vertical cloud extent . . . 41
4.2 Machine Learning . . . 42
4.2.1 Model concept and tuning . . . 42
4.2.2 Explainable Machine Learning using SHAP values . . . 45
4.3 DYAMOND simulations . . . 46
4.3.1 Cloud types classification and liquid fraction . . . 46
4.3.2 Sea ice concentration . . . 48

5 Clouds from the satellite perspective 49
5.1 Cloud type occurrence frequency . . . 49
5.2 Cloud phase . . . 53
5.2.1 Cloud phase correlation on the vertical and horizontal cloud extent . . . 54
5.2.2 Cloud phase dependence on the cloud top temperature . . . 55
5.2.3 Vertical phase distribution of mixed-phase clouds . . . 59
5.2.4 Cloud phase dependence on the sea ice concentration and aerosol concentration . . . 60
5.3 Cloud radiative effect . . . 65
5.3.1 Mean cloud radiative effect of different cloud types . . . 65
5.3.2 Dependence of the cloud radiative effect on the cloud phase . . . 68
5.3.3 Contribution of different cloud types to the total SWCRE and LWCRE . . . 69
5.4 Uncertainties . . . 71

6 Applying an explainable machine learning technique to investigate parameter importance for cloud phase 73
6.1 Importance of the parameters for the cloud phase prediction . . . 73
6.2 Overview of the influence of the parameters on the cloud phase prediction . . . 75
6.3 Influence of dust on the cloud phase prediction . . . 77
6.4 Influence of sea salt on the cloud phase prediction . . . 80
6.5 Influence of sea ice coverage on cloud phase and correlation with sea salt . . . 82
6.6 Uncertainties . . . 83

7 Comparison of clouds from the satellite perspective with ICON model simulations from the DYAMOND project 85

7.1 Cloud type occurrence 85
7.2 Cloud phase fractions 88
7.3 Liquid fraction as a function of the cloud top temperature 90
7.4 Liquid fraction in low-level and mid-low-level clouds over sea ice and over open ocean in the Arctic 93
7.5 Uncertainties 94

8 Conclusions and outlook **97**
8.1 Conclusions 97
8.2 Outlook 101

A Appendices **105**
A.1 Appendix to Chap. 5 105
A.1.1 Seasonal cycle of cloud type frequencies 105
A.1.2 Cloud radiative effect over the Arctic and the Southern Ocean 105
A.2 Appendix to Chap. 6 109
A.3 Appendix to the Chap. 7 120

B Bibliography **123**

C List of Figures **147**

D List of Tables **153**

1. Introduction

Clouds cover large areas of the Earth's oceans and turn the view from space of the „blue" planet into a planet with blue and white patches. Satellite observations have shown a cloud fraction of 72 % over oceans (King et al., 2013). Clouds play as well a large role in the atmospheric weather and climate system. They are the largest source of uncertainty in the climate feedbacks (Arias et al., 2021). Their effect on global warming is still uncertain, which is related to their poor representation in current models. Their effect on global warming strongly depends on their height and their thermodynamic phase, as ice and liquid interact differently with radiation. Higher clouds tend to be ice clouds which lead to a warming effect, as they prevent the release of longwave radiation to space. Contrarily, low clouds tend to be liquid clouds, which mainly reflect solar shortwave radiation back to space and therefore lead to a cooling effect. As clouds can occur in multiple layers at the same time, the total effect is not always that clear. Furthermore, there is also a temperature range where both liquid and ice can physically occur at the same time, which is called mixed-phase temperature regime. In that regime, models produce especially large biases related to the phase, which can lead to radiative errors, and thereby further impacts for example surface temperatures.

There is a long-standing shortwave radiative bias in climate models over the Southern Ocean, which has been slightly improved in the last version of the Coupled Model Intercomparison Project (CMIP6) simulations, but models still show biases south of 55 °S (Cesana et al., 2022). The Arctic shows as well radiative biases related to the representation of clouds (Wei et al., 2021). The CMIP6 models mainly show an overestimation of the cloud fraction over the Arctic leading to an underestimation of the surface shortwave flux, and an overestimated warming longwave effect (Wei et al., 2021). Both Cesana et al. (2022) and Wei et al. (2021) also highlight the large intermodel spread, which also shows the large uncertainties in the representation of clouds.

Besides the uncertainties in models, there is also a large uncertainty in the general understanding of the small-scale ice production mechanisms. The formation of secondary ice is one example for the currently poor understanding how ice is produced in the atmosphere. There are several proposed mechanisms based on laboratory studies, but the importance of these mechanisms in atmospheric conditions is still unclear. Another uncertainty is related to the relevance of specific aerosols, small particles suspended in the air, which are required for the nucleation of ice particles in clouds at temperatures higher than −38 °C, so-called ice nucleating particles (INPs). Until now, it is not known which ice nucleating particles are most relevant in which regions of the Earth, how hey are distributed horizontally and vertically and which underlying mechanisms might be important for their production. Both of these mechanisms also

show another source of uncertainty in general, as cloud processes occur on scales of micrometers to millimeters, while the currently highest possible grid resolution of global models are in the range of 1 km to 2 km. The development of suitable parameterizations to represent these small scale processes on larger sales needs a comprehensive understanding of all these mechanisms with the potential to improve the representation of clouds and their phase in models.
To address these uncertainties this thesis provides a comprehensive study of clouds and their phase, focusing on the region of the Southern Ocean and the Arctic Ocean. In the first part mainly satellite observations, but also reanalysis for some parameters are used. After a first characterization of the cloud occurrence and properties like their height, their temperature of occurrence, their phase, and their vertical and horizontal extents, the thesis also analyses possible factors proposed to influence cloud phase, like temperature, sea ice, and aerosol types and amounts. The questions which are addressed for the Arctic Ocean and the Southern Ocean within this thesis are the following:

- How frequent are different cloud types (identified based on their heights)? (Sec. 5.1)
- Which phase do the different clouds typically have, and which cloud types occur most frequent in the mixed-phase temperature regime? (Sec. 5.1 and Sec. 5.2)
- How does the vertical and horizontal extent of clouds correlate with cloud phase? (Sec. 5.2.1)
- What is the phase distribution as a function of the temperature in different cloud types and how is cloud phase vertically distributed within mixed-phase clouds? (Sec. 5.2.3, Sec.5.2.2)
- How does cloud phase correlate with sea ice cover and the amount of specific aerosol types? (Sec. 5.2.4)
- How large is the top of the atmosphere cloud radiative effect for different cloud types and how does it vary with different cloud phase? How large is the contribution of specific cloud types to the total cloud radiative effect? (Sec. 5.3.1, Sec. 5.3.2, Sec. 5.3.3)

Furthermore, the thesis aims to quantify the importance of some factors for the cloud phase using a machine learning method. Besides the importance, it also investigates the spatial distribution of the importance of various factors to improve the understanding of their possible influences.

- Which of the following parameters, temperature, sea ice, dust, and sea salt, are most important for determining cloud phase and how does the importance vary regionally? Is there a dependence of the importance on other parameters? (Chap. 6)

By comparing the cloud occurrence and the cloud phase from the satellite observations with model output, a first insight into possibilities for improvement of the model representation is gained.

- ❄ What are the differences in cloud occurrence and cloud phase between satellite observations and simulations with the ICOsahedral Nonhydrostatic model (ICON)? Does a coupled (atmosphere-ocean) ICON simulation show an improved correlation between sea ice and cloud phase as satellite observations compared to uncoupled simulations? (Chap. 7)

Before addressing these questions, the next chapter provides a theoretical background starting with an explanation how droplets and ice crystals form in clouds, describing how cloud particles can interact, and how different particles interact with radiation. The chapter continues with a general characterization of the Arctic Ocean and the Southern Ocean with respect to atmospheric and ocean conditions and focusing on clouds and ice nucleating particles. A last part describes the already mentioned radiative biases based on clouds over these regions in more detail.
Chapter 3 describes different datasets used within this thesis, as the cloud categorization based on active satellite instruments, further satellite-based dataset like sea ice information or cloud radiative effects, and reanalysis of aerosols. A second part of the chapter describes the setup of the models, from which the output data is used for a comparison. Chapter 4 describes the different methods, as for example how the different cloud types are defined and classified, how the liquid fraction of clouds is calculated, and how the correlation of cloud phase with sea ice and aerosols is investigated, but also how a cloud object is defined to investigate the horizontal and vertical extent of a cloud. A second section of this chapter describes the used machine learning method and used method to make the machine learning model explainable. It further provides an overview of the performance of the machine learning models. The last section of this chapter describes then how the previously described method differs for the analysis of the model data. Afterwards, Chap. 5, Chap. 6, and Chap. 7 address the previously mentioned research questions. The last Chap. 8 summarizes the results of this thesis and provides an outlook, in which further research to improve the representation of clouds and their phase in models is discussed.

2. Background

This chapter provides a background with Sec. 2.1 giving a theoretical overview of cloud microphysics focusing on the formation of cloud droplets and ice crystals, their interaction in clouds, as well as the interaction between radiation and cloud particles. Section 2.2 describes general characteristics of the Arctic Ocean and the Southern Ocean and presents differences of the regions. The first part focuses on the atmospheric conditions, as well as ocean currents and sea ice presence. The second part presents a literature review on the availability of ice nucleating particles over the regions. Section 2.3 describes previous studies about clouds and their phase over the Southern Ocean and the Arctic Ocean. Furthermore, the large uncertainties in the radiation budget of weather and climate models over these regions due to uncertainties in the representation of clouds and their phase are described motivating the further research.

2.1. Cloud microphysics

This first section describes some theoretical concepts of cloud microphysics answering the question how cloud droplets form, and how ice particles are generated by primary or secondary ice formation. Further, the interaction between different cloud particles is described. The last part presents an overview of the interaction between radiation and cloud particles and also presents the theoretical background on how these interactions can be used in remote sensing techniques to observe clouds and their phase.

2.1.1. Droplet formation

The formation of cloud droplets depends on the availability of humidity, the temperature, the saturation of the air, but also on the availability of specific aerosols. The nucleation of the liquid phase from the vapour phase happens mainly heterogeneously in the atmosphere interacting with soluble aerosols, which reduces the equilibrium vapor pressure, and can lead to deliquescence below saturation. Once a liquid solution droplet has formed the droplet has to be activated to become a cloud droplet. This transition is based on the Köhler theory (Köhler, 1936), which describes the equilibrium saturation ratio (S_K) between the vapor and the solution droplet (Lamb and Verlinde, 2011).

$$S_K = 1 + \underbrace{\frac{A_K}{r_d}}_{\text{Kelvin}} - \underbrace{\frac{B_K i N_s}{r_d^3}}_{\text{Raoult}} \tag{2.1}$$

The Köhler equation (see Eq. 2.1) combines the Kelvin effect (curvature effect) (Thomson, 1871) and the Raoult effect (solute effect) (Raoult, 1887, 1889), where r_d is the equilibrium radius of the droplet, N_s is the number of moles of the solute in the particle, and i is the van't Hoff factor describing the dissociation of the solute. A_K is defined in Eq. 2.2, where σ_{LV} is the surface tension, n_L is the liquid molar density, R is universal gas constant ($R = 8.314\,\mathrm{Jmol^{-1}K^{-1}}$), and T is the temperature. B_K is defined in Eq. 2.3 and only depends on the liquid molar density. In general, it can be said, that the curvature effect (Kelvin) increases the equilibrium vapor pressure of the water, while the solute effect (Raoult) decreases the equilibrium vapor pressure (Lamb and Verlinde, 2011).

$$A_K = \frac{2\sigma_{LV}}{n_L R T} \tag{2.2}$$

$$B_K = \frac{3}{4\pi n_L} \tag{2.3}$$

By calculating the maximum of the Köhler equation, a critical supersaturation (see Eq. 2.4), and a corresponding critical radius (see Eq. 2.5) can be defined, which describes a threshold between smaller haze particles and cloud droplets. This critical radius has to be reached to allow small droplets to grow through condensation to a cloud droplet. This process is described as the activation of cloud droplets.

$$S_c = 1 + \left(\frac{4A_K^3}{27 B_K i N_s}\right)^{\frac{1}{2}} \tag{2.4}$$

$$r_c = \left(\frac{3 B_K i N_s}{A_K}\right)^{\frac{1}{2}} \tag{2.5}$$

To enable the formation of a cloud droplet in atmospheric conditions, the presence of cloud condensations nucleis (CCN) is required, as they lead to a reduction of the critical supersaturation. Without the presence of CCNs, supersaturations of several hundred percents would be required to nucleate liquid droplets, which is unrealistic in atmospheric conditions. The larger the dry CCN particle is, the stronger is the reduction of the critical supersaturation. Clouds in the atmosphere have maximal supersaturations of 10 % in deep convection. Typical dry CCN sizes are in the order of 0.1 µm, activating at supersaturations of about 0.1 % and thereby enabling the nucleation of liquid droplets in typical atmospheric conditions (Lamb and Verlinde, 2011).

2.1.2. Primary ice formation

Ice can only form in the atmosphere if the temperature is lower than 0 °C, with an increasing freezing probability for a decreasing temperature. Further parameters influencing the formation of ice in clouds are saturation as well as dynamical and environmental conditions. Besides temperature, the availability of ice nucleating particles plays a large role, as can be seen in the following. Theoretically, ice can form from the liquid phase or directly from the vapor phase through deposition. Nevertheless, the initial

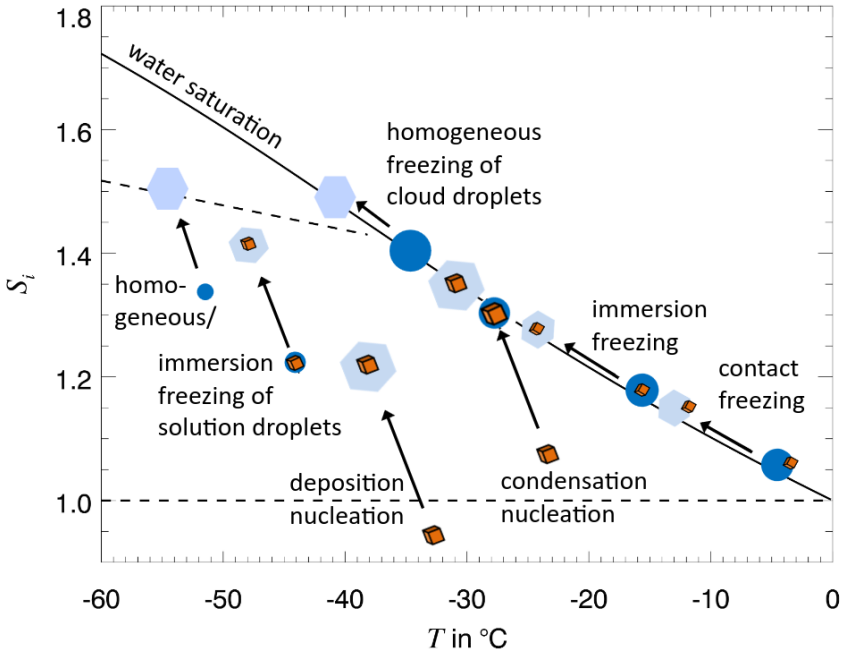

Figure 2.1.: Schematic of homogeneous and heterogeneous freezing from Hoose and Möhler (2012). S_i is the supersaturation with respect to ice and T is the temperature.

formation of ice from the vapor phase without the participation of specific surfaces of particles is unlikely due to a strong decrease of entropy from the vapor phase to the ice phase. Therefore, further description focuses on homogeneous nucleation from supercooled liquid droplets and heterogeneous nucleation.

Homogeneous nucleation is the formation of ice from existing pure supercooled cloud droplets and only occurs at temperatures colder than −38 °C (compare Fig. 2.1). The heterogeneous nucleation describes the formation of ice through different processes including ice nucleating particles (INPs).

These particles provide a surface facilitating the first nucleation of ice. There have been many studies investigating different materials and their activity as INP. A summary is shown for example by Kanji et al. (2017) in Fig. 2.2. One of the most common types of INPs in the atmosphere is dust, activating over a wide range of temperatures. Dust can originate from deserts, but also from dry soils like agricultural lands (Kanji et al., 2017). Biological particles are generally known to be activating at high temperatures. Such biological components are for example present in aerosols from vegetation or soils like fungal spores, pollen, or bacteria, but can also be part of sea spray aerosols containing for example phytoplankton or marine exudates (Kanji et al., 2017). Section 2.2.2 will further describe the most relevant INPs over polar oceans.

Heterogeneous freezing can occur in various processes (see Fig. 2.1) such as contact freezing, which describes the instantaneous freezing once an INP gets in contact with a cloud droplet. The immersion freezing describes the freezing of a cloud droplet already including an INP. The condensation nucleation describes the process of condensation of vapor on an INP and the following freezing of the just condensed

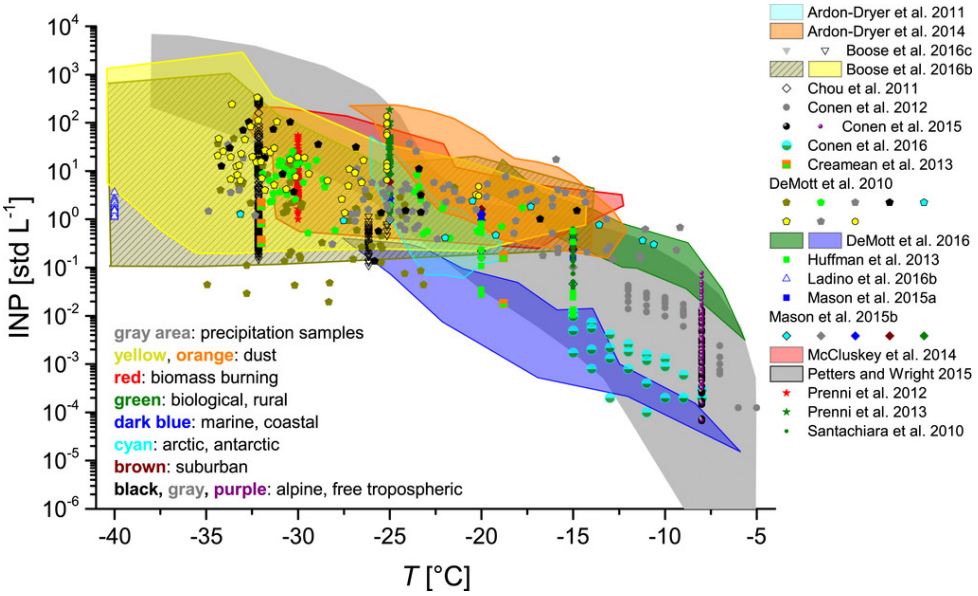

Figure 2.2.: Summary of INP concentrations taken from studies of field measurements conducted globally from Kanji et al. (2017). For details about different sources of the datasets, see Kanji et al. (2017). © American Meteorological Society. Used with permission.

water. Contrary to the previous processes the deposition nucleation describes the direct deposition of water vapor on the surface of an INP.

The shape and habit of ice particles strongly depend on the temperature and saturation conditions (Libbrecht, 2005; Fukuta and Takahashi, 1999; Chen and Lamb, 1994). Libbrecht (2005) shows different regimes for different temperatures. So do plates mainly occur between temperatures larger than $-2\,°C$ and for temperatures lower than $-10\,°C$, while columns occur mainly between temperatures of $-2\,°C$ and $-10\,°C$. For higher supersaturation, especially above water saturation the formation of dendrites is possible in the temperature range of about $-2\,°C$ and especially between $-10\,°C$ and $-20\,°C$, which is also called the denritic growth layer (von Terzi et al., 2022; Takahashi, 2014; Takahashi et al., 1991).

2.1.3. Secondary ice formation

It has been found that primary ice formation is not sufficient to describe the number of ice particles measured in observations (Kanji et al., 2017). Therefore, other ice processes than primary ice must be responsible for the increased number of ice particles observed. Secondary ice can be formed by small fragments from already existing ice particles. These fragments can form through various processes. Korolev and Leisner (2020) describe six processes producing secondary ice, namely the droplet fragmentation during freezing, the splintering during riming, which is also called Hallet-Mossop process, the fragmentation during ice-ice collision, the ice fragmentation during the thermal shock, the fragmentation during sublimation, and the activation of INPs in transient supersaturation. They also pinpoint the need of further laboratory studies on the different mechanisms, as there are still large gaps in the understand-

ing of these processes, the necessary conditions, and thus their relevance in real clouds. Takahashi et al. (1995) showed a strong production of ice particles during collisions between two graupel particles.

2.1.4. Cloud particle interactions

The interaction of different cloud particles can change their properties like particle size, particle mass, or the thermodynamic particle phase. Such processes are for example the collisions between particle types, such as a collision between two cloud droplets, a rain droplet with a cloud droplet, an ice particle and a cloud droplet (riming), or two ice particles (aggregation). These collisions can lead to larger particles by coalescence, but can also form new particles due to fragmentation and disruption, as already described for ice in Sec. 2.1.3. Riming usually leads to the accretion of the ice particle. During the riming process secondary ice may be produced by the release of small splinters. Rain can form by the collision of cloud droplets through the warm phase, leading to the growth of the droplets, until their size is large enough to fall out of the cloud. This is mainly relevant over the tropical oceans outside of the Intertropical Convergence zone, while rain over the midlatitude oceans and continents is dominated by mixed-phase and ice clouds, which means that rain is produced by the melting of falling ice particles (Mülmenstädt et al., 2015).

Figure 2.3 shows the phase diagram of water based on the Clausius-Clapeyron-Equation for saturation vapor pressure with respect to liquid ($p_{\mathrm{sat,liq}}$, see Eq. 2.6-2.7) and with respect to ice ($p_{\mathrm{sat,ice}}$, see Eq. 2.8-2.9). In both equations R is the gas constant for water vapor ($R = 461.5\,\mathrm{Jkg^{-1}K^{-1}}$), l_v is the latent heat for vaporization of water ($l_v = 2.5\times10^6\,\mathrm{Jkg^{-1}}$), l_s is the latent heat for sublimation ($l_s = 2.8\times10^6\,\mathrm{Jkg^{-1}}$). As a reference point for p_0 and T_0, the triple point is used with a saturation vapor pressure of 6.11 hPa and a temperature of 273.15 K. The triple point describes conditions where all three phases can coexist in equilibrium. If cloud droplets and ice particles exist, the ice particles will grow at the expense of the cloud droplets. The reason is that the saturation water vapor pressure is higher over water (see Eq. 2.6) compared to the saturation water vapor pressure over ice (see Eq. 2.8). This is also shown in Fig. 2.3 for temperatures lower than 0 °C by the blue and orange lines. Due to this difference the cloud water droplets evaporate and the ice particles will grow via depositional growth. This is called Wegener-Bergeron-Findeisen process.

$$p_{\mathrm{sat,liq}} = p_0 \exp\left(\frac{l_v}{R}\left(\frac{1}{T_0} - \frac{1}{T}\right)\right) \tag{2.6}$$

$$= 6.11\,\mathrm{hPa}\exp\left(\frac{2.5\times10^6\,\mathrm{Jkg^{-1}}}{461.5\,\mathrm{Jkg^{-1}K^{-1}}}\left(\frac{1}{273.15\,\mathrm{K}} - \frac{1}{T}\right)\right) \tag{2.7}$$

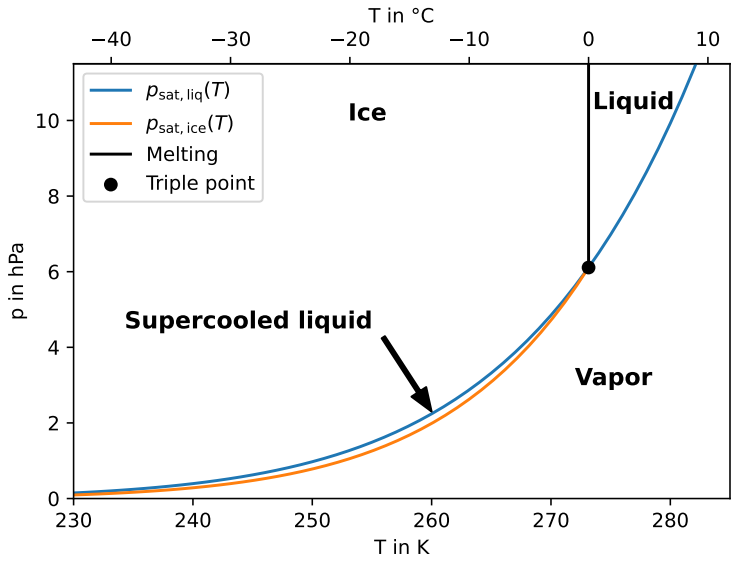

Figure 2.3.: Phase diagram of water adapted from Lamb and Verlinde (2011). p is the partial pressure, $p_{\text{sat,liq}}$ is the saturation vapor pressure with respect to water (blue curve), $p_{\text{sat,ice}}$ is the saturation vapor pressure with respect to ice (orange curve). The black line represents the melting curve. The area between the blue curve and the orange curve for temperatures lower than 0 °C shows the conditions for the presence of meta-stable supercooled liquid water.

$$p_{\text{sat,ice}} = p_0 \exp\left(\frac{l_s}{R}\left(\frac{1}{T_0} - \frac{1}{T}\right)\right) \tag{2.8}$$

$$= 6.11\,\text{hPa} \exp\left(\frac{2.8\times10^6\,\text{Jkg}^{-1}}{461.5\,\text{Jkg}^{-1}\text{K}^{-1}}\left(\frac{1}{273.15\,\text{K}} - \frac{1}{T}\right)\right) \tag{2.9}$$

2.1.5. Cloud particle interaction with radiation

Cloud particles interact with radiation by scattering and absorption. This is on the one hand important for the understanding of the energy balance of the Earth, and on the other hand provides a possibility for the observation of clouds by remote sensing techniques. The properties of the cloud particles determine their interaction with radiation. Particle size, their shape, the number concentration, and the particle phase are relevant parameters. The size parameter x is described in Eq. 2.10 and illustrated in Fig. 2.4, with the radius of the scattering object r, and the wavelength λ of the radiation. The size parameter determines different scattering regimes. The larger the size parameter is, the stronger is the forward scattering in the Mie regime (Lamb and Verlinde, 2011).

$$x = \frac{2\pi r}{\lambda} \tag{2.10}$$

Radar and lidar instruments are typically used to observe aerosols, clouds, and rain. Typical wavelengths of a lidar and a radar are also shown in Fig. 2.4, which demonstrates that the radar is more sensitive

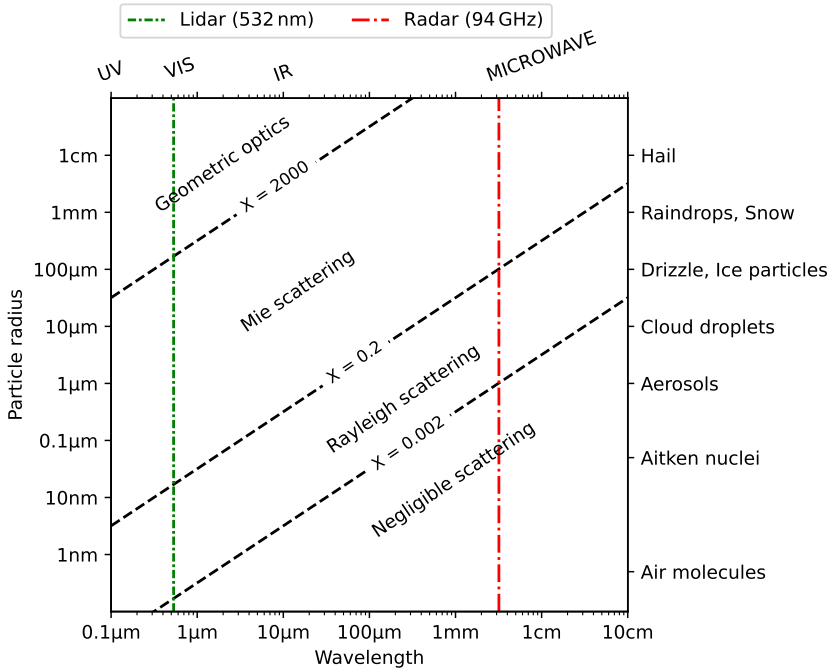

Figure 2.4.: Scattering as function of the radius and the wavelength. The size parameter x (Eq. 2.10) shows edges of different scattering regimes. The typical wavelength of a radar and lidar are shown by colored lines, and the right axis shows typical radii of different scattering objects in the atmosphere. Adapted from Petty (2006).

to larger particles like rain droplets, or snow, while the lidar is more sensitive to smaller cloud droplets or aerosols. A common parameter from the radar is the the radar reflectivity factor (Z) (see Eq. 2.11), with the equivalent spherical diameter (D), and the number distribution of particles ($N(D)$). It shows that the radar reflectivity factor is strongly dependent on the particle size. The radar reflectivity factor also relates to the received power of the radar ($\overline{P}_r$) by Eq. 2.12 assuming Rayleigh scattering. R is the target range describing the distance between the scattering object and the radar. C_r is the radar constant, which depends on specific radar characteristics like the gain function of the antenna, the pulse duration, or transmitted power (Andronache, 2018; Rauber and Nesbitt, 2018).

$$Z = \int_0^\infty N(D) D^6 \mathrm{d}D \tag{2.11}$$

$$Z = C_r R^2 \overline{P}_r \tag{2.12}$$

As already mentioned, the lidar is more sensitive to smaller particles due to its shorter wavelength compared to the radar. The lidar equation describes the received power as function of the range ($P(R)$) and is shown in Eq. 2.13 (Wiegner et al., 2014), with the lidar specific constant C_l including for example information of the emitted power or the receiver area. $\beta_{\mathrm{backscat}}(R)$ is the backscatter coefficient, and $\beta_{\mathrm{ext}}(R)$ is

the extinction coefficient, which is defined by the sum of the scattering coefficient (β_{scat}) and absorption coefficient (β_{abs}).

$$P(R) = \frac{C_l \beta_{\text{backscat}}(R)}{R^2} \exp\left(-2 \int_0^R \beta_{\text{ext}}(R')\mathrm{d}R'\right) \tag{2.13}$$

The absorption and scattering coefficients are defined in Eq. 2.14 and Eq. 2.15, with the scattering cross section σ_{scat}, and the absorbing cross section σ_{abs}. In the Rayleigh regime the scattering cross section and the absorbing cross section show the proportionality given by Eq. 2.16 and Eq. 2.17 (Petty, 2006).

$$\beta_{\text{abs}} = \int_0^\infty \sigma_{\text{abs}} N(r)\mathrm{d}r \tag{2.14}$$

$$\beta_{\text{scat}} = \int_0^\infty \sigma_{\text{scat}} N(r)\mathrm{d}r \tag{2.15}$$

$$\sigma_{\text{scat}} \propto \frac{r^6}{\lambda^4} \tag{2.16}$$

$$\sigma_{\text{abs}} \propto \frac{r^3}{\lambda} \tag{2.17}$$

The depolarization ratio δ (see Eq. 2.18) of the received lidar signal, defined as the fraction of orthogonal polarizes signal ($P_\perp$) and the parallel polarized signal ($P_\parallel$) can also provide information about cloud phase, as spherical particles tend to not change the polarization, while non-spherical particles do (Schotland et al., 1971). Liquid cloud droplets are usually spherical, while ice particles are not, but have varying shapes, as described in Sec. 2.1.2. Nevertheless, other factors like multiple scattering influence the polarization and have to be considered, when using the depolarization for phase discrimination (Hu et al., 2001).

$$\delta = \frac{P_\perp}{P_\parallel} \tag{2.18}$$

This section described briefly the theory of cloud formation by the formation of liquid droplets and ice crystals, and the important role of aerosols acting as CCN and INP. Furthermore, interactive processes between cloud particles, which can change cloud properties, have been briefly mentioned and described. The last section gave an overview how cloud particles interact with radiation by scattering and absorption, and how these interactions can be used to observe clouds and cloud properties with remote sensing instruments like lidar and radar. After this description of small-scale cloud particle processes, the next section will provide an overview of the geographical regions investigated in this study.

2.2. Characteristics of the Arctic and the Southern Ocean regions

This section describes the characteristic conditions found in the Arctic and the Southern Ocean and their underlying phenomena and processes. The first part describes geographical, atmospheric, and oceanic

conditions, and provides a brief overview of the Arctic Amplifications and climate change observations in the Southern Ocean. The second part summarizes previous literature on ice nucleating particles over the Arctic and the Southern Ocean and the relevance of different INP types in these regions.

2.2.1. Atmospheric and oceanic conditions

The Arctic and the Southern Ocean are characterized by a low amount of incoming solar radiation, especially in winter due to their high latitudes. Nevertheless, the Arctic and the Southern Ocean show fundamental differences in their characteristics, based on their different land-sea distributions and conditions.

The Southern Ocean surrounds the continent Antarctica, which is covered by thick ice sheets, while the Arctic Ocean is mainly surrounded by land surfaces, and characterized by large areas of sea ice. Figure 2.5 shows the sea ice cover in both hemispheres in March and September, averaged over the years 2007 and 2008, and highlights the seasonal variation of the sea ice cover. The atmospheric circulation over the Southern Ocean is characterized by strong westerly winds due to the initially southward flow from the high pressure area at the southern part of the Hadley cell. The southward flow is then turned by the Coriolis force forming strong westerlies. Frequently, extratropical cyclones form along the westerly zone in the Southern Ocean. In general, the air in the Southern Ocean is rather pristine due to very few anthropogenic pollutions. Over the Arctic Ocean the wind circulation is stronger influenced by land surfaces compared to the Southern Ocean. Between Greenland and Scandinavia the Gulf Stream leads to warmer temperatures, and cyclones transport warm air in their warm sectors pole-wards. Further north, the atmospheric circulation is characterized by the polar easterlies induced by the polar high pressure system. Temperature inversions occur frequently over the Arctic induced by the long-wave radiative cooling of the surface due to no or low solar radiation. The strength of the inversion shows an annual cycle with stronger inversions in winter and weaker inversions in summer (Wang et al., 2022; Tjernström and Graversen, 2009).

The Antarctic Circumpolar current is the most powerful oceanic current on the globe, connecting three oceans, and surrounding the Antarctic continent (Diansky et al., 2021). Due to this strong eastward flowing current, the meridional transport of heat of warmer ocean water and cold polar ocean water is inhibited (Diansky et al., 2021). The current is induced by wind, and density gradients due to temperature and salinity (Williams, 2015). The global ocean circulation leads to the upward transport of nutrient rich deep water to the surface in the Southern Ocean (Landwehr et al., 2021; Liggett et al., 2015). The availability of these nutrients is also responsible for many biological activities in the Southern Ocean, which are important for the production of biological INPs, described in Sec. 2.2.2. Figure 2.6 from Landwehr et al. (2021) shows a nice schematic overview of many processes characterizing the Southern Ocean, including the westerly winds, the Antarctic Circumpolar Current, the nutrient rich water, as well as sea spray production, its connection to clouds, which are associated with extratropical cyclones, and radiative processes of clouds.

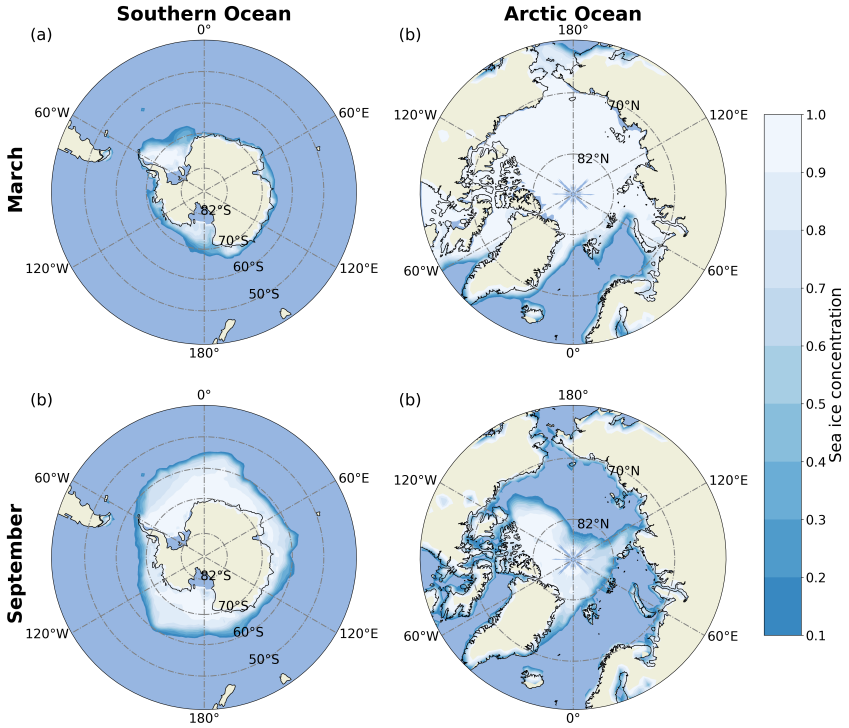

Figure 2.5.: Sea ice concentration in March and September averaged for 2007 and 2008 to illustrate sea ice cover over the Southern Ocean and the Arctic Ocean. Data are from Cavalieri et al. (1996) (version 1) provided by the National Snow and Ice Data Centre (NSIDC). Reprinted from Dietel et al. (2023).

Contrary to the Southern Ocean, the Arctic Ocean has only limited connections to other oceans due to the surrounding land cover (Serreze and Barry, 2014). The surface currents are illustrated in Fig. 2.7. The Pacific ocean is connected via the Bering Strait. The Beaufort Gyre is an anticyclonic motion of the upper ocean in the central Arctic (Serreze and Barry, 2014). At the east cost of Greenland, there is a cold southward flow, while in general the area between Greenland and Scandinavia is characterized by transport of warm water to the Arctic.

The Arctic warms faster with climate change compared to the global mean, which is called Arctic Amplification. Rantanen et al. (2022) states that the Arctic warms four times faster compared to the global average, while Meredith et al. (2019) stated that the Arctic surface air temperature increased twice as the global average during the last two decades. The reason for the amplification lies in different feedbacks mechanisms occurring in the Arctic associated with global warming. Until now, it is not yet fully understood which processes contribute most to the Arctic amplification. One main driver is the loss of sea ice and snow cover, which impacts the albedo resulting in less shortwave reflection of the open ocean and of darker land surfaces, and thereby stronger warming (Meredith et al., 2019). Previdi et al. (2021) reviews that the temperature feedback of the Arctic has the largest contribution to the Arctic Amplification. The temperature feedback can be decomposed into two separate feedbacks, one related to the fact that the outgoing long-wave radiation does not depend linearly on the temperature, but through the Stefan Boltzmann law. This means that an increase of the temperature of 1 °C leads to stronger increase

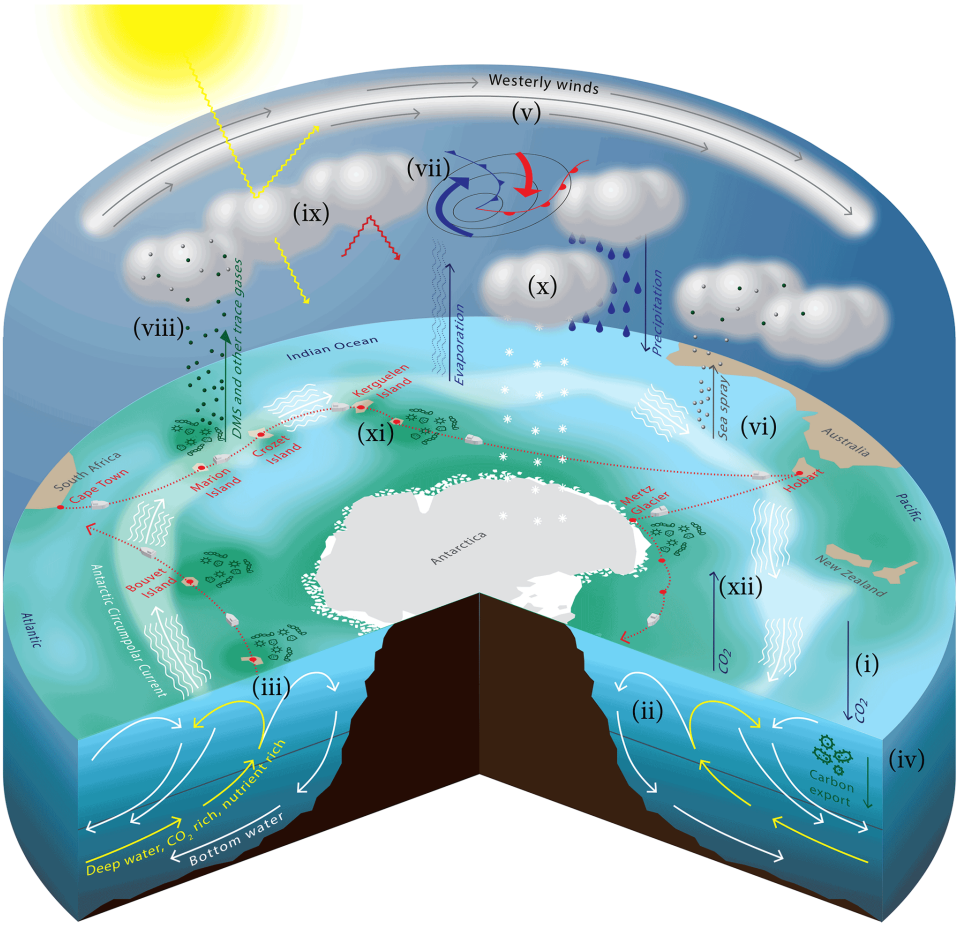

Figure 2.6.: Conceptual illustration of selected Southern Ocean processes, with (i) CO_2 uptake, (ii) formation of bottom water, (iii) upwelling of nutrient-rich water, (iv) biological carbon pump, (v) westerly storm track, (vi) formation of sea spray, (vii) cyclone activity and low-level cloud deck, (viii) emission of biogenic gases and secondary aerosol formation, (ix) cloud-modulated radiation budget, (x) evaporation and precipitation, (xi) nutrient (iron)-rich areas near islands through the island mass effect, (xii) meltwater inducing phytoplankton blooms. Figure and adapted caption from Landwehr et al. (2021).

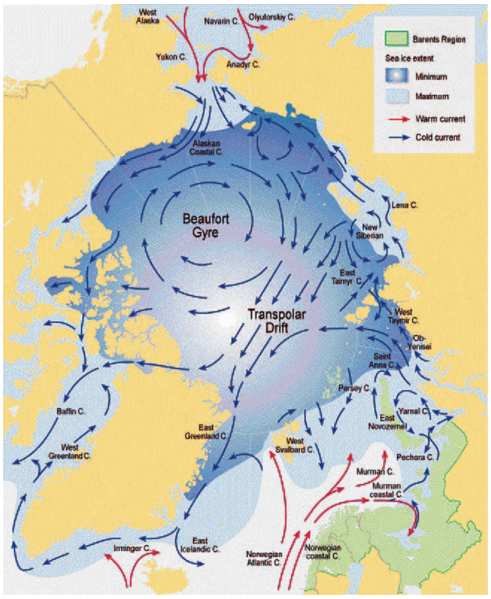

Figure 2.7.: Arctic Ocean surface circulation. Red arrows indicate warm Atlantic Ocean currents and blue arrows indicate cold Arctic surface currents. North Atlantic drift waters entering the Arctic west of Svalbard flow counterclockwise at depth (the warm core is at roughly 300 meters) and exit through the Fram Strait (not shown). Figure and caption from Tremblay et al. (2007). ©2007, IEEE

of the outgoing long-wave radiation in low latitudes compared to high latitudes, due to their generally colder temperatures (Previdi et al., 2021). The second component of the temperature feedback is the lapse-rate feedback. Globally, the upper troposphere warms stronger compared to the lower troposphere, while in the Arctic the warming is stronger in the lower troposphere compared to the upper troposphere (Linke et al., 2023; Previdi et al., 2021). This impacts the outgoing long-wave radiation, as it depends on the vertical tropospheric temperature structure. The outgoing long-wave radiation is higher, if the upper troposphere warms stronger compared to the surface, and is lower if the surface warms stronger compared to the upper troposphere (Boeke et al., 2021). This describes the positive lapse-rate feedback in the Arctic, and some studies argue that the lapse-rate feedback is a primary cause of the Arctic Amplification (Boeke et al., 2021). Other processes, contributing to the Arctic Amplification, are heat and moisture fluxes in the atmosphere, heat transports of the ocean, and changes in frequencies and properties of clouds (Meredith et al., 2019; Serreze and Barry, 2011).

In contrast to the Arctic, the Antarctic doesn't show such a generally strong amplification of climate warming. The western part of Antarctica shows a warming, especially west of the Antarctic Peninsula, which is also associated with the melting of ice shelves contributing to sea level rise (Meredith et al., 2019). Contrary, the eastern part shows no significant temperature change (Meredith et al., 2019; Turner et al., 2009). Screen et al. (2018) shows a pole-ward shift of the troposheric westerly winds around Antarctica related to climate change. The Southern Ocean plays a large role for the transfer of atmospheric heat to the ocean, and the redistribution of the heat across the oceans (Meredith et al., 2019).

2.2.2. Ice nucleating particles over polar oceans

Despite recent activities of observational campaigns in remote oceans like the Southern Ocean Clouds, Radiation, Aerosol Transport Experimental Study (SOCRATES), the Measurements of Aerosols, Radiation, and Clouds over the Southern Ocean (MARCUS), the Clouds, Aerosols, Precipitation, Radiation, and atmospherIc Composition Over the southeRn oceaN (CAPRICORN) (McFarquhar et al., 2021), and the Multidisciplinary Drifting Observatory for the Study of Arctic Climate (MOSAiC) (Shupe et al., 2022), there is still a lack of knowledge about the INP concentrations, and most important INP sources over the Arctic Ocean and the Southern Ocean. Welti et al. (2020) show a summary of global ship-based INP measurements. INP concentrations over ocean are generally lower than INP concentrations over continents.

The INP concentration found in the Southern Ocean seem to be lower compared to the Arctic Ocean (Porter et al., 2022; McFarquhar et al., 2021; Welti et al., 2020; Bodas-Salcedo et al., 2016). This is probably related to the importance of aerosol transport to the Southern Ocean, while in the Arctic Ocean anthropogenic and terrestrial sources from continents are much closer compared to the relatively remote Southern Ocean (Radenz et al., 2021; Vergara-Temprado et al., 2018).

Recent studies suggest a high contribution of biogenic parts in sea spray aerosols from the sea surface microlayer, which are highly ice active at warm temperatures (Porter et al., 2022; Inoue et al., 2021; Twohy et al., 2021; Ickes et al., 2020; Wilson et al., 2015). They also propose a high relevance of these sea spray aerosols, especially in the rather pristine remote oceans like the Southern Ocean. Figure 2.8 shows the production of such sea spray aerosol by rising air bubbles in the water, which then burst when reaching the ocean surface. During the bursting process small film drops and later on a larger jet drop is produced and released to the air. Especially the smaller film drops seem to contain organic materials from the sea surface microlayer. Another mechanism to produce sea spray aerosols is by the wind friction on wave crests (Boucher, 2015).

Huang et al. (2021) shows an overview of biological INPs, and provides also a review of sea spray aerosols and its biological parts acting as INP. Irish et al. (2019b) showed correlations between INP concentrations and meteoric water. Meteoric water originates from precipitation flowing over terrestrial surfaces and reaching the ocean. Thereby, it can provide additional nutrients for the production and growth of marine microorganisms. Meteoric water may induce a major source of INPs in the sea surface microlayer and bulk sea water (Irish et al., 2019b). Ickes et al. (2020) found a strong diversity of ice nucleation ability of different sea surface microlayer samples at high temperatures. It was suggested that the strong ice nucleation availability at high temperatures is not caused by the marine algal cultures they investigated. Wilson et al. (2015) proposed phytoplankton cell exudates as one reason for the high ice-nucleating ability of the microlayer samples. Shi et al. (2023) showed that sea spray aerosols can also be lifted into higher altitudes by cyclones over the Southern Ocean.

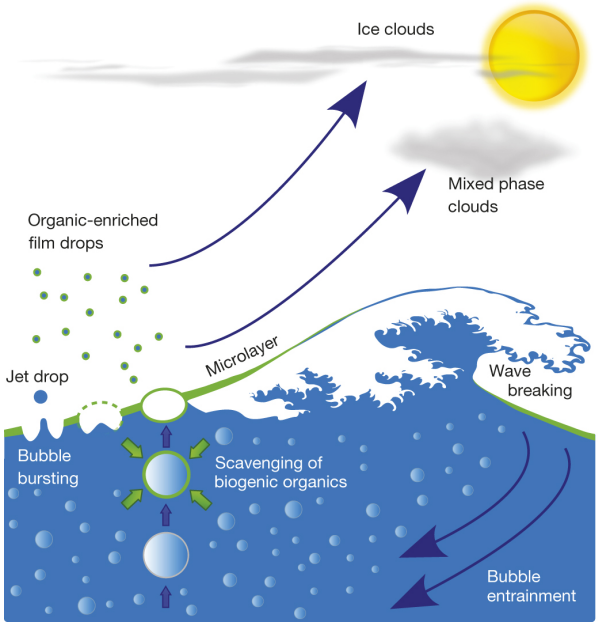

Figure 2.8.: Sea-spray aerosol particles enriched in organic material are generated when bubbles burst at the air–sea interface. Figure and caption with permission from Wilson et al. (2015).

Kawai et al. (2023) supposed Arctic dust to have an important role in the lower troposphere in the Arctic. Dust is a generally known to be an effective INP (compare Fig. 2.2, Kanji et al. (2017)). It is mainly produced by wind erosion of dry soils, which leads to the movement of larger particles, which can break if they are lifted to the air, but fall back on earth due to gravitational forces. The thereby produced smaller fractional particles can be suspended to the air (Boucher, 2015). Mineral dust aerosols are mainly produced over continents with dry soils without vegetation and can also be transported over large distances (Boucher, 2015).

There have been studies investigating the relevance of the different INP types over the Southern Ocean (McCluskey et al., 2018; Wilson et al., 2015), and the Arctic (Ocean) (Kawai et al., 2023; Porter et al., 2022; Inoue et al., 2021; Ickes et al., 2020; Irish et al., 2019a; Si et al., 2019; Wilson et al., 2015). Kawai et al. (2023) showed an importance of local Arctic dust for the INP concentration in the lower troposphere in summer and fall. Porter et al. (2022) showed high INP concentrations with biological parts and suggested the ocean close to the Russian coast as a source of wind-driven sea spray. Sze et al. (2023) and Wex et al. (2019) show higher INP concentrations in summer than in winter in the Arctic with a highly heat sensible fraction, pointing up highly ice active biological INPs. Hartmann et al. (2020) show generally low Arctic INP concentrations, but higher concentrations in the marine boundary layer. Irish et al. (2019a) supposed a higher importance of mineral dust than sea salt for samples from the Canadian Arctic. Inoue et al. (2021) found high INP concentrations close to marginal ice zone with high contents of organic carbon and sea salt highlighting the importance of marine organics in INPs. McCluskey et al. (2019) compared simulated number concentrations of INPs with observations of the North Atlantic and the Southern Ocean. Furthermore, the relative contribution of sea spray and mineral dust was shown,

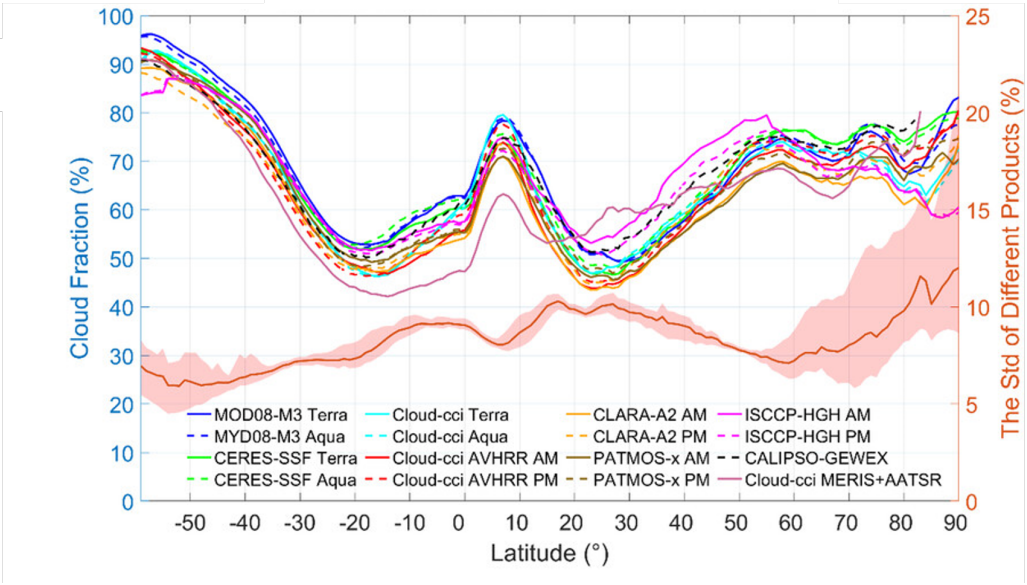

Figure 2.9.: The global latitude variation of daytime cloud fraction from 2003 to 2016. The bottom solid line represent the standard deviation of all products. Adapted figure from Liu et al. (2022). © American Meteorological Society. Used with permission.

with sea spray being more frequent in lower levels, while dust shows a higher contribution in higher levels.

Overall, the previous studies suggest an importance of marine organics over remote oceans, but the summary also highlights the need of further research on ice nucleation particles over remote oceans to improve the understanding of underlying processes and especially the relevance of different INPs in these regions.

2.3. Clouds over the Arctic and the Southern Ocean and related radiative biases

This section presents a literature review of clouds over the Arctic and the Southern Ocean, describing frequencies of cloud occurrences, cloud properties, and underlying processes. Furthermore, radiative biases related to clouds over these regions will be described and discussed. Both the Arctic Ocean, and the Southern Ocean are known to show high cloud frequencies (Siebesma et al., 2020; Houze, 2014; Mace et al., 2009), being slightly larger over the Southern Ocean compared to the Arctic Ocean (Liu et al., 2022). This can also be seen in Fig. 2.9 from Liu (2022) showing the cloud fraction as function of the latitude from different satellite observations. Especially, clouds at low levels occur frequently and can persist relatively long due to long-wave cooling at cloud top, and thereby induced turbulence and entrainment.

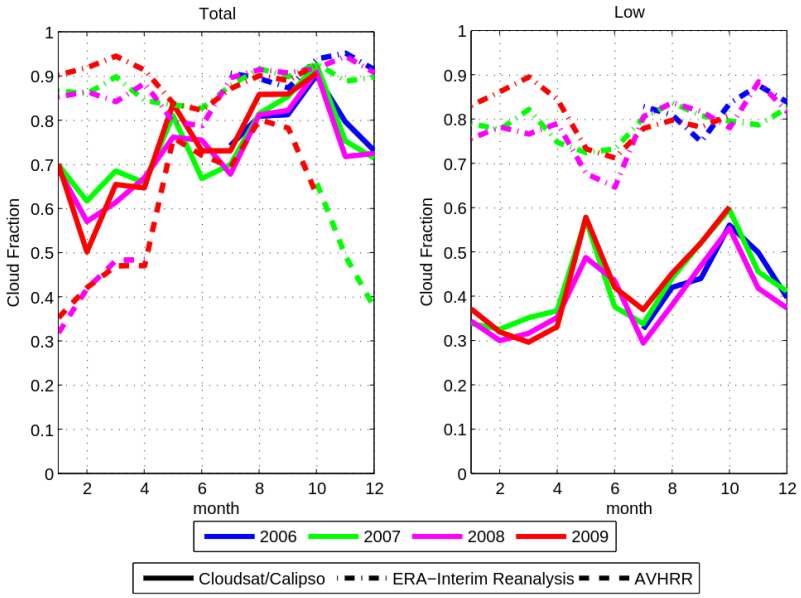

Figure 2.10.: Annual cycles of total- and low-level cloud fraction from 2006 to 2009 for the Arctic Ocean as derived from CloudSat/CALIPSO, ECMWF Reanalysis-Interim (ERA-Interim) and an Advanced Very High Resolution Radiometer (AVHRR)-based retrieval from the Satellite Application Facility on Climate Monitoring (CM-SAF). For low-level clouds no data is available from AVHRR. Figure and adapted caption from Zygmuntowska et al. (2012).

2.3.1. Arctic clouds

The Arctic shows cloud frequencies mainly larger than 50 % to 60 % throughout the year, exceeding 70 % to 90 % in the summer months (Siebesma et al., 2020; Houze, 2014; Zygmuntowska et al., 2012; Intrieri et al., 2002). Figure 2.10 shows the annual cycle of the cloud fraction from different datasets. The high occurrence of low-level clouds in summer months over the Arctic Ocean is related to a northward transport of warm air over the cold ocean surface, leading to condensation due to the cooling of the northward transported air. Due to this process, mainly stratiform low-level clouds form. A different formation process occurs if cold air from the northern snow-covered continents or sea ice is transported southwards over the relatively warm open ocean. This leads to the warming of the air mass and the ocean provides a strong source of humidity leading to small scale convection forming stratocumulus clouds. This phenomena is also called marine cold-air outbreak (Siebesma et al., 2020; Houze, 2014). Persistent Arctic mixed-phase clouds are often associated with weak synoptic forcing and subsidence (Morrison et al., 2012). Case studies of mixed-phase low clouds over the Arctic showed that water vapor advection is an important large-scale factor for the development of low clouds, while vertical velocity seem to play a minor role (Pinto, 1998).

Shupe (2011) investigated cloud phase of Arctic clouds from observatories and found a frequency of ice in clouds of about 60 % to 70 % throughout the year, while liquid water in clouds shows the highest frequencies in late summer and fall, related to higher temperatures and available moisture. The annually

averaged frequency of mixed-phase clouds is found to be between 25 % and 47 % depending on the location and shows highest frequencies in late summer and fall.
Morrison et al. (2012) also summarizes various interacting processes leading to the persistence of the mixed-phase clouds, which are inherent unstable due to the Wegener-Bergeron Findeisen process. Feedbacks between local processes of turbulence, updrafts, and radiative cooling are one way of explaining the persistence of mixed-phase clouds. Another one is based on large-scale advection leading to a moisture inversion at cloud top and entrainment. In surface-coupled clouds the induced surface warming increases instability and can thereby also help to sustain mixed-phase clouds. Furthermore, the fall-out of the ice particles due to gravitational force, also known as ice virga, reduces the impact of the Wegener-Bergeron-Findeisen process and helps sustaining the supercooled liquid water in the cloud (Morrison et al., 2012).

2.3.2. Clouds over the Southern Ocean

Over the Southern Ocean, clouds are mainly low clouds connected to the warm and cold sector of extratropical cyclones (McFarquhar et al., 2021; Mace et al., 2009; IPCC, 2013). The Southern Ocean is characterized by the Antarctic Circumpolar Current and very strong westerly winds, as described in Sec. 2.2. Connected to these westerly winds are frequent strong cyclones (Lin et al., 2023).
Xi et al. (2022) investigated data of the MARCUS field campaign and found a total cloud fraction of 77.9 % over the Southern Ocean with highest frequencies of low-level and deep convective clouds. Furthermore, high frequencies of mixed-phase clouds (54.5 %) have been found (Xi et al., 2022). Zaremba et al. (2020) characterized cloud top phases of clouds in the cold sector based on airborne remote sensing observations during SOCRATES and found that 91.7 % of clouds with subfreezing temperatures contain supercooled liquid water in the top 96 m. 79.9 % of the cases are found to be entirely liquid (Zaremba et al., 2020). Schima et al. (2022) found as well high probabilities of about 80 % of supercooled liquid water at cloud top of convective and stratiform clouds analyzing SOCRATES data. They also state, that ice production was associated with convective activity with highest probabilities 200 m below cloud top (50 % to 70 %), while stratiform cloud show a probability of ice production lower than 30 %. Mace et al. (2021) analyzed space-born and surface-based lidar and radar observations over the Southern Ocean and found that supercooled clouds are typically thinner than 1 km and rarely contain ice.
Huang et al. (2015) compared clouds over the North Atlantic and the Southern Ocean. They found high frequencies of boundary layer clouds in both regions. The occurrence of supercooled liquid water was found to be higher over the Southern Ocean compared to the North Atlantic, especially during the summer period. Mid-level clouds occur more frequently over the Southern Ocean, as well especially in summer. Except for the clouds connected to cyclone events, marine cold air outbreaks also occur over the southern hemisphere, if cold air from Antarctica is transported northwards to the warmer open ocean (Papritz et al., 2015; Bracegirdle and Kolstad, 2010). Such marine cold air outbreaks occur equally frequent over the Arctic and the Southern Ocean, but with less extreme values over the Southern Ocean

(Kolstad, 2011; Bracegirdle and Kolstad, 2010). Several studies highlighted the high occurrence of supercooled liquid clouds over the Southern Ocean (Huang et al., 2012; Hu et al., 2010). Hu et al. (2010) found that more than 95 % of low-level clouds over high latitudes within the mixed-phase temperature regime are water clouds. They further found that the presence of supercooled water is highest over snow- and ice-covered surfaces in high latitudes.

2.3.3. Radiative biases in models[1]

The following part summarizes previous research on the representation of clouds in weather and climate models with a focus on the region of the Arctic and the Southern Ocean. A literature review on uncertainties and biases related to clouds and their phase is presented, as they can lead to large biases in the simulated radiation of climate models.

Radiative biases over the Southern Ocean

Cloud phase has a major influence on the Earth's radiation budget due to different scattering, absorption and emission properties of liquid droplets and ice particles. Weather and climate models show strong biases in the shortwave radiation over the Southern Ocean related to biases in the representation of clouds and their phase (e.g. Cesana et al., 2022; Forbes and Ahlgrimm, 2014). Although in the recent sixth phase of the Coupled Model Intercomparison Project (CMIP6), models have improved their representation of clouds compared to the results of CMIP5, the cloud feedback remains the largest source of uncertainty in climate feedbacks (Arias et al., 2021; Forster et al., 2021). The CMIP5 results (Taylor et al., 2012) showed large radiative biases over the Southern Ocean caused by a lack of supercooled liquid water mainly in the cold sector of cyclones (Arias et al., 2021; McFarquhar et al., 2021; Bodas-Salcedo et al., 2016). Cesana et al. (2022) showed that CMIP6 simulations reduced the average radiative bias over the Southern Ocean by increasing the number of low- and mid-level clouds. Models with more complex microphysics than only temperature depedent liquid and ice partitioning tend to show a better representation of the liquid phase fraction, but all models struggle to generate the correct shortwave reflection south of 55 °S (Cesana et al., 2022). This is shown in Fig. 2.11 from Cesana et al. (2022), which also highlights the strong variations between the different CMIP6 models, which have a typical horizontal resolution of about 100 km (Cesana et al., 2022).
Zelinka et al. (2020) showed that the increased climate sensitivity in CMIP6 compared to CMIP5 is related to an increase of the shortwave low cloud feedback in the extratropics. The increased feedback is based on a stronger reduction in cloud cover and weaker increased cloud liquid water path with warming, due to the changes made to the amount of supercooled liquid water to reduce the long-standing biases (Zelinka et al., 2020). Contrary to previous results, where "too few and too bright" stratocumulus clouds were simulated, CMIP6 results show too many stratocumulus clouds over the Southern Ocean, which

[1] Parts of this section have already been submitted to Atmospheric Chemistry and Physics as part of the introduction in Dietel et al. (2023)

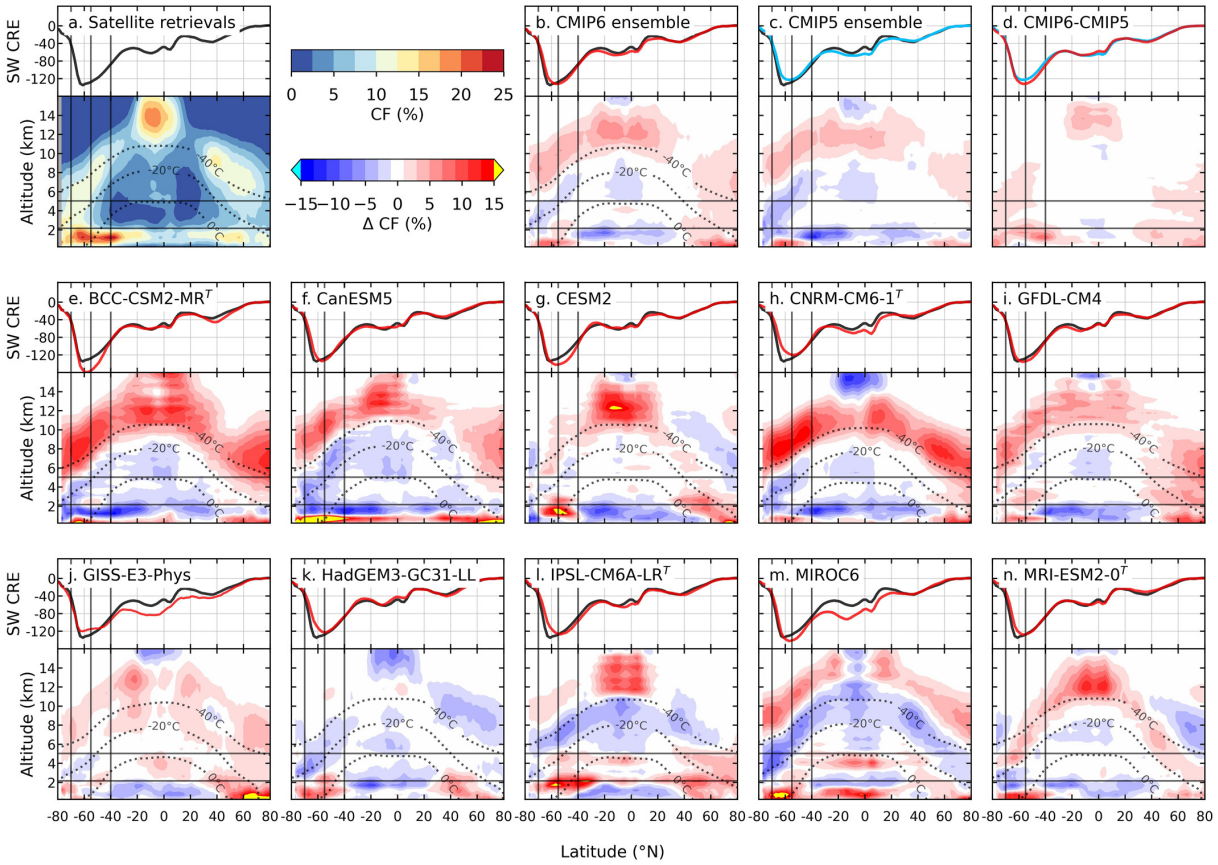

Figure 2.11.: Relationship between cloud fraction (CF) profiles and shortwave cloud radiative effect at the top of the atmosphere (SWCRETOA). During the austral summer zonal profiles of cloud fraction (%) for General Circulation Model-Oriented CALIPSO Cloud Product (2008–2015) and cloud fraction biases (%) for the Coupled Model Intercomparison Project (CMIP) lidar simulator outputs, and zonal means of SWCRETOA for Clouds and the Earth's Radiant Energy System (2008–2015, black line) and for the CMIP outputs (red line, Wm^{-2}) in the upper part of each subplot. The 0, −20, and −40 °C isotherms (dotted black lines) help locate mixed-phase temperatures. The Southern Ocean and low- and mid-levels are emphasized by horizontal black lines and the vertical black lines mark the 40 °S, 70 °S, and 55 °S where the 0 °C isotherm meets the surface. Figure and adapted caption with permission from Cesana et al. (2022).

are not bright enough compared to observations (Schuddeboom and McDonald, 2021). To improve the radiative balance over the Southern Ocean, the accurate representation of stratocumulus clouds in simulations should remain a priority (Schuddeboom and McDonald, 2021). Desai et al. (2023) showed the underestimation of the ice phase below cloud top in low-level clouds over the Southern Ocean in the Energy Exascale Earth System Model version 1 (E3SMv1). Besides low-level clouds, CMIP6 models also struggle to simulate the correct optical properties and regime variability of mid-level topped clouds forming in the boundary layer over the Southern Ocean leading to errors in the shortwave reflection (Cesana et al., 2022). Based on the different definitions of cloud types, the results of previous papers differ in finding the source of the radiative biases either in low-level stratocumuls clouds only (Schuddeboom and McDonald, 2021) or in low-level and mid-level clouds (Cesana et al., 2022). Furthermore, there is a lack of studies investigating mid-level clouds, which were described as the "forgotten clouds" by Vonder Haar et al. (1997). Until now the number of studies on mid-level clouds (Alexander and Protat, 2018; Kayetha and Collins, 2016; Mason et al., 2014; Sassen and Wang, 2012; Zhang et al., 2010; Smith et al., 2009; Fleishauer et al., 2002) is limited and they often only examine case studies, or focus on specific mid-level clouds, such as optically thin ice clouds or liquid-layer topped clouds.
Besides the large errors over the Southern Ocean, the representation of low-level clouds in the Arctic also shows large uncertainties in model simulations (Taylor et al., 2019).

Radiative biases over the Arctic

Taylor et al. (2019) also pinpoint the need of an improved understanding of the ice formation and the cloud phase partitioning. Wei et al. (2021) showed a too high cloud fraction over the Arctic in CMIP6 simulations compared to various satellite observations leading to the underestimation of the shortwave radiation at the surface. Figure 2.11 also shows an increased bias in the cloud fraction over the Arctic region from CMIP5 to CMIP6, even if this was not the scope of the study from Cesana et al. (2022). The overestimated cloud fraction over the Arctic in CMIP6 leads to an underestimation of the shortwave radiation reaching the surface due to cloud reflection, and to an underestimation of the surface energy longwave loss due to the absorption of longwave radiation in clouds (Wei et al., 2021). Tjernström et al. (2021) showed that the Integrated Forecasting System (IFS) of the European Centre for Medium-Range Weather Forecasts (ECMWF) shows too much cloud occurrence below 3km and not enough between 3km and 5km. A too high cloud cover below 3km was also seen by McCusker et al. (2023) in the Met Office Unified Model (UM) and in the IFS. Comparing model results with observations from the Multidisciplinary drifting Observatory for the Study of Arctic Climate expedition (MOSAiC, see Shupe et al. (2022)) during winter, all operational and experimental forecast system models underestimated the liquid water path (LWP) and overestimated the ice water path (IWP) (Solomon et al., 2023). Klein et al. (2009) showed as well too small LWP in cloud-resolving model and single-column model simulations compared to observations for a case study of Arctic single-layer clouds, but simulated IWP being generally consistent with observations.

2.3.4. Summary

The previous section provided an overview of the characteristics over the Arctic Ocean and the Southern Ocean, starting with the general difference of the land-sea distribution, and consequences on the ocean currents, and wind patterns. A generally high frequency of clouds over these regions especially in low and middle heights have been found with all cloud phases being frequently observed. An importance of marine organic INPs in this regions has been shown, while there are still gaps in the knowledge of the sources and the quantification of their relevance with respect to other aerosol types. It has also been shown that large uncertainties in weather and climate models are found in these regions based on the representation of clouds and their phase, leading to radiative biases in climate models.
This highlights the need of further research on the phase of clouds in low and middle heights over these regions to understand underlying processes and provide the knowledge to improve their representation in models, which is the scope of this work.

3. Data

This chapter describes the datasets used for this work. First, definitions of the regions of the Arctic Ocean and the Southern Ocean are mentioned, as well as the investigated times. The second section provides information of the main dataset, providing the information of clouds and their phase from active satellite observations. Furthermore, data on the sea ice concentrations from a passive microwave satellite instrument, the reanalysis dataset of aerosols mixing ratios, and the satellite-based data of cloud radiative effects are described. The third section describes the data used to investigate the representation of clouds and their phase in ICON-model simulations provided as part of the model-intercomparison project DYAMOND. A brief overview of the model setup, used schemes, and grid resolutions is provided for each used simulation.

3.1. Region and time

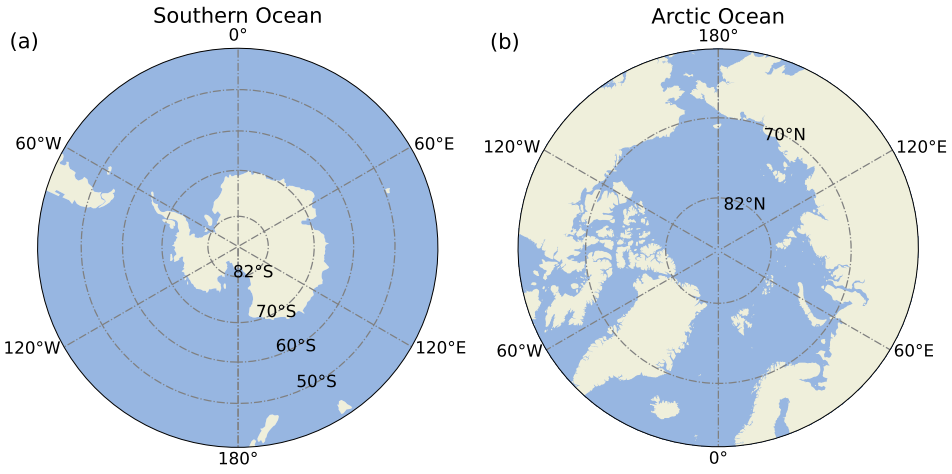

Figure 3.1.: Maps of the investigated regions. Panel (a) shows the Southern Ocean, and panel (b) shows the Arctic Ocean. The pole-ward boundary of 82 °S and 82 °N is shown by a dashed line and based on the boundary of CloudSat and CALIOP observations due to their orbital track.

This work investigates clouds over the Southern and the Arctic Ocean (see Fig. 3.1). The Southern Ocean is defined as a region with latitudes between 82 °S and 40 °S. The Arctic Ocean is defined by latitudes between 60 °N and 82 °N. Both definitions are used throughout this thesis, unless another definition is mentioned explicitly, as in Sec. 5.3 about cloud radiative effects. 82 °N and 82 °S are the polar borders of observations from CloudSat and the Cloud-Aerosol Lidar and Infrared Pathfinder Satellite Observation

(CALIPSO). Generally, only columns over the ocean and sea ice are investigated, while profiles over land surfaces are excluded from the analysis to reduce uncertainties due to orographic effects. Mainly, data for the full years of 2007 and 2008 are used, as the data availability of the dataset is optimal in these two years, without larger gaps. This can be seen in Fig. 3.2 which shows the number of DARDAR profiles over the Arctic Ocean and the Southern Ocean available per day. Only in the analysis of the DYAMOND data and their comparison with observations, different times are used, which are described in detail in Sec. 3.3.1, Sec. 3.3.2, and Sec. 3.3.3.

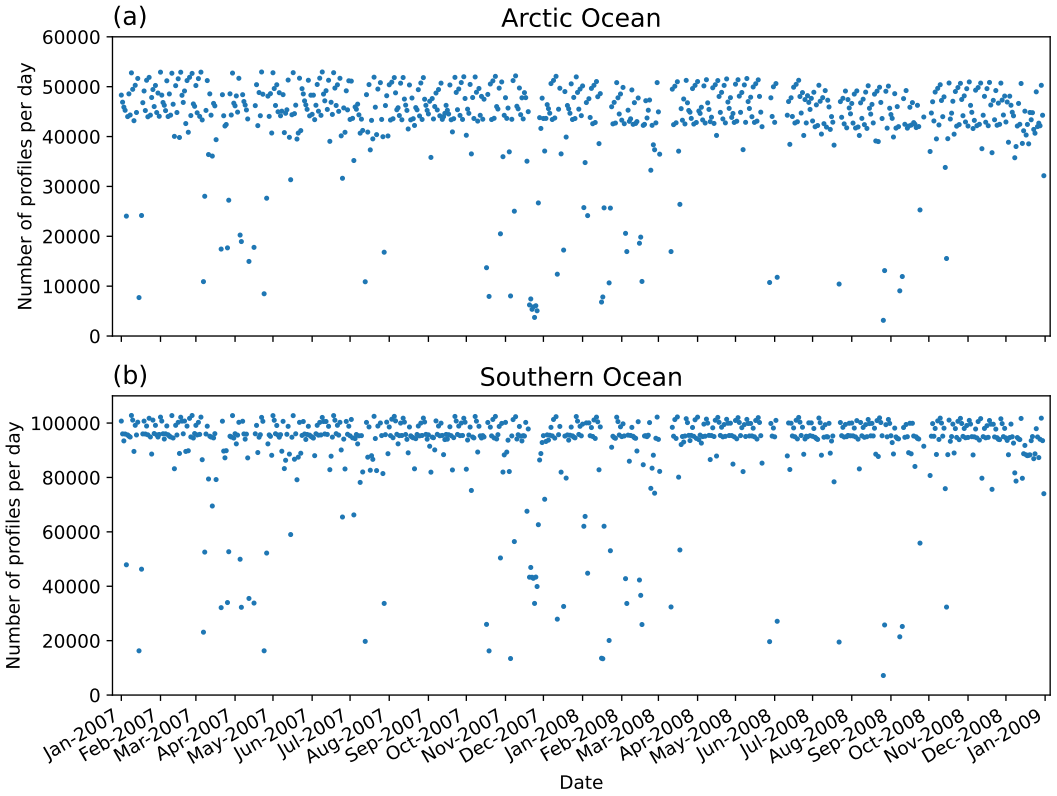

Figure 3.2.: Number of DARDAR profile observations per day from 1 January 2007 until 31 December 2008. The generally higher numbers over the Southern Ocean compared to the Arctic Ocean are due to the larger region (40 °S - 82 °S) of the defined Southern Ocean compared to definition of the Arctic Ocean (60 °N - 82 °N).

3.2. Observational data and reanalysis

The following subsections will describe the different observational datasets and reanalysis used within this thesis. The observations are satellite based and partly include additional analyses from the Euro-

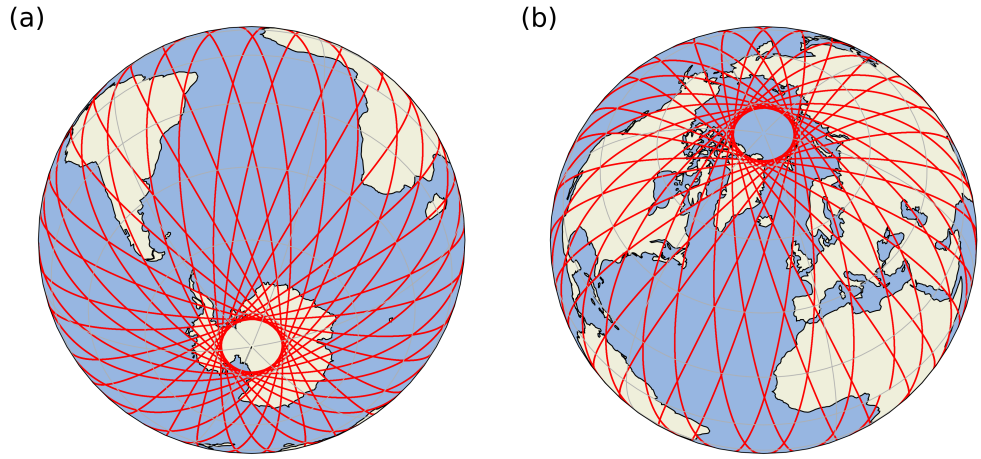

Figure 3.3.: Track of the sun-synchronous orbit of the A-Train, which the CloudSat and CALIPSO satellite are part of. The northern and southern boundary of observations at 82 °N/S due to the orbital track is also shown.

pean Centre for Medium-Range Weather Forecasts (ECMWF), and are described in Sec. 3.2.1 - 3.2.4. Furthermore, reanalysis data for aerosols are used and described in Sec. 3.2.3.

3.2.1. Cloud phase categorization from DARDAR

A detailed phase categorization of cloud profiles is provided in the raDAR/liDAR (DARDAR) dataset (Delanoë and Hogan, 2008, 2010; Sourdeval et al., 2018) from ICARE (Institut de Combustion, Aérothermique, Réactivité et Environnement) Data and Service Centre. The dataset is mainly based on observations from CloudSat (Stephens et al., 2002) and from the Cloud-Aerosol Lidar and Infrared Pathfinder Satellite Observations (CALIPSO) (Winker et al., 2009, 2010). The CloudSat satellite has a 94-GHz cloud profiling radar (CPR) onboard. CALIPSO carries the Cloud-Aerosol Lidar with Orthogonal Polarization (CALIOP), a lidar with orthogonal polarization, and two wavelengths, namely 532 nm and 1064 nm. Both CloudSat and CALIPSO are part of the A-Train following a polar sun-synchronous orbit (compare Fig. 3.3). The A-Train constellation is a formation of several satellites following the same track, to observe the same or similar part of the Earth with different satellite instruments and thereby provide a comprehensive dataset. For example, CloudSat flies about 15 s ahead of CALIPSO to overlap the footprint of the radar signal with the one of the lidar signal during at least 50 % of the time. Stephens et al. (2008) stated that analysis showed that the overlap occurs in more than 90 % of the time. CALIPSO and CloudSat were launched in April 2006.

The advantage of the usage of active remote sensing instruments like radar and lidar compared to passive instruments is the vertically resolved information. Active remote sensing instruments emit radiation by sending out a pulsed signal and measure the signal coming back due to reflection and scattering. Using

the time difference between the emission of the signal and the detection of the returning signal, which is the travel time of the signal, information on the distance of the object which scattered or reflected the signal can be gained.

The following paragraph describes some technical details about the instruments CALIOP onboard the satellite CALIPSO (based on Winker et al. (2009)) and the CPR onboard CloudSat (based on Stephens et al. (2002, 2008)), because they provide the main information for later described cloud phase categorization. The beam sent by CALIOP has diameter of 70 m at the surface of the Earth, while the diameter of the receiver footprint is 90 m at the Earth's surface. By sending a laser pulse every 0.0496 s ($\equiv$ 20.16 Hz) a footprint is provided every 335 m along the ground track. The initial vertical sampling resolution is 30 m. To reduce required telemetry bandwidth, and as spatial scales of atmospheric phenomena increase with increasing height, the signal is averaged depending on the height before downlinking. From ground until a height of 8.2 km, the horizontal resolution is 0.33 km and the vertical resolution is 30 m. From a height of 8.2 km until heights of 20.2 km the horizontal resolution is 1 km, and the vertical resolution is 60 m. The vertical resolution of the CPR is 500 m, and the horizontal resolution is 1.3 km to 1.4 km cross-track and 1.7 km to 1.8 km along-track (Winker et al., 2009; Stephens et al., 2002, 2008).

By combining the observations of the CPR and CALIOP, the DARDAR project provides retrieved cloud properties with a horizontal grid resolution of 1.5 km, corresponding to the CloudSat footprint, and a vertical resolution of 60 m, corresponding to the vertical resolution of CALIOP observations. For this thesis, we use the second version of the DARDAR-MASK dataset providing a cloud phase categorization. A detailed description of the algorithm can be found in Ceccaldi et al. (2013). To distinguish between liquid and ice in clouds, the reflectivity from the CloudSat radar, the CALIOP backscatter of the 532 nm channel, and the wet bulb temperature from the ECMWF AUXillary (ECMWF-AUX) data are mainly used. Due to the shorter wavelength of the lidar, it is more sensitive to smaller particles and to a large number of particles like supercooled droplets and many small ice crystals. Contrary, the radar is sensitive to larger particles like rain droplets or large ice crystals, as explained in Sec. 2.1.5. The combination of both of these instruments is one of the most accurate methods to distinguish vertical cloud phase.

The next paragraph describes parts of the algorithm and is based on the information given by Ceccaldi et al. (2013) and Delanoë and Hogan (2010). Using certain thresholds for the backscatter information from the lidar, and the reflectivity from the radar, a combined cloud mask is generated. The lidar information is also used to distinguish between aerosol and clouds. Artificial cloud top information from the radar signal, caused by the change of the original resolution of the radar signal of 500 m to 60 m, are removed using the lidar information. Table 4.1 shows the different categories resulting from the DARDAR algorithm. An overview of the algorithm for the categories used in this study are shown in the decision tree in Fig. 3.4. Summarizing the diagram for rain categories, the rain is categorized for a radar reflectivity larger than -17 dBZ, with further details depending on the lidar signal, and the cloud phase, the rain is originating from. The cloud phase categorization is strongly based on the wet bulb temperature (T_w) from ECMWF-AUX. The liquid phase is set, if T_w is larger or equal than 0 °C, or if a strong backscatter

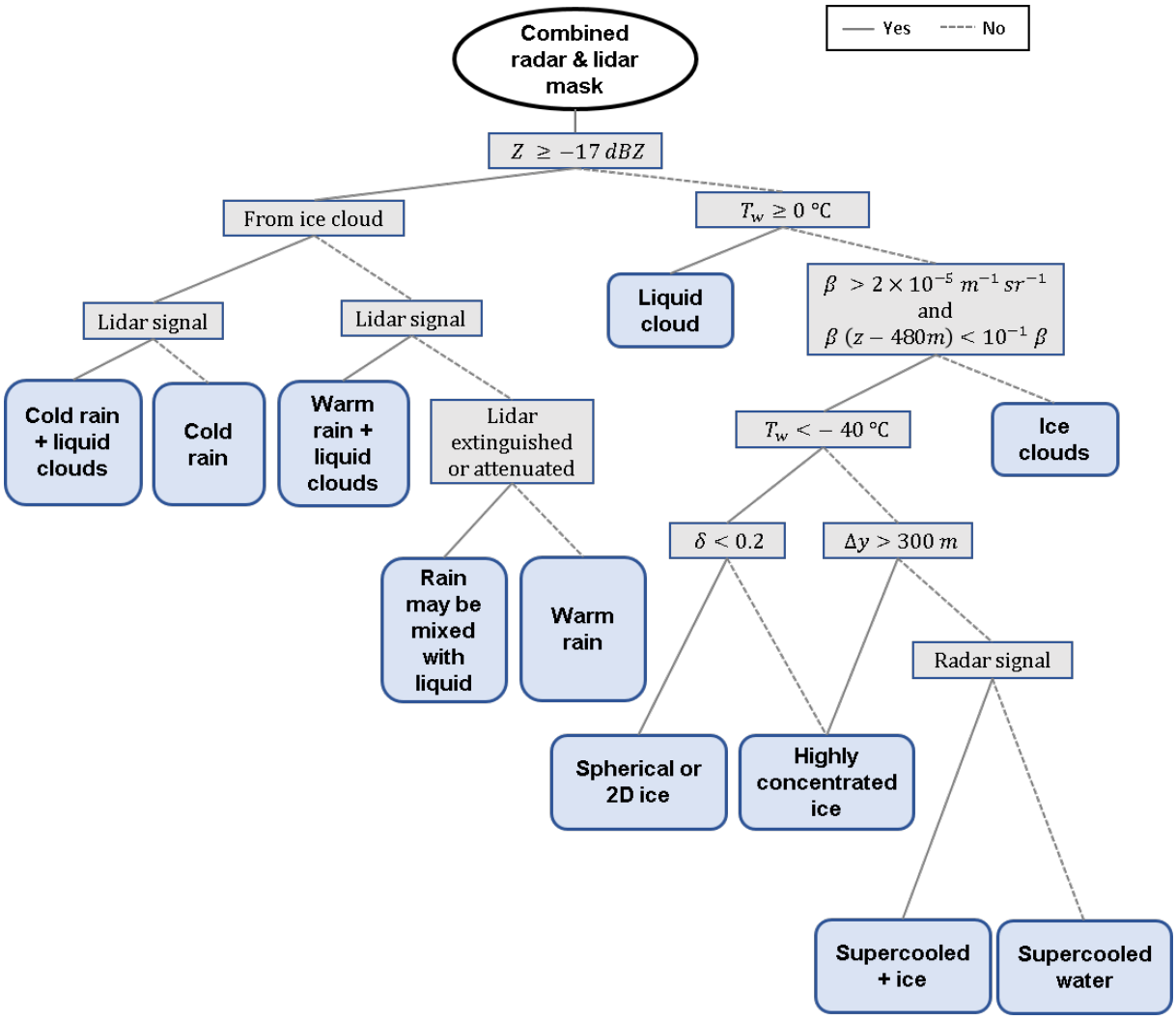

Figure 3.4.: Overview of the DARDAR algorithm to categorize cloud phase. Z is the radar reflectivity, β is the backscatter signal of the 532 nm wavelength from CALIOP, δ is the depolarization ratio, Δz the vertical extent of the layer, and T_w is the wet bulb temperature based ECMWF-AUX. The condition with $\beta > 2 \times 10^{-5}\,\mathrm{m^{-1}sr^{-1}}$ and $\beta(z - 480\,\mathrm{m}) < 10^{-1}\beta$ describes that the lidar backscatter should drop by a factor of 10 within the next 480 m below the pixels, where the lidar backscatter is larger than $2 \times 10^{-5}\,\mathrm{m^{-1}sr^{-1}}$. The category *Multiple scattering due to supercooled liquid water* is not included in the decision tree, but is based on an already classified supercooled liquid layer. If the lidar signal is not completely attenuated by that layer, and the radar shows no signal below that supercooled liquid layer, but the lidar does, these pixels are classified as *Multiple scattering due to supercooled liquid water*. The information of the decision tree are based on Ceccaldi et al. (2013) and Delanoë and Hogan (2010). Adapted from Ceccaldi et al. (2013).

signal from the lidar is observed in the mixed-phase temperature regime, which strongly decreases due to attenuation. For T_w lower than −40 °C, and if the signal is mainly based on the radar observation, the cloud phase is assumed to be ice. Further details can be seen in Fig. 3.4, and found in Ceccaldi et al. (2013), or Delanoë and Hogan (2010).
Nevertheless, there are uncertainties related to instrument characteristics. One of the largest uncertainties is the strong attenuation of the lidar signal by supercooled liquid cloud layers. This can lead to the extinction of the lidar signal by supercooled liquid clouds resulting in no information about any supercooled liquid below an already existing supercooled liquid cloud layer. It might also lead to an underestimation of the vertical extent of supercooled liquid layers, but Hogan et al. (2003) showed that supercooled liquid layers tend to be vertically thin (100 m-200 m) using various ground-based and air-bone remote sensing instruments in combination with in-situ instruments. Alexander et al. (2021) also states that supercooled liquid layers tend to be vertically thinner than about 300 m citing Barrett et al. (2020), Ansmann et al. (2009), and Hogan et al. (2003). The observations of Barrett et al. (2020) and Hogan et al. (2003) are based on aircraft observations close to the UK, while Ansmann et al. (2009) used lidar observations over Cape Verde. Another uncertainty is related to the surface clutter of the radar and possible extinction of the lidar signal from upper cloud layers leading to the underestimation of clouds at heights of 0.2 km to 1.0 km by a factor of 3 compared to a surface-based lidar (Alexander and Protat, 2018).
Besides the phase categorization mask of DARDAR, the temperature from the ECMWF provided along with the CloudSat products as part of the ECMWF-AUX is used to analyze the cloud top temperature of each cloud profile.

3.2.2. Sea ice concentration from DMSP

To investigate the influence of sea ice coverage on the cloud phase, the daily sea ice concentrations from Nimbus-7 Scanning Multichannel Microwave Radiometer (SMMR), and the Defense Meteorological Satellite Program (DMSP) with the two sensors, the Special Sensor Microwave Imager (SSM/I) and the Special Sensor Microwave Imager/Sounder (SSMIS) (Cavalieri et al., 1996) is used. The version 1 data (NSIDC-0051) are available at the National Snow and Ice Data Center as part of the Cooperative Institute for Research in Environmental Sciences (CIRES) at the university of Colorado Boulder. The sea ice concentration is based on the brightness temperature observed from the passive microwave radiometers and provided on a polar stereographic projection with a grid cell resolution of 25 km times 25 km (Cavalieri et al., 1996). The brightness temperature is defined as the corresponding temperature of a black body that produces the same radiance as that measured by the satellite instrument.

3.2.3. Aerosol mixing ratios from CAMS reanalysis

Aerosols may have a large influence on the phase of cloud, as some of them act as ice nucleating particles. The ECMWF Atmospheric Composition Reanalysis 4 (EAC4) (Inness et al., 2019) from the Copernicus

Atmosphere Monitoring Service (CAMS) provides aerosol mixing ratios. Detailed information on the model configurations can be found in Inness et al. (2019). Various aerosol types, namely dust, sea salt, organic matter, black carbon, or sulphate aerosol are provided. Dust is provided in three size modes, namely 0.03 µm to 0.5 µm, 0.5 µm to 5 µm, and 5 µm to 20 µm. Sea salt is provided in three slightly different size modes, namely 0.03 µm to 0.55 µm, 0.55 µm to 0.9 µm, and 0.9 µm to 20 µm. Organic matter and black carbon are each provided in two categories with hydrophobic and hydrophilic aerosols. The horizontal resolution is about 80 km and the temporal resolution is 3-hourly (Inness et al., 2019). The aerosol optical depth (AOD) from the Moderate Resolution Imaging Spectroradiometer (MODIS) and from the Advanced Along-Track Scanning Radiometer (AATSR) is assimilated by a 4D-Var data assimilation system of ECMWF's Integrated Forecast System (IFS) (Inness et al., 2019). The production of sea salt from ocean surfaces is parameterized depending on the horizontal wind speed at 10 m ($u_{10\,\mathrm{m}}$) (Monahan et al., 1986). The dust emission parameterization is described in Ginoux et al. (2001) and depends as well mainly on $u_{10\,\mathrm{m}}$, and on the elevation in a surrounding area of 10°. A minimum threshold for the wind speed, depending on surface wetness, particle density and diameter, and air density, is used to enable dust emissions. Lapere et al. (2023) compare CAMS sea salt reanalysis with a few station observations in the Arctic and Antarctic and show in their Fig. 7 that most stations show strong Pearson correlation coefficients despite partly high normalized mean biases.
For the analysis, the different size modes of each aerosol type and the different categories (hydrophobic and hydrophilic) are summed up and the vertically averaged mixing ratio of the values collocated to each cloud profile is used.

3.2.4. Cloud radiative effects from 2B-FLXHR-LIDAR

The cloud radiative effect (CRE) of various cloud types at the top of the atmosphere (TOA) is analyzed as part of this thesis using the version P1_R05 of the CloudSat 2B-FLXHR-LIDAR product (Henderson et al., 2013; L'Ecuyer et al., 2008). The cloud radiative effect is defined as the difference between the net flux in clear-sky conditions and the net flux in all-sky conditions. The net flux is calculated as the difference between the upward flux ($F_\uparrow$) and the downward flux ($F_\downarrow$) (see Eq. 3.1) (L'Ecuyer et al., 2008).

$$CRE = (F_\uparrow - F_\downarrow)_{\mathrm{clear-sky}} - (F_\uparrow - F_\downarrow)_{\mathrm{all-sky}} \tag{3.1}$$

The radiative transfer algorithm estimates radiative fluxes based on CloudSat, CALIPSO, and MODIS products including cloud information like the ice water content, the liquid water content and the effective radius, precipitation information, but also aerosol information from CALIPSO, as well as temperature and humidity profiles from ECMWF analyses (Henderson et al., 2013). Further flux calculations are performed after removing all clouds to calculate the CRE.
The net cloud radiative effect (NETCRE) is calculated by summing up the longwave cloud radiative effect (LWCRE) and the shortwave cloud radiative effect (SWCRE).

Ham et al. (2017) provides a validation study comparing the CREs from the 2B-FLXHR-LIDAR dataset with the CERES-Calipso-CloudSat-MODIS (CCCM) and found global mean differences mostly smaller than $5\,\mathrm{Wm^{-2}}$, with the TOA SWCRE showing mostly more negative values over the Southern Ocean in CCCM compared to the 2B-FLXHR-LIDAR product. For a domain in the Southern Ocean (60 °W-0 °W, 60 °S-50 °S) CCCM shows a TOA SWCRE of $-158.7\,\mathrm{Wm^{-2}}$, while the 2B-FLXHR-LIDAR shows a TOA SWCRE of $-133.0\,\mathrm{Wm^{-2}}$. Over the Arctic Ocean, the signal is similar for longitudes between 100 °W and 100 °E with stronger negative values in CCCM than in the 2B-FLXHR-LIDAR, but shows the opposite for other longitudes with stronger negative values in 2B-FLXHR-LIDAR than in CCCM. But they also state that CCCM overestimates the SWCRE in midlatitude storm-track regions compared to CERES observations, due to larger cloud optical depths in CCCM.
Henderson et al. (2013) compared TOA fluxes from 2B-FLXHR-LIDAR with CERES and found a strong correlation with reduced biases compared to the previous CloudSat-only product (2B-FLXHR). The remaining biases in SW fluxes ($3.7\,\mathrm{Wm^{-2}}$ to $4.4\,\mathrm{Wm^{-2}}$) are related to uncertainties from the CloudSat estimates of liquid water content. In general, the 2B-FLXHR-LIDAR dataset benefits from the combined usage of the data from CPR on CloudSat, CALIOP on CALIPSO, and MODIS onboard of the Aqua satellite providing comprehensive information on cloud and aerosol locations and properties (Henderson et al., 2013).

3.3. Model data from different DYAMOND ICON runs

The DYnamics of the Atmospheric general circulation Modeled On Non-hdydrostatic Domains (DYAMOND) (Stevens et al., 2019) initiative was a model intercomparison study. Several storm-resolving models simulated the same 40 days for two phases, the DYAMOND Summer phase from 1 August 2016 to 10 September 2016, and the DYAMOND Winter phase from 20 January 2020 to 1 March 2020. The output of three ICOsahedral Nonhydrostatic (ICON) simulations described in the following sections is used for this thesis. An overview of the used ICON simulations is shown in Tab. 3.1.
The investigated DYAMOND ICON simulations use a one-moment graupel microphysics scheme, which is slightly extended to the prognostic five-category scheme (Zängl et al., 2015). The extensions are described in Seifert (2008) and concern cloud ice sedimentation. Doms et al. (2021) provide a detailed description of the three category ice scheme, including snow, rain, graupel, cloud ice, and cloud water as categories. Unfortunately, only cloud ice and cloud water are available as 3D output variables, while graupel, rain, and snow are only available as vertically integrated 2D variables from the DYAMOND simulations. The initial formation of ice from liquid droplets in the used one-moment microphysics scheme is only based on temperature (Doms et al., 2021). No aerosol information is used to assume a concentration of INPs. The formation of cloud water is based on the saturation and it is assumed that a sufficient number of CCN is present to initiate condensation if the air is saturated (Doms et al., 2021).

Table 3.1.: Overview of the analyzed DYAMOND ICON simulations

Model run	Grid resolution	Simulated time	Coupled
ICON-NWP Summer 2.5	2.5 km	1 Aug. 2016 - 10 Sep. 2016	No
ICON-NWP Winter 2.5	2.5 km	20 Jan. 2020 - 1 Mar. 2020	No
ICON-SAP Winter 2.5	5 km	20 Jan. 2020 - 1 Mar. 2020	Yes

The DYAMOND simulations use daily operational sea ice concentrations and sea surface temperature from ECMWF as initial data and boundary conditions (Stevens et al., 2019).

3.3.1. ICON-NWP Summer 2.5

The DYAMOND Summer ICON-NWP 2.5 simulation is a global simulation of the atmosphere with 2.5 km grid spacing (R2B10) and 90 vertical levels in the atmosphere. The first 10 days are the spin-up period, while the 30 days afterwards from 11 August are used for the analysis of this thesis. Mainly, three 3-hourly output variables on model levels from the simulations are used for this thesis, namely the temperature, the total specific cloud ice content (diagnostic), and the total specific cloud water content (diagnostic).

3.3.2. ICON-NWP Winter 2.5

The DYAMOND Winter ICON-NWP 2.5 simulation with a 2.5 km grid spacing (R2B10) is based on the same settings as the previously described ICON-NWP Summer 2.5 simulation, but simulated the period from 20 January 2020 until the 1 March 2020. Similarly to the summer simulation, the first 10 days are the spin-up period, while the 30 days afterwards from the 31 January are used for the analysis in this thesis.

Here we use the same variables as from the summer simulations, namely temperature, the mass fraction of cloud ice in air, and the mass fraction of cloud water in air. There might be slight uncertainties of the analysis due to the difference in the provided variables, as the summer simulation only provides the diagnostic variables of cloud ice and cloud water (*tot_qc_dia*, *tot_qi_dia*), while the winter simulation provides the prognostic variables (*cli*, *clw*).

Furthermore, the time step 00:00:00 is missing in the output of the winter simulation due to a setup problem of the ICON-NWP. To investigate if this leads to differences in the results, the influence of the 00:00:00 output time step in the DYAMOND summer dataset is analyzed. A comparison between the analysis of the summer results including the 00:00:00 output time step and excluding the 00:00:00 output time step is done. It is found that the results show almost no differences. The cloud type occurrences only change by not more than 0.03 % (see Fig. A.18). The fraction of the different phases showed a maximum difference of 0.3 % (compare Fig. A.19). Furthermore, the mean mass liquid fraction in Fig. A.20 also shows very similar results. Even though the differences might be stronger in the winter season,

the very small changes in the summer dataset suggests that the impact of the missing output time step in the winter dataset is small, and the results of the summer DYAMOND, the winter DYAMOND dataset, and the observations can still be compared.

3.3.3. Coupled ICON-SAP Winter 5

To analyze the differences in cloud phase over sea ice and over open ocean in model data, the coupled ICON-Sapphire (ICON-SAP) (Hohenegger et al., 2023) run with a horizontal grid resolution of 5 km (R2B09) is used. This run is part of the DYAMOND winter simulations and therefore runs from 20 January to 1 March 2020 with an analysis period from 31 January to 1 March 2020. Contrary to the previously described ICON atmosphere-only simulations, the ICON-SAP coupled run also simulates the ocean including sea ice, while the other simulations use ECMWF operational daily sea-ice concentrations as initial and boundary data (Stevens et al., 2019). The ICON-SAP model includes three model components, which are described in Hohenegger et al. (2023). Firstly, the atmosphere ICON model includes the dynamical core solving 3D non-hydrostatic Navier-Stokes equations with mass and energy conservation. Three parameterizations are used, which namely are the Radiative Transfer for Energetics - Rapid Radiation Transfer Model for General circulation model applications-Parallel (RTE-RRTMGP) for the radiation (Pincus et al., 2019), the one-moment graupel microphysics scheme (Baldauf et al., 2011) for cloud microphysical processes, and the Smagorinsky scheme (Smagorinsky, 1963) with modifications by (Lilly, 1962) for the turbulence. Secondly, the ocean is simulated with the ICON-OCEAN model (ICON-O) (Korn et al., 2022; Korn, 2018), including the ocean biogeochmistry simulated by the HAMburg Ocean Carbon Cycle (HAMOCC) model (Ilyina et al., 2013). The sea ice is influenced by a thermodynamic component describing freezing and melting (Semtner, 1976), and a dynamical component using a Finite-Element Sea Ice Model (FESIM) (Danilov et al., 2015). Thirdly, the ICON-LAND model simulated the land surface processes (including biogeochemistry) by using the Jena Scheme for Biosphere-Atmosphere Coupling in Hamburg (JSBACH) (Reick et al., 2021). The coupling between the ocean and the atmosphere is done by the Yet Another Coupler (YAC) (Hanke et al., 2016), while the coupling between the land and atmosphere is done implicitly by the turbulence routine. This section is mainly based on the description by Hohenegger et al. (2023).

4. Methodology

This chapter describes the methodology used within this thesis to investigate clouds, their phase, and the correlations with possible influencing factors based on the dataset described in the previous chapter. The first section describes the analysis of satellite-based data including collocated reanalysis. The second section describes the used machine learning method to investigate the importance of different parameters for cloud phase, as well as the dependence of the importance on other parameters. The third section describes the analysis of the ICON model data, which is in principle similar to the one using the observational data, but differs as well in some parts due to the availability of the provided datasets and variables from the model output.

4.1. Observations

The first section starts with a a brief description of the preprocessing and the focus on single-layer clouds. Afterwards, it is described how clouds are classified into different categories based on their cloud top height and cloud base height. Different ways of calculating the liquid fraction of clouds based on the provided phase categories are explained. The collocation and conditions of the sea ice and aerosol data are described in the following two parts. A last part of this section describes, how the vertical and horizontal extent of cloud objects are calculated.

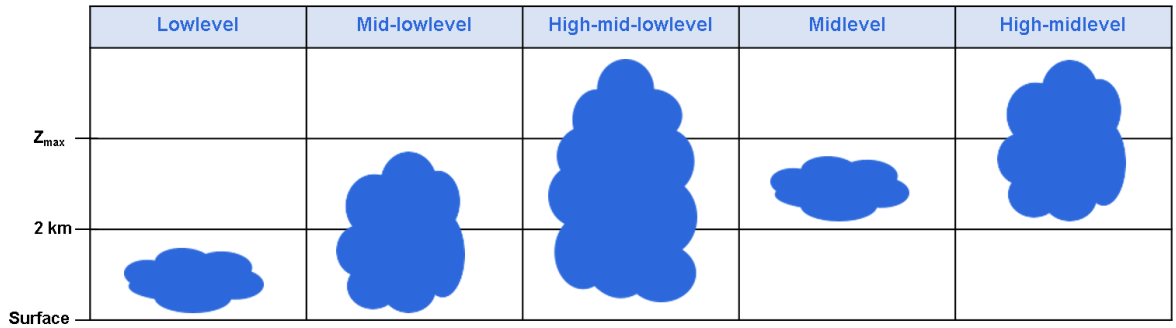

Figure 4.1.: Schematic of the different cloud types classified by their top and base heights. The upper threshold Z_{max} is a value between 4 km and 7 km depending on the latitude and described in Sec. 4.1.2. Reprinted from Dietel et al. (2023).

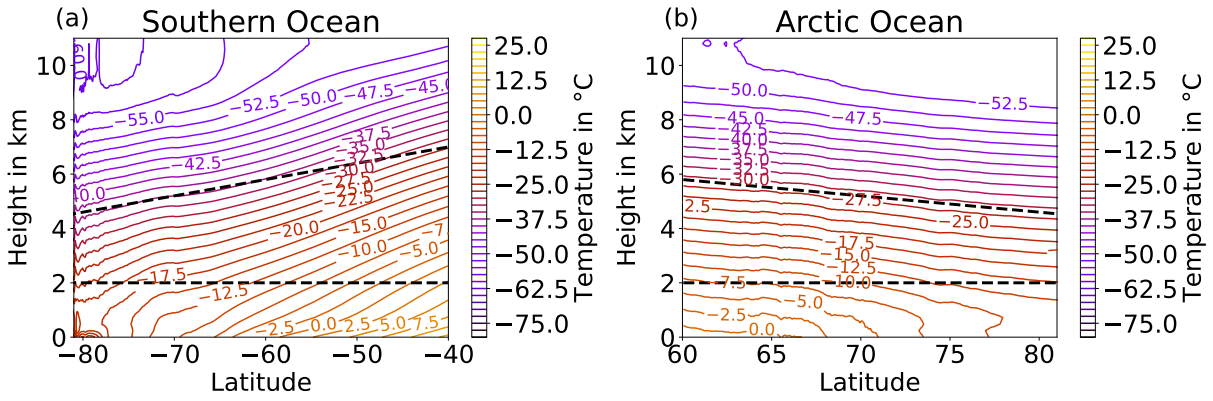

Figure 4.2.: Zonal mean temperature over the Southern Ocean (a) and the Arctic Ocean (b). The colored contours show the zonal mean temperature averaged between 2007 and 2008. The data are based on ECMWF reanalysis data, which are collocated to the DARDAR dataset. The black dashed lines indicate the thresholds of the atmosphere layers, to define the different cloud types. The lower threshold is at 2 km, the upper threshold height decreases polewards following Eq. 4.1. Reprinted from Dietel et al. (2023).

4.1.1. Collocating datasets and preprocessing

As a first step, the DARDAR data were collocated with the 2B-CLDCLASS-LIDAR dataset, which means that only profiles are considered that occur in both datasets. Only profiles with a single cloud layer are considered to reduce uncertainties due to the influence of overlapping clouds. This means that only profiles are considered that contain a single connected cloud layer from the phase mask of DARDAR without any gaps in between, as discontinuities don't allow a continuous analysis of e.g. the vertical phase distribution within a cloud. Thereby, multi-layer clouds are excluded from this study, which reduces the number of cloud profiles by about 50 %. Table 4.1 shows all categories from the DARDAR-MASK v2 classification and describes which of them we consider as a cloud and as which thermodynamic cloud phase they are assigned to. We calculate the cloud base height (CBH), the cloud top height (CTH), and the vertical extent for each cloud profile.

4.1.2. Cloud type classification

To distinguish between cloud types, the CBH and the CTH are used. Figure 4.1 shows a schematic of the cloud types investigated in this thesis. The troposphere is divided into three layers. The lower troposphere layer is defined from 0 km to 2 km. The middle troposphere layer is defined from 2 km to a threshold $Z_{\max}$, which increases from 4 km at the pole to 7 km at 40 ° based on the latitude (*lat*), see Eq. (4.1). Consequently, the highest layer in the troposphere is then defined by heights larger than the previously described threshold $Z_{\max}$. The two thresholds $Z_{\max}$ and 2 km defining the three tropospheric layers, are also shown in Fig. 4.2 with the dashed lines. The thresholds for the definitions are based on the definitions from the World Meteorological Organization (2017). Regarding the vertical distribution of the annual mean temperatures in Fig. 4.2, the threshold $Z_{\max}$ is also mostly parallel to the isotherms, which

Table 4.1.: DARDAR-MASK categories and how they are considered for the cloud phase analysis in this study

DARDAR-MASK v2	Considered Phase
Presence of liquid unknown	-
Surface and subsurface	-
Clear sky	-
Ice clouds	Ice
Spherical or 2D ice	Ice
Supercooled water	Liquid
Supercooled + ice	Mixed
Cold rain	-
Aerosol	-
Warm rain	-
Stratospheric clouds	-
Highly concentrated ice	Ice
Top of convective towers	-
Liquid cloud	Liquid
Warm rain + liquid clouds	Liquid
Cold rain + liquid clouds	Liquid
Rain may be mixed with liquid	Liquid
Multiple scattering due to supercooled water	Liquid

shows one of the reasons for the chosen threshold decreasing polewards. Furthermore, the threshold $Z_{\max}$ is in the upper part of the mixed-phase temperature regime.

$$Z_{\max} = \begin{cases} 4\,\mathrm{km} + \frac{7\,\mathrm{km}-4\,\mathrm{km}}{-40^\circ-(-90^\circ)} \cdot (90^\circ - lat) & \text{, if } lat > 0. \\ 4\,\mathrm{km} + \frac{7\,\mathrm{km}-4\,\mathrm{km}}{-40^\circ-(-90^\circ)} \cdot (90^\circ + lat) & \text{, if } lat < 0. \end{cases} \tag{4.1}$$

Low-level clouds (L) are defined by a CBH and CTH between 0 km and 2 km, compare first column in Fig. 4.1. The second column in Fig. 4.1 shows mid-low-level clouds (ML) with CBH below 2 km and CTH between 2 km and $Z_{\max}$. Clouds with CBH between 0 km and 2 km and CTH larger than $Z_{\max}$ are called high-mid-low-level clouds (HML), see third column in Fig. 4.1. Mid-level clouds (M) have their CBH and their CTH between 2 km and $Z_{\max}$, shown in the forth column in Fig. 4.1. The last column in Fig. 4.1 shows high-mid-level clouds (HM) with CTH larger than $Z_{\max}$ and CBH between 2 km and $Z_{\max}$.

4.1.3. Phase analysis by calculating the liquid fraction

The liquid fraction f is calculated for each vertical cloud column by

$$f = \frac{n_{\mathrm{liq}} + 0.5 \cdot n_{\mathrm{mix}}}{n_{\mathrm{liq}} + n_{\mathrm{mix}} + n_{\mathrm{ice}}} \tag{4.2}$$

with n_{liq} being the number of liquid pixels of the cloud profile, n_{mix} being the number of mixed-phase pixels, and n_{ice} as the number of ice pixels. Due to the absence of better information it is assumed that half of each mixed-phase vertical bin consists of liquid droplets and half of it consists of frozen ice crystals, as the mixed-phase category is mainly based on a signal from both the radar and the lidar. Based on these calculations, a liquid fraction which is larger than 0 and less than 1 refers to mixed-phase cloud profiles. In the following, „liquid fractions“ or „vertical liquid fractions“ refer to this definition of f, unless otherwise stated.

The cloud top liquid fraction f_{CT} is calculated with Eq. 4.3 only considering the phase of cloud top pixels, i.e., the uppermost 60-m layer in each column that DARDAR defines as cloud. In Eq. 4.3 N_{liq} is the total number of liquid cloud top pixels, N_{mix} is the total number of mixed-phase cloud top pixels, and N_{ice} is the total number of ice pixels at cloud top. f_{CT} is not meaningful for a single cloudy pixel, but is statistically evaluated for all clouds with a given cloud top temperature.

$$f_{\mathrm{CT}} = \frac{N_{\mathrm{liq}} + 0.5 \cdot N_{\mathrm{mix}}}{N_{\mathrm{liq}} + N_{\mathrm{mix}} + N_{\mathrm{ice}}} \tag{4.3}$$

Instead of only investigating cloud top phase and cloud top temperature, the phase of each cloudy pixel can also be referred to the temperature of each cloudy pixel. This liquid fraction is further referenced as f_{T} and calculated by Eq. 4.4 with the total number of liquid pixels ($N_{\mathrm{liq}}^{\mathrm{cloudy}}$), the total number of mixed-phase pixels ($N_{\mathrm{mix}}^{\mathrm{cloudy}}$), and the total number of ice pixels ($N_{\mathrm{ice}}^{\mathrm{cloudy}}$). The phase of the pixels refers to Tab. 4.1 showing the considered phase for each DARDAR-MASK category. The difference of the calculation compared to Eq. 4.3 is the consideration of all cloudy pixels, and referencing them to their temperature, instead of considering cloud top temperature.

$$f_{\mathrm{T}} = \frac{N_{\mathrm{liq}}^{\mathrm{cloudy}} + 0.5 \cdot N_{\mathrm{mix}}^{\mathrm{cloudy}}}{N_{\mathrm{liq}}^{\mathrm{cloudy}} + N_{\mathrm{mix}}^{\mathrm{cloudy}} + N_{\mathrm{ice}}^{\mathrm{cloudy}}} \tag{4.4}$$

Figure 4.3 illustrates the three different ways to calculate the liquid fraction, and shows which parameters in the cloud column are considered in which calculation.

4.1.4. Sea ice concentration

The sea ice concentration closest to each cloud profile is used to analyze a possible influence of sea ice on the cloud phase (see Sec. 5.2.4). More precisely, open and sea-ice-covered ocean are distinguished. Open ocean is defined by a sea ice concentration of 0 %. For this analysis, a sea ice concentration larger or equal than 80 % is considered as sea-ice covered, which is based on the nomenclature from the World Meteorological Organization (JCOMM Expert Team on Sea Ice, 2009). Over the Southern Ocean, 72 % to 82 % of the cloud profiles occur over open ocean, 10 % to 16 % of the cloud profiles are over closed sea ice with the interval referring to the fraction for different cloud types. 8 % to 13 % of the cloud profiles over the Southern Ocean are over open ice with a sea ice concentration larger than 0 and lower

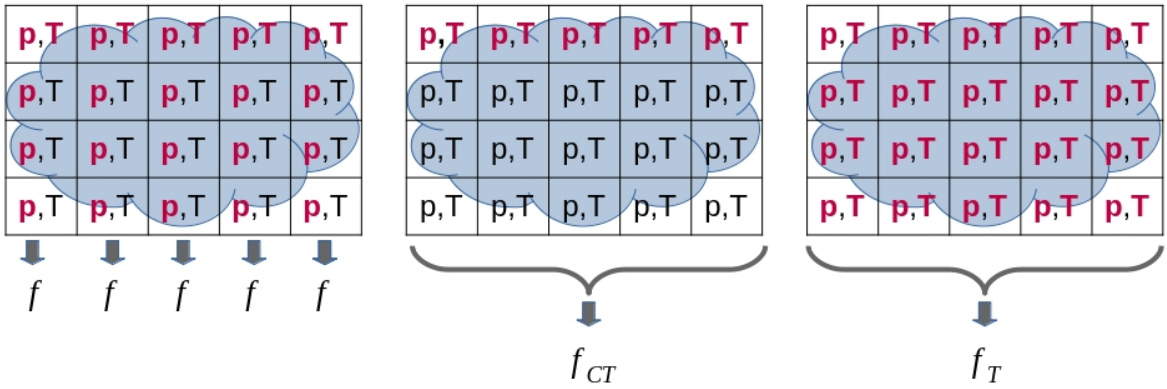

Figure 4.3.: Schematic illustration of the three different ways to calculate the liquid fraction. *p* refers to the detected phase of each cloudy pixel and *T* refers to the temperature of the pixel. The left picture corresponds to the vertical liquid fraction defined in Eq. 4.2, the middle picture corresponds to the cloud top liquid fraction defined in Eq. 4.3, and the right picture corresponds to the Eq. 4.4.

than 80 %, which are not analyzed in this study. Over the Arctic Ocean, the fraction of cloud profiles over open ocean is much lower with 33 % to 37 %, a higher fraction of the cloud profiles (43 % - 50 %) is over sea ice, and 17 % -23 % of the cloud profiles occur over open ice. To investigate the differences in cloud phase depending on the sea ice concentration, the mean liquid fraction of cloud profiles over the open ocean are compared with the mean liquid fraction of cloud profiles over sea ice. For each CTT-bin of 2 °C the distribution of the liquid fraction over ocean are compared to the distribution of the liquid fraction over sea ice, and it has been tested if the two distributions differ significantly using a Z-test and a p-value of 0.05.

4.1.5. CAMS aerosol reanalysis

CAMS reanalysis were collocated to the DARDAR profiles. The mixing ratio of the different size modes of each aerosol type are summed up, to only consider aerosol types, without a size dependence. For the analysis the mean aerosol mixing ratios in the cloud profiles observed by the DARDAR dataset are calculated. The difference between the mean liquid fraction of clouds with a high aerosol type mixing ratio, greater than the 75th percentile, and the mean liquid fraction of clouds with a low aerosol type mixing ratio, less than the 25th percentile, are calculated as a function of the CTT with a bin size of 2 °C. For both the low-high aerosol comparison the difference of the liquid fractions is only calculated if there are at least 500 cloud profiles in both categories for each CTT bin. These analysis are based on the statistics of individual profiles and no spatial analysis is done for this part.

4.1.6. Horizontal and vertical cloud extent

In Sec. 5.2.1, the horizontal extent of the various cloud types and the correlation of the cloud phase with the horizontal extent is investigated. To examine the horizontal cloud extent, the time difference

between a specific cloud profile and the next cloud profile of the same cloud type along the satellite track is analyzed. If this time difference is less or equal than 0.2 s, which is the usual time difference to the next profile and corresponds to the resolution of the CloudSat profiles, the cloud profiles are considered as the same cloud. Time differences larger than 0.2 s indicate a gap of about 1 km between the cloud profiles, and the cloud profiles are therefore considered as separate clouds in absence of better information. Based on this separation, the phase of one cloud object, consisting of horizontally connected cloud profiles, is investigated. Only if all profiles are fully liquid, the cloud is considered as a liquid cloud. The same is valid for an ice cloud. Mixed-phase cloud objects either consist of ice profiles next to liquid profiles, or contain any mixed-phase profiles. In addition to the horizontal extent of the cloud, we also calculate the vertical extent by subtracting CBH from CTH for each vertical profile. For each cloud object, based on horizontally "connected" cloud profiles, the mean of the vertical extent of the single profiles is calculated to obtain the mean vertical extent of the cloud object. The horizontally connected profiles are only used for the analysis in Sec. 5.2.1. All other results are based on the single cloud profiles, no matter if they are connected or not.

4.2. Machine Learning

To investigate the importance of the different parameters on cloud phase, machine learning models are trained for different cloud types over the Southern and Arctic Ocean to predict the liquid fraction. SHapley Additive exPlanation (SHAP) values (Lundberg and Lee, 2017; Lundberg et al., 2020) are used to analyze the influence of various parameters on the predictions. The following parts describe the used dataset, the model training, and the usage of the SHAP values. An advantage of this method, is the possibility to investigate the importance of one parameter as function of other parameters. For example, the influence of dust on the prediction of the liquid fraction will be investigated as a function of the location given by latitude and longitude information (see Sec. 6.3).

4.2.1. Model concept and tuning

Based on the analysis of the satellite observations, four parameters, which influence cloud phase constitute the input for the machine learning model. The parameters are the cloud top temperature (see 3.2.1), the sea ice concentration (see Sec.3.2.2), the sea salt mixing ratio (see Sec. 3.2.3), and the dust mixing ratio (see Sec.3.2.3). Section 3.2.1 - 3.2.3 describes how data were collocated and for example how the mean aerosol mixing ratio in a cloud is defined in this study. Table 4.2 shows the total number of profiles of specific cloud types available from the two-year dataset. A random subsample of these datasets is used to train the machine learning models (see Table 4.3). A second distinct subsample with the same number of elements as the training set is used for validation and calculating the model scores.
A Histogram-based Gradient Boosting Regression Tree model is used, provided by python package scikit-learn (Pedregosa et al., 2011), because this is faster compared to other gradient boosting regres-

Table 4.2.: Sample size of the two-year dataset

	Low-level	Mid-level	Mid-low-level
Arctic Ocean	6 382 596	653 599	2 042 150
Southern Ocean	15 815 984	1 510 808	4 996 282

Table 4.3.: Sample size to train the machine learning models and to validate the model by the same number of different samples.

	Low-level	Mid-level	Mid-low-level
Arctic Ocean	3 000 000	300 000	1 000 000
Southern Ocean	5 000 000	700 000	2 000 000

sion models and efficient for datasets with a sample size larger than 10 000. The reason for the increased speed is that the numerical feature values are binned before the gradient boosting. In gradient boosting decision trees most of the training time and memory is spend on finding the optimal split. The previous transformation of the feature values into bins of histograms reduces the training process for finding the optimal split (Tamim Kashifi and Ahmad, 2022).

To find the optimal setting for the hyperparameters, grid search is used, provided by scikit-learn as GridSearchCV after a manual testing of parameters. Table 4.4 shows the used hyperparameter grid and the selected hyperparameters, which resulted in the best performance. A 3-fold cross validation is used for the grid search to find the optimal hyperparameters using the mean absolute error as a scoring function. Section A.2 shows further analysis of the model performance and the hyperparameter tuning.

Table 4.4.: Hyperparamter grid used to tune the model with grid search. Bold numbers are the chosen parameters for each model, which showed the best performance.

Hyperparameter	Region	Low-level	Mid-level	Mid-low-level
learning_rate	AO	0.1, **0.3**, 0.5	**0.1**, 0.3, 0.5	**0.1**, 0.3, 0.5
	SO	0.1, **0.3**, 0.5	0.1, **0.3**, 0.5	0.1, **0.3**, 0.5
max_iter in 1000	AO	**20**, 50, 100	2, 4, 6, **8**	2, 5, **10**, 20
	SO	20, 50, 70, **100**	1, 2, 5, **10**	5, 10, **20**
min_samples_leaf	AO	**10**, 30	**5**, 10, 30	**10**, 30
	SO	**10**, 30	**5**, 10, 30	**10**, 30
early_stopping	AO	True	True	True
	SO	True	True	True
n_iter_no_change	AO	20	70	20
	SO	70	70	20
tol	AO	10^{-22}	10^{-25}	10^{-22}
	SO	10^{-25}	10^{-25}	10^{-22}

The mean absolute error for both the training dataset and the validation dataset after the tuning is shown in Tab. 4.5 and in Fig. 4.4. The model predicting the liquid fraction of mid-low-level clouds shows the

Table 4.5.: Mean absolute error between the predicted liquid fraction and the observed liquid fraction for the validation dataset and in brackets for the training dataset.

	Low-level	Mid-level	Mid-low-level
Arctic Ocean	0.19 (0.15)	0.17 (0.13)	0.06 (0.05)
Southern Ocean	0.22 (0.19)	0.22 (0.16)	0.09 (0.08)

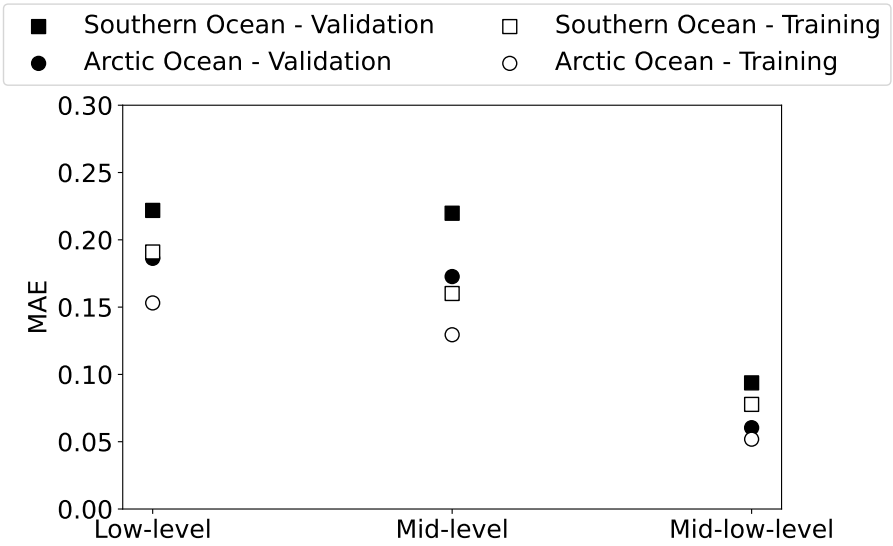

Figure 4.4.: Mean absolute error (MAE) in trainings and validation datsets of the different models of the different cloud types over each region.

best performance. Generally, the performance is better for clouds over the Arctic Ocean compared to the Southern Ocean. A possible reason for this may be other parameters not considered in this setting, which influence cloud phase over the Southern Ocean. The performance of the training dataset is better compared to the validation dataset, which is expected, but it is still in a similar range, which is important to avoid overfitting.

Table 4.6 shows the Pearson correlation coefficient between the predicted liquid fractions and the observed liquid fraction for the trainings dataset and the validation dataset. Similar to the mean absolute error the correlation coefficient also shows, that the performance is better for clouds over the Arctic Ocean compared to the Southern Ocean. The lowest correlation coefficient is shown for the model of low-level clouds over the Southern Ocean. The correlation coefficient shows in general lower values for

Table 4.6.: Pearson correlation coefficient between the predicted liquid fraction and the observed liquid fraction for the validation dataset and in brackets for the training dataset.

	Low-level	Mid-level	Mid-low-level
Arctic Ocean	0.73 (0.83)	0.81 (0.90)	0.85 (0.91)
Southern Ocean	0.61 (0.73)	0.72 (0.86)	0.77 (0.86)

low-level clouds compared to mid-level clouds, while the mean absolute error shows a similar performance between low-level and mid-level clouds. In general, a strong correlation coefficient between the predicted liquid fraction and the observed liquid fraction is found. Nevertheless, there is still space for improvement of the model, for example by adding more parameters as inputs and investigate their influence in future studies. To investigate further possibilities to improve the model, the mean absolute error can be investigated as function of the feature parameters, like it is shown for the cloud top temperature in Fig. 4.5. Areas with relatively high error in the current model could provide hints, for which parameter ranges other influences might be important, which are not yet considered in the model. Figure A.11, Fig. A.12, and Fig. A.13 show the mean absolute error as function of the remaining feature values, namely sea ice concentration (SIC), averaged dust mixing ratio in the cloud, and averaged sea salt mixing ratio in the cloud. Possible further features, which could be included in future studies could for example focus on dynamical features such as vertical wind speeds or the coupling of the cloud to the surface. So far the performance is sufficient to investigate the influence of the used parameter on the prediction, which is the scope of this work.

4.2.2. Explainable Machine Learning using SHAP values

SHAP values show the quantitative contribution of each feature value to the prediction and thereby provide a method to explain influences of various features on the prediction in the model. Furthermore, the dependence of this influence on other feature can be investigated. The prediction of the model ($f(x)$) for each sample can then be explained by Eq. 4.5 with $E[f(x)]$ representing the expected value, which corresponds to the average of the trainings value, and $SHAP$ being the SHAP value for each feature showing the influence on the prediction.

$$f(x) = E[f(x)] + \sum_{\text{Features}} SHAP \tag{4.5}$$

SHAP values are calculated in this study for a subset of 500 000 samples of the validation datasets, except for mid-level clouds over the Arctic Ocean, where the validation dataset is smaller and only has 300 000 samples. The reason for only calculating the SHAP value for a smaller sample size are the high computational costs and long run times. The Tree Explainer method from the python package shap (Lundberg and Lee, 2017; Lundberg et al., 2020) is used to calculate the SHAP values. The features in this study are cloud top temperature, sea salt mixing ratio, dust mixing ratio, and sea ice concentration. Figure 4.6 shows an example for one sample of a mid-level clouds over the Southern Ocean, which is not meant to be representative, but illustrates the information SHAP values provide.

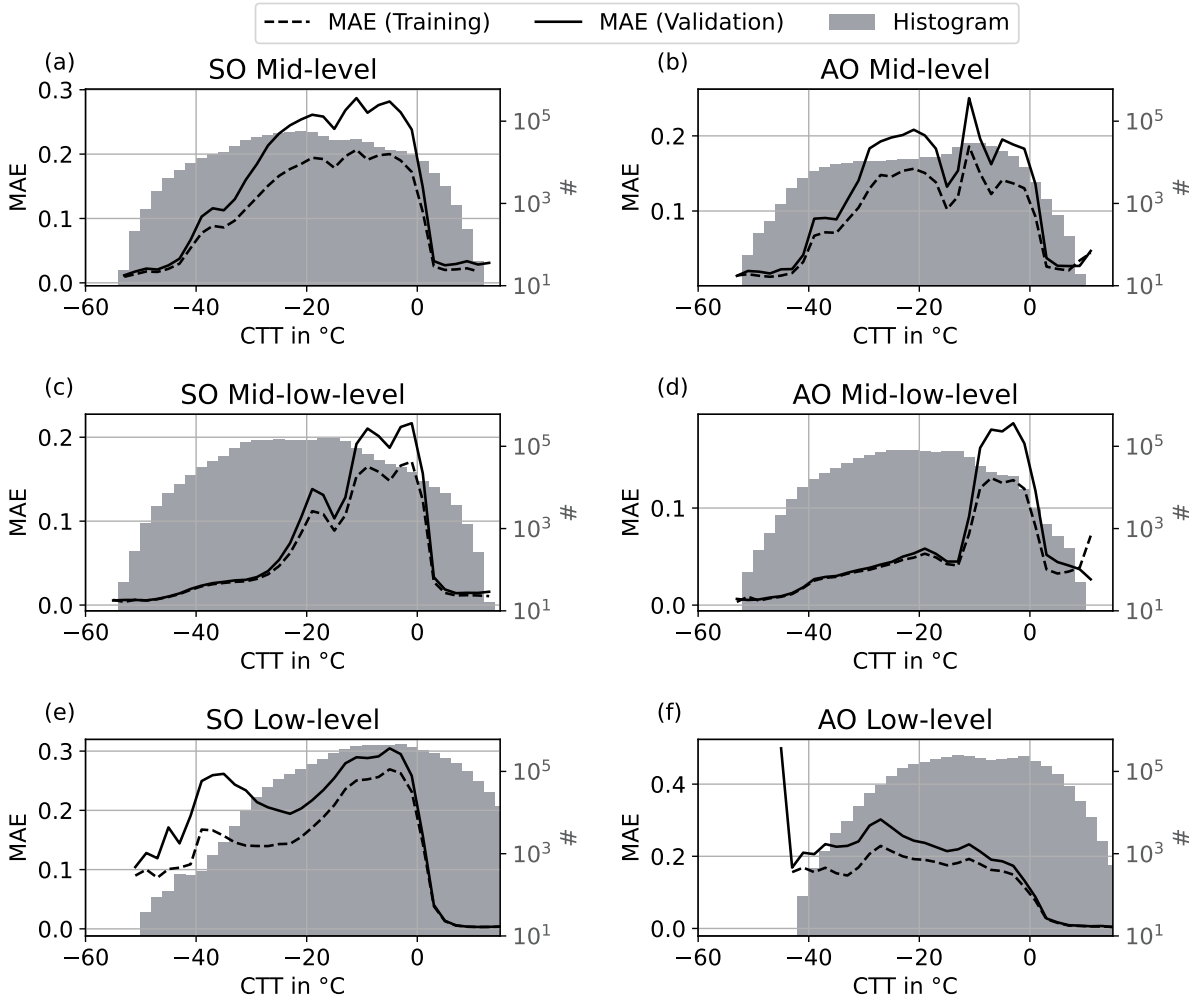

Figure 4.5.: Histogram of the cloud top temperature (CTT) in gray (corresponding to the right y-axis). The lines show the mean absolute error (MAE) as a function of CTT (corresponding to the left y-axis). Line type correspond to the training dataset and the validation dataset as shown in the legend.

4.3. DYAMOND simulations

This section describes the analysis of the representation of clouds and their phase using ICON model data. As the analysis is similar to the one described from Sec. 4.1.1 to Sec. 4.1.4, it is mainly focused on differences, and further explained how the observational data are compared to the model data.

4.3.1. Cloud types classification and liquid fraction

The DYAMOND ICON simulations are compared with the DARDAR satellite observations in a statistical sense instead of comparing the same situations in time and space (see Sec. 6). The same definitions of the regions of the Arctic Ocean and the Southern Ocean, as described in Sec. 3.1, are used for the DYAMOND dataset. Due to the different availability of the data, the time period of the DYAMOND simulations as mentioned in Sec. 3.3 are compared with the same days of the years 2007 and 2008 in the

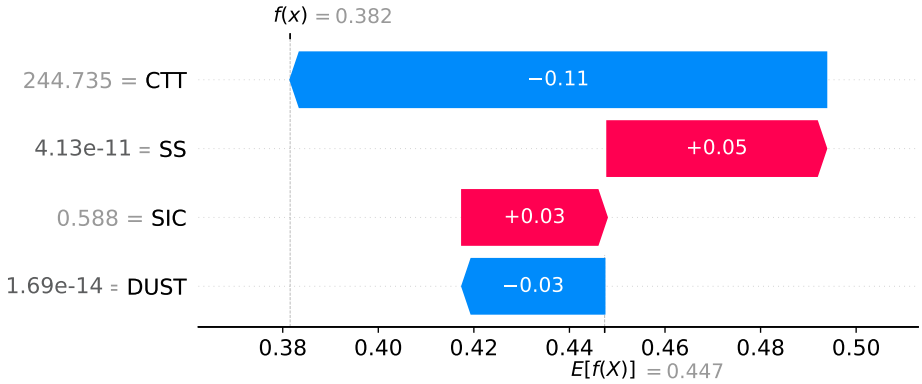

Figure 4.6.: Example to illustrate the information of SHAP values. The example shows results for one sample of a mid-level clouds over the Southern Ocean. The bars represent the SHAP values for different features with blue showing a negative SHAP value, which reduces the liquid fraction, and red showing a positive SHAP value increasing the liquid fraction. The feature values for this sample are shown on the left hand side, namely cloud top temperature (CTT) in K, sea salt mixing ratio (SS) in $\mathrm{kg\,kg^{-1}}$, sea ice concentration (SIC), and dust mixing ratio (DUST) in $\mathrm{kg\,kg^{-1}}$. The prediction of the liquid fraction ($f(x)$) of the model starts with the expected value $E[f(x)]$, which corresponds to the averaged liquid fraction of mid-level clouds over the Southern Ocean. By adding all of the SHAP values to the expected value $E[f(x)]$ (going from the bottom to the top of the figure), the result shows the prediction ($f(x) = 0.382$). Note that this figure is not shown as a representative result for mid-level clouds over the Southern Ocean, but to illustrate the information SHAP values provide.

DARDAR dataset. The usage of data from different years for observations and simulations introduces some uncertainty to the comparison, but as large regions are investigated, it is assumed that the results are representative. The DYAMOND results of the two regions are compared with the DARDAR results of the two regions. The analysed quantities are the frequency of the different cloud types, the frequency of the different phases of the different cloud types, as well as the liquid fraction as a function of the cloud top temperature. The cloud type, the phase, and the liquid fraction are calculated for each grid column of the DYAMOND dataset.

To determine a cloudy grid cell in the ICON output, we use a threshold of $1 \times 10^{-8}\,\mathrm{kgkg^{-1}}$ (Costa-Surós et al., 2020) for the total cloud mass, which is the sum of the mass fraction of cloud liquid water and the mass fraction of cloud ice. Cloud profiles over land surfaces are excluded from the analysis to reduce orographical effects. Furthermore, grid columns with a cloud free area between cloudy pixels are excluded, and only grid columns with a continuous single cloud layer are considered for the detailed analysis to reduce uncertainties from discontinuities. The frequency of such "multi-layer" clouds is discussed in Sec. 7.1.

The different cloud types are distinguished the same way, as it is described in Sec.4.1.2 for the satellite observations, using the same threshold for CBH and CTH.

The liquid fraction in simulations (f_{DYAMOND}) is calculated differently compared to the liquid fraction of the satellite observations, because the simulations provide the mass mixing ratio of liquid and ice. The liquid mass fraction of each grid box $f_{\mathrm{DYAMOND}}^{\mathrm{grid\,box}}$ is calculated by Eq. 4.4 and averaged vertically in each cloud column to compare it to the liquid fraction of the satellite observations based on the pixel-wise

Table 4.7.: Conditions for the distinction between cloud phases based on the liquid fraction (f_{DYAMOND}).

Considered phase	Ice	Mixed-phase	Liquid
Conditions	$f_{\mathrm{DYAMOND}} \leq 0.01$	$0.01 < f_{\mathrm{DYAMOND}} < 0.99$	$f_{\mathrm{DYAMOND}} \geq 0.99$

phase categories. Equation 4.7 shows the corresponding formula, where $N_{\mathrm{cloudy\,grid\,boxes}}$ is the number of cloudy grid boxes in the vertical cloud column, m_{liq} is the specific cloud water content, and m_{ice} is the specific cloud ice content.

$$f_{\mathrm{DYAMOND}}^{\mathrm{grid\,box}} = \frac{m_{\mathrm{liq}}}{m_{\mathrm{liq}} + m_{\mathrm{ice}}} \tag{4.6}$$

$$\begin{aligned} f_{\mathrm{DYAMOND}} &= \frac{1}{N_{\mathrm{cloudy\,grid\,boxes}}} \sum_{\mathrm{cloudy\,grid\,boxes}} f_{\mathrm{DYAMOND}}^{\mathrm{grid\,box}} \\ &= \frac{1}{N_{\mathrm{cloudy\,grid\,boxes}}} \sum_{\mathrm{cloudy\,grid\,boxes}} \frac{m_{\mathrm{liq}}}{m_{\mathrm{liq}} + m_{\mathrm{ice}}} \end{aligned} \tag{4.7}$$

Section 7.2 investigates the fraction of different cloud phases for different cloud types over the Southern and the Arctic Ocean. To distinguish between liquid clouds, ice clouds, and mixed-phase clouds, different conditions of the calculated liquid fraction (f_{DYAMOND}) are used, and shown in Tab 4.7.

4.3.2. Sea ice concentration [1]

Section 7.4 investigates the correlation of the phase of low-level and mid-low-level clouds with the sea ice coverage using the output from a coupled DYAMOND ICON simulation (ICON-SAP) with 5 km grid spacing. The used definitions for open ocean and sea ice are the same as for the observational data, described in Sec. 3.2.2, with a sea ice concentration of 0 % for open ocean and a sea ice concentration of larger or equal to 80 % considered as sea ice cover.

[1] These calculations have been done as part of the Bachelor Thesis of Sarah Paratoni (Paratoni, 2023), who was supervised by the candidate, Dr. Lena Frey and Prof. Dr. Corinna Hoose. The following text in this section are created by the candidate.

5. Clouds from the satellite perspective [1]

This chapter presents the analysis of clouds over the Southern and Arctic Ocean with active satellite observations, focusing mainly on the cloud phase. First, the frequency of different cloud types, and their seasonal cycle over both regions are shown (Sec. 5.1), as well as the frequency of the cloud phase in different cloud types (Sec. 5.2). It is further described how the horizontal and vertical cloud extent varies for different cloud types with different cloud phases (Sec. 5.2.1). Section 5.2.2 presents how the liquid fraction of the cloud types varies with cloud top temperature, and Sec. 5.2.2 shows how the vertical phase distribution is in mixed-phase clouds. The following section 5.2.4 examines how sea ice, and different aerosol types correlate with cloud phase, but also investigates whether there is a difference between the aerosol content over sea ice and over the open ocean. The final section 5.3 of this chapter investigates the cloud radiative effects of the different cloud types (Sec. 5.3.1), how they vary with different cloud phases (Sec. 5.3.2), and how large the contribution of different cloud types is to the total cloud radiative effect over both regions (Sec. 5.3.3). Major contributions of this chapter are from:
Dietel, B., O. Sourdeval, and C. Hoose, 2023: Characterisation of low-base and mid-base clouds and their thermodynamic phase over the Southern and Arctic Ocean. *EGUsphere [preprint]*, 1–38, `https://egusphere.copernicus.org/preprints/2023/egusphere-2023-2281/`.

5.1. Cloud type occurrence frequency

The occurrence frequency of the different cloud types in the two years 2007 and 2008 with respect to the total number of observed DARDAR profiles including cloud-free profiles is shown in Fig. 5.1. Low-level clouds are most frequent with an occurrence of 25.6 % over the Southern Ocean and 21.5 % over the Arctic Ocean, see magenta color in Fig. 5.1. Mid-low-level clouds occur in about 8.1 % of the profiles over the Southern Ocean and in about 6.9 % over the Arctic Ocean. Mid-level clouds are much less frequent compared to low-level clouds. Nevertheless, they are not negligible and show similar frequencies as high-mid-level clouds, while high-mid-low-level clouds are twice as frequent. The fraction of multi-layer and other clouds is slightly larger over the Southern Ocean with 44.7 % compared to 40.4 % over the Arctic Ocean. The "Multi-layer/Others" category is not comparable to a proper multi-layer cloud category, as there is neither a threshold for the minimum vertical extent of a cloud layer nor for the cloud-free layer. Even small cloud-free gaps of 60 m within a cloud layer fall into this category,

[1] Most of the content of this chapter is from Dietel et al. (2023). Additional paragraphs are the description of the annual cycle of cloud type occurrence frequencies in Sec. 5.1, and parts of Sec. 5.3.1 about the differences of the CRE over sea ice, and the latitudinal dependence of the CRE.

because we exclude such profiles in our analysis as our focus in this study is on single-layer clouds and we want to reduce uncertainties introduced by discontinuities. Future studies could analyze the "Multi-layer / Others" category in more detail and investigate the sensitivity of the fractions to thresholds for a minimum vertical extent of cloud layers and gaps between cloud layers to distinguish between vertically overlapping cloud layers and smaller discontinuities in cloud layers. The fraction of clear-sky profiles is higher over the Arctic Ocean with 19.9 % compared to 10.6 % over the Southern Ocean. Generally, the cloud type occurrence frequencies over the Southern Ocean are very similar to the ones over the Arctic Ocean except for a slightly higher occurrence of low-level and mid-low-level clouds over the Southern Ocean.

Sassen and Wang (2008) investigated the frequency of specific cloud types as a function of the latitude with the 2B-CLDCLASS dataset based on CloudSat observations from 15 June 2006 to 15 June 2007 distinguishing between clouds over ocean and clouds over land. Although the cloud type definition and distinction criteria differ to the ones we use we still compare some similar cloud types. Our frequency of the low-level cloud category compares quite well to the stratus and stratocumulus (St+Sc) with frequencies between 20 and 30 % in similar latitudes over ocean. They find a higher fraction of high clouds between 1 % and 10 % compared to our result of about 1.4 %. The mid-level and mid-low-level clouds can be best compared to altocumulus (Ac) ($\approx 5\,\%$) and altostratus (As)($\approx 20\,\%$) clouds which both show higher frequencies compared to our results. The way how multi-layer clouds are considered in our study and the study of Sassen and Wang (2008) introduces a bias, because Sassen and Wang (2008) would still classify the overlapping cloud types, which leads to higher frequencies in their cloud categories compared to our results, as we consider them in a separate category as multi-layer clouds. This could explain some of the discrepancies between the observed numbers. Mace and Zhang (2014) also showed a cloud coverage of about 35 % of clouds with cloud tops lower than 3 km over the Southern Ocean and 25 % over the Arctic Ocean, which is similar to our result including the fact that the definitions differ to ours.

The temperature has a large influence on cloud phase, as mixed-phase clouds can only exist in the temperature range between 0 °C and −38 °C. Therefore, we investigate the relative frequencies of the different cloud types with respect to the total number of single-layer cloud profiles, as a function of their cloud top temperature (CTT), shown in Fig.5.3. In the mixed-phase temperature regime the fraction of low-level clouds is high. Low-level clouds show a slightly higher fraction over the Arctic Ocean compared to the Southern Ocean for CTT colder than −13 °C. Mid-low-level clouds also show a high frequency reaching a maximum of 0.6 over the Southern Ocean and 0.4 over the Arctic Ocean respectively at a temperature of around −30 °C. We see higher fractions of mid-level clouds over the Southern Ocean than over the Arctic Ocean for CTT colder than −15 °C, where already high-mid-level clouds exist over the Arctic Ocean. Regarding the mixed-phase temperature regime, low-level, mid-low-level and mid-level clouds are the dominating types of single-layer clouds in this temperature range. Therefore, further analysis and interpretations in this work will focus on these cloud types.

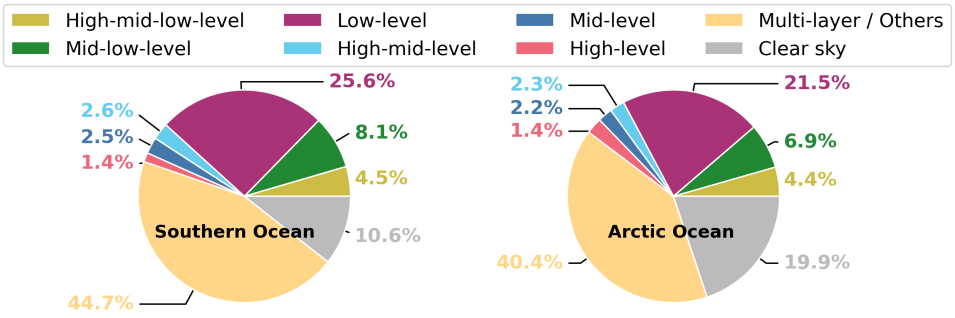

Figure 5.1.: Frequency of different cloud type occurrence. The frequency is calculated as the total number of DARDAR-profiles containing a specific cloud type, observed during two years 2007 - 2008, and divided by the total number of DARDAR-profiles available including cloud-free profiles. Reprinted from Dietel et al. (2023).

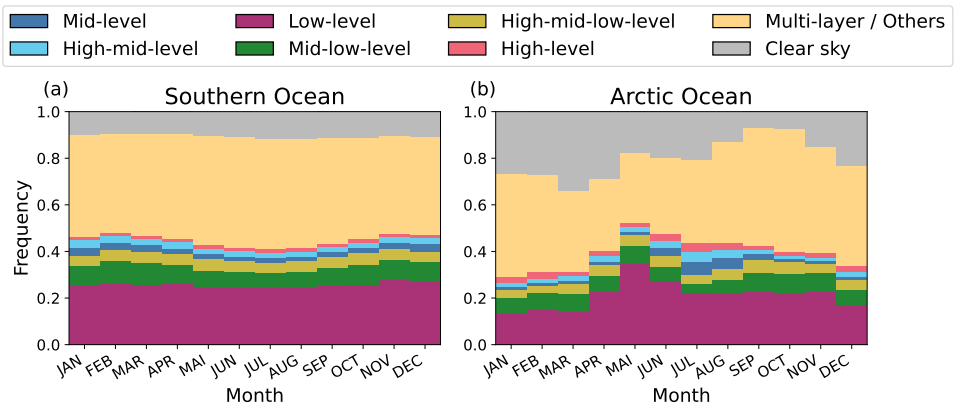

Figure 5.2.: Annual cycle of the frequency of different cloud type occurrence.

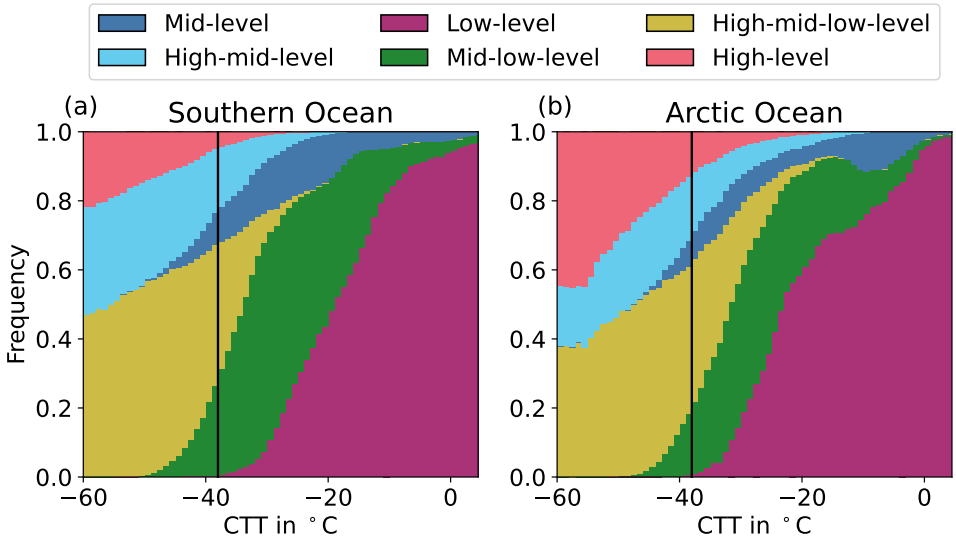

Figure 5.3.: Stacked bars of the relative frequency of different cloud types only considering single-layer clouds as a function of cloud top temperatures (CTTs). The black line shows the lower temperature boundary of the mixed-phase temperature regime at −38 °C. Reprinted from Dietel et al. (2023).

The seasonal cycle of the frequency of different cloud types over the Southern Ocean and the Arctic Ocean is shown in Fig. 5.2. The Southern Ocean shows less seasonal variations compared to the Arctic Ocean. This is influenced by the different latitude definitions of the Southern Ocean (40 °S – 82 °S) and the Arctic Ocean (60 °N – 82 °N). Due to the more pole-ward region of the Arctic Ocean, the seasonal cycle in our results is stronger over the Arctic Ocean. Nevertheless, comparing the frequencies of cloud types with respect to single layer clouds for specific latitudes the Arctic Ocean shows still more seasonal variation compared to the Southern Ocean (see Fig. A.4 and Fig. A.5). A possible reason could be the different land distributions over the two regions, which may lead to a larger influence from land surfaces in the Arctic. This pattern is in agreement with seasonal cycles of cloud cover as shown by Listowski et al. (2019) for the Southern Ocean, by Kay et al. (2016b) for the Arctic Ocean, and by Kay et al. (2016a) for both regions using similar data based on CALIPSO and partly CloudSat. The Arctic Ocean shows a lower cloud cover in the winter season (DJF) compared to summer (JJA) and fall, and Kay et al. (2016b) show the strongest seasonal differences over land surfaces and high latitude ocean possibly covered by sea ice in winter. Listowski et al. (2019) and Kay et al. (2016b) show lower cloud fraction in JJA compared to DJF over the Southern Ocean, but generally cloud fractions are higher than 60 % throughout the year. Kay et al. (2016b) show as well stronger seasonal differences over the Arctic Ocean compared to the Southern Ocean, similar to this analysis in Fig. 5.2. In the present work higher cloud fractions are observed over the Southern Ocean compared to the Arctic Ocean, which is in line with literature (Liu et al., 2022).

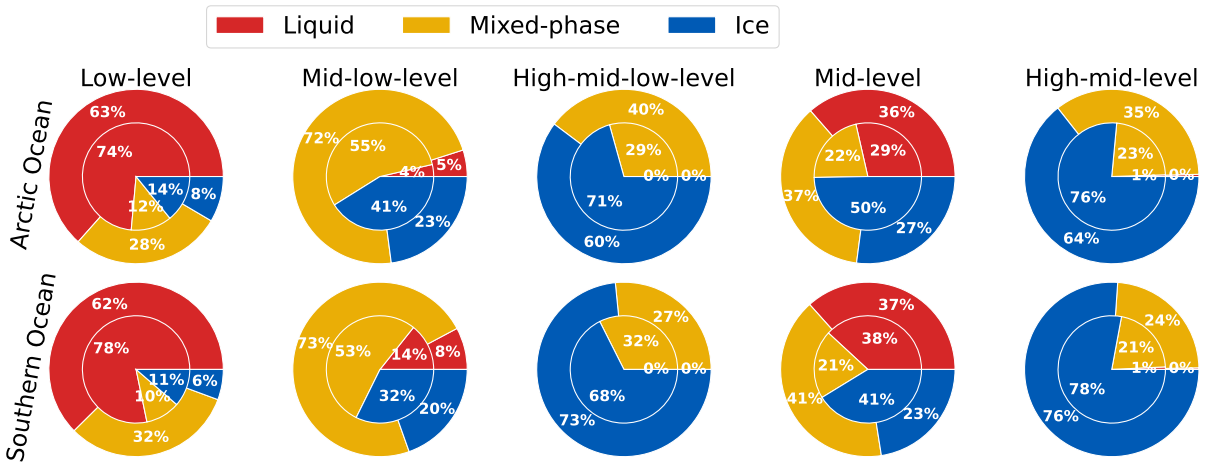

Figure 5.4.: Cloud phase distributions of various cloud types (columns) over the Southern Ocean (lower row) and the Arctic Ocean (upper row). The outer pie charts include all cloud profiles of a cloud type, while the inner pie charts only consider cloud profiles, where the lidar signal is not fully extinguished by the cloud. The phases liquid, ice, and mixed-phase refer to the liquid fraction described in Sec. 4 and Eq. 4.2. Liquid corresponds to a liquid fraction of 1, ice to a liquid fraction of 0, and the mixed-phase category refers to liquid fractions larger than 0 but smaller than 1. Reprinted from Dietel et al. (2023).

5.2. Cloud phase

We will now investigate the thermodynamic phase of the different cloud types (Fig. 5.4).
Low-level clouds are mainly liquid clouds with a percentage of 62 % to 63 %, a third of them (28 % to 32 %) are mixed-phase clouds, and a small fraction are pure ice clouds (6 % to 8 %). The inner pie charts in Fig. 5.4 consider only cloud profiles where the lidar is not attenuated. We can see a decrease in the fraction of mixed-phase clouds to a percentage of 10 % to 12 % for low-level clouds. Contrarily, the relative ice fraction and liquid fraction increases, when considering only profiles where the lidar is not fully attenuated. Regarding the mid-low-level clouds in the second column of Fig. 5.4 a high fraction are mixed-phase profiles (72 % to 73 %), a small fraction (5 % to 8 %) are liquid profiles, while 20 % to 23 % are ice profiles. High-mid-low-level are mainly ice profiles (60 % to 71 %) and a smaller fraction (29 % to 40 %) of mixed-phase profiles, but no liquid profiles. Mid-level clouds are liquid profiles in 36 % to 37 % of the cases. A larger proportion of the mid-level clouds are mixed-phase profiles with a frequency of 37 % to 41 %. 23 % to 27 % of mid-level clouds are ice profiles. Regarding the differences for mid-level cloud profiles where the lidar signal is not extinguished the fraction of mixed-phase profiles decreases, while the fraction of ice profiles increases, and the fraction of liquid profiles slightly decreases over the Arctic Ocean. High-mid-level clouds show a similar distribution to high-mid-low-level clouds with large fraction of 64 % to 78 % being ice profiles, and 21 % to 35 % being mixed-phase profiles, but almost no liquid profiles (0 % to 1 %) probably due to low cloud top temperatures with homogeneous ice formation.

Regarding the differences in the results considering all profiles of a cloud type, shown in the outer pie charts in Fig. 5.4 and only considering profiles where the lidar is not extinguished, shown in Fig. 5.4, we can generally see a decrease of the fraction of mixed-phase profiles, which indicates that in mixed-phase profiles the lidar is frequently extinguished. The reduction of the absolute numbers of profiles is strongest for mixed-phase clouds, which is the reason for the decrease of the relative fraction of mixed-phase profiles, while the relative fraction of ice and liquid profiles mostly increases. This might lead to uncertainties in the further analysis.
In general, all cloud types show quite high fractions of mixed-phase cloud profiles. The frequencies of the different phases are very similar between the Southern Ocean and the Arctic Ocean.
We don't compare the fractions of the cloud phase to previous literature (Mayer et al., 2023; Listowski et al., 2019; Huang et al., 2012) at this point, as the percentages strongly depend on the definitions and considerations of the cloud types and on the calculation and consideration of cloud phases, which vary a lot in the different studies. More detailed comparisons to previous research will be done in the following subsections investigating different aspects of the cloud phase, such as the cloud phase as a function of cloud top temperature.

5.2.1. Cloud phase correlation on the vertical and horizontal cloud extent

We now investigate if clouds consisting of different phases and at different levels show differences in their horizontal and vertical extent. The calculation of the horizontal and the vertical extent of the cloud objects is described in Sec. 4.
Figure 5.5 shows the results for the Southern Ocean and the Arctic Ocean. In general, ice clouds have a larger vertical extent, while liquid clouds show only a small vertical extent, but reach a larger horizontal extent compared to ice clouds.
Mixed-phase clouds show a broader distribution and can reach both large vertical and/or horizontal extent. In mid-low-level (ML) clouds the horizontal extent is larger for mixed-phase clouds compared to liquid clouds, both over the Southern Ocean and the Arctic Ocean. The horizontal extent of liquid and mixed-phase clouds of the same cloud type are similar. Comparing the horizontal extent of mixed-phase and ice clouds, we can see that mixed-phase high-mid-low-level (HML) clouds have a smaller horizontal extent compared to ice-phase HML clouds. Other cloud types show the opposite signal with mixed-phase clouds having a larger horizontal extent compared to ice clouds of the same cloud type, except for high-mid-level (HM) clouds, which have a similar horizontal extent.
The results are very similar between clouds over the Southern Ocean and the Arctic Ocean. Regarding the difference between the cloud types, the vertical structure is mainly forced by the definition of the cloud types, based on cloud base heights and cloud top heights, which also constrain the maximum vertical extent. The vertical extent of mixed-phase and ice clouds is generally very similar.
The small vertical extent of liquid clouds is probably influenced by different factors. The liquid phase of the investigated clouds is presumably dominated by smaller supercooled liquid droplets. These are

mainly detected by the lidar, while the radar is able to detect the liquid phase for larger droplets and rain. Therefore, the extinction of the lidar signal, due to strong attenuation, probably has a strong influence on the result of the small vertical extent of the liquid clouds. Thus, this result is at least partly coming from the limited penetration depth of the lidar signal in supercooled liquid clouds. Nevertheless, there have been studies using other observation techniques, such as ground-based remote sensing, showing that supercooled liquid cloud layers tend to be shallow (Ansmann et al., 2009).
Mixed-phase clouds show a larger vertical extent compared to liquid clouds in all cloud types and both over the Southern Ocean and the Arctic Ocean. This is also in line with theoretical knowledge about polar mixed-phase clouds. Typically, heterogeneous ice nucleation occurs in the supercooled liquid layer, the Wegener-Bergeron-Findeisen process leads to the growth of the ice crystals, which then fall from these liquid layers and form virga. Including the virga in the cloud extent, the cloud extent increases with the formation of ice compared to the supercooled liquid cloud.
Zhang et al. (2014) investigated the spatial scales of altocumulus clouds with globally collocated CloudSat/CALIPSO observations and found a vertical extent of 1.96 km (± 1.10 km) and a horizontal extent of 40.2 km (± 52.3 km). The results for the vertical extension matches quite well, with our result for mid-level clouds being slightly smaller, while the mean horizontal extent in our analysis is smaller (3.89 km-6.24 km). However, the horizontal extent is strongly influenced by excluding specific cases like multi-layer cloud profiles, which could lead to shorter horizontal scales, due to an overlap with a different cloud layer. Other uncertainties occur in clouds having CTH and CBH close to the thresholds of the cloud type definition, which for example can lead to a cloud being partly classified as low-level and partly as mid-low-level by increasing CTH. This cloud would be considered as two separate clouds, as they aren't considered as the same cloud type.

5.2.2. Cloud phase dependence on the cloud top temperature

We now investigate how the cloud phase correlates with the cloud top temperature, especially in the mixed-phase temperature regime between −35 °C and 0 °C. Figure 5.6 shows the cloud phase as a function of the cloud top temperature (CTT) for the different cloud types in panel (a), and the liquid fraction of cloud top phase in panel (b), as it was explained in Sec. 4.
First of all, we can see the high liquid fraction in low-level clouds especially over the Southern Ocean at relatively low temperatures between −40 °C and −17 °C in Fig. 5.6. Mid-level clouds show high liquid fractions as well, while mid-low-level clouds show rather small liquid fractions. A small liquid fraction can also be observed for high-mid-level clouds, with high-mid-level clouds occurring at lower temperature compared to mid-low-level clouds. Regarding the cloud top liquid fraction f_{CT} in panel (b) in Fig. 5.6, the liquid fraction increases for all cloud types compared to the vertical liquid fraction f, indicating a preferential occurrence of liquid at the cloud top.
Thinner cloud layers (L,M) have a higher liquid fraction compared to thicker cloud layers (HM, ML, HML) extending over several troposphere layers, which was already described in Sec. 5.2.1. We can

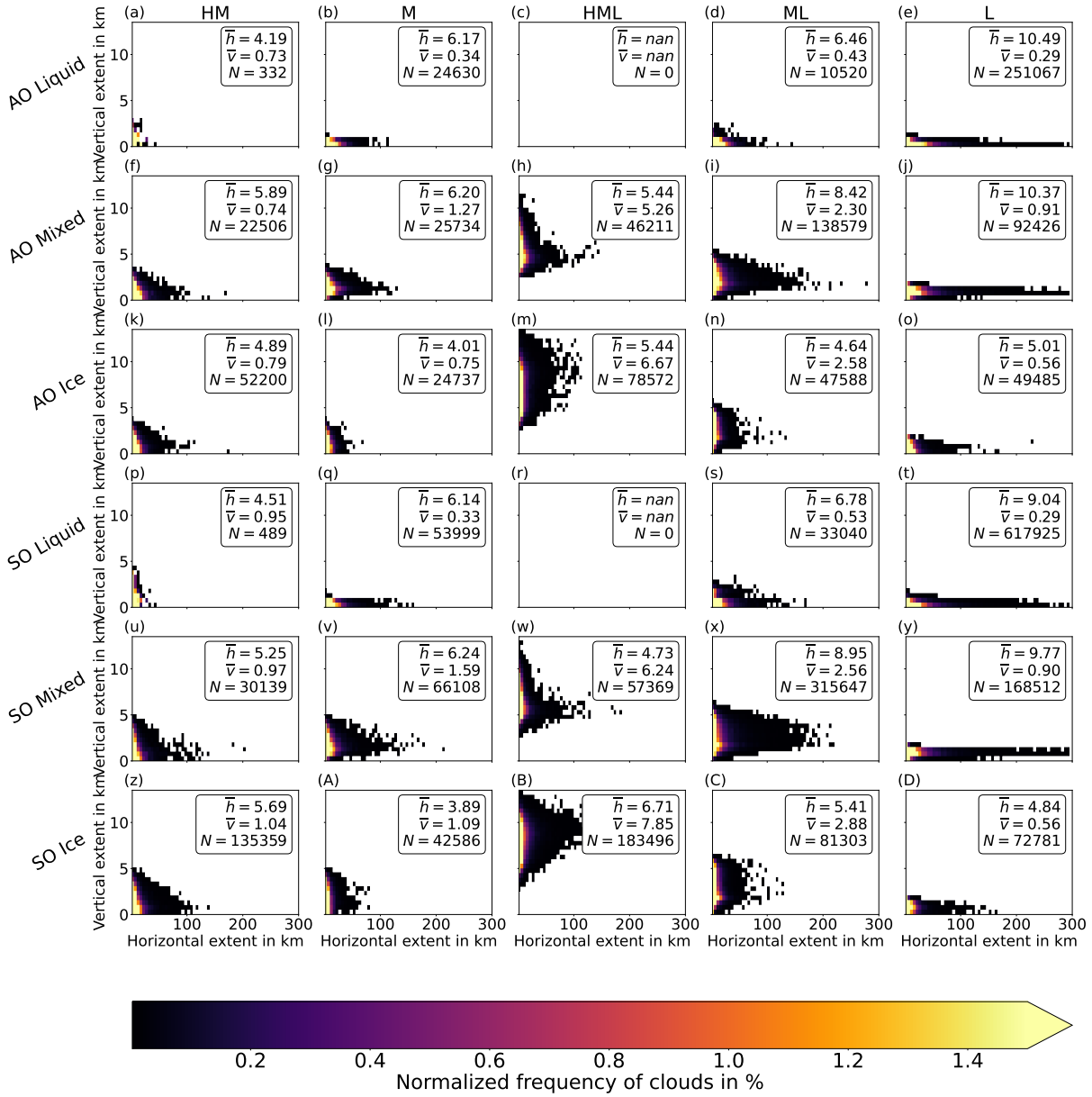

Figure 5.5.: 2-dimensional histogram of clouds with different phases regarding their horizontal and vertical extent. Minimum extent are 2 vertical layers, each 60m, and 2 horizontal profiles. Cloud profiles are considered as the same cloud, if the time difference to the next profile of the same cloud type is less or equal than 0.2 s (see. Sec.4). The unit of the horizontal extent is km, assuming one vertical profile having a horizontal distance of about 1.1 km to the next profile. $\overline{h}$ describes the mean horizontal extent in km, $\overline{v}$ describes the mean vertical extent. Reprinted from Dietel et al. (2023).

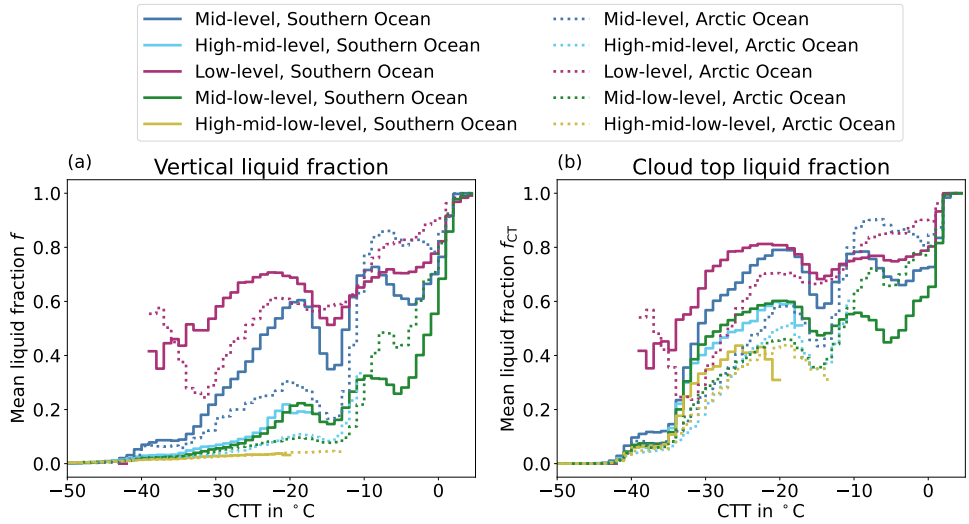

Figure 5.6.: Mean liquid fraction of profiles of different cloud types as a function of the cloud top temperatures (CTT). In panel (a) the liquid fraction f is calculated for each vertical cloud column and then averaged for each 1 °C bin of the CTT. The liquid fraction of each profile is calculated as described in Sec. 4, Eq. 4.2. In panel (b) only the cloud top phase is considered and the liquid fraction f_{CT} is calculated as described in Eq. 4.3, but only using the phase of all cloud top pixels of one specific cloud type. The liquid fraction is only shown if there are at least 500 cloud profiles in the temperature bin to ensure a statistical representativeness. Reprinted from Dietel et al. (2023).

even see this, if we only consider the cloud top phase, where the uncertainty introduced by the lidar extinction has no influence.

In general, the liquid fractions of clouds over the Southern Ocean are higher compared to the liquid fractions of clouds over the Arctic Ocean for CTT $< -10\,°C$, while for high temperatures (CTT $> -10\,°C$) the liquid fraction in clouds over the Arctic Ocean is larger compared to the Southern Ocean.

Further important features are the local minima in the liquid fraction mainly seen at a CTT around $-15\,°C$ and partly around $-5\,°C$. Interestingly, this feature has already been seen in many other studies (Nagao and Suzuki, 2022; **?**; Zhang et al., 2019; Alexander and Protat, 2018; Zhang et al., 2014; Riley and Mapes, 2009), but has only partly been investigated and sometimes not even described. Zhang et al. (2014) saw a similar peak in the mixed-phase fraction at $-15\,°C$, investigating the vertical and horizontal scales of Ac clouds, but focused more on the differences between different regions. **?** also showed the phenomena of increased ice formation at $-15\,°C$ and $-5\,°C$ and discussed many other studies, which have shown this behavior or which explain possible reasons. In the following, we will mention a few of them.

Riley and Mapes (2009) found an unexpected peak at $-15\,°C$ in the CloudSat echo, but studies have also shown the peak using lidar observations (Nagao and Suzuki, 2022), which hints that this effect is not due to an issue of a specific instrument. Regarding this temperature range, there are various studies describing different processes occurring around these temperatures, maybe even interacting and causing other processes. The ice habits strongly depend on the temperature, with column-needles occurring/growing at

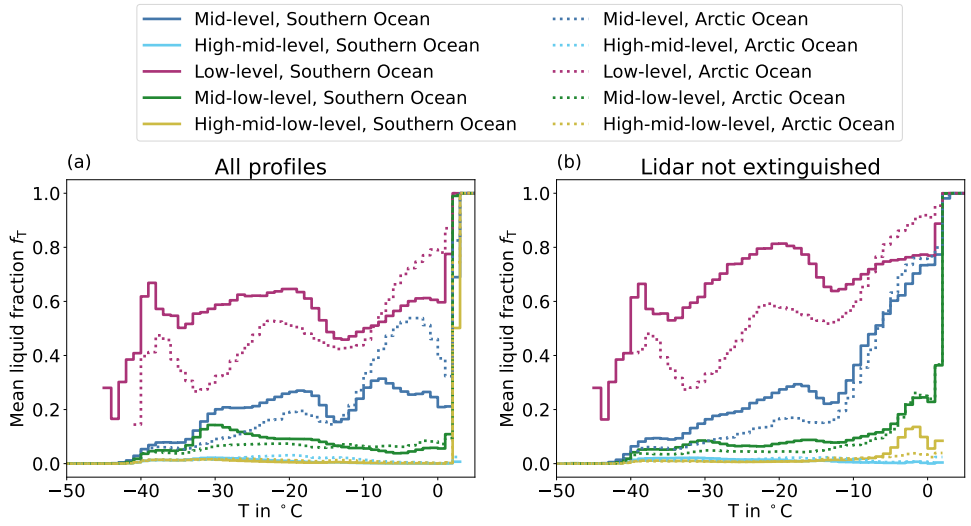

Figure 5.7.: Mean liquid fraction (f_T) based on the phase of all cloudy pixels and their temperature (see Eq.4.4) comparing the results considering all profiles (see panel a) and considering only profiles in which the lidar signal is not fully extinguished (see panel b).

temperatures around −5 °C and plate-stellar dendrites around temperatures of −15 °C (Avramov and Harrington, 2010; Fukuta and Takahashi, 1999). Especially, the dendritic growth zone occurring at −15 °C has also been investigated by other studies (von Terzi et al., 2022; Silber et al., 2021) and might lead to this increased ice fraction. The strong growth of the ice crystals around these temperatures also leads to an increased signal in the remote sensing instruments and therefore to an increased detection of ice. Another process correlating with dendritic ice crystals is an increased aggregation rate (Chellini et al., 2022), but also the possibility of secondary ice formation (Mignani et al., 2019; Sullivan et al., 2018) due to small fragments in case of collisions.

All of these processes might play a role as they affect each other. From the satellite perspective it is hard to pinpoint the increased ice fraction to specific processes, because it could even be a combination of processes and the relevance of processes might also vary depending on a specific region, time, and the conditions there. Nevertheless, the potential to even see these increased ice productions at specific temperatures is not yet fully exploited. The combination of this knowledge with other ground-based observations or laboratory experiments could improve our understanding of the cloud phase. This improved process understanding can also lead to a better representation in models, which contrary to our results show a rather smooth phase partitioning (e.g. McCoy et al., 2016).

Additionally, Fig. 5.7 shows the results using the method described in Sec. 4.1.3, Eq. 4.4. Compared to Fig. 5.6, the liquid fraction is mainly lower with strong differences in mid-level and mid-low-level clouds. This is consistent with several previous results. One is that ice clouds tend to be vertically thicker compared to liquid clouds (see Sec. 5.2.1), which explains the generally lower liquid fraction, if each pixel is accounted for its temperature instead of calculating a vertical liquid fraction assigned to its cloud top temperature. Furthermore, mixed-phase clouds tend to have liquid tops with precipitating ice below.

The precipitating ice layer is usually vertically thicker compared to the thin liquid layer at cloud top. The precipitating ice layer occurs at higher temperatures compared to the supercooled liquid at cloud top, which can be one explanation for the increased liquid fraction with decreasing temperature in mid-low-level clouds. The local minimum at −15 °C (see 5.2.2) is as well visible in low-level and mid-level clouds. Considering only profiles in which the lidar is not fully extinguished, the liquid fractions increases in low-level clouds, in mid-level, and mid-low-level clouds at high temperatures. The comparison between the consideration of all profiles and only profiles where the lidar is not extinguished can also be seen for the other two methods of calculating the liquid fraction in Fig. A.1 and Fig. A.2. The generally higher liquid fraction is expected in the analysis where only profiles are considered if the lidar is not extinguished. Therefore, some mixed-phase profiles are excluded, which reduces the number of lower liquid fractions and increases the relative contribution of purely liquid clouds. The differences due to different methods also highlight that comparisons between different studies should be made carefully, as different methods can lead to different results, but the combination of different methods can also provide an opportunity to improve the understanding by carefully investigating the differences.

5.2.3. Vertical phase distribution of mixed-phase clouds

We now investigate how the phase is distributed vertically within the clouds. For this purpose, we limit our analysis to mixed-phase clouds, as pure ice and pure liquid cloud profiles don't show a vertical phase distribution. We only consider cloud profiles, where the lidar is not fully extinguished to reduce the resulting uncertainties in the vertical phase distribution. To investigate the vertical phase distribution of mixed-phase clouds we analyze all cloud profiles in which either both liquid pixels and ice pixels are observed, or any mixed-phase pixels are observed in one vertical cloud column. Normalizing the height within the cloud, we calculate the fraction of liquid pixels at specific heights within the clouds, as well as the fraction of mixed-phase pixels (see Fig. 5.8).

Most of the mixed-phase clouds show an increased liquid fraction at cloud top, and it strongly decreases towards lower heights within the cloud, except for low-level clouds which show highest liquid fractions at lower heights of the cloud. Further investigations (not shown) of low-level clouds have shown that this might mainly be based on the category 'Multiple scattering due to supercooled liquid' (see Tab. 4.1). Most cloud types show also an increase of the liquid fraction at cloud base. Both, the increased liquid fraction at cloud base, and the generally high liquid fraction in low-level clouds at lower heights persist, if we restrict our analysis to cloud profiles with a maximum temperature of 0 °C, and are therefore not related to melting. So far, it is not yet clear if the increased liquid fraction at lower heights is based on uncertainties liek ground clutter or actually due to more liquid water in clouds and further research is needed.

The maximum of the fraction of mixed-phase pixels is located slightly below cloud top and most of the mixed-phase pixels are located in the upper half of the cloud. The structure of mixed-phase clouds with an increased liquid fraction at cloud top has been already seen in many other observations (Zhang

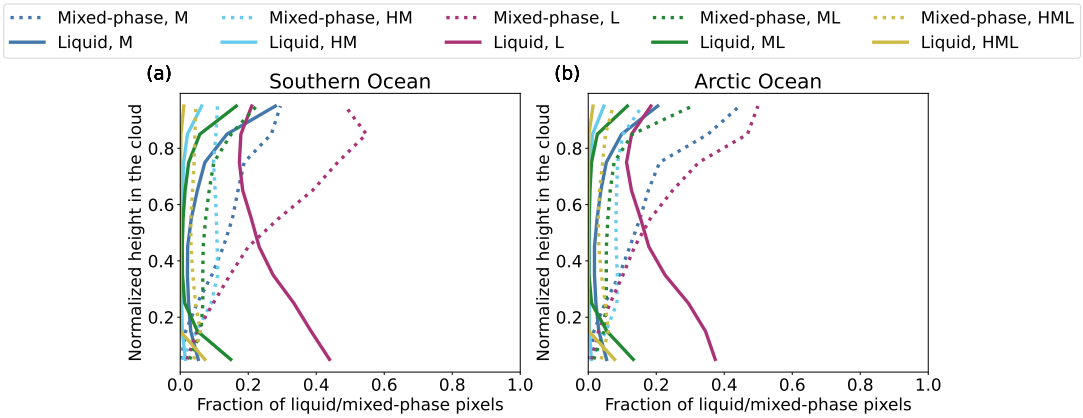

Figure 5.8.: Phase fraction at normalized cloud heights for mixed-phase clouds. Cloud types over the Southern Ocean are shown in panel a), cloud types over the Arctic Ocean in panel b). The solid lines show the fraction of liquid pixels at certain normalized heights, while the dotted lines show the fraction of mixed-phase pixels vertical bins. The normalized height at the y-axis is from 0 to 1 and values are calculated in steps of 0.1. Reprinted from Dietel et al. (2023).

et al., 2019; Carey et al., 2008; Fleishauer et al., 2002). Studies based on ground-based remote sensing instruments also observed liquid cloud tops with ice mainly below in mixed-phase clouds (Zhang et al., 2017; Kalesse et al., 2016; de Boer et al., 2011).

The increased fraction of liquid and mixed-phase pixels at cloud top is in line with the results found in Sec. 5.2.2 showing an increased cloud top liquid fraction compared to the vertical liquid fraction. The high frequency of supercooled liquid at cloud top was also shown by Schima et al. (2022) using airborne radar, lidar, and in-situ measurements collected during the Southern Ocean Clouds, Radiation, Aerosol Transport Experimental Study (SOCRATES).

5.2.4. Cloud phase dependence on the sea ice concentration and aerosol concentration

To investigate the differences in cloud phase as a function of the sea ice concentration, the mean liquid fraction of clouds over the open ocean are compared with the mean liquid fraction of clouds over sea ice. The detailed method is described in Sec. 4. Figure 5.9 shows the significant differences between the mean liquid fractions in clouds over ocean and the mean liquid fraction in clouds over sea ice for different cloud types as a function of the cloud top temperature. It's important to address the behavior at different temperatures, otherwise the generally lower temperatures over sea ice will naturally lead to a higher proportion of ice clouds.

Over the Southern Ocean the liquid fraction of clouds over sea ice is significantly higher compared to the clouds over the open ocean especially in low-level clouds, but also in mid-level and mid-low-level clouds. Over the Arctic Ocean we can see the same behavior for low-level clouds, but mid-level and mid-low-level clouds only show small signals for cloud top temperatures warmer than −10 °C. Furthermore, the difference of the liquid fractions is higher in low-level clouds, compared to mid-level or mid-low-level clouds. A similar result for low-level clouds has been found by Carlsen and David (2022) using a similar

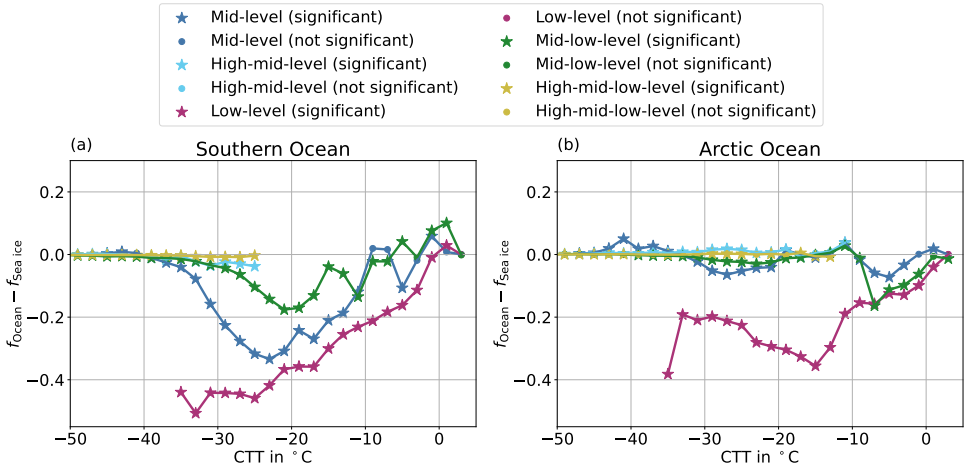

Figure 5.9.: Difference between the mean liquid fraction of clouds over ocean and the mean liquid fraction of clouds over sea ice as a function of the cloud top temperature. The significance of the two distributions of liquid fractions of clouds over ocean and clouds over sea ice is investigated using a Z-test with a p-value of 0.05 for each CTT-bin. Panel a) shows the results for the Southern Ocean, panel b) shows results for the Arctic Ocean. Data are only shown if there are at least 100 cloud profiles over ocean and 100 profiles over sea ice. Reprinted from Dietel et al. (2023).

dataset based on CloudSat and CALIPSO observations, but a different metric for the cloud phase. The hypothesis proposed in Carlsen and David (2022) is that due to the coverage of the ocean by sea ice, less sea spray aerosols can be released, which leads to less INPs over sea ice and thereby a higher fraction of liquid clouds.

Comparing CAMS reanalysis data in clouds over sea ice and in clouds over the ocean Fig. 5.10 shows a systematic difference in the sea salt concentration over sea ice and over open ocean with less sea salt over sea ice, which supports the hypothesis of Carlsen and David (2022). Sea salt acts hereby as a proxy for sea spray aerosols, as the ice nucleating part of the aerosols are usually biological components from the sea surface microlayer, like microorganisms acting as INP at high temperatures (Porter et al., 2022; Burrows et al., 2013; Després et al., 2012). Figure 5.10 also shows that in mid-level clouds over the Arctic sea ice, the mixing ratio of sea salt is slightly lower than the mixing ratio of organic matter, while in mid-level clouds over the Southern Ocean, sea salt shows much higher values compared to other aerosol types. The role of other aerosol types than sea salt may be higher in the Arctic compared to the Southern Ocean. This would also explain the missing correlation of sea ice with these clouds, which is shown in Fig. 5.9 (right panel, blue line). Furthermore, the transport of other aerosol types like dust is more important in the Arctic compared to the Southern Ocean. As the long-range transport occurs usually above the boundary layer, this is more relevant for mid-level or mid-low-level clouds or even higher clouds and might also reduce the effect of locally emitted sea spray aerosols for these clouds.

Nevertheless, a recent study of Papakonstantinou-Presvelou et al. (2022) investigated ice number concentrations in Arctic boundary layer ice clouds and found higher ice number concentration in clouds over sea ice compared to clouds over ocean, especially in the latitudes between 60° N and 70° N and for temper-

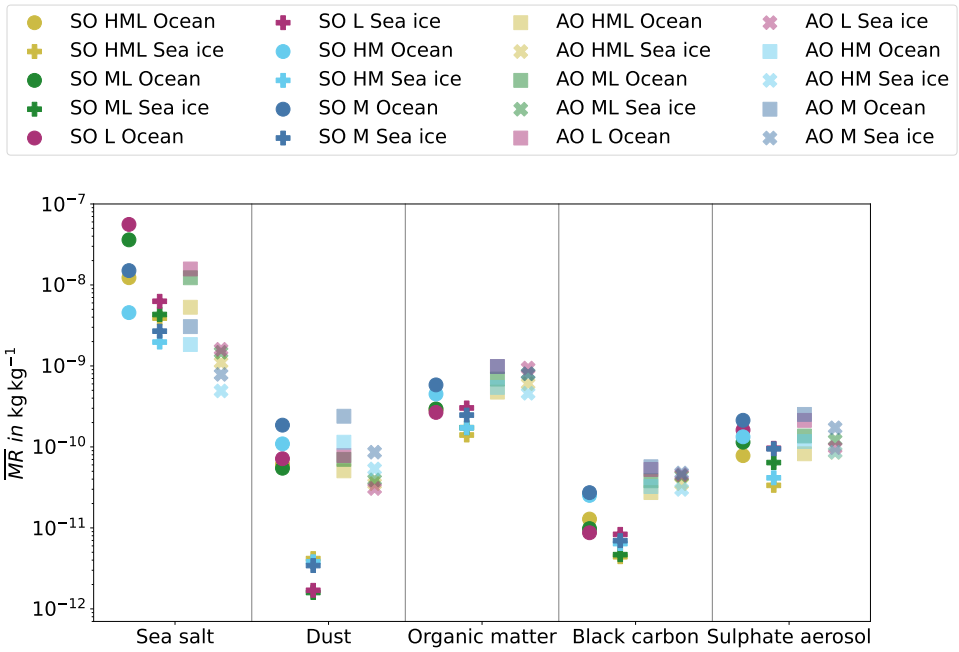

Figure 5.10.: Vertically averaged aerosol mixing ratios (MR) within the heights of a cloud column for different aerosol types. Shown is the mean for different categories, namely the Southern Ocean (SO - darker colours), Arctic Ocean (AO - lighter colour), clouds over sea ice (dots and squares) and clouds over the open ocean (plus and cross), and various cloud types (colours). Reprinted from Dietel et al. (2023).

atures between −10 °C and 0 °C, which may seem contradictory to our results of a lower liquid fraction over ocean and the assumption of less INPs over sea ice. The results of Papakonstantinou-Presvelou et al. (2022) may be influenced by secondary ice production caused by blowing snow particles, which is dependent on the wind velocity and is especially relevant for low-level clouds close to the ground. In addition, Papakonstantinou-Presvelou et al. (2022) investigate only ice clouds, while our study investigates the general cloud phase. Furthermore, Papakonstantinou-Presvelou et al. (2022) found the strongest difference in ice number concentrations at cloud top temperatures larger than −10 °C, while we found the strongest difference of cloud phase over open ocean and cloud phase over sea ice at lower temperatures. Nevertheless, the discrepancy of the different results show the need of further research to improve our understanding of the processes most relevant for cloud phase in remote regions.

We now investigate the correlation of the aerosol concentrations with the cloud phase. Figure 5.11 shows that low-level, mid-low-level and mid-level clouds show a stronger correlation with aerosol concentrations compared to high-mid-level clouds, which show a small signal over the Southern Ocean. High-mid-low-level clouds show no signal, possibly because they mostly consist of ice (see Fig. 5.6), but the attenuation of the remote sensing signals may introduce uncertainties here. The negative values in general show the decrease of the liquid fraction with high aerosol concentration and thereby a higher ice fraction, which is in line with the assumption of additional aerosols acting as additional INPs. Furthermore, the liquid fraction in low-level clouds over the Southern Ocean is lower in high sea salt conditions compared to low sea salt conditions. The content of other aerosol types only shows small changes in

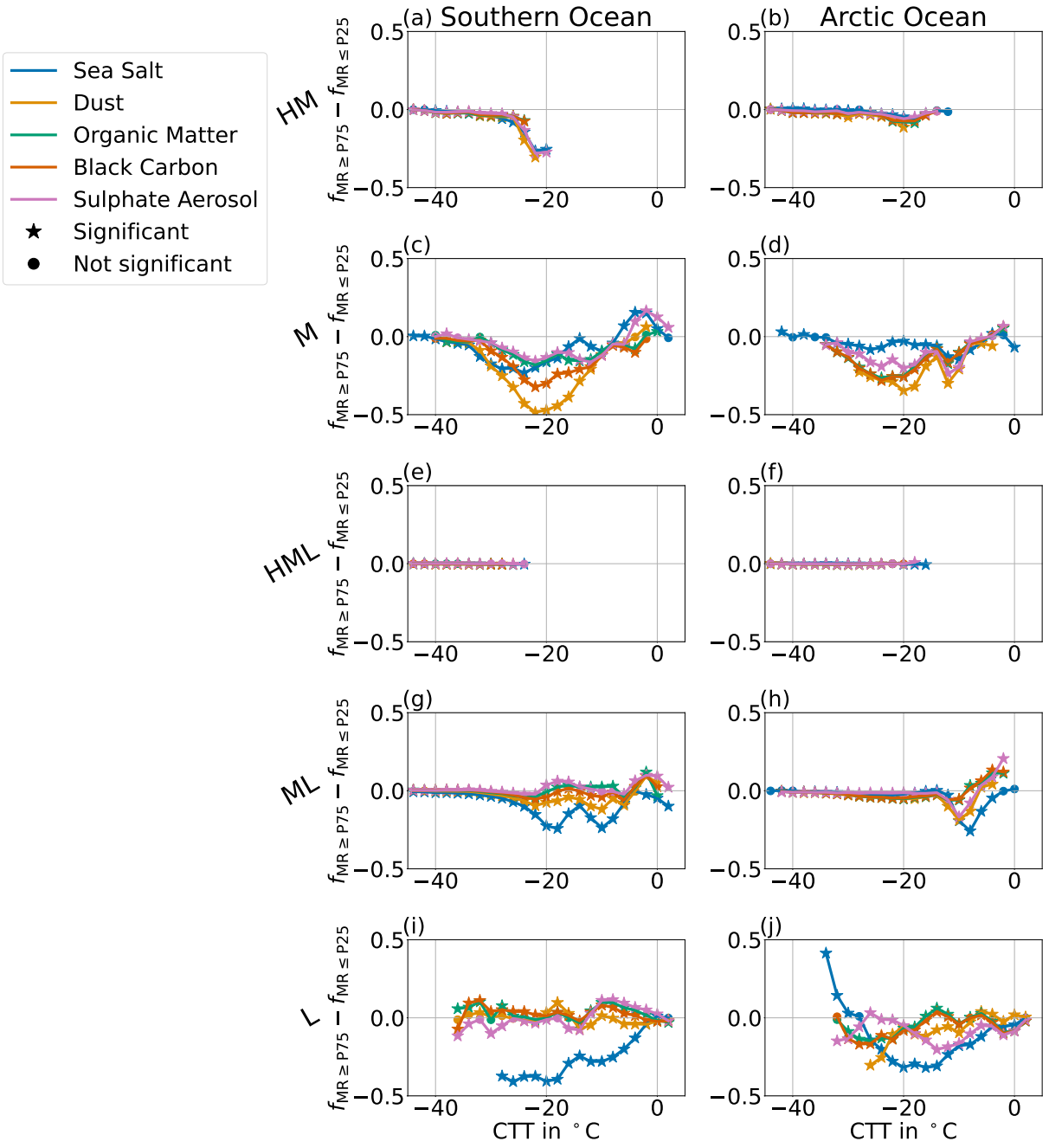

Figure 5.11.: Difference of the mean liquid fraction of clouds collocated with high mixing ratio of an aerosol type, larger than the 75th percentile, and the mean liquid fraction of a cloud collocated with low aerosol mixing ratio, lower than the 25th percentile. Negative values correspond to an increased ice fraction with higher aerosol concentrations. A Z-test with a p-value of 0.05 is used to investigate the significance of the difference. Data are only shown if there are at least 500 cloud profiles with low aerosol concentrations and 500 cloud profiles with high aerosol concentrations. Reprinted from Dietel et al. (2023).

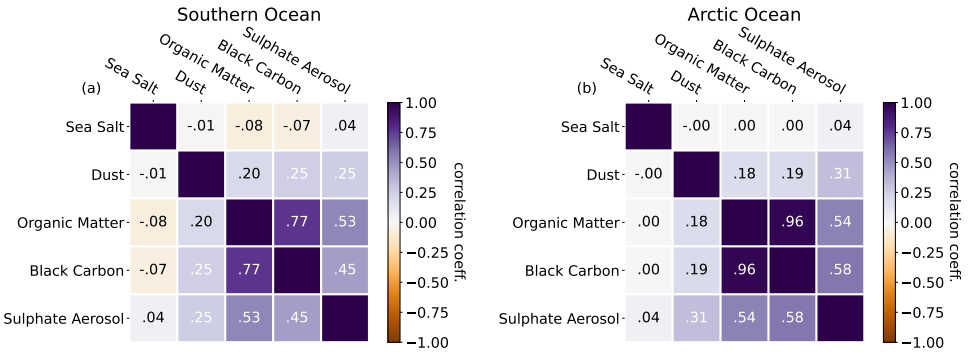

Figure 5.12.: Pearson's correlation coefficient of the mean mixing ratios of different aerosol categories within a cloud. Left panel shows results for the Southern Ocean, right panel for the Arctic Ocean. Reprinted from Dietel et al. (2023).

the liquid fraction (compare panel (i) in Fig. 5.11). Note, that we interpret sea salt here as a proxy for sea spray aerosols including biological parts, which can act as INP. The liquid fraction in low-level clouds over the Southern Ocean is lower if there are high sea salt concentrations compared to low sea salt concentrations, while the concentrations of other aerosol types only shows small differences in the liquid fraction. The liquid fraction in low-level clouds over the Arctic Ocean is lower in high sea salt conditions for a CTT larger than −28 °C, but there, other aerosol types may play a role (panel (j)). This could be explained by the fact that other aerosol sources are much closer and the transport plays probably a larger role there, compared to the very remote Southern Ocean. In mid-low-level clouds, sea salt aerosols show the largest differences in the liquid fraction between low and high aerosol conditions, but a generally smaller difference in the liquid fraction based on the sea salt conditions compared to low-level clouds.
In mid-level clouds over the Southern Ocean dust concentrations seem to play a large role, but also other aerosol types like black carbon or sea salt correlate with the liquid fraction. Over the Arctic Ocean mid-level clouds are as well influenced by many aerosol types and sea salt may play a minor role there. Interestingly, the correlation of sea salt, as a proxy for sea spray, with the cloud phase matches quite well with the correlation of sea ice with the phase regarding the different cloud types (compare Fig. 5.9). This supports the hypothesis of Carlsen and David (2022) that sea spray particles acting as INP foster the glaciation of low-level clouds.
Additional support for the hypothesis that sea spray aerosol strongly impact the phase of polar low clouds is given by the work of Griesche et al. (2021), who found a dependence of the Arctic cloud phase on the surface coupling, connected with marine INPs, but only for temperatures warmer than −15 °C, while we see a correlation of sea salt aerosol with the cloud phase for much lower temperatures. Griesche et al. (2021) observed a higher frequency of ice containing clouds, if the clouds are coupled to the surface compared to decoupled clouds using radiosonde data, and ground-based lidar and radar data. They propose increased marine biological INPs in the surface coupled boundary layer as the reason on the basis of recent in situ INP measurements in the Arctic. As this study takes place during the Arctic summer, temperatures close to the surface are rather high, compared to the winter season. Since our study

uses a two-year dataset, we assume that the influence of these marine biological INPs is also relevant at lower temperatures compared to Griesche et al. (2021). The relevant factor is probably the proximity of the cloud to the surface. This would also explain, why we see an influence of sea salt on the cloud phase at lower temperatures compared to Griesche et al. (2021).
To make sure that the phase influence is based on the aerosol concentration of a specific aerosol type and not just based on correlations between different aerosol types, we calculated the correlations coefficients of the different aerosol types within the different cloud types (see Fig. 5.12). Regarding correlations with sea salt, we can clearly see that there are only very low correlation coefficients with a most negative value of -0.08. Highest correlations (0.96) can be seen between organic matter and black carbon in the Arctic Ocean, but also over the Southern Ocean (0.77). Sulphate also correlates partly with organic matter or black carbon (0.45 - 0.58). Dust shows generally lower correlations with other aerosol types, with maximum correlations of 0.31 with sulphate aerosol. This strengthens the previously described hypothesis that sea spray seems to be an important INP in low-level and mid-low-level clouds with high concentrations leading to a reduced liquid fraction, and similar for dust in mid-level clouds.

5.3. Cloud radiative effect

We now investigate the cloud radiative effect (CRE) of the different cloud types and examine the influence of the cloud phase on the CRE. We further investigate the contribution of various cloud types to the total CRE over the Southern Ocean and the Arctic Ocean. To make the incoming solar radiation comparable between the Southern Ocean and the Arctic Ocean, we use equal latitude bands in this section for the two regions, namely 60 °S/N to 82 °S/N. In all other sections, the Southern Ocean is defined from 40 °S to 82 °S, as it is described in the Sec. 4. Nevertheless, there are still biases due to the different land distribution over the Southern Ocean and the Arctic Ocean, which leads to a higher cloud frequency in high latitudes over the Arctic Ocean compared to the Southern Ocean, because land surfaces like the Antarctic continent are excluded. For this analysis we consider both cloud profiles over the open ocean and cloud profiles over sea ice.

5.3.1. Mean cloud radiative effect of different cloud types

Panels (a) and (b) in Fig. 5.13 show the mean shortwave CRE (SWCRE), the longwave CRE (LWCRE), and the net CRE (NETCRE) of the different cloud types. High-mid-low-level and mid-low-level clouds show the highest SWCRE over the Southern Ocean, while over the Arctic Ocean mid-level clouds show the highest SWCREs. Over the Southern Ocean, the cloud types having high SWCRE are similar to the results from Oreopoulos et al. (2017), who investigated the CRE of similar cloud types globally with the same dataset. Over the Arctic Ocean, the SWCRE of the different cloud types is very similar and doesn't vary much. We find a generally stronger SWCRE over the Arctic Ocean compared to the global average from Oreopoulos et al. (2017), except for high-mid-low-level clouds over the Arctic Ocean. High-mid-

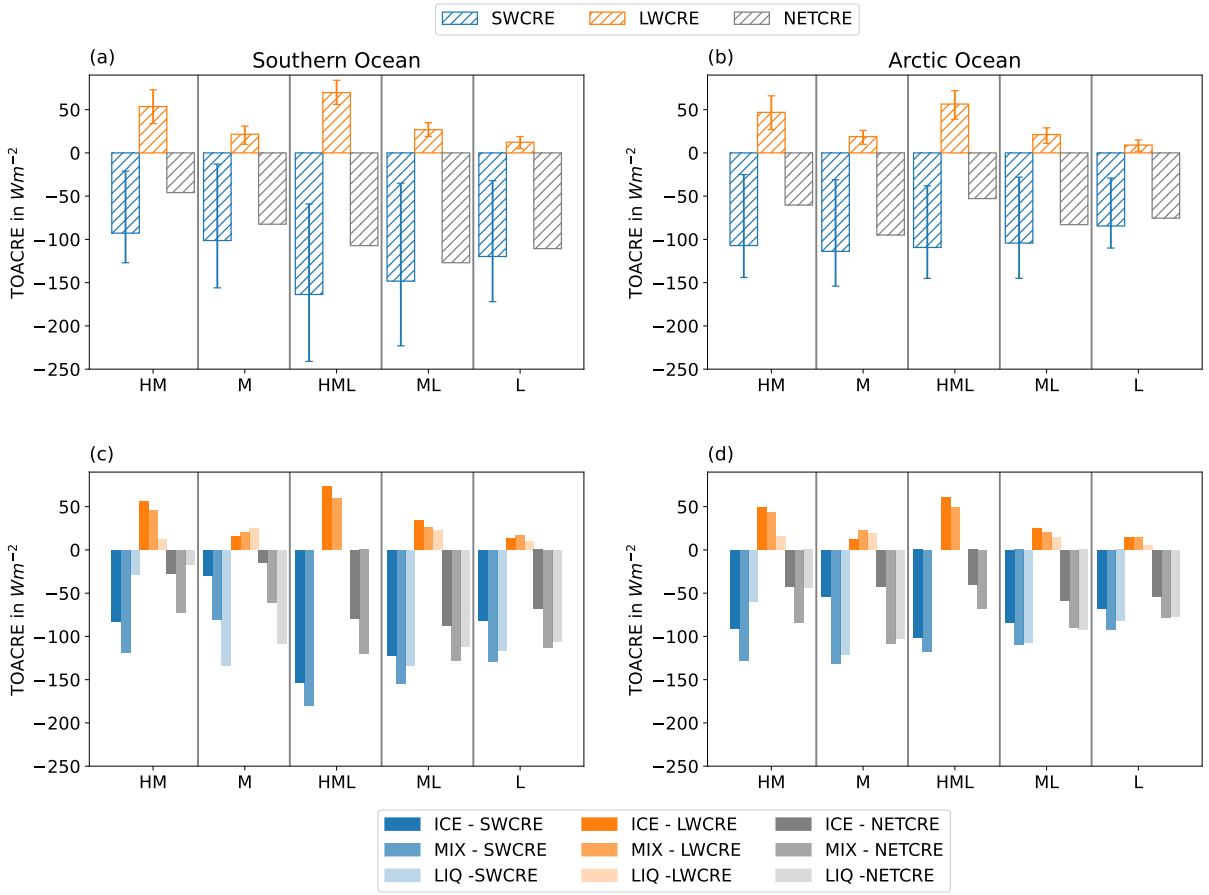

Figure 5.13.: Cloud radiative effects of different cloud types and with different cloud phases. The upper row shows the mean of the top of the atmosphere cloud radiative effect (TOACRE) for different cloud types, with the error bars showing the 25th and 75th percentiles. The lower row shows the mean top of the atmosphere cloud radiative effects (TOACRE) for various cloud types as a function of cloud phase. Shortwave cloud radiative effect (SWCRE) is shown in blue colors, longwave cloud radiative effect (LWCRE) is shown in orange colors, and net cloud radiative effect (NETCRE) in grey colors. The left column (panel (a) and (c)) shows the results for the Southern Ocean, while the right column shows the results for the Arctic Ocean (panel (b) and (d)). Note that there are no bars for liquid high-mid-low-level clouds in panel (c) and (d), as they don't occur. Reprinted from Dietel et al. (2023).

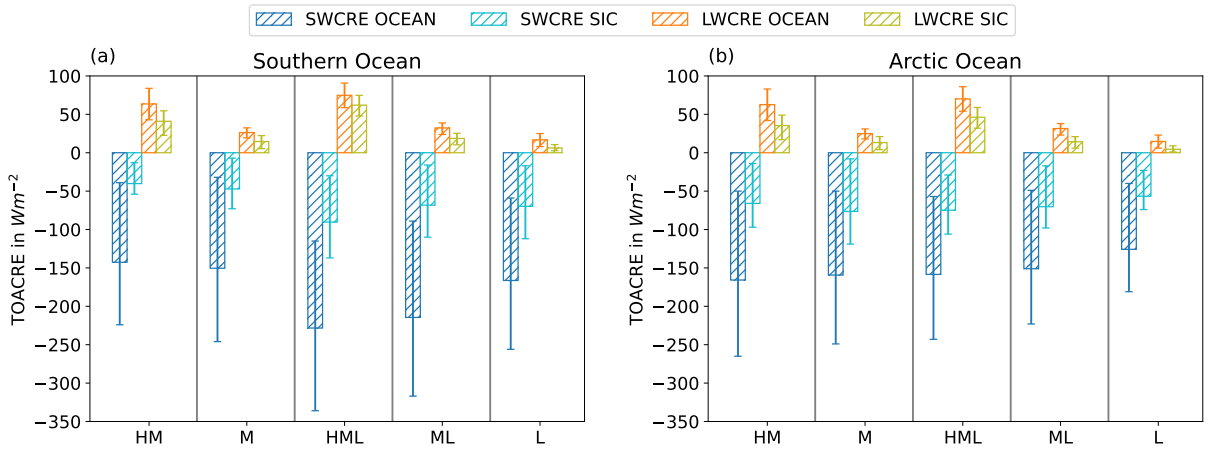

Figure 5.14.: Mean SWCRE and LWCRE of clouds over ocean and over sea ice for the Southern Ocean (left panel) and the Arctic Ocean (right panel).

level and mid-level clouds have a higher SWCRE over the Arctic Ocean compared to the Southern Ocean. Contrarily, high-mid-low-level, mid-low-level and low-level clouds show a higher SWCRE over the Southern Ocean compared to the Arctic Ocean.

A possible reason could be the distribution of sea ice, because the fraction of observed cloud profiles over sea ice is larger over the Arctic Ocean compared to the Southern Ocean due to the different land distributions in the two hemispheres. The SWCRE is lower for clouds over sea ice compared to clouds over open ocean (see Fig. 5.14) due to a higher albedo of sea ice compare to the open ocean. Figure 5.14 shows as well a higher LWCRE of clouds over ocean compared to cloud over sea ice, which is likely to be related to the higher outgoing longwave radiation over the ocean than over the sea ice. The difference in the SWCRE is larger than the difference in the LWCRE. However, the SWCRE of high-mid-low-level, mid-low-level, and low-level clouds is still higher over the Southern Ocean than over the Arctic Ocean, even if we only consider cloud profiles over the open ocean. Another reason for the difference in the SWCRE over the Arctic Ocean and the Southern Ocean may be a higher fraction of low-latitude clouds correlating with higher temperatures and more liquid clouds. This might be caused due to a higher land cover over the Arctic Ocean at low latitudes compared to the Southern Ocean. To investigate this, Fig. 5.15 shows the SWCRE of clouds over ocean as a function of the latitude. But even comparing the same latitudes, the SWCRE of high-mid-low-level, mid-low-level, and low-level clouds is still stronger over the Southern Ocean than over the Arctic Ocean except for higher latitudes than approx. 72 °N/S. Mid-level and high-mid-level clouds still show a stronger SWCRE over the Arctic Ocean. This suggests that the cloud properties over the Arctic Ocean differ from the ones over the Southern Ocean in for example the vertical extent or in optical properties which may be related to aerosols. In both regions high-mid-low-level clouds and high-mid-level clouds show the highest LWCRE. The LWCRE are similar over the Arctic Ocean and the Southern Ocean, with slightly larger effects over the Southern Ocean. McFarquhar et al. (2021) showed a lower surface SWCRE of about $-70\,\mathrm{Wm}^{-2}$ and a higher surface LWCRE of about

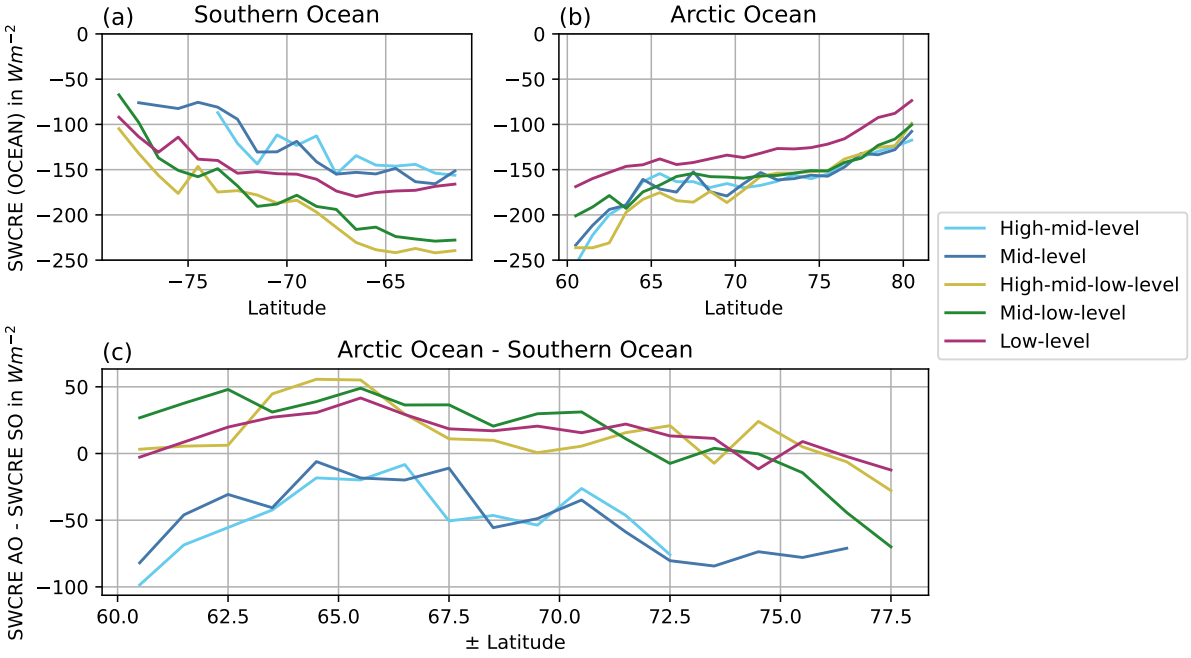

Figure 5.15.: Mean SWCRE of cloud types over ocean as function of the latitude for the Southern Ocean in panel (a) and for the Arctic Ocean in panel (b). Panel (c) shows the difference of the SWCRE over ocean between the Arctic Ocean and the Southern Ocean for the different cloud types as a function of the absolute value of the latitude.

50 Wm^{-2} for low clouds over the Southern Ocean observed during the Clouds Aerosols Precipitation Radiation and atmospheric Composition over the Southern Ocean (CAPRICORN) field study compared to our top of the atmosphere results. Further analysis are needed to distinguish differences in cloud type definitions, seasons, and regions, which may introduce large uncertainties to the comparison besides the difference of surface CRE and top of atmosphere CRE.

5.3.2. Dependence of the cloud radiative effect on the cloud phase

The phase of clouds has a large effect on their CRE, because numerous small liquid droplets are optically thicker than (few large) ice particles. Therefore, we investigate now the influence of the cloud phase on the CRE, shown in panel (c) and (d) in Fig. 5.13.

The highest SWCRE in all cloud types is observed from mixed-phase clouds, except for mid-level clouds over the Southern Ocean (see second column in panel (c), Fig. 5.13), where liquid clouds show a higher SWCRE compared to mixed-phase clouds. Matus and L'Ecuyer (2017) investigated the global TOACRE of different cloud phases with the same dataset, but didn't distinguish different cloud types and found the general highest SWCRE for liquid clouds, which highlights the complexity and dependence of the SWCRE on the region, the cloud types and their optical properties. Comparing the SWCREs of ice and liquid clouds, we can see that in most cloud types, the SWCRE is higher for liquid clouds compared to ice clouds, except for high-mid-level clouds, where ice clouds show a higher SWCRE. The behavior

of the high-mid-level clouds was unexpected, because cloud layers consisting of liquid droplets are in general optically thicker and should therefore show a stronger negative SWCRE compared to cloud layers containing ice particles, which are optically thinner. The stronger SWCRE of high-mid-level ice clouds compared to liquid clouds is probably explained by the larger vertical extent of ice clouds. Furthermore, the different vertical resolutions of the CloudSat radar and the CALIOP lidar can have an influence on the calculation of the vertical thickness and the calculated CREs. Oreopoulos et al. (2017) shows the strong correlation of the vertical thickness on the TOA SWCRE. This is probably also the reason, why mixed-phase clouds show mainly a stronger SWCRE compared to liquid clouds. The strong extinction of the lidar signal leads probably to an underestimation of the vertical thickness of the liquid clouds. Nevertheless, liquid clouds usually are not as vertically thick as ice clouds. Therefore, the possible underestimation of the vertical extent due to lidar extinction is not the main reason for the lower SWCRE in liquid clouds compared to mixed-phase clouds. It is rather the larger vertical extent in mixed-phase clouds due to precipitating ice virga and a thereby increased optical thickness.
Regarding the differences between the Southern Ocean and the Arctic Ocean, it can be seen that both the SWCRE and the LWCRE are mainly larger over the Southern Ocean compared to the Arctic Ocean. It can be also seen that over the Southern Ocean the SWCRE of clouds with low cloud bases (HML, ML, L) are quite high, while over the Arctic Ocean clouds with middle cloud base heights (HM, M) show high SWCRE. Generally, it can be seen that the cloud phase, but also the vertical extent of the cloud, has a large influence on the CREs of the different cloud types.

5.3.3. Contribution of different cloud types to the total SWCRE and LWCRE

To investigate the contribution of the different cloud types to the total SWCRE and LWCRE, we calculate the total sum of the SWCRE and the total sum of the LWCRE over the full two years 2007 and 2008 and normalize it by the total number of observed cloud profiles. The numbers are shown in Tab. A.1. We also calculate the total sum of the SWCRE and LWCRE of different cloud types. Figure 5.16 shows the contribution of the different cloud types to the total SWCRE and LWCRE as a percentage and indicates the large contribution of the low-level clouds with 26.0 % in the Southern Ocean and 33.3 % in the Arctic Ocean to the total SWCRE. This is related to their high occurrence shown in Fig. 5.1 and similarly shown by McFarquhar et al. (2021). Besides low-level clouds, mid-low-level and high-mid-low-level clouds show a large contribution to the SWCRE, but show higher LWCRE, compensating SWCRE. Mid-level clouds only contribute to a minor role to the total SWCRE with 2.2 % in the Southern Ocean, but show a higher contribution of 5.4 % in the Arctic Ocean. The contribution to the LWCRE of mid-level clouds over the Southern Ocean is 1.4 % and slightly larger over the Arctic Ocean with 2.5 %. The contribution of high-mid-level clouds to the SWCRE is small (1.2 %) over the Southern Ocean, but larger over the Arctic Ocean (5.2 %) with LWCRE contribution of 2.8 % over the Southern Ocean and 7.0 % over the Arctic Ocean.

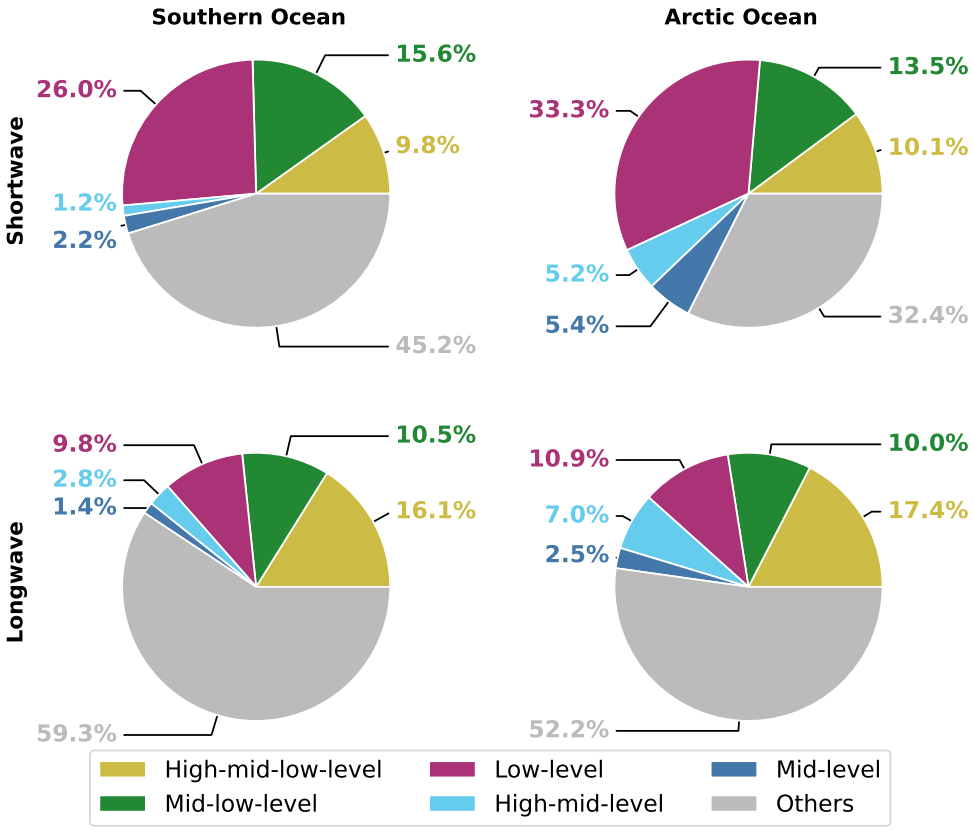

Figure 5.16.: Contribution of different cloud types to the total cloud radiative effects over 2 years at the top of the atmosphere over the Southern Ocean (SO) and the Arctic Ocean (AO) in percent. Reprinted from Dietel et al. (2023).

Regarding the total NETCRE (not shown), low-level clouds have the largest (negative) effect followed by mid-low-level clouds.
In summary, from an examination of various aspects of the cloud radiative effect, we see that mid-low-level clouds over the Southern Ocean have the highest net CRE, while over the Arctic Ocean mid-level clouds have the highest net CRE (see Fig. 5.13). In general mixed-phase clouds show a more negative SWCRE compared to ice and liquid clouds except for mid-level clouds over the Southern Ocean. Therefore, mixed-phase and liquid clouds show a higher net CRE compared to ice clouds. In general clouds over the Southern Ocean show a higher CRE compared to clouds over the Arctic Ocean. Investigating the contribution of different cloud types to the total CRE over the Southern Ocean and the Arctic Ocean, the low-level clouds contribute most in both regions due to their higher frequency compared to other cloud types (see Fig. 5.16).

5.4. Uncertainties

The combination of the different resolutions of the various datasets used in this study introduces uncertainties. While the DARDAR dataset has a very high spatial resolution ($\triangle h = 60\,\mathrm{m}, \triangle x = 1.5\,\mathrm{km}$), sea ice data and CAMS reanalysis have a much coarser spatial resolution. The temporal resolutions are also different, as the sea ice concentration is only available on a daily basis. Nevertheless, we think that due to the coarser resolution the temporal difference might play a minor role, as the sea ice concentration is only used to distinguish between sea ice conditions and open ocean. We don't consider small leads, cracks, etc., but rather want to distinguish between mostly sea-ice-covered ocean and open ocean.
For the aerosol reanalysis, the temporal resolution is 3-hourly and thereby introduces a temporal shift to the detection of single cloud profiles from the active satellite observations. Similar to the sea ice, the spatial resolution is rather coarse with 80 km. However, we don't investigate the total value of a mixing ratio within single cloud profiles, but rather investigate them in a statistical sense considering the upper and lower concentration quartiles (see Sec.5.2.4). Furthermore, we investigate the mean of aerosol mixing ratios in specific cloud types.
One of the largest uncertainties regarding the phase detection is the strong attenuation and partly full extinction of the lidar signal in supercooled liquid layers. This uncertainty is well known, but in combination with studies using ground-based observations the satellite perspective is still very useful and can lead to an improved understanding. Furthermore, we can interpret the liquid fraction used in this study as a lower boundary, which would even increase, if we could correct the lidar extinction and thereby the possible underestimation of the liquid phase. To examine the range of uncertainty, Fig. A.1 and Fig. A.2 show the results for the liquid fractions in the cloud types as a function of CTT, considering only profiles where the lidar is not fully extinguished, compared to considering all cloud profiles. Minor uncertainties are the extinction or attenuation of the radar signal in heavily raining clouds or deep convective systems,

but as we focus more on shallow clouds and not tropical deep convective systems, this only plays a minor role.

An uncertainty in the analysis of the cloud radiative effect is based on the assumptions made in the retrieval process of the 2B-FLXHR-LIDAR dataset. As the retrieval assumes a certain profile including liquid water content and ice water content based on different CloudSat products, such as the 2B-CWC or 2B-GEOPROF, this may not be consistent with the DARDAR dataset, which we use to calculate the liquid fraction for each cloud profile. However, we expect only minor differences as both, the 2B-FLXHR-LIDAR retrieval and the DARDAR retrieval are mainly based on CloudSat and CALIPSO observations.

6. Applying an explainable machine learning technique to investigate parameter importance for cloud phase

This chapter uses a machine learning model for the cloud types low-level, mid-level, and mid-low-level clouds, which are the most frequent cloud types in the mixed-phase temperature regime. The machine learning model predicts the liquid fraction f based on the features cloud top temperature (CTT), sea ice concentration, dust aerosol mixing ratio, and sea salt aerosol mixing ratio. Note that sea salt is used as a proxy for sea spray aerosol, which can include biological particles and thereby act as highly effective INP. Nevertheless, the following sections use the term sea salt to be consistent with descriptions in figures. A detailed description of the used machine learning model, the hyperparameter tuning, the input parameters, the model performance, and the usage of SHAP values can be found in Sec. 4.2.1-4.2.2. The following sections focus on the research results gained by using these machine learning models. A previous remark is made here the following results don't mean that specific aerosol are irrelevant and don't have an influence in specific clouds on their phase. For example laboratory have shown the ability of specific aerosols such as to nucleate ice. But this study represents a statistical analysis of correlations between typical aerosol concentrations in specific heights and the liquid fraction in specific clouds. Uncertainties of the underlying datasets were described in previous Sections (e.g. Sec. 3.2, 5.4). Section 6.1 describes the importance of the different features for the cloud phase in the different cloud types over both regions. An overview of the influence of the different parameters on cloud phase prediction is provided in Sec. 6.2. The influence of dust (see Sec. 6.3) and sea salt (see Sec. 6.4) on the cloud phase prediction is further investigated in detail with the spatial distribution of the influence and aerosol concentrations. Section 6.5 analyses the influence of sea ice with a focus on the possible connection to sea salt, as proposed in Sec. 5.2.4. The last Section 6.6 describes uncertainties of the previously provided results.

6.1. Importance of the parameters for the cloud phase prediction

First, the averaged importance of the input parameters for the prediction of the liquid fraction f in the different cloud types over the Southern and the Arctic Ocean are investigated and shown in Fig. 6.1. For all cloud types over both regions, cloud top temperature is most important, which is expected. The temperature is a known factor influencing cloud phase. The analysis considers the full range of observed cloud top temperatures and does not limit the analysis to the mixed-phase temperature regime, but includes cloud top temperatures larger than 0 °C and cloud top temperatures lower than −38 °C.

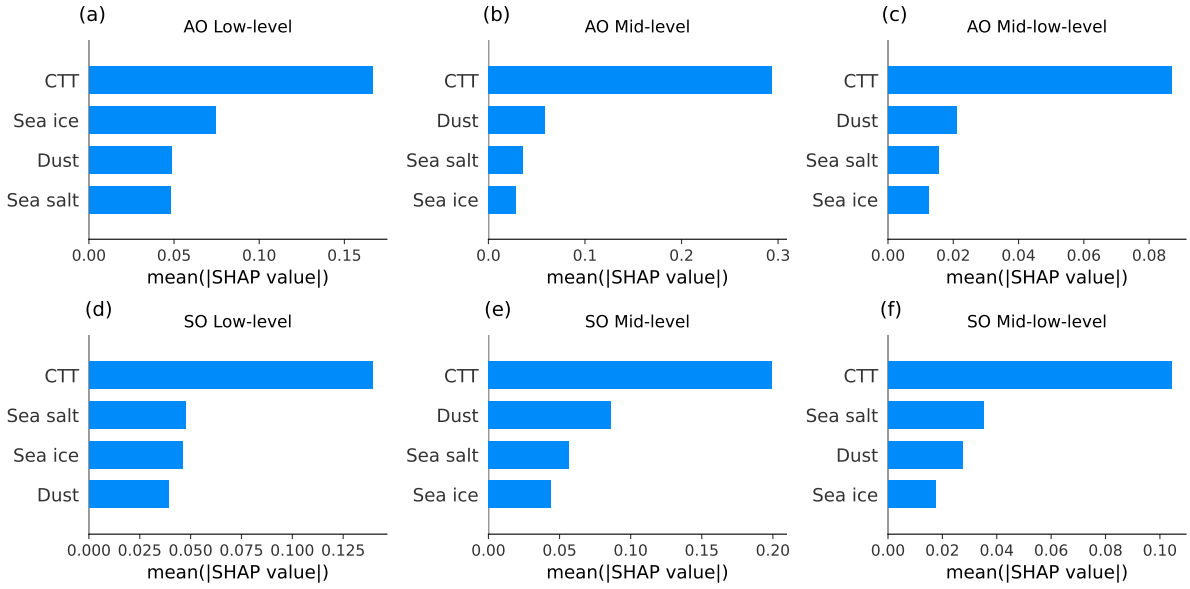

Figure 6.1.: Importance of different features for the prediction of the liquid fraction for different cloud types over the Southern Ocean (SO) and the Arctic Ocean (AO).

Outside of these two boundaries, the temperature strongly constrains the cloud phase. Also, in the mixed-phase temperature regime, temperature is a known influence with increasing freezing probabilities for lower temperatures. Regarding the second most important parameter in Fig. 6.1, differences between the cloud types, and regions are found. While sea ice is the second most important parameter in low-level clouds over the Arctic Ocean, sea salt is the second most important parameter in low-level clouds over the Southern Ocean. Mid-level clouds show in both regions dust as the second most important parameter. Mid-low-level clouds show again different parameters over the two regions with the Arctic Ocean showing dust, while the Southern Ocean showing sea salt. The result, that dust is more important in mid-level clouds can be related to the long-range transports of dust aerosols, which is found in mid, or high atmosphere levels, and rarely in lower levels due to the usual separation of the boundary layer by an inversion. It also seems reasonable that sea salt is more relevant in lower levels, close to the ocean source, where concentrations are usually highest as shown by Bian et al. (2019). This might also be the reason why sea salt is as well important in mid-low-level clouds over the Southern Ocean. Over the Arctic Ocean, sea salt seems to be less important compared to the Southern Ocean, which could be related to other aerosol sources in the Arctic, which are rarer over the Southern Ocean, where the air is in general cleaner compared to the Arctic Ocean. This is due to closer continental aerosol sources in the Arctic Ocean compared to the remote Southern Ocean. Another reason could be the larger importance of sea ice over the Arctic Ocean compared to the Southern Ocean with respect to their total ocean surface. Nevertheless, sea salt might also be relevant for low-level clouds in the Arctic Ocean, which other studies have shown, for example, if other aerosol sources are rare depending on the regions, season, and dynamical conditions.

6.2. Overview of the influence of the parameters on the cloud phase prediction

Figure 6.2 shows the distribution of SHAP values for the different cloud types and both regions. The distributions of the SHAP values depend on the one hand side on the importance of the features, but total values should be carefully compared between the different cloud types and regions, because the total values also depend on the base value of the model, which is the expected average liquid fraction and the corresponding distribution of the liquid fraction (compare Fig. A.9 and Fig. A.10).
First, the SHAP values of the cloud top temperature show the largest spread of SHAP values, which also highlights the importance of cloud top temperature. Furthermore, higher cloud top temperatures tend to have higher (more positive) SHAP values and vice versa, which is expected, as the freezing probability is increasing with decreasing temperature. The other distributions vary along the cloud type and region. Higher dust mixing ratios show mainly lower SHAP values, while lower dust mixing ratios correspond to higher SHAP values. The strongest (negative) impact on the model output by high dust mixing ratios can be seen in mid-level clouds. Sea salt shows a similar behavior as dust, with a tendency of high sea salt mixing ratios correlating with lower SHAP values compared to low sea salt mixing ratios. This could be explained by the possibility of sea salt and dust acting as INP and will be further analyzed and discussed in the following sections. The influence of sea ice on the model prediction differs for both, the cloud types and the regions. Except for mid-level clouds over the Arctic Ocean, low sea ice concentrations correlate with negative SHAP values, showing a decreasing effect on the predicted liquid fraction. Over the Southern Ocean, high sea ice concentrations mainly show positive SHAP values. In mid-level clouds over the Arctic Ocean, the distributions of the SHAP values for the sea ice concentration overlap more, and show a less clear signal. Nevertheless, low-level clouds over the Arctic Ocean show similar distributions for sea ice compared to low-level clouds over the Southern Ocean with low sea ice concentrations corresponding to negative SHAP values and higher sea ice concentrations corresponding to positive SHAP values.
Generally, a high importance of the temperature is shown, with higher temperatures leading to an increased predicted liquid fraction. Furthermore, the importance of dust in mid-level clouds can be seen, with higher dust concentrations corresponding to a decreased prediction of the liquid fraction, and a similar behavior for the sea salt mixing ratio in low-level clouds is shown.

As further sections also investigate the spatial distribution of the importance, Fig. 6.3 shows first the spatial distribution of the averaged liquid fractions for the different cloud types over both regions. Generally, it can be seen that the liquid fraction is higher for low-level clouds compared to mid-level clouds which show lower liquid fractions than mid-low-level clouds. Furthermore, the low-level clouds over the Arctic Ocean show a lower liquid fraction over the Atlantic sector and north of Scandinavia. The Southern Ocean shows mainly meridional gradients with a decreased liquid fraction in low-level clouds around 60 °S which increases again at higher latitudes. In mid-level clouds over the Southern Ocean mainly an

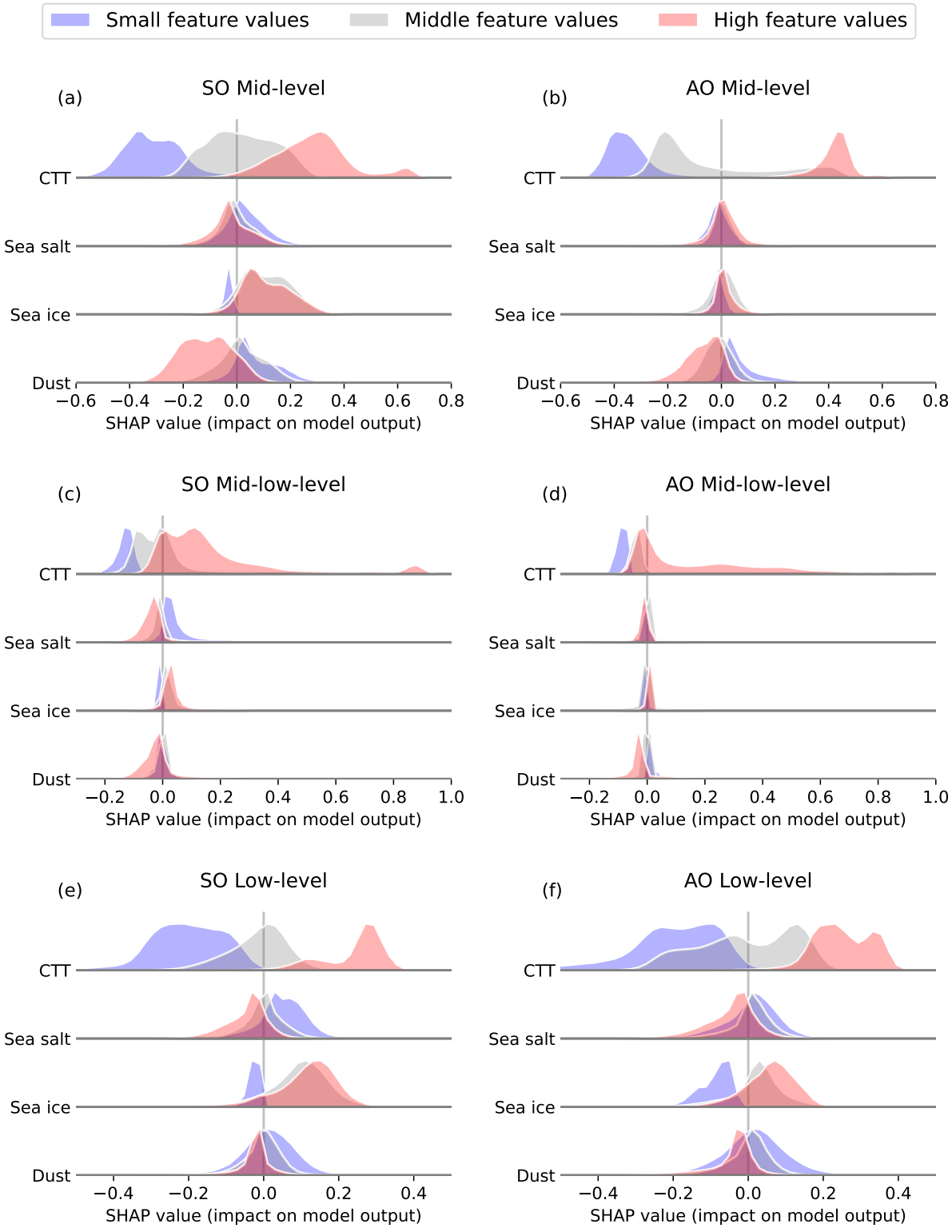

Figure 6.2.: Distribution of SHAP values of different features, cloud top temperature (CTT), sea ice concentration, dust aerosol mixing ratio, and sea salt aerosol mixing ratio. The colors correspond to small ($X \leq P25$), middle ($P25 < X \leq P75$), and high ($P75 < X$) values, based on the 25th percentile ($P25$) and the 75th percentile ($P75$) of the feature values, except for sea ice. Small sea ice values refer to values of zero, middle sea ice refers to values larger than 0 and lower or equal than 0.8, while high values refer to values larger than 0.8. Each distribution represents a probability density function based on a density estimation using Gaussian kernel. Each distribution is scaled by the maximum value of the distribution to improve readability.

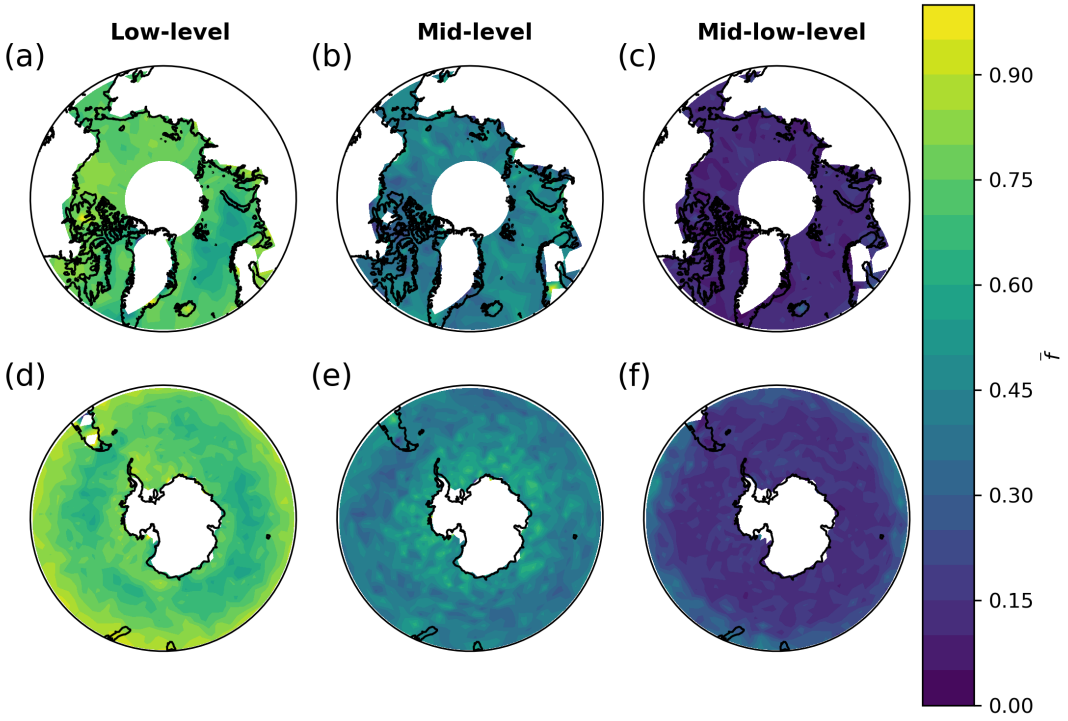

Figure 6.3.: Map of the averaged liquid fraction in the different cloud types over the Arctic Ocean (upper row) and the Southern Ocean (lower row).

increased liquid fraction with higher latitudes is observed, while the averaged liquid fraction in mid-low-level clouds is generally low. Possible reasons for this distribution are investigated and discussed in the further sections.

6.3. Influence of dust on the cloud phase prediction

The previous results have shown an importance of dust, which is now further investigated in detail. Figure 6.4 shows the correlation of the influence of dust on the prediction of the liquid fraction in the model as a function of the dust mixing ratio. The general signal is similar to the result from Fig. 6.1, showing the largest absolute values in mid-level clouds, while low-level and mid-low-level show values closer to zero. In mid-level clouds, a decreasing SHAP value for dust with increasing dust mixing ratio is shown. Theoretically, this could be explained by low dust mixing ratios, representing cleaner air, with therefore less INPs, and higher liquid fractions, while high dust mixing ratios, representing high INP concentrations, could lead to an increased ice formation and therefore lower liquid fractions. In mid-level clouds, the averaged SHAP value drops below 0 at a dust mixing ratio larger than about $10^{-11}\,\mathrm{kg\,kg^{-1}}$. In low-level clouds over the Arctic Ocean the SHAP values for dust show slightly negative values for high dust mixing ratios, but much smaller compared to the SHAP values in mid-level clouds.

Figure 6.5 shows the spatial distribution of the averaged SHAP value of dust depending on the latitude and longitude on a map. Mid-level clouds over the Southern Ocean show clearly the strongest positive

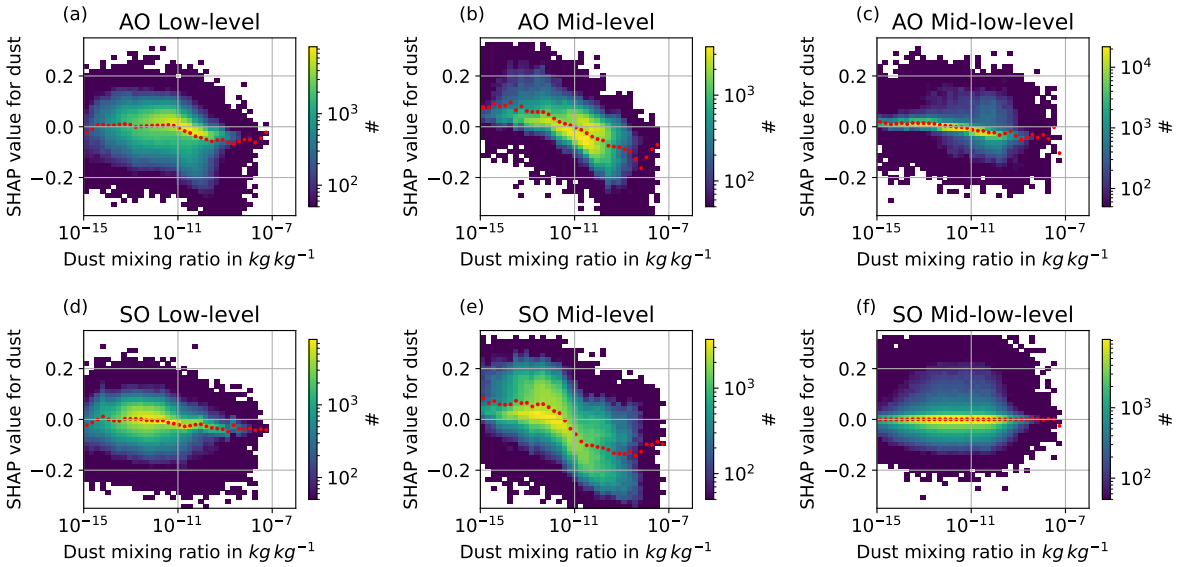

Figure 6.4.: 2D-histograms of the SHAP values for dust as a function of the dust mixing ratio. The red dots represent the mean as a function of the dust mixing ratio.

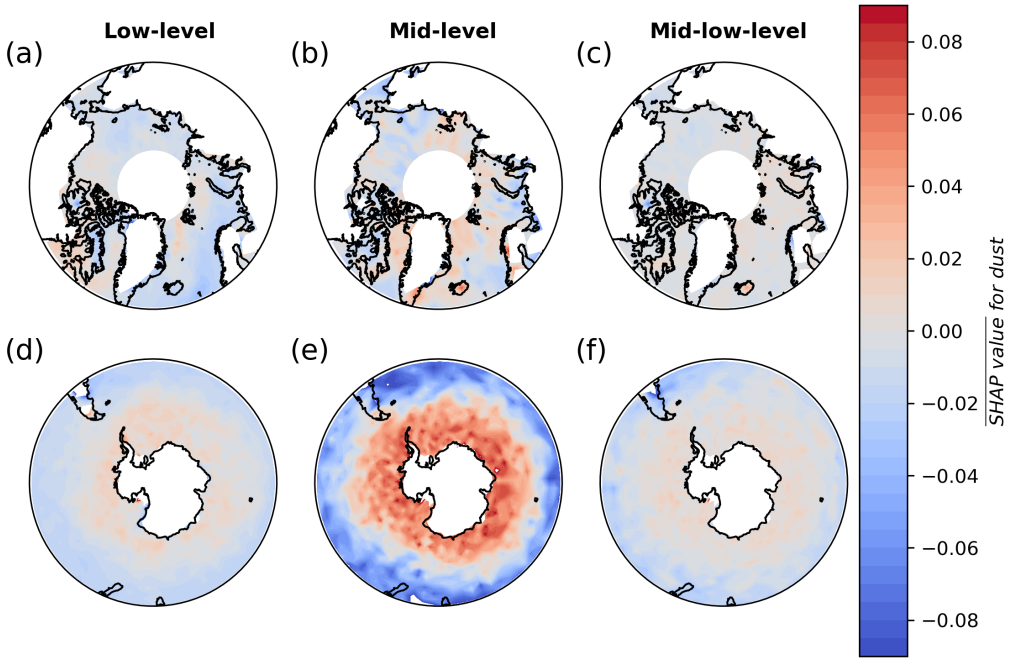

Figure 6.5.: Map of the averaged SHAP value for dust ($\overline{SHAP\ value}$ for *dust*). The upper row (panel (a), (b), and (c)) shows the Arctic Ocean, while the lower row (panel (d), (e), and (f)) shows the Southern Ocean. Red colors represent positive SHAP values, showing an enhancement of the predicted liquid fraction due to the dust mixing ratio, while blue colors show a reduction of the predicted liquid fraction due to the dust mixing ratio leading to increased ice formation.

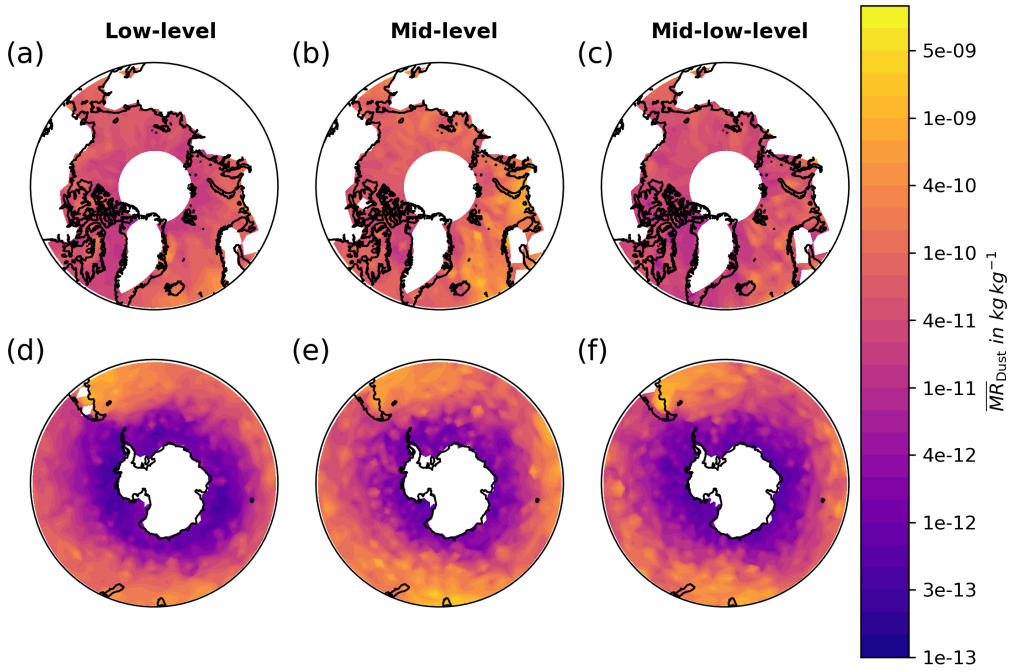

Figure 6.6.: Map of the averaged dust mixing ratio ($\overline{MR}_{\mathrm{Dust}}$). The dust mixing ratio is based on CAMS reanalysis and averaged over the heights where a cloud has been observed from satellite observations. The upper row (panel (a), (b), and (c)) shows the Arctic Ocean, while the lower row (panel (d), (e), and (f)) shows the Southern Ocean.

and negative SHAP values and show a strong increase with higher latitudes. Such a latitudinal dependence can also be seen in low-level and mid-low-level clouds over the Southern Ocean, but with much smaller absolute values. This is probably related to the dust mixing ratio, which is lower at high latitudes compared to lower latitudes (see Fig. 6.6). The latitudinal gradient may be related to the Antarctic polar front and the Antarctic Circumpolar Current (ACC), which reduce the meridional transport of dust aerosol to very high latitudes due to strong westerly winds around Antarctica. Over the Arctic Ocean, the meridional gradient is much lower compared to the Southern Ocean, and regional differences can be seen. In mid-level clouds over the Arctic Ocean, the dust mixing ratio (see Fig. 6.6) is higher over the Atlantic sector and north of West-Russia compared to the region north of East-Russia and Canada. The varying importance of dust could be related to the varying importance of other aerosol types with their sources being at northern hemisphere continents and thereby closer to the Arctic Ocean compared to the very remote Southern Ocean. This can also be a reason for the lower importance of dust in mid-level clouds over the Arctic Ocean compared to the Southern Ocean, where other aerosol types might occur less. The dust mixing ratios over the Southern Ocean show slightly higher values in mid-level clouds compared to low-level clouds (see Fig. 6.6), but the absolute SHAP values are much lower in low-level clouds. This suggests, that dust plays a minor role in low-level clouds over the Southern Ocean, where sea salt might be present. This will be investigated in the next section.

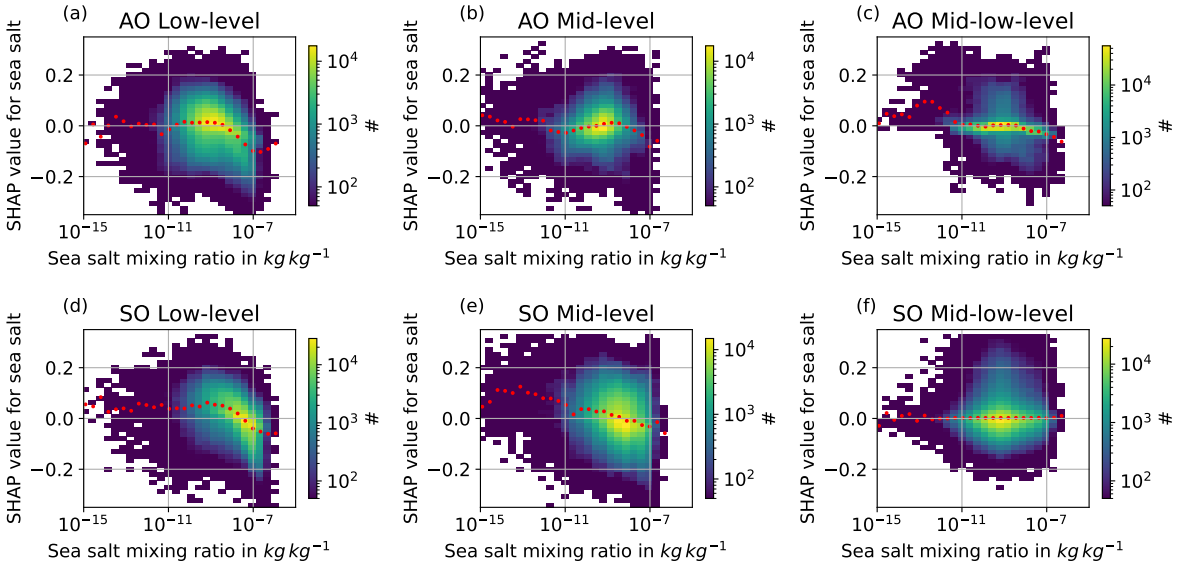

Figure 6.7.: 2D-histogram of the SHAP values for sea salt as a function of the sea salt mixing ratio. Red dots represent the mean as a function of the sea salt mixing ratio.

6.4. Influence of sea salt on the cloud phase prediction

This section investigates the influence of sea salt on the prediction of cloud phase. The SHAP values for sea salt decrease for a high sea salt mixing ratio in low-level clouds (see Fig. 6.7). The SHAP values for sea salt show negative values for a sea salt mixing ratios higher than approx. $5\times10^{-9}\,\mathrm{kg\,kg^{-1}}$ in low-level clouds over the Arctic Ocean, and for sea salt mixing ratios higher than approx. $10^{-8}\,\mathrm{kg\,kg^{-1}}$ over the Southern Ocean. The other cloud types show a lower correlation between the SHAP value of sea salt and the sea salt mixing ratio. Mid-level clouds over the Southern Ocean show a correlation, but mainly with higher positive SHAP values for lower concentrations. Mid-level clouds over the Arctic Ocean show as well slightly negative SHAP values for high sea salt concentrations, but these concentrations occur much less frequent in these cloud types compared to low-level clouds. Regarding the spacial distribution of the influence of sea salt on the cloud phase prediction, Fig. 6.8 shows the strongest signals in low-level clouds. Over the Southern Ocean, there is again a strong meridional gradient, similar to the results for dust in the previous Section. This may be again related to the polar front, strong westerly winds, and Antarctic Circumpolar Current. But unlike dust, sea salt has not to be transported, but is produced over remote oceans. The production of sea salt aerosols depends on various parameters. One of the most important ones is the wind speed, which is high at the polar front. The sea salt emission in the CAMS reanalysis is as well a function of the wind speed at 10 m (see Sec. 3.2.3). In theory, sea surface temperatures (SSTs) also influences the production of sea salt aerosols, with high SSTs showing higher production rates (Spada et al., 2013), but this is not considered in the parameterization of the CAMS reanalysis. Spada et al. (2013) indicated, that models with SST-dependent emission schemes

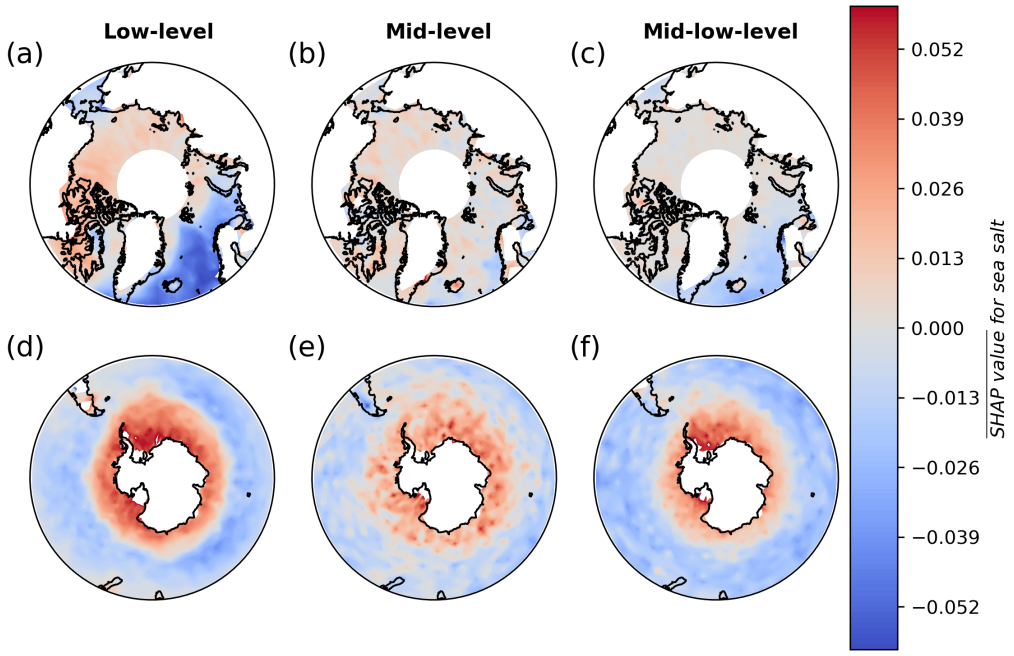

Figure 6.8.: Map of the averaged SHAP value of sea salt ($\overline{SHAP\ value}$ for *sea salt*). Similar to Fig. 6.5, but for the SHAP values of the sea salt.

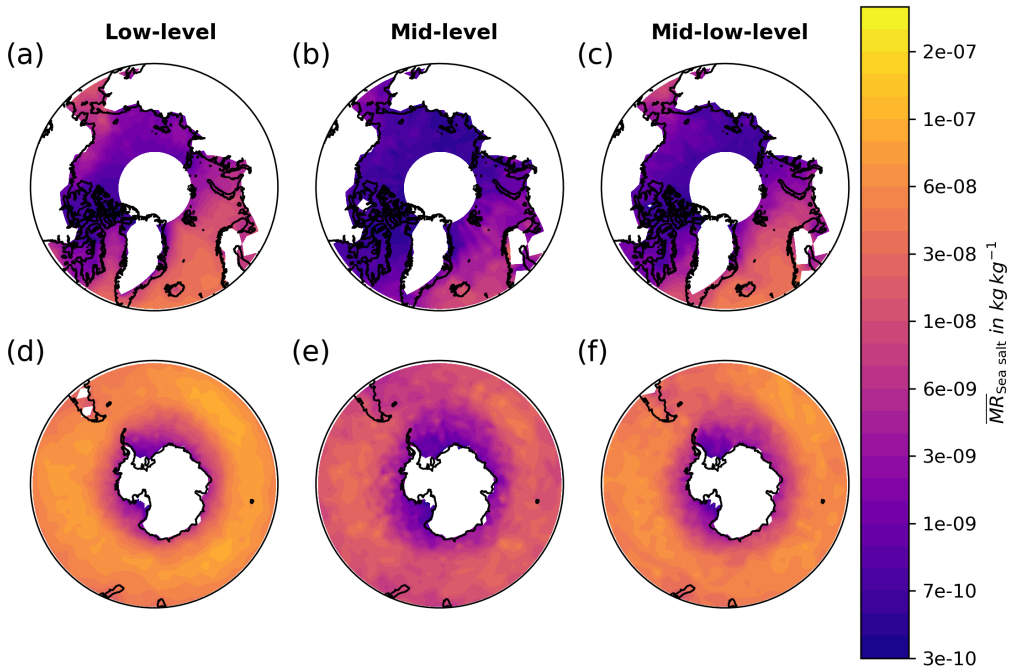

Figure 6.9.: Map of the averaged sea salt mixing ratio ($\overline{MR}_{\text{Sea salt}}$). Similar to Fig. 6.6, but for sea salt. Note that the color scale for the mixing ratios is different from the color scale in Fig. 6.6 for dust.

show improved performance. Shi et al. (2023) showed that cyclones are responsible for the upwards transport of sea salt aerosol, which may be a reason for the higher dust concentrations close to the west wind zone, where cyclones occur frequently compared to regions close to the Antarctic continent. Another factor influencing the sea salt production is probably sea ice coverage, preventing the release of sea salt aerosol from the ocean (Carlsen and David, 2022), which could also explain the positive SHAP values further pole-ward. In low-level clouds over the Arctic Ocean, the most negative values can be found over the Atlantic Sector. This region is usually characterized by southerly winds, transporting warm air northwards, and leading therefore to higher temperatures. Related to this is the reduced sea ice coverage in this region compared to other parts of the Arctic Ocean. Similar to the Southern Ocean, regions known to have warmer temperatures, high wind speeds, and low sea ice coverage seem to show a larger impact of sea salt aerosols on the cloud phase of low-level clouds. Figure 6.9 shows correlating high sea salt mixing ratios with the strong negative SHAP values in low-level clouds over the Arctic Ocean in Fig. 6.8. In low-level clouds over the Southern Ocean, the strong meridional gradient in the SHAP values for sea salt is partly correlating with the sea salt mixing ratio in low-level clouds in Fig. 6.9. Close to Antarctica the concentrations of sea salt are lower, but in general high in low levels over the Southern Ocean. Note, that the range of the color bar values are different in Fig. 6.6 and Fig. 6.9, as they are shown to investigate the spatial distribution of the different aerosol types. Figure A.14 and Fig. A.17 in Sec. A.2 show the same figures with equal color bar ranges to compare the total mixing ratios of dust and sea salt. A general lower mixing ratio of dust compared to sea salt is observed, with a stronger meridional gradient over the Southern Ocean for dust compared to sea salt. We can also see a similar distribution in the SHAP values for mid-low-level clouds compared to the corresponding low-level clouds over the same hemisphere, with smaller magnitudes in mid-low-level clouds than in low-level clouds. The distribution of the SHAP values for sea salt in mid-level clouds looks rather patchy, but still shows a meridional gradient over the Southern Ocean.

6.5. Influence of sea ice coverage on cloud phase and correlation with sea salt

Regarding the spatial distribution of the influence of sea ice on the prediction of the liquid fraction (compare Fig. 6.10), regions with sea ice occurrence show positive SHAP values in low-level clouds. This means that sea ice leads to an increased prediction of the liquid fraction in low-level clouds. In mid-level clouds over the Southern Ocean, a similar influence is found compared to low-level clouds. This result matches with the previous result from Sec. 5.2.4 showing the strongest correlations between sea ice and increased liquid fraction in low-level clouds over both hemispheres, and in mid-level clouds over the Southern Ocean. In this section is was also hypothesized, that the sea ice cover leads to a reduction of sea salt release from the ocean, which can be a reason for the increased liquid fractions over sea ice. To investigate this behavior in the machine learning model, Figure 6.11 shows the difference between normalized 2D-histograms, once considering only cloud profiles over ocean and once considering cloud

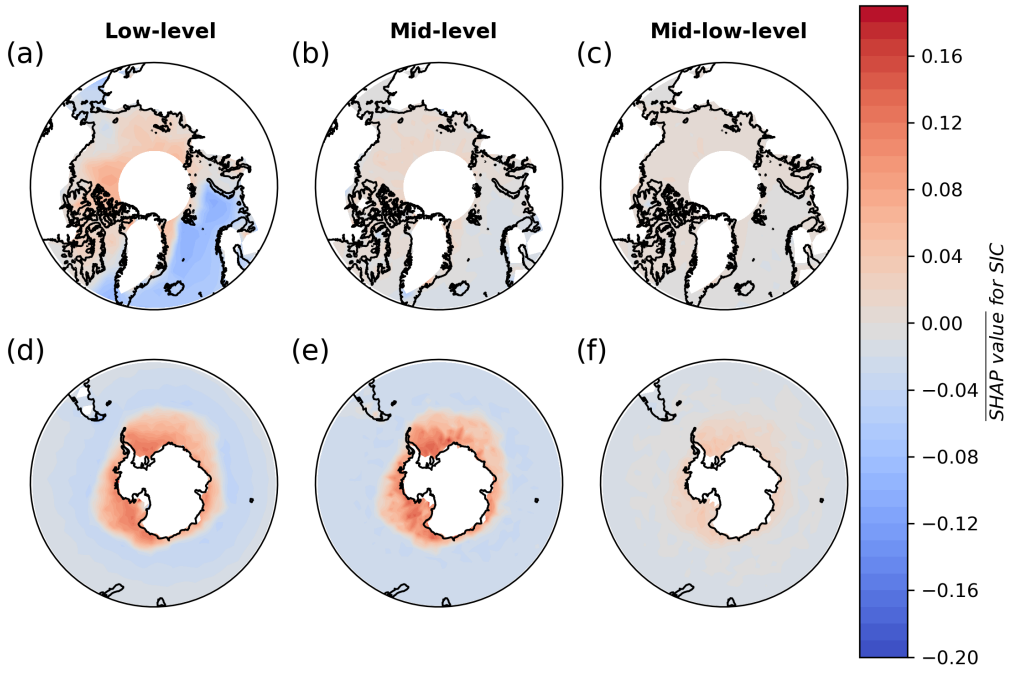

Figure 6.10.: Map of the averaged SHAP values of the sea ice concentration ($\overline{SHAP\ value}$ for SIC). Similar to Fig. 6.6, but for sea ice concentration.

profiles over sea ice. In low-level it is shown that high sea salt mixing ratios occur more frequently over the open ocean and this correlates as well with lower SHAP values for sea salt. In the other cloud types a correlation between sea salt and sea ice can be seen as well, with higher sea salt concentrations over the open ocean, but the influence of sea salt on the phase prediction (shown by the SHAP value) shows almost no change.

6.6. Uncertainties

This section discusses uncertainties of the previous results. Several uncertainties related to the model performance are already described in Sec. 4.2.1, and Sec. A.2. An important uncertainty is related to the interpretation of SHAP values. They show the importance and influence of parameters on the model prediction, but have to be carefully interpreted as generally valid results, as missing information in the model can lead to misinterpretation. For example, our model does not use information of the dynamical situation, while it is known, that this can have an influence on cloud phase. But as small scale dynamics are highly uncertain in models, this information is not used in this study. In future studies, one could investigate, if the model predictions changes, if large-scale dynamical information are provided. This would require the collocations of an additional reanalysis dataset, as the DARDAR-MASK dataset only provides collocated horizontal wind speed from the ECMWF. Furthermore, uncertainties of the provided datasets, e.g. cloud phase or aerosol information from reanalysis can also lead to uncertainties of the

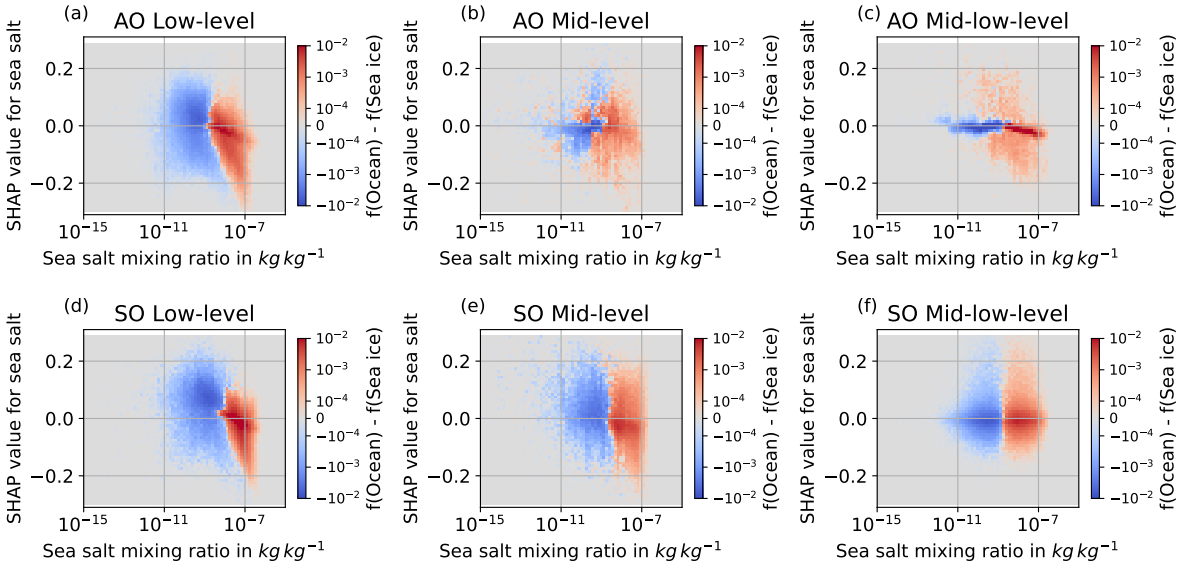

Figure 6.11.: Difference between normalized 2D-histograms once considering only cloud profiles over ocean and once considering only cloud profiles over sea ice.

resulting interpretations of the model results. In chapter 3, and Sec. 5.4 uncertainties of different dataset are mentioned and discussed.

The availability of sea salt acting as an INP is strongly dependent on the chemical composition of the sea salt, especially on the availability of biological components. These components have been shown to be highly ice nucleating active at high temperatures. Though this study assumes biological particles are part of the sea salt particles from reanalysis, because previous studies suggest this (Porter et al., 2022; Inoue et al., 2021; Twohy et al., 2021; Ickes et al., 2020; Wilson et al., 2015), the availability of such components and their dependence on environmental conditions and seasons has to be further investigated to improve the understanding on the underlying production mechanisms of sea salt containing biological components. Lapere et al. (2023) investigates the representation of sea salt in CMIP6 models and shows that over the poles, there are large discrepancies between observations and simulations. The simulations strongly depend on the representation of the sources, which need improvement for example in the wintertime sea salt source of blowing snow.

7. Comparison of clouds from the satellite perspective with ICON model simulations from the DYAMOND project

This section shows a comparison between satellite observations using the DARDAR dataset with ICON DYAMOND simulations. The ICON DYAMOND Summer simulation is used to compare satellite observations from 10 August to 10 September averaged from 2007 and 2008 to simulations from 10 August to 10 September 2016. This comparison refers to August/September in the following chapter. The ICON DYAMOND Winter simulation is used to compare satellite observations averaged from 30 January to 1 March of 2007 and 2008 to simulations of 30 January to 1 March 2020 and refers to February in the following chapter. In Section 4.3 the detailed method has been described. The first section of this chapter (Sec. 7.1) compares the cloud type frequencies from the satellite observations with the ones from the simulations. The following Sec. 7.2 compares the frequencies of different cloud type phases between satellite observations and simulations. Section 7.3 investigates the liquid fraction of the cloud types as a function of the cloud top temperature, and compares satellite observations with simulations. Section 7.4 has been part of the Bachelor Thesis of Sarah Paratoni (Paratoni, 2023) and investigates the difference between the liquid fraction of low-level and mid-low-level clouds over sea ice and over open ocean in the Arctic from satellite observations and a coupled ICON DYAMOND simulation. The final section (Sec. 7.5) addresses uncertainties of the analysis and the results.

7.1. Cloud type occurrence

The relative frequencies of different cloud types in satellite observations are compared with ICON DYAMOND simulations. Figure 7.1 shows the results for August/September, using the DYAMOND Summer simulations and February using the DYAMOND Winter simulations. In both seasons and both regions the DYAMOND results show less clear-sky scenes than the satellite results with the largest difference of the clear-sky occurrence (factor ≥ 3) in February over the Arctic Ocean. The cloud fraction in summer (August/September) is higher compared to winter (February) over the Arctic Ocean, which also has been observed in other studies (Liu et al., 2012; Intrieri et al., 2002; Houze Jr. and Houze Jr., 1994). Intrieri et al. (2002) show similar cloud occurrences compared to the DARDAR observations and also found an increase of the occurrence of multiple cloud layers in August/September compared to February. The fraction of multi-layer clouds in our analysis are generally higher in simulations compared to observations. Further studies focusing on multi-layer clouds could investigate how large the contribution of clouds with small discontinuities is and how large the fraction of „real “ multi-layer clouds is. This

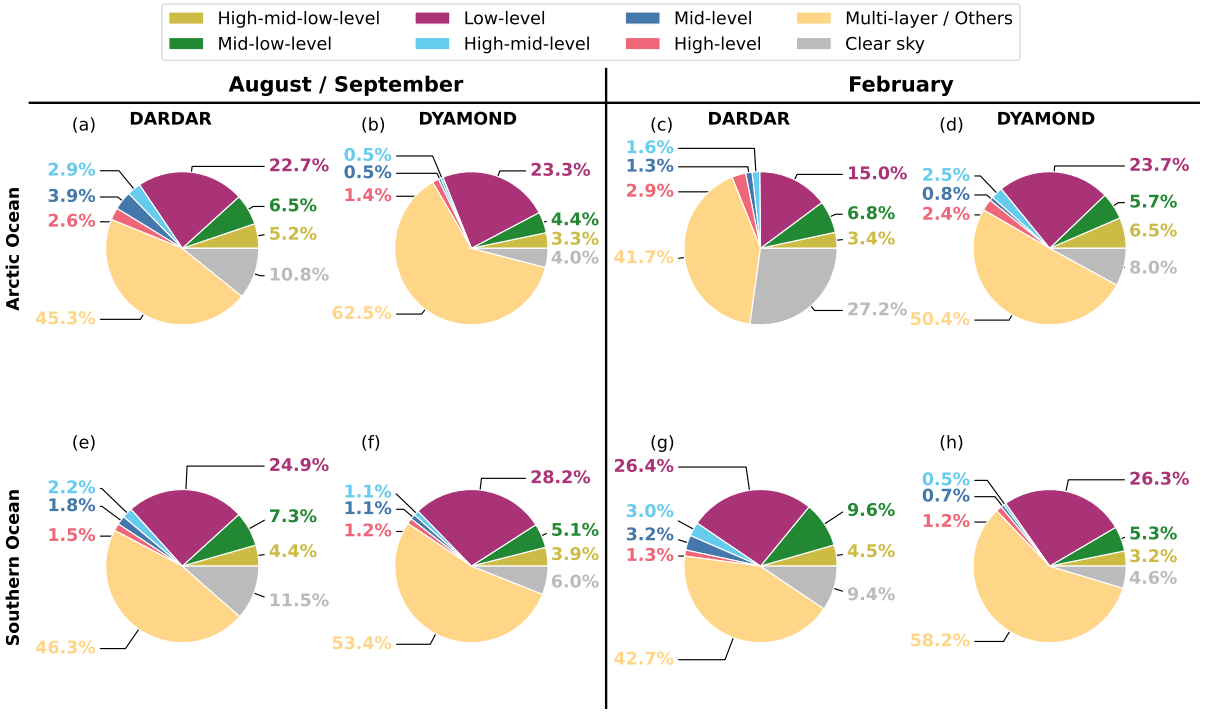

Figure 7.1.: Relative frequency of different cloud types in percent as fraction of the total number of observations of the summer period (10 August to 10 September) and of the winter period (30 January to 1 March). Panel (a), (b), (c), and (d) show the results for the Arctic Ocean, panel (e), (f), (g) and (h) for the Southern Ocean. The first column and the third column show the results of the satellite observations using the DARDAR dataset and consider the years 2007 and 2008. The second column and the fourth column show the results of the DYAMOND simulations considering the same days but for the year 2016 for August/September and the year 2020 for February.

could for example be done by applying a threshold for the minimal vertical extent of the cloud layers as well as for the cloud-free layer in between.

The frequency of low-level clouds is slightly overestimated in the model, except for February over the Arctic Ocean, where the model shows a strong overestimation (23.7 %) compared to the observations (15.0 %). Most other cloud types are underestimated in the model. This can be a hint that the seasonal cycle is not correctly simulated in the model, but further analysis are needed to confirm. In all comparisons, the frequency of mid-level clouds is underestimated in the simulations with a stronger difference seen over the respective summer hemispheres. In August/September over the Arctic Ocean the underestimation is strongest with a factor larger than 7, in February over Southern Ocean the overestimating factor is between 2 and 3. The respective winter hemispheres only show an overestimation by a factor smaller than 2. Mid-low-level clouds are underestimated in all simulations by a factor between 1.1 and 1.8. High-mid-level clouds are as well mainly underestimated in simulations by factor between 2 and 6, except in February over the Arctic Ocean, where an overestimation in the simulation can be seen. High-level clouds are slightly underestimated in simulations, but only by a factor less than 2. The analysis suggest, that the clouds in simulations are too low and mid-level clouds are underrepresented.

Over the Southern Ocean, the seasonal difference is lower which can be related to the different latitudinal boundaries of the two regions with the Arctic Ocean being more pole-ward and therefore showing a stronger seasonal cycle. Nevertheless, in Sec. 5.1 it was already referred to Fig. A.4 comparing cloud type frequencies of the same latitudes of the Arctic Ocean and the Southern Ocean suggesting a stronger seasonal cycle over the Arctic Ocean compared to the Southern Ocean. Figure A.21 shows the same analysis as Fig. 7.1, but as a relative frequency of specific cloud types with respect to all single-layer cloud profiles.

Figure 7.2 shows the fraction of the frequency of different single-layer cloud types as a function of their cloud top temperature. In the respective winter seasons a high fraction of low-level clouds over a large cloud top temperature range can be seen. In the mixed-phase temperature regime between −38 °C and 0 °C, mid-low-level clouds and a smaller fraction of mid-level clouds occur besides the low-level clouds. In the respective summer seasons, a high fraction of mid-low-level clouds around a cloud top temperature of −20 °C are observed. Besides the general agreement of cloud type fractions along cloud top temperature, the mixed-phase temperature regime also shows differences in observations and simulations, especially between the distributions of low-level, mid-level and mid-low-level clouds. The observations of August/September over the Arctic Ocean show a higher fraction of mid-level and mid-low-level clouds around a cloud top temperature of −15 °C compared to the simulations, where low-level clouds dominate at this temperature regime. The simulations over the Southern Ocean underestimate the fraction of mid-low-level and mid-level clouds at cloud top temperatures between −30 °C and −20 °C, and overestimate the fraction of low-level clouds compared to observations. In February, the observations over the Southern Ocean show higher fractions of mid-level and high-mid-level clouds with cloud top temperatures of about −20 °C compared to the simulations, while the Arctic Ocean simulations underestimate

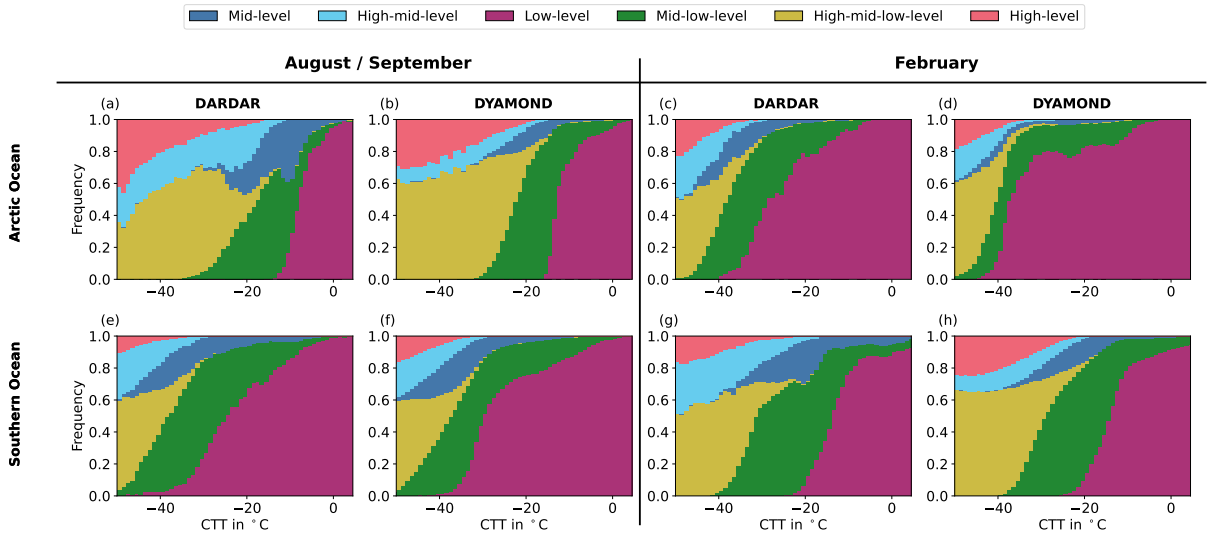

Figure 7.2.: Stacked frequency of occurrence of single-layer cloud types as a function of the cloud top temperature from 10 August to 10 September on the left hand side and from 30 January to 1 March on the right hand side. Columns with DARDAR header use satellite observations of the year 2007 and 2008, while DYAMOND columns refer to ICON simulations of August/September 2016 and February 2020.

the fraction of mid-low-level and mid-level clouds around −30 °C and clearly overestimate the fraction of low-level clouds. In August/September over both regions, and in February over the Southern Ocean, high-mid-level clouds are underestimated at cloud top temperature colder than −40 °C, while high-level clouds are overestimated in simulations compared to observations.

7.2. Cloud phase fractions

This section compares the fraction of liquid, ice, and mixed-phase clouds between the DARDAR and the DYAMOND dataset with the conditions of considering a cloud profile as liquid, mixed-phase or ice-phase given in Chap. 4. Figure 7.3 shows the results for the August/September period, while Fig. 7.4 shows results for February. In low-level and mid-level clouds the simulations clearly/strongly underestimate the fraction of liquid clouds. In low-level clouds the mixed-phase fraction is mainly overestimated, except for low-level clouds in February over the Arctic Ocean. The fraction of iced low-level clouds is overestimated in the respective winter season. In mid-level clouds the ice-fraction is generally overestimated in simulations, while the mixed-phase fraction is underestimated in the respective winter seasons in simulations. In mid-low-level clouds, the liquid fraction is overestimated except for February over the Arctic Ocean, where a strong overestimation of the ice phase is found. In high-mid-level clouds the simulations show a higher fraction of ice clouds and a corresponding lower mixed-phase fraction compared to the observations, while liquid clouds are almost not present in both, simulations and observations. In high-mid-low-level clouds simulations show lower fractions of ice clouds, and a higher fraction of mixed-phase clouds, but the uncertainty in observations might also be high due to attenuation and extinction of the active remote sensing signal.

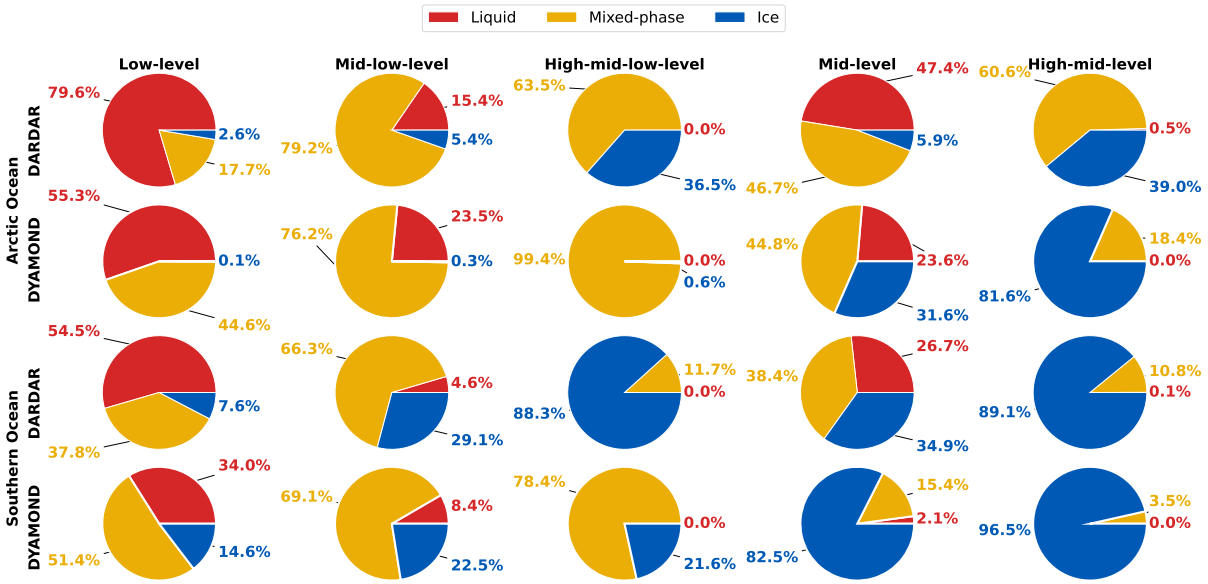

Figure 7.3.: Frequency of the cloud phase for the different cloud types (columns) over the Arctic Ocean (upper two rows) and the Southern Ocean (lower two rows) comparing results from DARDAR (upper row respectively) and DYAMOND (lower row respectively). The considered period is from 10 August to 10 September.

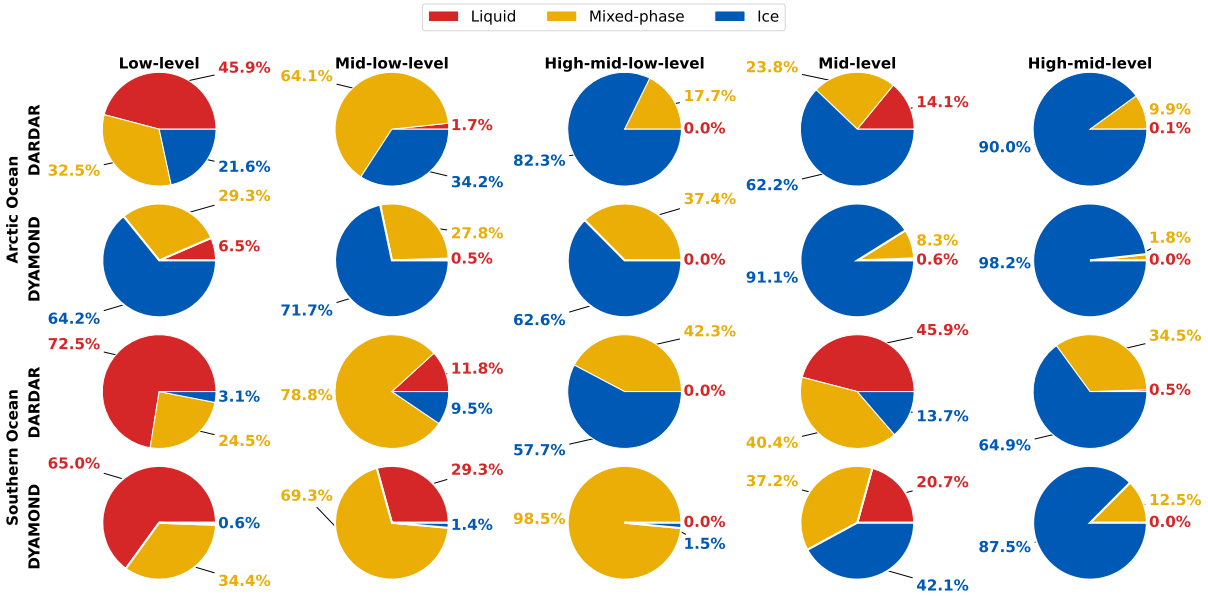

Figure 7.4.: Same as Fig. 7.3, but for the period from 30 January to 1 March using the DYAMOND winter datast.

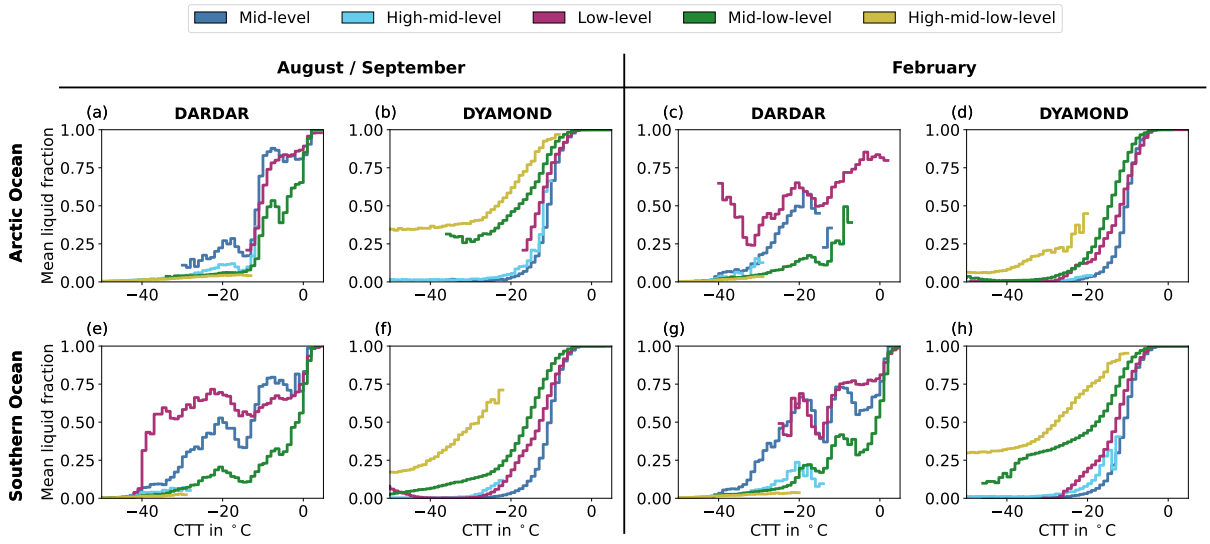

Figure 7.5.: Mean liquid fraction over the Arctic Ocean (top row) and the Southern Ocean (bottom row) for different cloud types in the DARDAR observations and the DYAMOND simulations for the August/September period and the February period. Note that the liquid fraction from DARDAR (f) refers to a pixel fraction based on the phase category while the liquid fraction for DYAMOND (f_{DYAMOND}) refers to an averaged mass fraction as described in Sec. 4.1.3 and Sec. 4.3.1.

Generally, in more shallow clouds like low-level or mid-level DYAMOND ICON simulations tend to underestimate the fraction of purely liquid clouds and overestimate either the fraction of ice cloud, or the fraction of mixed-phase clouds. This shows that the ICON simulations miss to produce or maintain enough liquid clouds over both polar regions. In mid-low-level clouds the ice fraction is sightly underestimated, except for the Arctic Ocean in February.

7.3. Liquid fraction as a function of the cloud top temperature

Figure 7.5 shows the mean liquid fraction as a function of the cloud top temperature for the different cloud types. The mean liquid fraction in Fig. 7.5 is only shown, if the number of profiles in the 1 °C temperature bin is larger or equal than 100. Figure A.22 shows the corresponding histogram.
Regarding the Arctic Ocean, the liquid fraction of mid-level and low-level clouds in August/September strongly decreases in observations between cloud top temperatures of −8 °C and −13 °C. The liquid fraction only reaches values of 1 at cloud top temperatures of approx. 0 °C, while the simulation shows a liquid fraction of 1 until cloud top temperatures of approx. −5 °C. The liquid fraction of mid-level clouds differs strongly at a cloud top temperature of −20 °C, with higher liquid fractions in observations. High-mid-level and high-mid-low-level clouds show a liquid fraction of 0 in observations for cloud top temperatures lower than −15 °C, where simulations show liquid fractions larger than 0.5. In February, the liquid fraction of mid-level and low-level clouds in observations is higher at low temperatures compared to August/September, while the simulations show a similar mean liquid fraction in August/September and

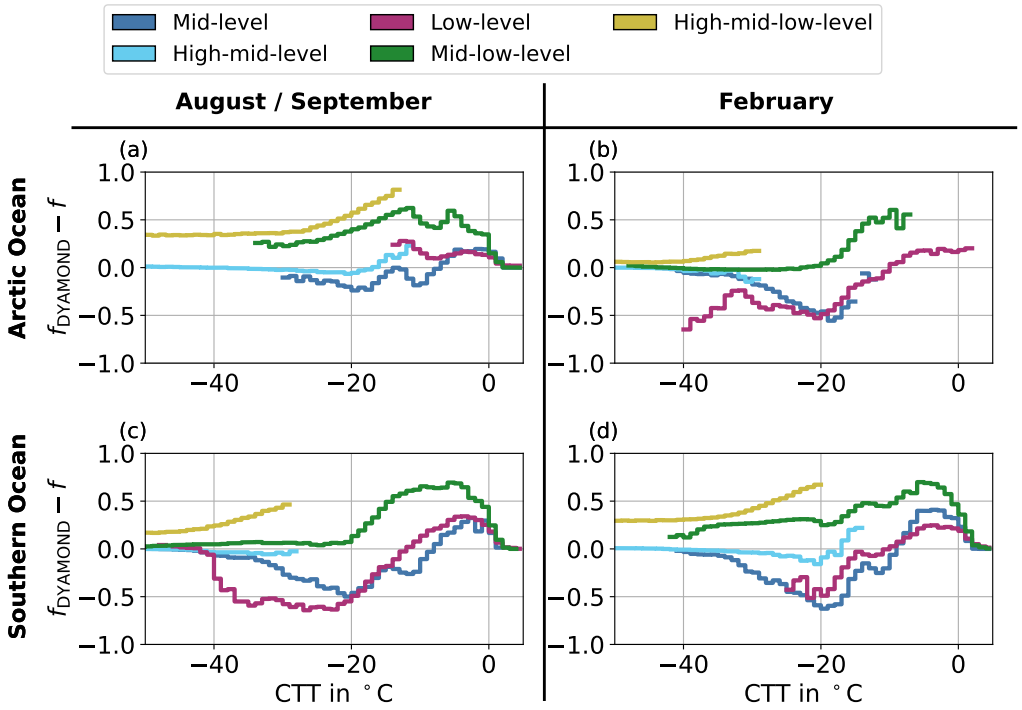

Figure 7.6.: Difference between the mean liquid fraction in clouds in the DYAMOND simulations ($f_{DYAMOND}$) and the mean liquid fraction in clouds in DARDAR observations (f) over the Arctic Ocean (top row) and the Southern Ocean (bottom row) for different cloud types for the August/September period and the February period. Mean liquid fractions are shown in Fig. 7.5. Note that the liquid fraction from DARDAR refers to a pixel fraction based on the phase category, while the liquid fraction for DYAMOND refers to an averaged mass fraction as described in Sec. 4.1.3 and Sec. 4.3.1.

February. Only the liquid fraction of mid-low-level and high-mid-low-level clouds is lower in February compared to August/September in simulations.
Regarding the Southern Ocean, the liquid fraction of low-level clouds in August/September stays high until low cloud top temperatures and strongly decreases at a cloud top temperature of about −40 °C. This is not the case for the simulations, which show mainly lower liquid fractions and reaches 0 at a temperature of −25 °C, where observations show still a mean liquid fraction higher than 0.6. Mid-level clouds in the observations show as well high liquid fractions at low cloud top temperatures, but lower compared to low-level clouds. In simulations, the liquid fraction of low-level and mid-level clouds is very similar, but shows generally lower liquid fractions compared to observations. In February, low-level and mid-level clouds show similar liquid fractions, except for a lower liquid fraction in mid-level clouds compared to low-level clouds between a cloud top temperatures of −10 °C and 0 °C. The simulations show as well similar liquid fractions in low-level and mid-level clouds, again with lower liquid fractions compared to observations.
In Sec. 5.2.2 the minima in the liquid fraction of low-level and mid-level clouds in the DARDAR observations has been mentioned. Regarding the different seasons, we can see that these minima, or strong decreases in the liquid fractions can also be seen in both seasons, and both regions, but not in simulations. This might also hint at ice production processes not resolved and/or not properly described or parameterized in the simulations.
Figure 7.6 shows the difference between the simulations from DYAMOND and the observations from DARDAR. Generally, the liquid fraction of low-level and mid-level clouds is mainly underestimated for cloud top temperatures colder than −10 °C in simulations, except for low-level clouds in August/September over the Arctic Ocean. At warm cloud top temperatures (> −10 °C) the simulations overestimate the liquid fraction in low-level and mid-level clouds. The liquid fraction of mid-low-level clouds is overestimated in all seasons and in all simulations compared to the observations, which is also the case for high-mid-low-level clouds. The overestimation in simulations has to be carefully interpreted, because of the uncertainty of the observations due to attenuation and extinction of active remote sensing signals, which might also lead to an underestimation of the liquid fraction in the observations. The more the underestimation of the liquid fraction in low-level and mid-level clouds in simulations should be taken into account, as the underestimation might even be stronger due to the mentioned uncertainties in the observations.

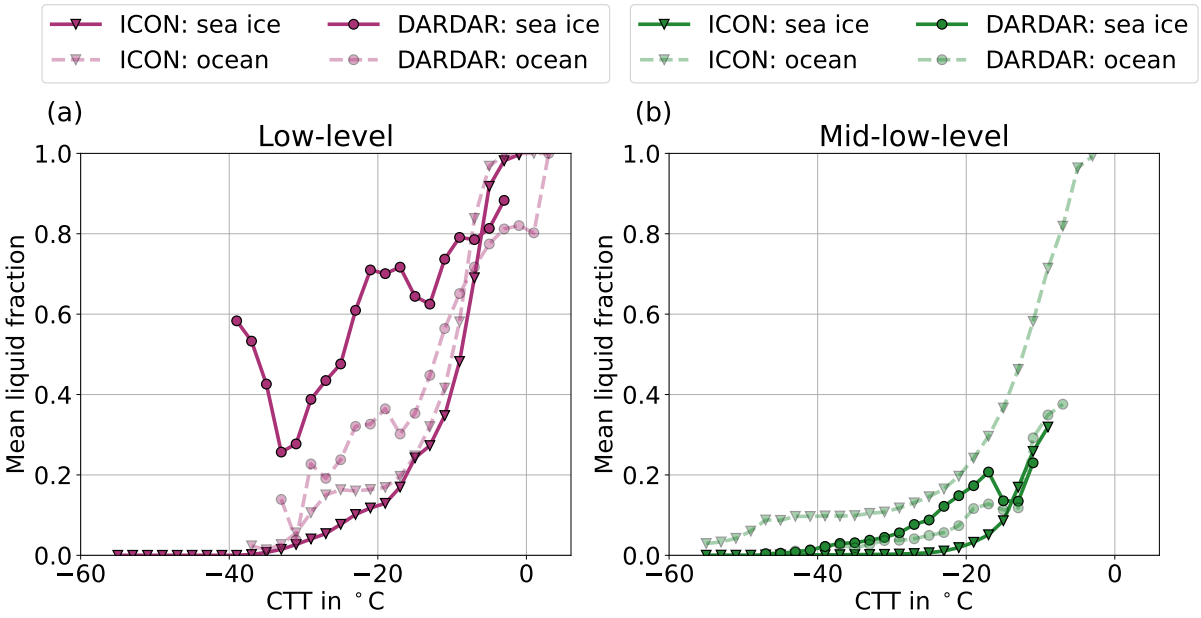

Figure 7.7.: Mean liquid fraction over ocean (light colors) and over sea ice (dark colors) from DARDAR observations (dots) and in ICON-SAP simulations (triangles) as a function of the cloud top temperature. A minimum number of 100 profiles is required to calculate the mean liquid fraction in observations and simulations. Otherwise the mean liquid fraction is set to a NAN-value. Adapted from Paratoni (2023).

7.4. Liquid fraction in low-level and mid-low-level clouds over sea ice and over open ocean in the Arctic [1]

As previous results from observations (see Sec. 5.2.4) have shown that the liquid fraction is different in some clouds over open ocean compared to sea ice, this is now investigated using simulation data. The coupled DYAMOND ICON simulation with a horizontal grid resolution of 5 km is used to analyze the liquid fraction of low-level and mid-low-level clouds over open ocean and over sea ice in the Arctic. The simulation is part of the DYAMOND-winter simulations and we analyze therefore the simulation period from the 31 January 2020 to the 1 March 2020 and observations from 31 January to 1 March of the years 2007 and 2008.

Figure 7.7 shows the results from observations and from the simulation. As already described in Sec. 5.2.4, the liquid fraction of low-level clouds in observations is higher over sea ice compared to the open ocean. Contrary, the simulations show almost no difference and even the opposite signal with higher liquid fraction over ocean than over sea ice for cloud top temperatures between −20 °C and −30 °C. In mid-low-level clouds the liquid fraction in observations is as well higher in clouds over sea ice compared to clouds over ocean, but the difference is much smaller compared to low-level clouds. In simulations, the difference shows again the opposite signal compared to the observations, with a higher liquid fraction

[1] These calculations have been done as part of the Bachelor Thesis of Sarah Paratoni (Paratoni, 2023), who was supervised by the candidate, Dr. Lena Frey and Prof. Dr. Corinna Hoose. The following figures and text in this section are created by the candidate.

over ocean than over sea ice for all cloud top temperatures. The difference is also larger compared to low-level clouds.
Overall the simulations and observations show a completely different signal. Further investigations are needed to point out the reason for these differences. A possible reason is the simplistic treatment of aerosols and INPs within the one-moment scheme and the parameterizations of the production of ice particles. The one-moment scheme doesn't consider any aerosols for the formation of ice, but uses a simply temperature dependent approach. To address this hypothesis a comparison to a simulation using prognostic aerosols and a coupling to cloud microphysics should be investigated. Furthermore, dynamical correlations with cloud phase related to sea ice could be investigated, for example by analyzing the coupling of low-level clouds to the surface, as it was done by Griesche et al. (2021), who found a higher ice fraction in clouds, if they are coupled to the surface.

7.5. Uncertainties

This section addresses uncertainties of the comparison between the results based on satellite observations and the results from different ICON simulations as part of the DYAMOND project.
A first point to mention are differences in the resolutions between observations and simulations. The vertical grid resolution of the DARDAR dataset is 60 m, while the vertical grid resolution of ICON with 90 levels decreases with height, starting from 20 m at the lowest level and increasing to 400 m around a height of 10 km. Also, the original resolution of the CloudSat and CALIOP observations differs, CALIOP provides the lidar information on a vertical resolution of 60 m, while the radar information from CloudSat has an original vertical resolution of 500 m. The horizontal grid resolutions are as well different, but in a similar range, with DARDAR data having a horizontal resolution of 1.5 km, while the used simulations have a horizontal grid resolution of 2.5 km for the atmosphere-only simulations, and 5 km for the coupled ICON simulation. Another uncertainty is introduced by the the comparison of the same days of different years in observations and simulations. To address this uncertainty, Fig. 7.8 shows the 2-meter temperature difference of the same days in different years from the fifth generation ECMWF reanalysis (ERA5) (Hersbach et al., 2023a,b). For the comparison in August/September, hourly reanalysis data are used and then averaged over the mentioned days (10 August - 10 September), while for February the monthly averaged 2-meter temperature is used. The ERA5 reanalysis have a resolution of 0.25°. The differences are strongest in the Arctic Ocean in February, while the other differences are lower. Nevertheless, the horizontally averaged difference ($\overline{\Delta T_{2\mathrm{m}}}$) is below 1 K for both regions in both seasons. This suggests that observations and simulations of the same days in different years can still be compared in a statistical sense, as the analyzed regions are large enough.
A further difference and thereby introduced uncertainty of the comparison is based on the different calculation of the liquid fraction in observations and in simulations (compare Sec. 4.1.3 and Sec. 4.3.1). While the liquid fraction in observations is calculated from numbers of pixels categorized as liquid-, ice-

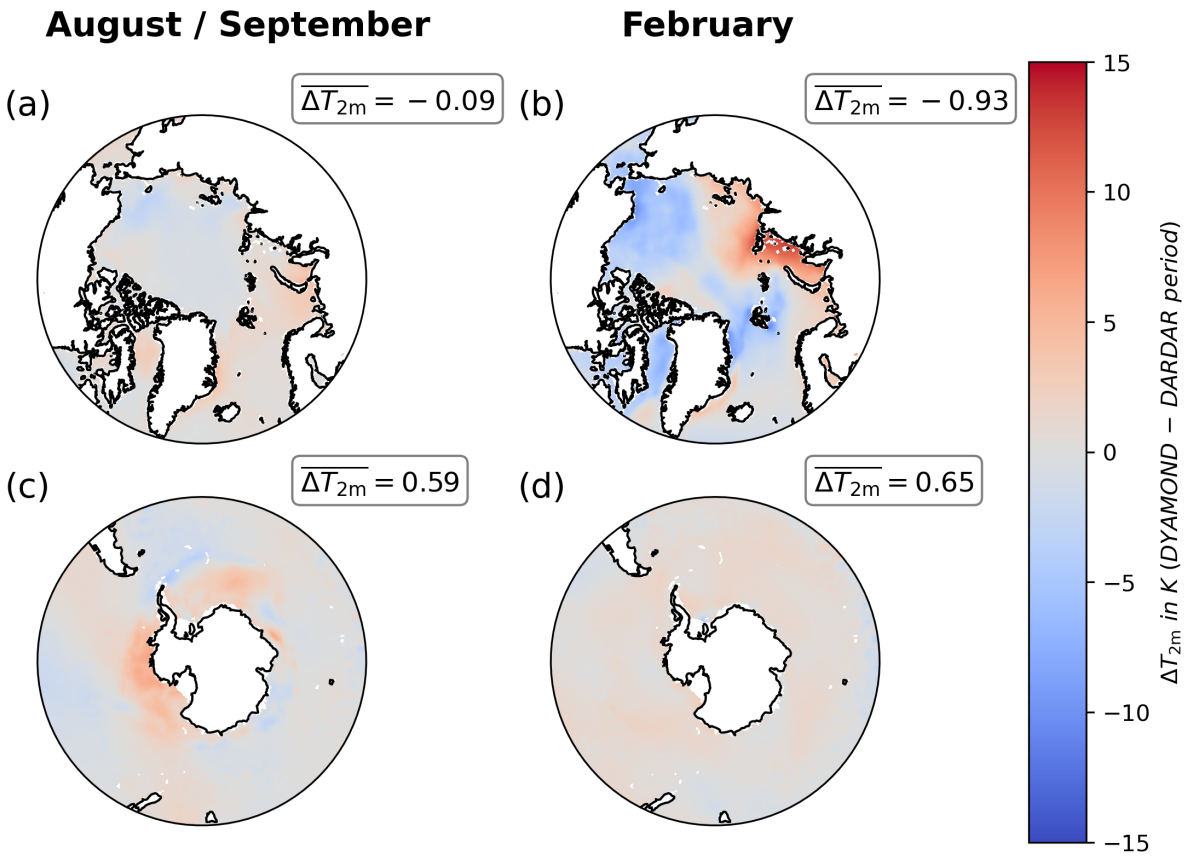

Figure 7.8.: Difference between the monthly averaged ERA-5 2-meter temperature (Hersbach et al., 2023b) of the corresponding year of the used DYAMOND dataset and the year of the used DARDAR dataset. The left column refers to the period from 10 August to the 10 September and shows the difference between the the year 2016 and the average of 2007 and 2008 (panel (a) and (c)). The right columns shows the difference of the monthly mean of February 2020 and the average of February 2007 and 2008. Panel (a) and (b) show results for the Arctic Ocean, panel (c) and (d) show results for the Southern Ocean.

, or mixed-phase, the liquid fraction in simulations is calculated from mass fractions of ice and liquid. Furthermore, the used satellite observations also include uncertainties due to instrument sensitivities and limitations, like attenuation, extinction, or multiple scattering of the active remote sensing signals, as well as uncertainties from the analysis temperature provided by ECMWF and used within the DARDAR retrieval process. A possibility to address these uncertainties are evaluations in the observational space. A alternative solution to these uncertainties, and the difference in the calculation of the liquid fraction would be the usage of a satellite simulator like COSP (CFMIP Observation Simulator Package), developed by the Cloud Feedback Model Intercomparison Project (CFMIP) community (Bodas-Salcedo et al., 2011). The simulator uses model output to simulate what specific satellite instruments and sensors would detect. Usually, radiative transfer simulations are needed to calculate the signal an active sensor would measure. Afterwards, the DARDAR retrieval would have to be applied to the calculated CloudSat and CALIOP "observations". As this analysis requires additional calculations, modeling, and computational costs, and the provided variables from the DYAMOND simulations are limited, this was not investigated in this study, but may be the way forward for further detailed comparisons.

8. Conclusions and outlook

This chapter summarizes the main results of this thesis and provides a brief outlook of further research needed to improve the process understanding of cloud phase over the Arctic and the Southern Ocean and their representation in models. Section 8.1 summarizes the three result chapters (Chap. 5, Chap. 6, and Chap. 7) and answers the proposed questions from the introduction. Section 8.2 provides further ideas on future research with some focusing on the provided methods and analysis to investigate specific results in more details, and others more generally pointing at the need of further research with other methodologies like laboratory experiments and in-situ observations to improve general understanding.

8.1. Conclusions

By analyzing a comprehensive two-year dataset of collocated information including vertically resolved cloud phase information from satellite-based active sensors, satellite-based sea ice concentrations, re-analysis of aerosols, and cloud radiative effects, a deep insight into the connections between various parameters and their possible influence on cloud phase has been gained.
Chapter 5 analyzed general frequencies and characteristics of cloud types, defined by their cloud top height and their cloud base height over the Arctic Ocean and the Southern Ocean.

- How frequent are different cloud types based on their heights?

A generally high frequency of low-level clouds could be seen for the Arctic Ocean (21.5 %) and the Southern Ocean (25.6 %). Clouds spanning the mid-level range also amount up to 15 % with mid-low-level clouds contributing by about 6.9 % to 8.1 %, high-mid-low-level clouds by about 4.4 % to 4.5 %, high-mid-level by 2.3 % to 2.6 %, and mid-level by 2.2 % to 2.5 %.

- Which phase do the different clouds typically have, and which cloud types occur most frequent in the mixed-phase temperature regime?

Low-level, mid-level, and mid-low-level clouds are the only cloud types which occur as liquid, mixed-phase, and ice clouds, and they also make a large contribution to the cloud frequency in the mixed-phase temperature regime. All investigated cloud types show a fraction of 24 % or more mixed-phase clouds.

- How does the vertical and horizontal extent of clouds correlate with cloud phase?

Liquid clouds are shown to be vertically thinner compared to ice clouds, whereby the vertical extent is partly influenced by the algorithm of the DARDAR retrieval (classifying thicker clouds as ice clouds) and the different vertical resolutions of the original CloudSat signal mainly detecting ice and CALIOP mainly detecting liquid. Regarding the horizontal extent, ice clouds tend to be horizontally smaller compared to liquid clouds. Mixed-phase clouds are vertically and horizontally large.

- ❄ What is the phase distribution as a function of the temperature in different cloud types and how is cloud phase vertically distributed within mixed-phase clouds?

Low-level and mid-level clouds show the highest liquid fractions followed by mid-low-level clouds. The liquid fraction is higher over the Southern Ocean for cloud top temperatures lower than −10 °C compared to the Arctic Ocean and lower for cloud top temperature higher than −10 °C. The reason for this is not yet clear and has to be investigated in future research. Possible reasons for the differences may be different aerosol contributions, but also different cloud dynamics could play a role. Two local minima of the liquid fraction are observed around a cloud top temperature of −15 °C and −5 °C which hints at ice processes occurring at these temperatures. Habit dependent vapor growth is discussed as a reason, especially for the temperature range at −15 °C, which is known as the dendritic growth layer, but also secondary ice production may play a role or even a combination of both processes due to interacting effect may be relevant. In mixed-phase clouds, the liquid phase mainly occurs at cloud top, with ice precipitating from these supercooled liquid layers, which is a known structure of mixed-phase cloud in polar regions. Nevertheless, low-level clouds show an increasing liquid phase in lower parts of the cloud, which is mainly based on multiple scattering and it has to be further investigated if ground clutter from the radar may play a role here.

- ❄ How does cloud phase correlate with sea ice cover and the amount of specific aerosol types?

Low-level clouds show a significantly higher liquid fraction if they occur over sea ice compared to open ocean. Over the Southern Ocean the same is found for mid-level and mid-low-level clouds, while over the Arctic Ocean, these clouds types only show a signal for very high cloud top temperatures ($CTT \geq -10\,°C$). Carlsen and David (2022) found a similar behaviour in low-level clouds over both hemispheres and proposed that sea ice prevents the release of sea spray aerosols, which acts as INP. By investigating collocated aerosol reanalysis, this thesis supports this hypothesis showing that sea salt concentrations (used as a proxy for sea spray aerosols) are lower over sea ice than over open ocean. Low-level clouds showed decreased liquid fractions for high sea salt concentrations. In higher altitudes for mid-level clouds the liquid fraction correlates more with other aerosol types like dust, probably related to aerosol transport.

- ❄ How large is the top of the atmosphere cloud radiative effect for different cloud types and how does it differ with different cloud phases? How large is the contribution of specific cloud types to the total cloud radiative effect?

The strongest shortwave cloud radiative effects are shown by high-mid-low-level and mid-low-level clouds over the Southern Ocean. Over the Arctic Ocean, the shortwave cloud radiative effect is similar between the different cloud types. The longwave cloud radiative effect is largest in cloud types with high cloud tops (High-mid-level and high-mid-low-level) in both regions. The shortwave cloud radiative effect is higher over the Southern Ocean than over the Arctic ocean in high-mid-low-level, mid-low-level, and low-level clouds, while high-mid-level and mid-level clouds show stronger effects over the Arctic Ocean than over the Southern Ocean. Mixed-phase clouds show in general a higher cloud radiative effect compared to ice and liquid clouds, except for mid-level clouds over the Southern Ocean, where liquid clouds show a higher shortwave cloud radiative effect. For all cloud types, the negative shortwave cloud radiative effect is larger than the positive longwave cloud radiative effect leading to negative net cloud radiative effects. Due to the higher frequencies of occurrence of the low-level clouds, they contribute most (26.0 % - 33.3 %) to the shortwave cloud radiative effect followed by mid-low-level clouds (13.5 % - 15.6 %).

Chapter 6 analysed specifically low-level, mid-level and mid-low-level clouds over the Arctic Ocean and the Southern Ocean, as they show occurrences of liquid, ice, and mixed-phase cloud profiles and contribute to the cloud fraction in the mixed-phase temperature regime. A machine learning technique has been used to investigate the importance of four major parameters, namely cloud top temperature, sea ice concentration, sea salt mixing ratio, and dust mixing ratio to determine cloud phase. Besides a general importance, Chap. 6 also investigates the spatial distribution of the importance of various factors to improve the understanding of possible influences on that importance.

- ❄ Which of the following parameters, temperature, sea ice, dust, and sea salt, are most important for determining cloud phase and how does the importance vary regionally? Is there a dependence of the importance on other parameters?

First, it has been found, that the temperature is most important to determine cloud phase, which is expected, as there are strong boundaries of the temperature for the occurrence of liquid water ($T \geq -38\,^{\circ}\mathrm{C}$) and for the occurrence of the ice phase ($T \leq 0\,^{\circ}\mathrm{C}$), as well as an increasing freezing probability for lower temperatures. Nevertheless, the importance of the other parameters varies for different cloud types and regions. Sea salt seems to play a more important role in low-level clouds over open ocean. In the Arctic Ocean, high sea salt concentrations at low-level cloud heights are mainly found in the Atlantic sector and north of Scandinavia correlating with a decreasing effect on the prediction of the liquid fraction in the machine learning model. The distribution of sea salt over the Arctic Ocean is probably related to sea ice cover, which prevents the release of sea salt. Over the Southern Ocean a strong meridional gradient in the effect of sea salt is observed, which correlates with the mixing ratio of sea salt. Sea salt decreases the liquid fraction at lower latitudes, where high sea salt concentrations

are found. The meridional gradient could have two reasons. One is based on the strong westerly winds around Antarctica leading to an increased sea salt mixing ratio due to increased bubble bursting. Another reason is related to the prevention of the release of sea salt due to sea ice cover at high latitudes, which this analysis also points at.
Dust shows a larger impact on mid-level clouds in the machine learning model. This could be explained by the larger heights, at which dust is transported in the atmosphere, contrary to sea salt, which is emitted from the ocean surface. Over the Southern Ocean, there is as well a strong meridional gradient of the influence of dust correlating with the dust concentration in mid-level clouds. A possible explanation for that strong gradient can be the strong westerly winds, which inhibit the pole-ward transport of dust to high latitudes in the Southern Ocean. Over the Arctic Ocean, the distribution of dust concentrations is much smoother with a lower meridional contrasts than over the Southern Ocean, which also leads to weaker contrasts of the influence of dust. Nevertheless, high dust correlations lead to a decreased liquid fraction in the prediction of the machine learning model. Instead of strong regional gradients and due to closer sources, the influence is probably more dependent on the temporal wind patterns transporting dust to the Arctic, but without a strong regional pattern observed on average.
Over the Southern Ocean, these results generally suggest a reduced availability of dust in mid-level clouds and of sea salt in low-level clouds over high latitudes, which has an increasing effect on the liquid fraction. This may compensate or counteract the effect of generally decreasing temperature with higher latitudes, leading to a constant or even slightly increasing liquid fraction with increasing latitude over the Southern Ocean. In the Arctic Ocean, a decreased liquid fraction is observed in low-level clouds over the Atlantic Sector, which may be related to the presence of sea spray aerosols.

Chapter 7 compared the cloud type occurrence, the cloud phase frequencies, and the liquid fraction as a function of cloud top temperature between satellite observations and ICON model output for February and August/September.

- What are the differences in cloud occurrence and cloud phase between satellite observations and simulations with the ICOsahedral Nonhydrostatic model (ICON). Does a coupled ICON simulation shows the same correlation between sea ice and cloud phase as satellite observations?

By comparing the cloud occurrence and the cloud phase from the satellite observations with ICON model output, a first insight into possibilities to improve cloud representation in models is gained. Regarding the cloud type frequencies, the strongest bias is seen for mid-level and high-mid-level cloud in the respective summer hemispheres over the Arctic Ocean and the Southern Ocean, where they are strongly underestimated in the model simulations by factors between 4.5 and 7.8 compared to observations. All other cloud types are comparable to the observations within a factor equal or lower than 2. Regarding the frequencies of cloud phase, a general underestimation of the fraction of liquid clouds in simulations

compared to observations is found for low-level and mid-level clouds over both regions, in both seasons. With respect to cloud top temperature, it has been found that the liquid fraction is especially underestimated for cloud top temperatures lower than $-10\,°C$, while for higher cloud top temperature the liquid fraction is overestimated. This suggests that ice is formed at too high temperatures over these regions in mid-level and low-level clouds. In mid-low-level clouds, the fraction of liquid clouds and the liquid fraction is mainly overestimated in simulations compared to observations. In high-mid-low-level clouds the model simulations underestimate the fraction of ice profiles and overestimate the liquid fraction, but there is also uncertainty of the active remote sensing signals in vertically thick clouds due to attenuation and extinction, which may lead to an underestimation of the liquid fraction in observations. None of the simulations show the local minima found in observations, hinting at ice processes not well represented in the model. While observations show an increased liquid fraction in low-level and mid-low-level clouds over sea ice compared to the open ocean over the Arctic, simulations show the opposite signal. Further research is needed to investigate the reason. One hypothesis is the lower sea spray concentration over sea ice, which is not considered in the model simulation, as there is no aerosol dependence of the phase, while many dynamical processes related to sea ice are considered in the coupled run.

Overall, various factors influence cloud phase over the Southern Ocean and the Arctic Ocean. Even if many results are similar between both regions, some may be due to different reasons compensating each other. Figure 8.1 shows a schematic summary of possibly relevant aspects influencing the phase of low-level and mid-level clouds. At lower levels sea spray emitted from open ocean seems to influence the ice formation process. Sea ice is discussed to prevent the release of sea spray aerosols, which leads to a higher liquid fraction in clouds over sea ice compared to the open ocean. In mid-level clouds, INPs from atmospheric transport like dust seem be more relevant compared to sea spray. Over the Southern Ocean it is suggested that strong westerly winds generate sea spray aerosols, but also prevent the poleward transport of dust. Over the Arctic Ocean, the transport of other aerosol types is not prevented by such strong winds compared to the Southern Ocean. Both the Arctic Ocean and the Southern Ocean are relatively pristine areas, but the distribution of available INPs may influence and even compensate regional temperature effects within a certain range.

8.2. Outlook

Further research based on the presented work is needed to investigating the representation of clouds in other models using different implementations of the cloud phase. Models which simulate aerosol processes in more detail and consider them for the ice formation can be especially helpful to improve the understanding of the importance of various factors for cloud phase. Such analysis can also be used to investigate the discrepancy of observations and simulations between the cloud phase over sea ice

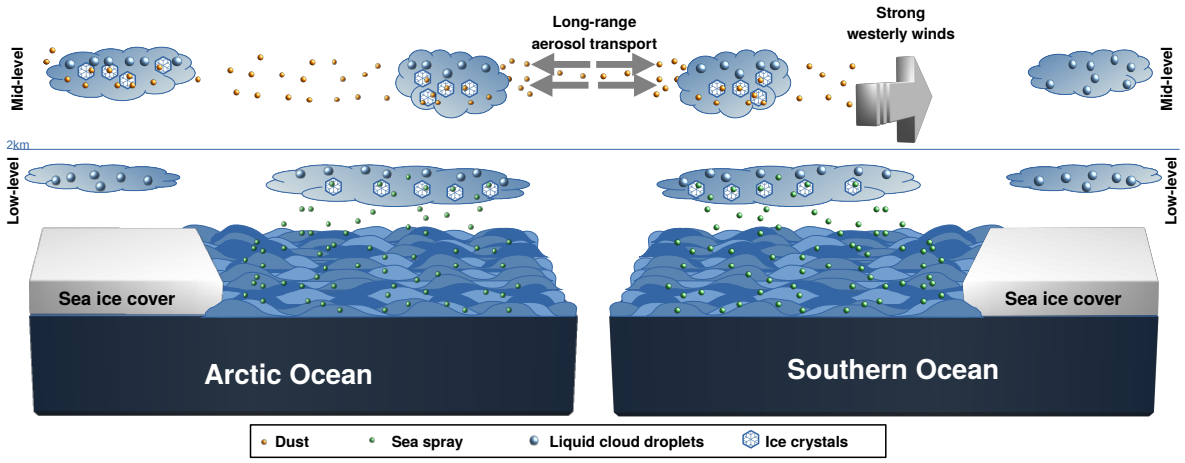

Figure 8.1.: Summary schematic of some possibly relevant aspects influencing the phase of low-level and mid-level clouds over the Arctic Ocean and the Southern Ocean. Sea spray (small green spheres) emitted from the open ocean seems to influence low-level clouds by acting as INP. Sea ice prevents the release of sea spray aerosol leading to more liquid clouds over sea ice. But also wind velocities are influencing sea spray release and availability. Mid-level clouds are more affected by transported aerosols like dust (small orange spheres). Over the Arctic Ocean the mean annual distribution is rather smooth, while the distribution over the Southern Ocean shows a strong meridional gradient, probably related to strong westerly winds preventing the pole-ward transport of dust leading to more liquid clouds at high latitudes.

compared to open ocean. Furthermore, dynamical aspects like surface coupling could be investigated to see if these changes are relevant for the cloud phase change over sea ice.
The use of satellite simulators such as COSP can reduce uncertainties in the comparison between satellite observations and model output. This can also help to reduce uncertainties related to the lidar attenuation and extinction, which may lead to an underestimation of the liquid fraction in observations.
Further research can also focus on the improvement of the presented machine learning model predicting the liquid fraction by integrating dynamical aspects as input features. An example can be vertical velocities, stability indices, or the connection of the cloud profiles to large-scale dynamical weather regimes, like front areas, post-front areas, or other areas of cyclones.
Further research is needed to quantify aerosols, which can act as INP on larger scales and understand their underlying processes and requirements for their production, like biological components of marine organics. Regionally different mineralogy of dust may also have an influence on their ability to nucleate ice and the investigation of such regional differences can also be a topic of further research to improve the knowledge about the global distribution of INPs and regional differences. If such an information on the regional availability of INPs is available, extending the "only" temperature-dependent ice formation with the information of INP availabilities over the Arctic Ocean and the Southern Ocean may improve the phase representation of low-level and mid-level clouds in models.
Further laboratory experiments are also needed to improve the understanding of secondary ice production from ice-ice collisions with dendrites, which is discussed as a reason for a decreased liquid fraction at cloud top temperatures around $-15\,°C$ or $-5\,°C$, which is not seen in simulations.
Besides the investigation of the cloud phase over the Southern Ocean and the Arctic Ocean, the presented analyses can be extended to mid-latitudes or tropical regions to investigate the distribution of cloud phase and also possible influences in other regions of the Earth. Nevertheless, uncertainties of the analysis may be different compared to the ones presented in this thesis, as cloud characteristics differ between the high latitude regions and low-latitude regions. A main difference are for example deep convective systems with heavy rain frequencies in tropical regions, which may lead to radar attenuation. Therefore, uncertainties would have to be examined when extending the presented analysis to lower latitudes.
The Earth Cloud Aerosol and Radiation Explorer (EarthCARE) satellite mission may provide further possibilities to study cloud phase and improve understanding of cloud and aerosols. EarthCARE carries 4 instruments, namely the ATmospehric LIDar (ATLID), a Multi-Spectral Imager (MSI), a BroadBand Radiometer (BBR), and a cloud profiling radar (CPR) including Doppler measurements. Two main differences between the radar and lidar instrument of EarthCARE and CloudSat and CALIOP are mentioned. First the Doppler measurements of the radar which allows the observation of vertical velocities of cloud particles, and second the high spectral resolution of the lidar with a shorter wavelength of 355 nm, which allows the detection of optically thinner clouds compared to CALIOP (Wehr et al., 2023). The launch of EarthCARE is planned for 2024 and the provided data may lay the foundation for a further improved the understanding of clouds and their thermodynamic phase.

A. Appendices

A.1. Appendix to Chap. 5

To provide an impression of the influence of the lidar extinction on the analysis of the liquid fraction, Fig. A.1 and A.2 are shown. The difference between an analysis considering all cloud profiles (panel a) and an analysis considering only cloud profiles, where the lidar is not fully extinguished (panel b) are shown. If the lidar is not extinguished, an increased liquid fraction is observed. For one thing, this shows that the lidar is more often extinguished in mixed-phase profiles and ice profiles containing ice particles, leading to a higher averaged liquid fraction, if these profiles are not considered. The general structure of the results don't change, for example the presence of the local minima of the liquid fraction described in Sec. 5.2.2, the higher liquid fractions in low-level and mid-level clouds, and the comparisons between the liquid fractions over the Southern Ocean and the Arctic Ocean are shown.
Figure A.3 shows a histogram of the cloud top temperature for different cloud types, showing the high number of observed cloud profiles during the two years 2007 and 2008 from satellite observations. This also highlights the representativeness of the results for mid-level, low-level and mid-low-level clouds for the whole mixed-phase temperature range, while high-mid-level, and high-mid-low-level clouds rarely occur at cloud top temperatures higher than $-15\,°C$ and $-10\,°C$. This is based on the required height for the cloud classification and the occurring temperatures there.

A.1.1. Seasonal cycle of cloud type frequencies

Figure A.4 shows the seasonal cycle of the cloud type frequencies, similar to Fig. 5.2, but only for a small latitude region from 60 °S to 62 °S, and from 60 °N to 62 °N to reduce the influence of the different latitude boundaries of the used definitions for the Southern and the Arctic Ocean (40 °S and 60 °N). It shows, that the stronger seasonal cycle of cloud type frequencies over the Arctic Ocean (compare Sec. 5.1) is not only related to the different definition of the regions of the Southern Ocean and the Arctic Ocean, but is probably also related to different conditions over the Southern Ocean, and the Arctic Ocean. Figure A.5 shows the relative frequency of cloud types with respect to the total number of single-layer clouds types, as well for the limited latitude range between 60 °S/N and 62 °S/N.

A.1.2. Cloud radiative effect over the Arctic and the Southern Ocean

In Sec. 5.3.3 the contribution of different cloud types to the cloud radiative effect over the Arctic and the Southern Ocean is analyzed. To calculate the contribution, the cloud radiative effects over two years

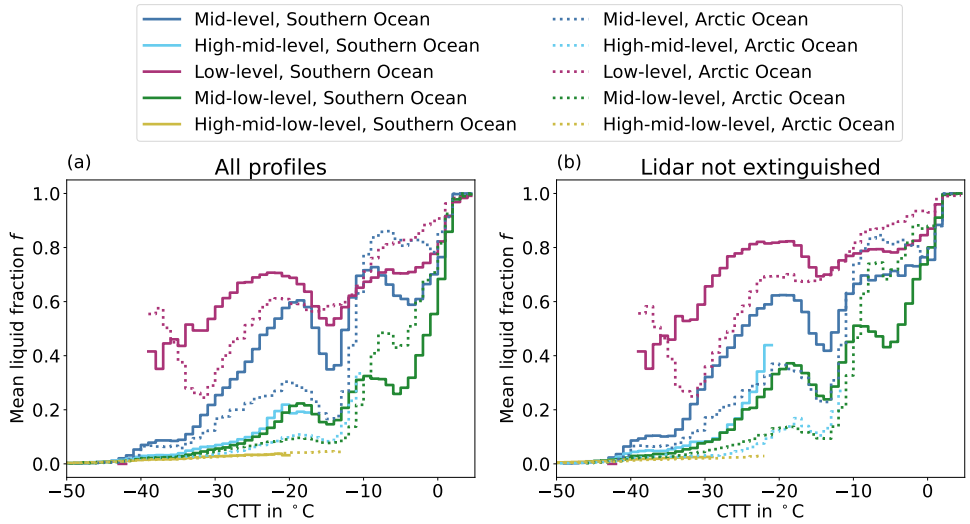

Figure A.1.: Comparison of the mean liquid fraction (f) for different cloud top temperatures (CTT) between an analysis considering all profiles (see panel a), and an analysis considering only profiles in which the lidar signal is not fully extinguished (see panel b). The liquid fraction is calculated for each vertical cloud column and then averaged for each 1 °C bin of the CTT. The liquid fraction of each profiles is calculated as described in Sec. 4 and Eq. 4.2. Reprinted from Dietel et al. (2023).

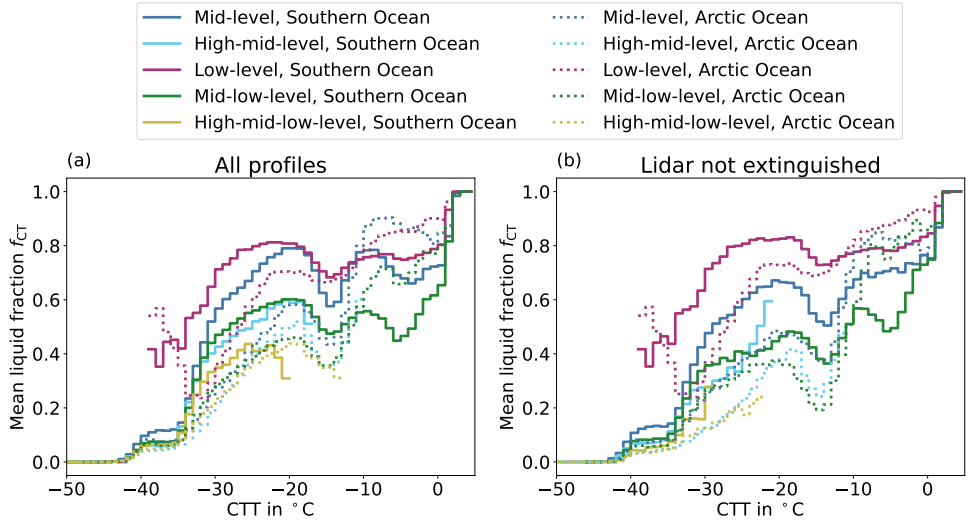

Figure A.2.: Mean cloud top liquid fraction (f_{CT}) based on the phase of all cloud top pixels and cloud top temperature (CTT) comparing the results considering all profiles (see panel a) and considering only profiles in which the lidar signal is not fully extinguished (see panel b). The cloud top liquid fraction is calculated by Eq. 4.3. Reprinted from Dietel et al. (2023).

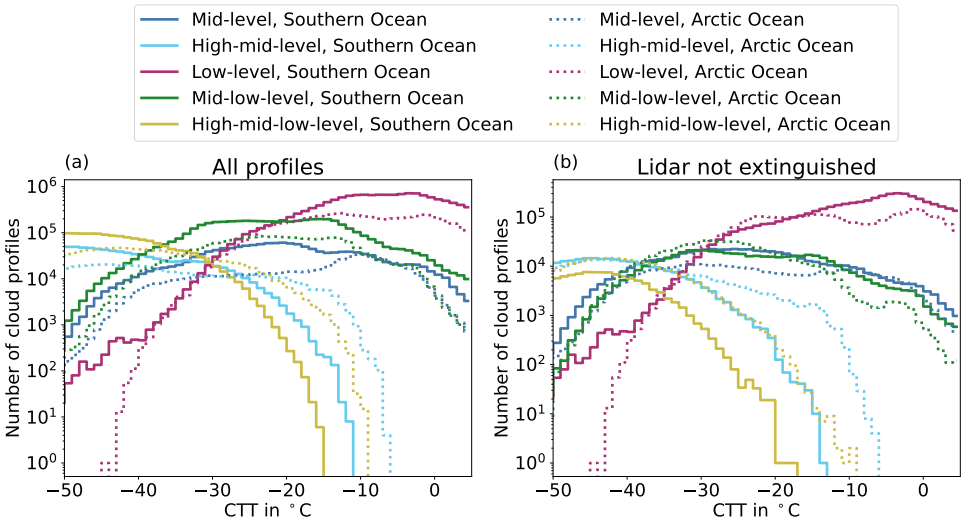

Figure A.3.: Histogram of the cloud top temperatures (CTT) for different cloud types considering all profiles (panel a) and considering only profiles in which the lidar signal is not fully extinguished (panel b).

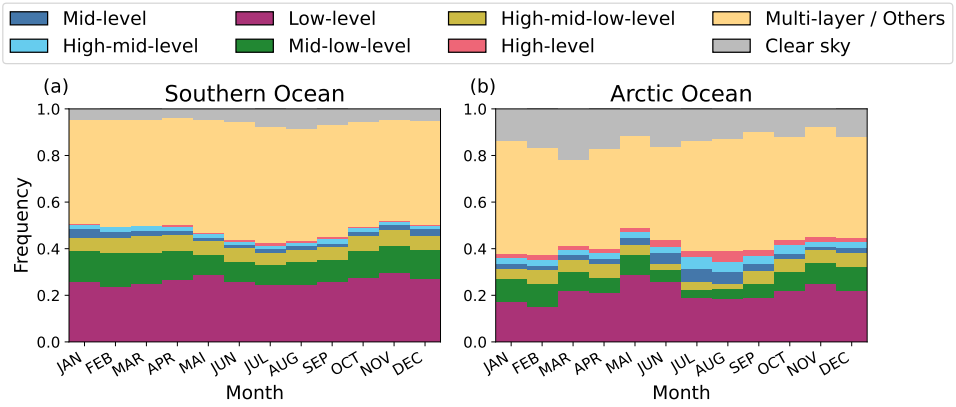

Figure A.4.: Annual cycle of the frequency of different cloud type occurrences for the same latitudes in the Arctic and the Southern Ocean, namely 60 °S/N to 62 °S/N.

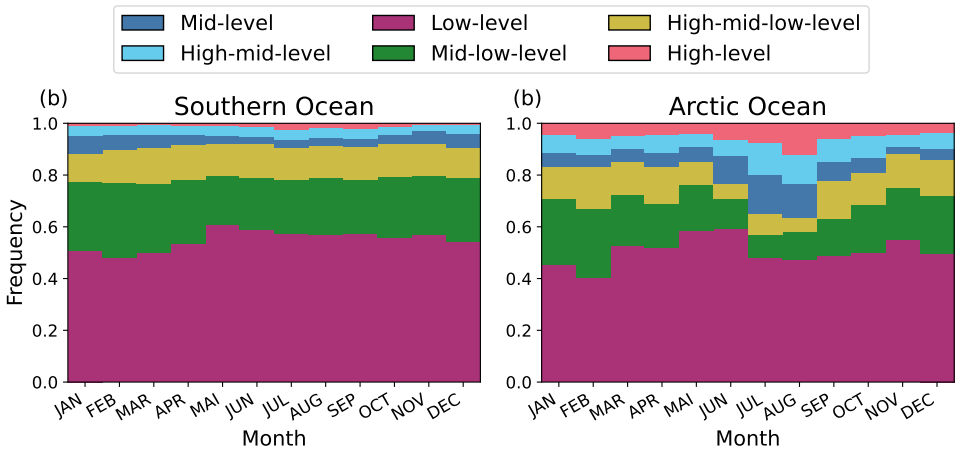

Figure A.5.: Annual cycle of the relative frequency of different single-layer cloud type occurrence with respect to the total number of single-layer clouds for the same latitudes in the Arctic and the Southern Ocean, namely 60 °S/N to 62 °S/N.

were summed up and normalized by the number cloud profiles. The result is shown in shown in Table A.1.

Table A.1.: Cloud radiative effect summed up over two years and normalized by the total number of observed cloud profiles.

	Shortwave	Longwave	Net
Arctic Ocean	-39.1 Wm^{-2}	18.7 Wm^{-2}	-20.4 Wm^{-2}
Southern Ocean	-43.2 Wm^{-2}	24.9 Wm^{-2}	-18.3 Wm^{-2}

A.2. Appendix to Chap. 6

Figure A.6 shows the model performance with the mean absolute error as a function of all combinations of the hyperparameters given by the grid in Tab. 4.4, sorted from the worst to the best fit. A better performance for the training dataset compared to the test dataset is shown, which is expected. Although the difference between the mean absolute error of the trainings dataset and the test dataset increases, which is a sign of overfitting, the mean squared error of the test dataset still improves until the end.
Figure A.7 and A.8 show the model performance for the training dataset and the test dataset as a function of three hyperparameters, for which several values are given in the grid (compare Tab. 4.4). The three parameters are the maximal number of iterations of the boosting process, corresponding to the number of trees, the learning rate, and the minimum number of samples per leaf. It can be seen, that the chosen set corresponds to the best performance with the lowest mean absolute error.
Figure A.9 and Fig. A.10 show the distribution of the liquid fraction from the observations and the distribution of the predicted liquid fractions with Fig. A.9 showing the results of the training dataset and Fig. A.10 showing the results of the validation dataset.
Figure A.11, Fig. A.12, and Fig. A.13 show the mean absolute error (MAE) as a function of a feature value and the corresponding histograms of the feature values. Figure A.11 shows the MAE as function of the sea ice concentration, Fig. A.12 shows the MAE as a function of the dust mixing ratio, and Fig. A.13 shows the MAE as function of the sea salt mixing ratio.

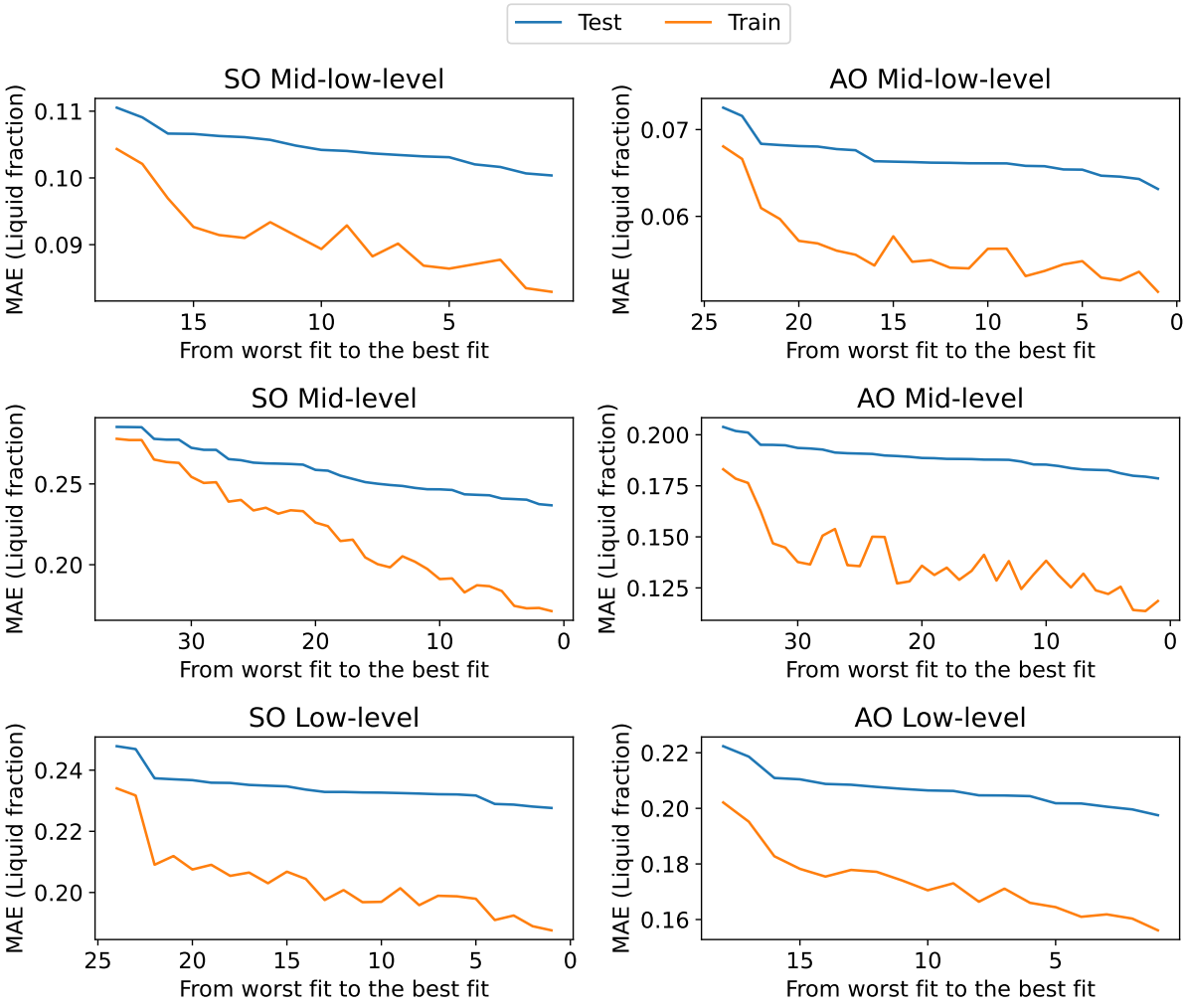

Figure A.6.: Mean absolute error (MAE) of the liquid fraction during the grid search over different combinations of hyperparameters sorted from the worst fit to the best fit.

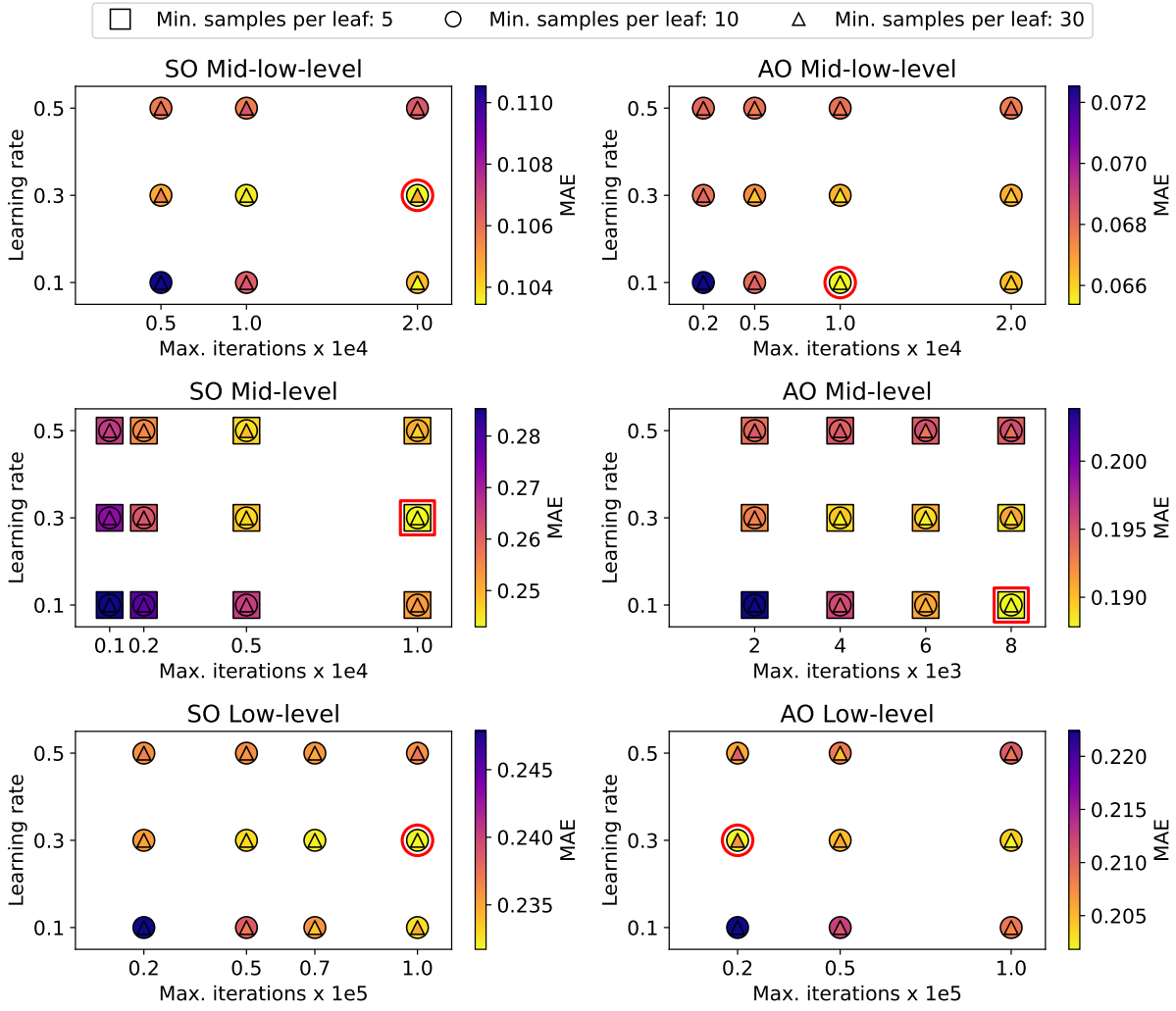

Figure A.7.: Mean absolute error (MAE, shown as the color) as a function of the maximal iterations (x-axis), the learning rate (y-axis), and the minimum number of samples per leaf (marker type) for the training dataset. The red markers shows the combinations, which is chosen in the end by the automatic grid search.

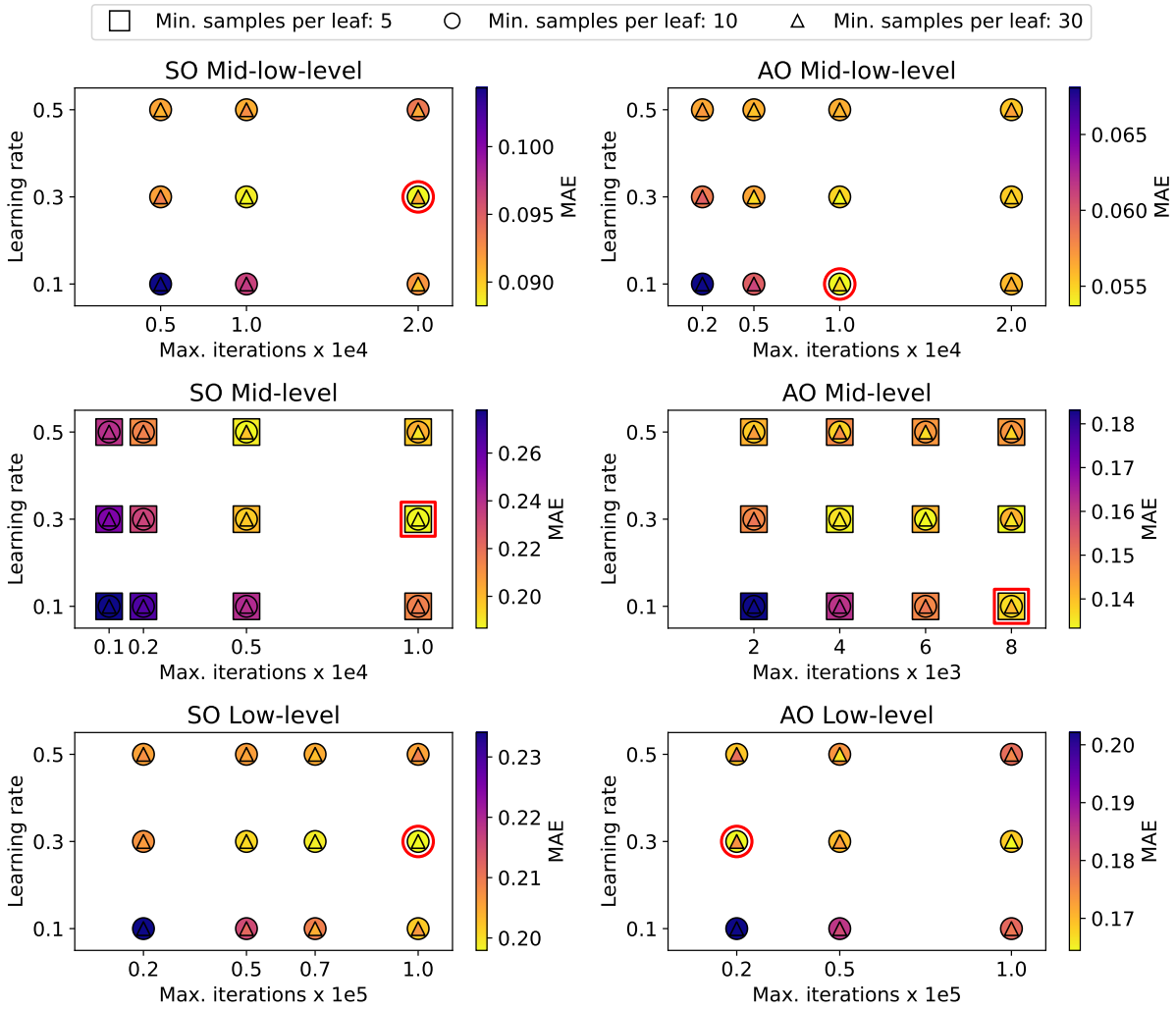

Figure A.8.: Same as in Fig. A.7 but for the test dataset of the cross validation.

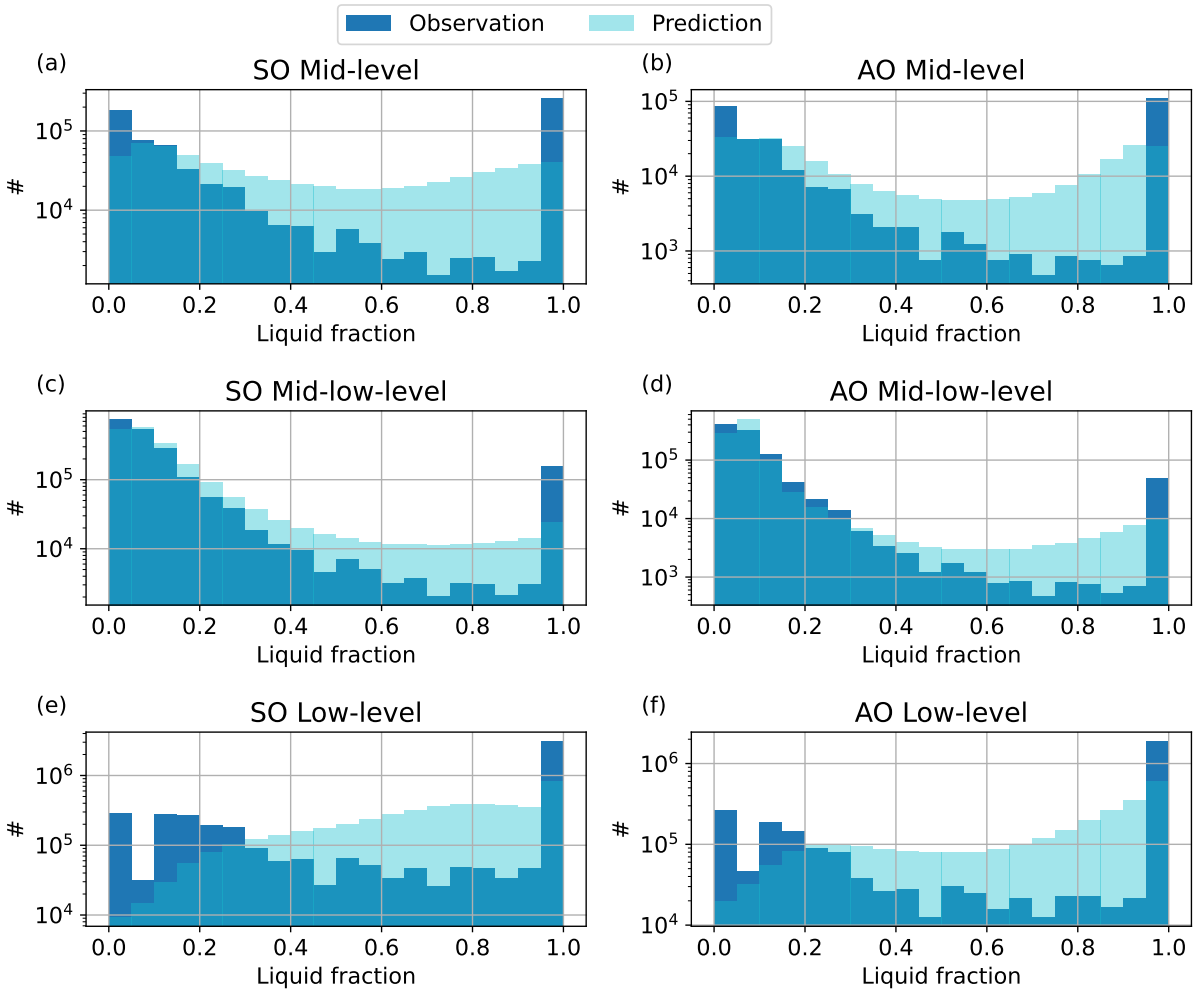

Figure A.9.: Histogram of the predicted liquid fraction and the observed liquid fraction from the training dataset.

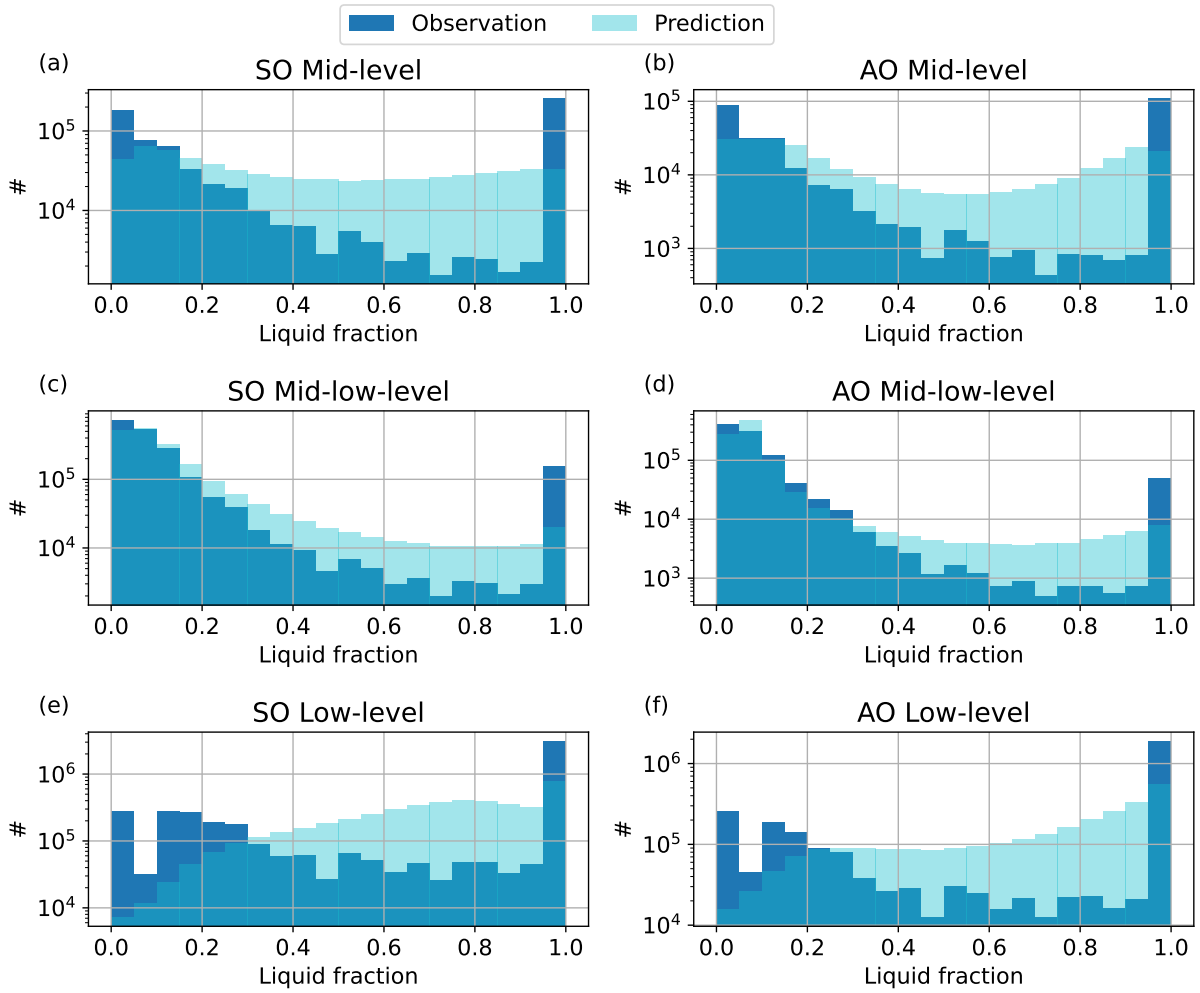

Figure A.10.: Histogram of the predicted liquid fraction and the observed liquid fraction from the validation dataset.

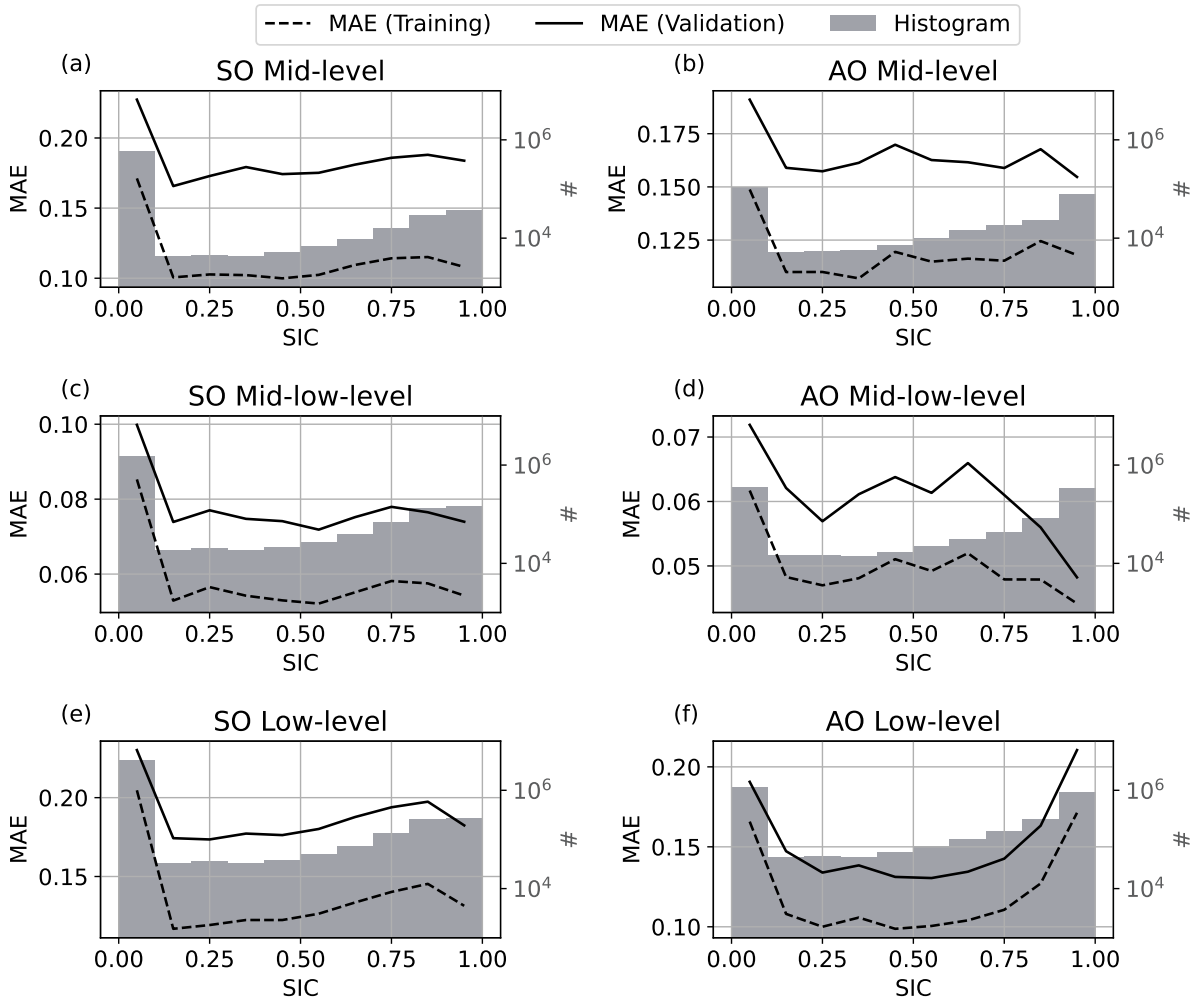

Figure A.11.: Histogram of the sea ice concentration (SIC) in gray (corresponding to the right y-axis). The lines show the mean absolute error (MAE) as a function of the SIC (corresponding to the left y-axis). Line type correspond to the training dataset and the validation dataset as shown in the legend.

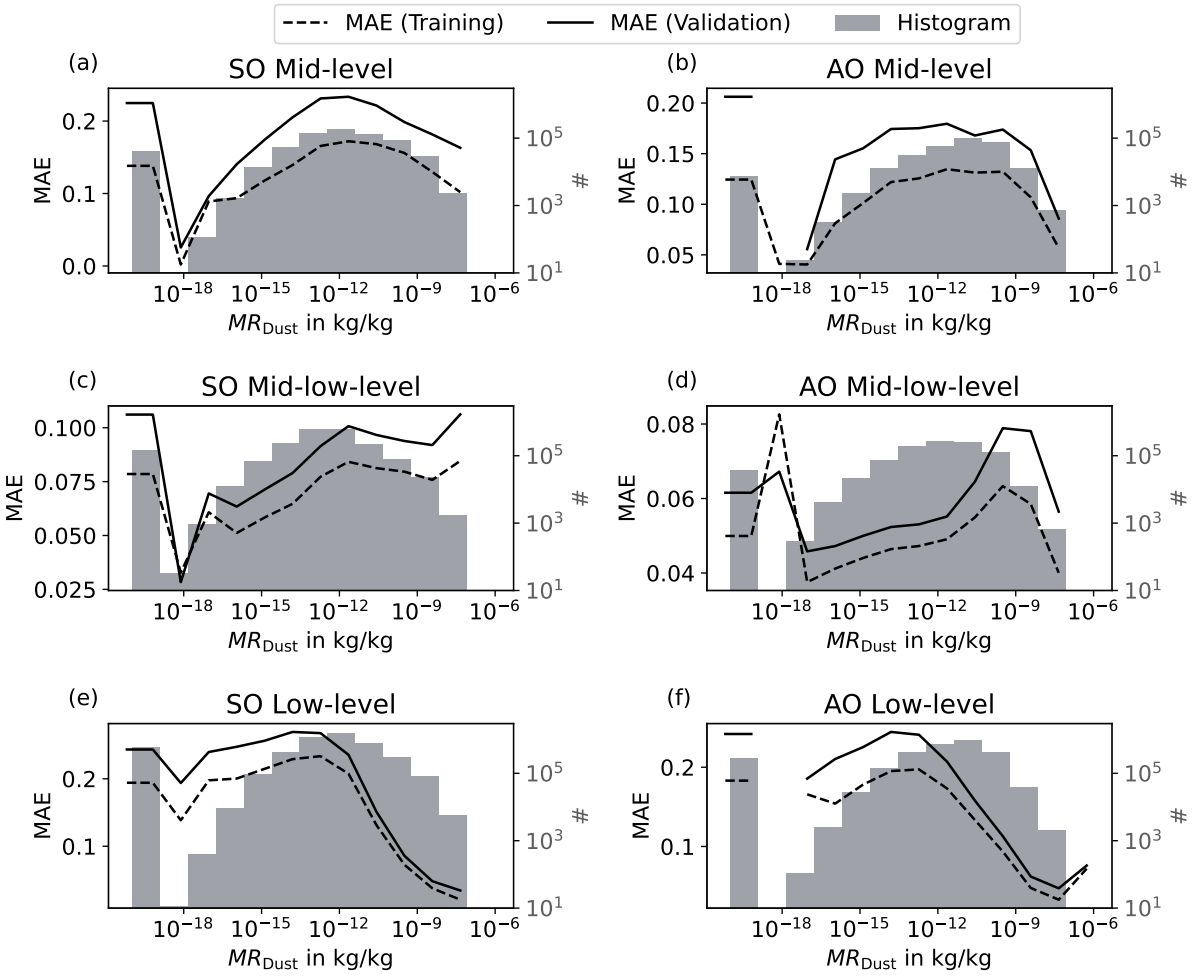

Figure A.12.: Histogram of the dust mixing ratio (MR_{Dust}) in gray (corresponding to the right y-axis). The lines show the mean absolute error (MAE) as a function of dust mixing ratio (corresponding to the left y-axis). Line type correspond to the training dataset and the validation dataset as shown in the legend.

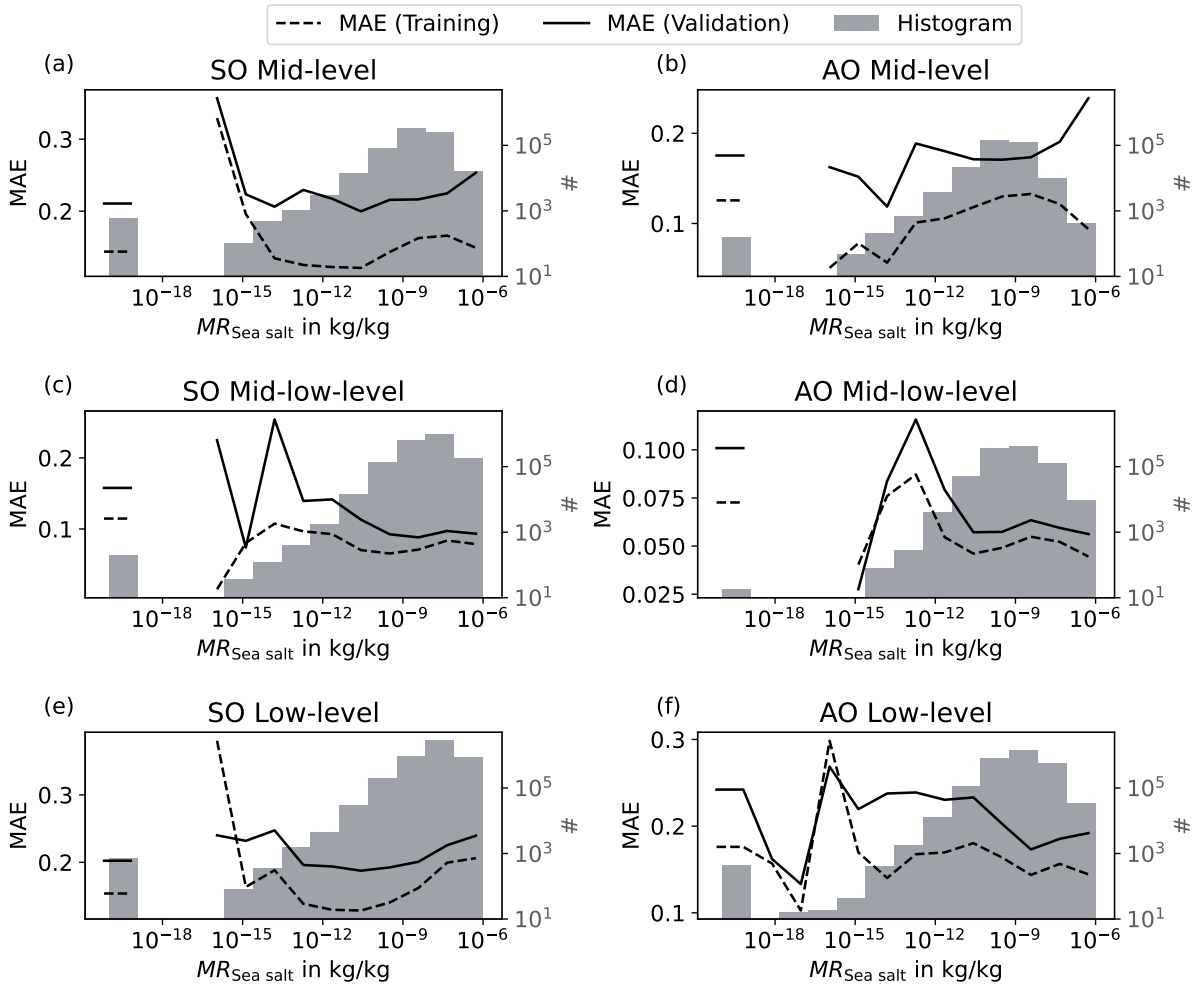

Figure A.13.: Histogram of the sea salt mixing ratio ($MR_{\text{Sea salt}}$) in gray (corresponding to the right y-axis). The lines show the mean absolute error (MAE) as a function of sea salt mixing ratio (corresponding to the left y-axis). Line type correspond to the training dataset and the validation dataset as shown in the legend.

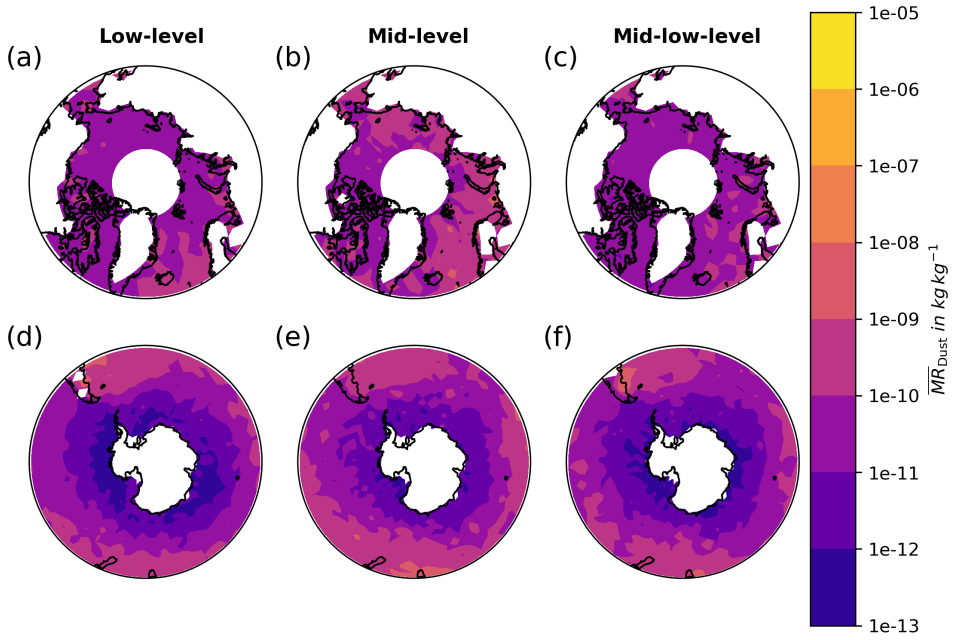

Figure A.14.: Map of the averaged dust mixing ratio ($\overline{MR}_{\mathrm{Dust}}$) with different range of the color bar. The dust mixing ratio is based on CAMS reanalysis and averaged over the heights where a cloud has been observed from satellite observations. The upper row (panel (a), (b), and (c)) shows the Arctic Ocean, while the lower row (panel (d), (e), and (f)) shows the Southern Ocean. The figure is the same as Fig. 6.6, but with a different color bar range, namely the same as in Fig. A.17 to compare the mixing ratios between the different aerosol types.

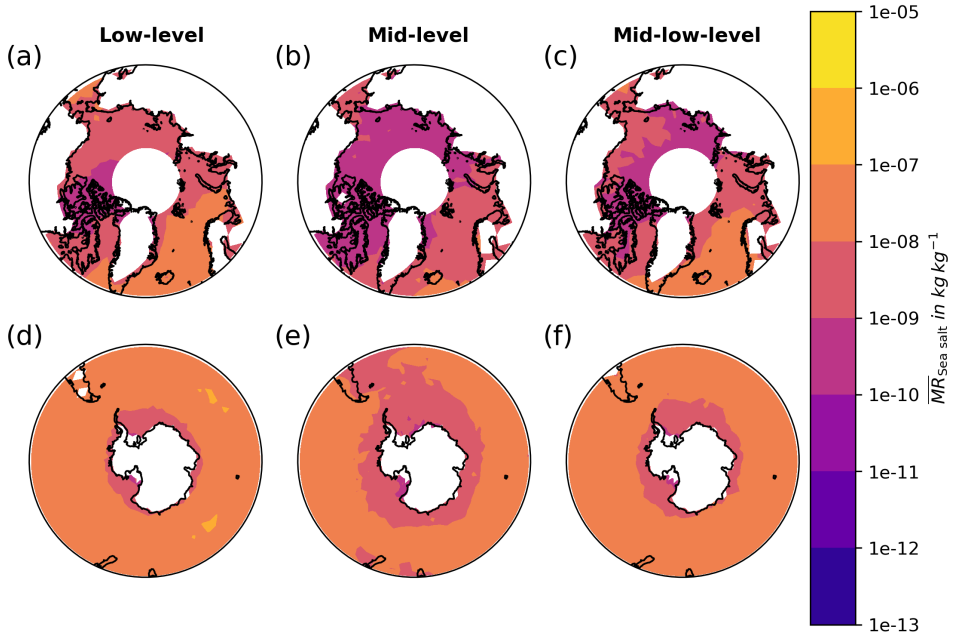

Figure A.15.: Map of the averaged sea salt mixing ratio ($\overline{MR}_{\mathrm{Sea\ salt}}$) with different range of the color bar. The sea salt mixing ratio is based on CAMS reanalysis and averaged over the heights where a cloud has been observed from satellite observations. The upper row (panel (a), (b), and (c)) shows the Arctic Ocean, while the lower row (panel (d), (e), and (f)) shows the Southern Ocean. The figure is the same as Fig. 6.9, but with a different color bar range, namely the same as in Fig. A.14f to compare the mixing ratios between the different aerosol types.

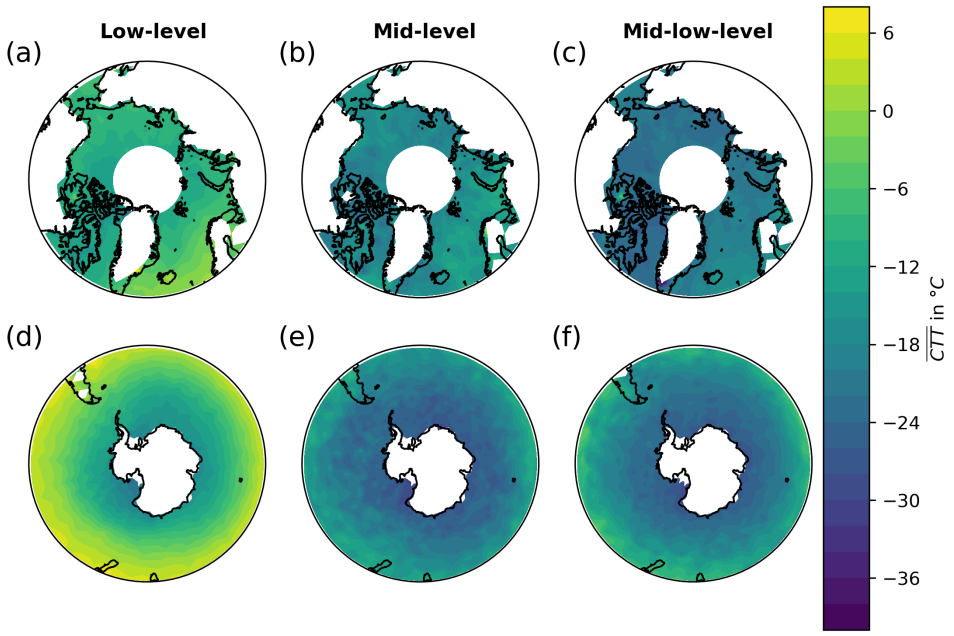

Figure A.16.: Map of the averaged cloud top temperature (CTT) of the different cloud types over the Arctic Ocean and the Southern Ocean.

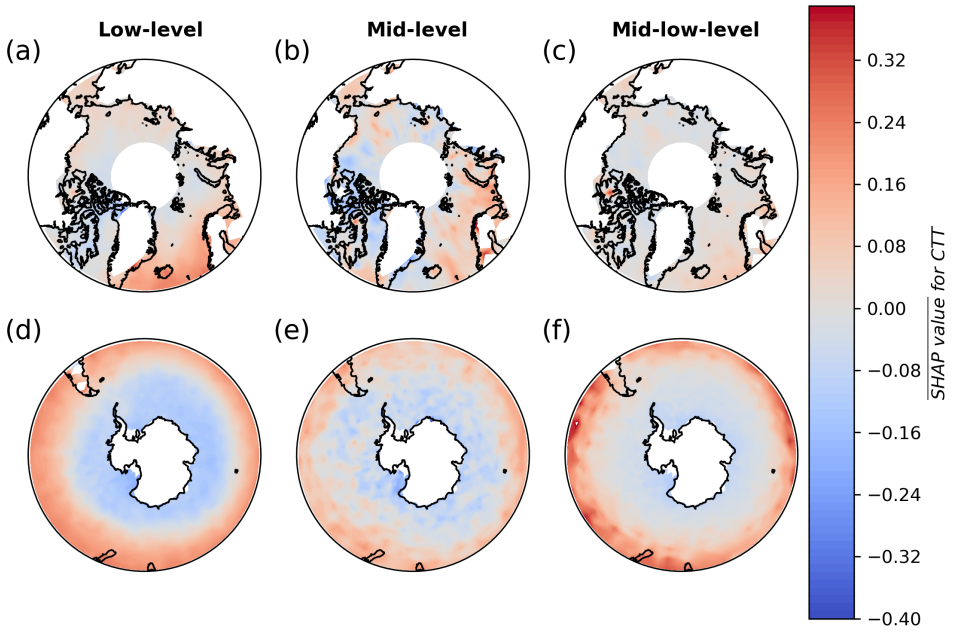

Figure A.17.: Map of the SHAP value for the cloud top temperature ($\overline{SHAP\ value}$ for CTT). The upper row (panel (a), (b), and (c)) shows the Arctic Ocean, while the lower row (panel (d), (e), and (f)) shows the Southern Ocean. Red colors represent positive SHAP values, showing an enhancement of the predicted liquid fraction due to the cloud top temperature, while blue colors show a reduction of the predicted liquid fraction due to the cloud top temperature leading to an increased ice formation.

A.3. Appendix to the Chap. 7

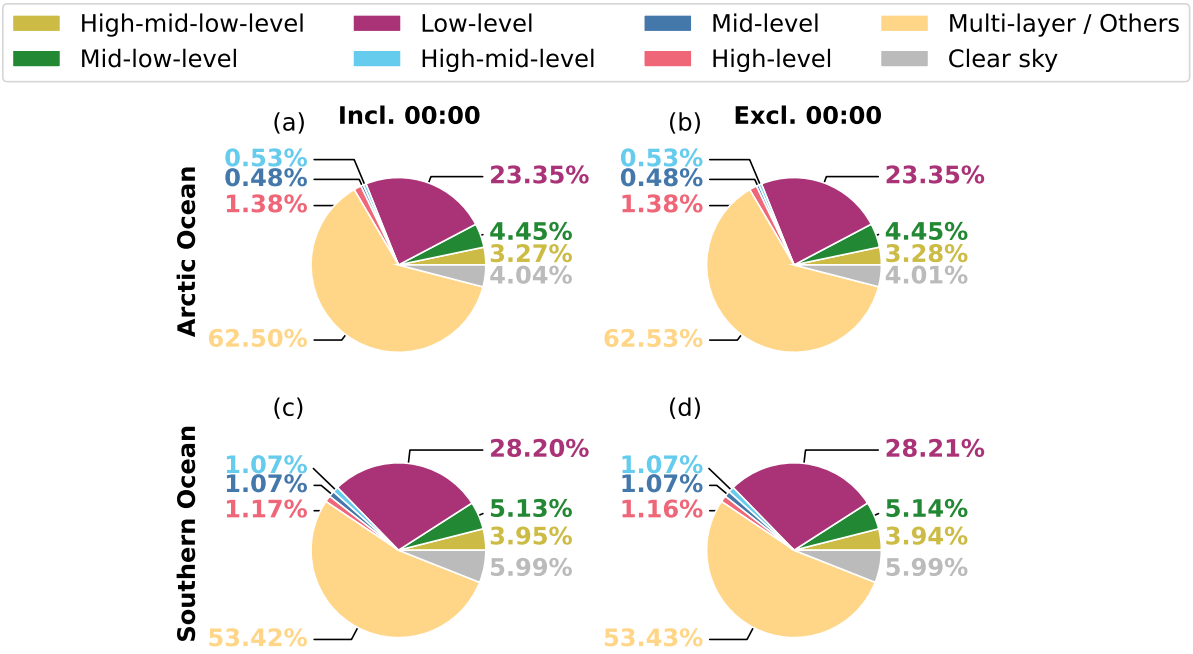

Figure A.18.: Comparison of the cloud type frequencies in the DYAMOND Summer dataset including the 00:00:00 output time step in panel (a) and (c), and excluding the 00:00:00 output time step in the panel (b) and (c).

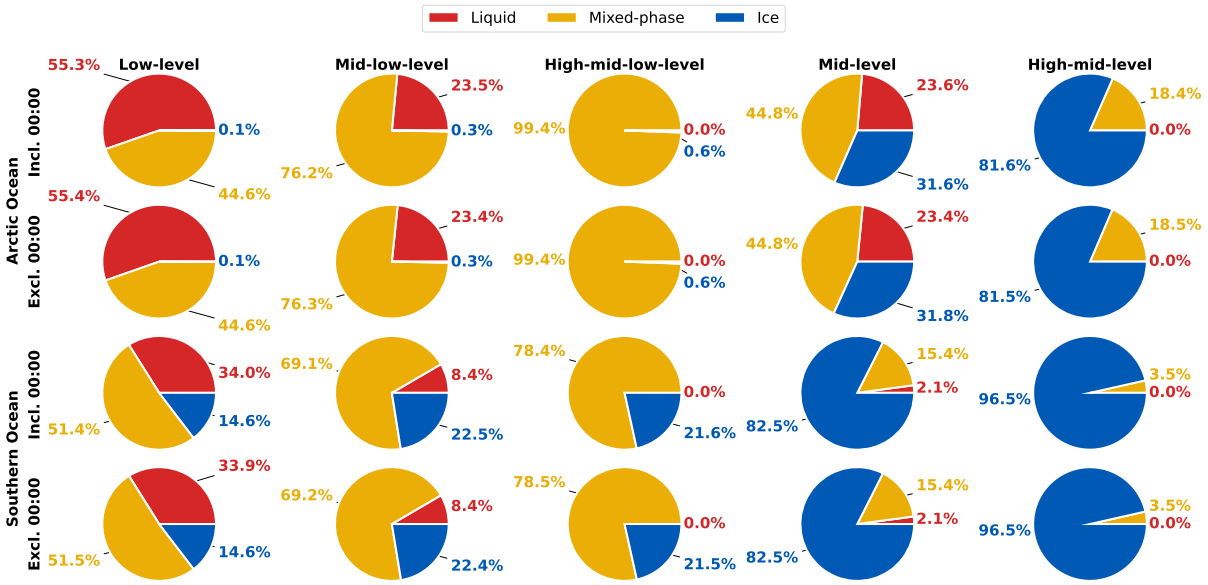

Figure A.19.: Comparison of the frequencies of the cloud phases in the different cloud types for the DYAMOND Summer dataset, once excluding the 00:00:00 output time step, and once including the 00:00:00 output time step.

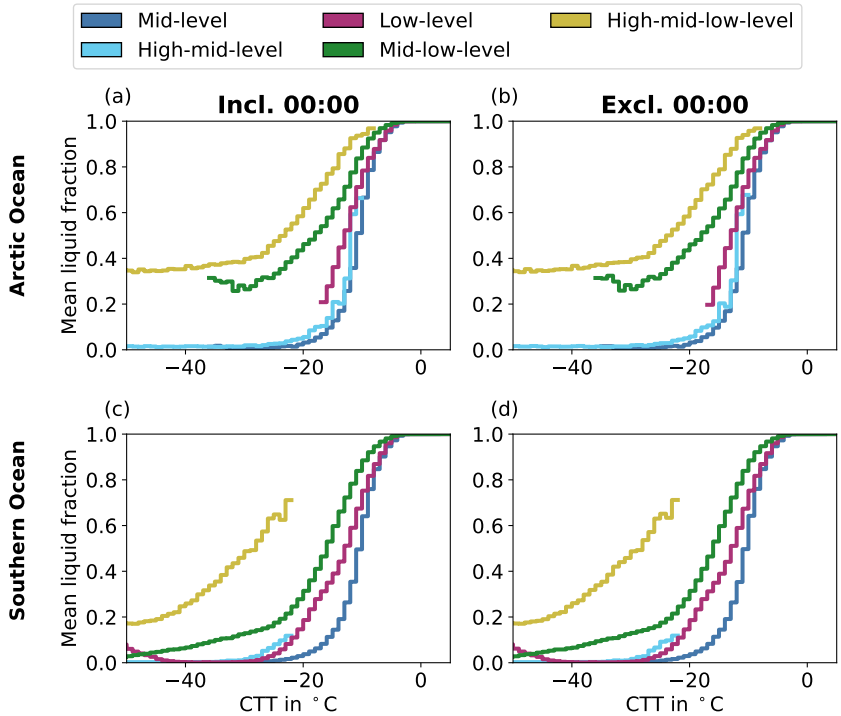

Figure A.20.: Comparison of the mean mass liquid fraction in the DYAMOND summer dataset with once including the 00:00:00 output time step, and once excluding the 00:00:00 output time step.

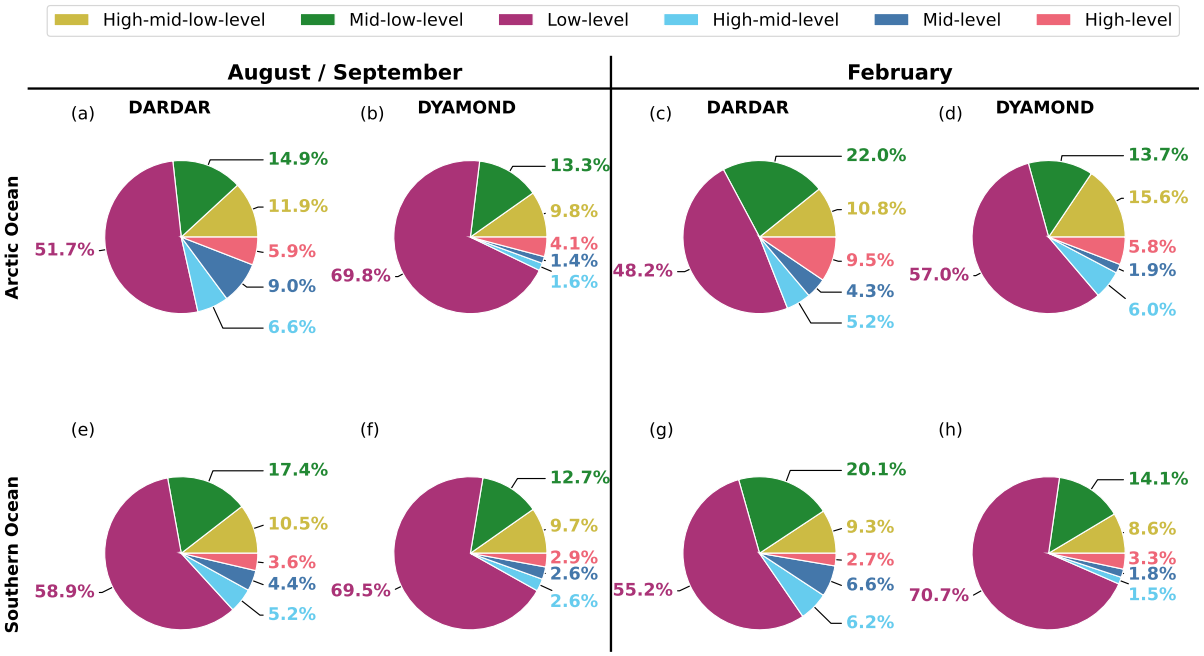

Figure A.21.: Cloud type frequencies with respect to the number of single-layer clouds comparing DARDAR and DYAMOND results. The left hand side (panel a, b, e, f) compares DARDAR observations from the 10 August to 10 September of 2007 and 2008 to the ICON-2.5km DYAMOND summer simulations of 10 August to 10 September 2016. The right hand side (panel c, d, g, h) compared DARDAR observations from 30 January to 1 March of 2007 and 2008 to ICON-2.5km DYAMOND winter simulations from 30 January to 1 March 2020.

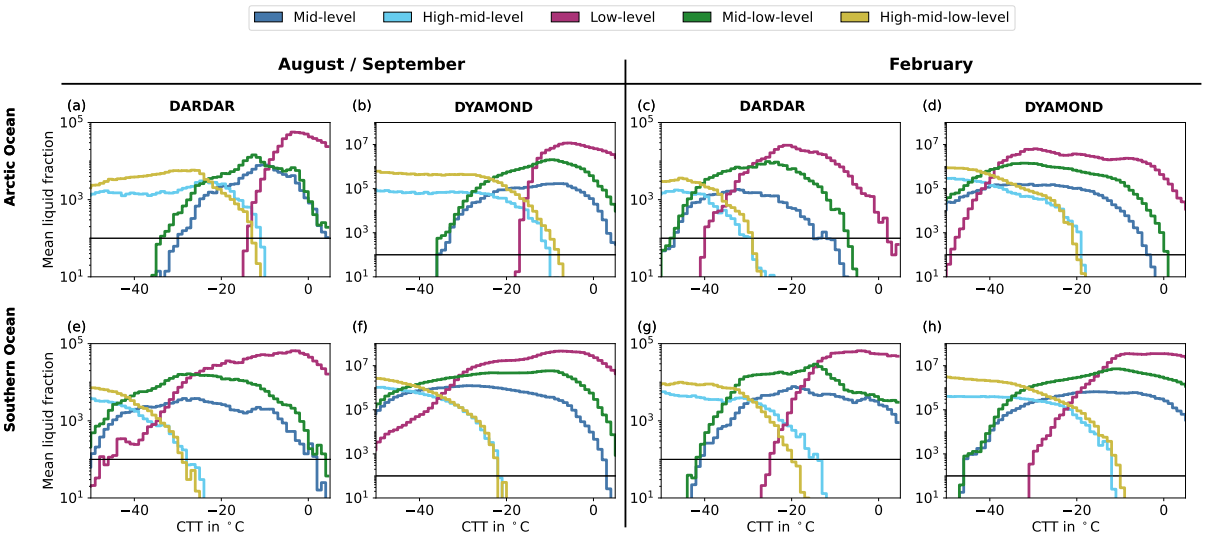

Figure A.22.: Histograms of the total number of cloud type profiles as function of cloud top temperature. The left hand side (panel a, b, e, f) compares DARDAR observations from the 10 August to 10 September of 2007 and 2008 to the ICON-2.5km DYAMOND summer simulation of 10 August to 10 September 2016. The right hand side (panel c, d, g, h) compares DARDAR observations from 30 January to 1 March of 2007 and 2008 to ICON-2.5km DYAMOND winter simulation from 30 January to 1 March 2020. The black horizontal line shows a value of 100, which is used as a minimum number of profiles per bin for further calculation (e.g. in Fig. 7.5).

B. Bibliography

Alexander, S. P., G. M. McFarquhar, R. Marchand, A. Protat, É. Vignon, G. G. Mace, and A. R. Klekociuk, 2021: Mixed-Phase Clouds and Precipitation in Southern Ocean Cyclones and Cloud Systems Observed Poleward of 64°S by Ship-Based Cloud Radar and Lidar. *Journal of Geophysical Research: Atmospheres*, **126 (8)**, e2020JD033 626, https://onlinelibrary.wiley.com/doi/abs/10.1029/2020JD033626.

Alexander, S. P. and A. Protat, 2018: Cloud Properties Observed From the Surface and by Satellite at the Northern Edge of the Southern Ocean. *Journal of Geophysical Research: Atmospheres*, **123 (1)**, 443–456, https://agupubs.onlinelibrary.wiley.com/doi/abs/10.1002/2017JD026552.

Andronache, C., 2018: *Remote Sensing of Clouds and Precipitation / Edited by Constantin Andronache*.

Ansmann, A., M. Tesche, P. Seifert, D. Althausen, R. Engelmann, J. Fruntke, U. Wandinger, I. Mattis, and D. Müller, 2009: Evolution of the ice phase in tropical altocumulus: SAMUM lidar observations over Cape Verde. *Journal of Geophysical Research: Atmospheres*, **114 (D17)**, https://onlinelibrary.wiley.com/doi/abs/10.1029/2008JD011659.

Arias, P., N. Bellouin, E. Coppola, R. Jones, G. Krinner, J. Marotzke, V. Naik, M. Palmer, G.-K. Plattner, J. Rogelj, M. Rojas, J. Sillmann, T. Storelvmo, P. Thorne, B. Trewin, K. Achuta Rao, B. Adhikary, R. Allan, K. Armour, G. Bala, R. Barimalala, S. Berger, J. Canadell, C. Cassou, A. Cherchi, W. Collins, W. Collins, S. Connors, S. Corti, F. Cruz, F. Dentener, C. Dereczynski, A. Di Luca, A. Diongue Niang, F. Doblas-Reyes, A. Dosio, H. Douville, F. Engelbrecht, V. Eyring, E. Fischer, P. Forster, B. Fox-Kemper, J. Fuglestvedt, J. Fyfe, N. Gillett, L. Goldfarb, I. Gorodetskaya, J. Gutierrez, R. Hamdi, E. Hawkins, H. Hewitt, P. Hope, A. Islam, C. Jones, D. Kaufman, R. Kopp, Y. Kosaka, J. Kossin, S. Krakovska, J.-Y. Lee, J. Li, T. Mauritsen, T. Maycock, M. Meinshausen, S.-K. Min, P. Monteiro, T. Ngo-Duc, F. Otto, I. Pinto, A. Pirani, K. Raghavan, R. Ranasinghe, A. Ruane, L. Ruiz, J.-B. Sallée, B. Samset, S. Sathyendranath, S. Seneviratne, A. Sörensson, S. Szopa, I. Takayabu, A.-M. Tréguier, B. van den Hurk, R. Vautard, K. von Schuckmann, S. Zaehle, X. Zhang, and K. Zickfeld, 2021: Technical summary. *Climate Change 2021: The Physical Science Basis. Contribution of Working Group I to the Sixth Assessment Report of the Intergovernmental Panel on Climate Change*, Masson-Delmotte, V., P. Zhai, A. Pirani, S. Connors, C. Péan, S. Berger, N. Caud, Y. Chen, L. Goldfarb, M. Gomis, M. Huang, K. Leitzell, E. Lonnoy, J. Matthews, T. Maycock, T. Waterfield, O. Yelekçi,

R. Yu, and B. Zhou, Eds., Cambridge University Press, Cambridge, United Kingdom and New York, NY, USA, 33–144.

Avramov, A. and J. Y. Harrington, 2010: Influence of parameterized ice habit on simulated mixed phase Arctic clouds. *Journal of Geophysical Research: Atmospheres*, **115 (D3)**, https://onlinelibrary.wiley.com/doi/abs/10.1029/2009JD012108.

Baldauf, M., A. Seifert, J. Förstner, D. Majewski, M. Raschendorfer, and T. Reinhardt, 2011: Operational Convective-Scale Numerical Weather Prediction with the COSMO Model: Description and Sensitivities. *Monthly Weather Review*, **139 (12)**, 3887–3905, https://journals.ametsoc.org/view/journals/mwre/139/12/mwr-d-10-05013.1.xml.

Barrett, P. A., A. Blyth, P. R. A. Brown, and S. J. Abel, 2020: The structure of turbulence and mixed-phase cloud microphysics in a highly supercooled altocumulus cloud. *Atmospheric Chemistry and Physics*, **20 (4)**, 1921–1939, https://acp.copernicus.org/articles/20/1921/2020/.

Bian, H., K. Froyd, D. M. Murphy, J. Dibb, A. Darmenov, M. Chin, P. R. Colarco, A. da Silva, T. L. Kucsera, G. Schill, H. Yu, P. Bui, M. Dollner, B. Weinzierl, and A. Smirnov, 2019: Observationally constrained analysis of sea salt aerosol in the marine atmosphere. *Atmospheric Chemistry and Physics*, **19 (16)**, 10 773–10 785, https://acp.copernicus.org/articles/19/10773/2019/.

Bodas-Salcedo, A., P. G. Hill, K. Furtado, K. D. Williams, P. R. Field, J. C. Manners, P. Hyder, and S. Kato, 2016: Large Contribution of Supercooled Liquid Clouds to the Solar Radiation Budget of the Southern Ocean. *Journal of Climate*, **29 (11)**, 4213–4228, https://journals.ametsoc.org/view/journals/clim/29/11/jcli-d-15-0564.1.xml.

Bodas-Salcedo, A., M. J. Webb, S. Bony, H. Chepfer, J.-L. Dufresne, S. A. Klein, Y. Zhang, R. Marchand, J. M. Haynes, R. Pincus, and V. O. John, 2011: COSP: Satellite simulation software for model assessment. *Bulletin of the American Meteorological Society*, **92 (8)**, 1023–1043, https://journals.ametsoc.org/view/journals/bams/92/8/2011bams2856_1.xml.

Boeke, R. C., P. C. Taylor, and S. A. Sejas, 2021: On the Nature of the Arctic's Positive Lapse-Rate Feedback. *Geophysical Research Letters*, **48 (1)**, e2020GL091 109, https://onlinelibrary.wiley.com/doi/abs/10.1029/2020GL091109.

Boucher, O., 2015: *Atmospheric Aerosols: Properties and Climate Impacts*. Springer Netherlands, Dordrecht, https://link.springer.com/10.1007/978-94-017-9649-1.

Bracegirdle, T. J. and E. W. Kolstad, 2010: Climatology and variability of Southern Hemisphere marine cold-air outbreaks. *Tellus A: Dynamic Meteorology and Oceanography*, **62 (2)**, 202–208, https://doi.org/10.1111/j.1600-0870.2009.00431.x.

Burrows, S. M., C. Hoose, U. Pöschl, and M. G. Lawrence, 2013: Ice nuclei in marine air: Biogenic particles or dust? *Atmospheric Chemistry and Physics*, **13 (1)**, 245–267, https://acp.copernicus.org/articles/13/245/2013/.

Carey, L. D., J. Niu, P. Yang, J. A. Kankiewicz, V. E. Larson, and T. H. V. Haar, 2008: The Vertical Profile of Liquid and Ice Water Content in Midlatitude Mixed-Phase Altocumulus Clouds. *Journal of Applied Meteorology and Climatology*, **47 (9)**, 2487–2495, https://journals.ametsoc.org/jamc/article/47/9/2487/12992/The-Vertical-Profile-of-Liquid-and-Ice-Water.

Carlsen, T. and R. O. David, 2022: Spaceborne Evidence That Ice-Nucleating Particles Influence High-Latitude Cloud Phase. *Geophysical Research Letters*, **49 (14)**, e2022GL098 041, https://onlinelibrary.wiley.com/doi/abs/10.1029/2022GL098041.

Cavalieri, D., C. Parkinson, P. Gloersen, and H. J. Zwally, 1996: Sea Ice Concentrations from Nimbus-7 SMMR and DMSP SSM/I-SSMIS Passive Microwave Data, Version 1. *NASA National Snow and Ice Data Center Distributed Active Archive Center*, http://nsidc.org/data/NSIDC-0051/versions/1.

Ceccaldi, M., J. Delanoë, R. J. Hogan, N. L. Pounder, A. Protat, and J. Pelon, 2013: From CloudSat-CALIPSO to EarthCare: Evolution of the DARDAR cloud classification and its comparison to airborne radar-lidar observations. *Journal of Geophysical Research: Atmospheres*, **118 (14)**, 7962–7981, https://agupubs.onlinelibrary.wiley.com/doi/abs/10.1002/jgrd.50579, https://agupubs.onlinelibrary.wiley.com/doi/pdf/10.1002/jgrd.50579.

Cesana, G. V., T. Khadir, H. Chepfer, and M. Chiriaco, 2022: Southern Ocean Solar Reflection Biases in CMIP6 Models Linked to Cloud Phase and Vertical Structure Representations. *Geophysical Research Letters*, **49 (22)**, e2022GL099 777, https://onlinelibrary.wiley.com/doi/abs/10.1029/2022GL099777.

Chellini, G., R. Gierens, and S. Kneifel, 2022: Ice Aggregation in Low-Level Mixed-Phase Clouds at a High Arctic Site: Enhanced by Dendritic Growth and Absent Close to the Melting Level. *Journal of Geophysical Research: Atmospheres*, **127 (16)**, e2022JD036 860, https://onlinelibrary.wiley.com/doi/abs/10.1029/2022JD036860.

Chen, J.-P. and D. Lamb, 1994: The Theoretical Basis for the Parameterization of Ice Crystal Habits: Growth by Vapor Deposition. *Journal of the Atmospheric Sciences*, **51 (9)**, 1206–1222, https://journals.ametsoc.org/view/journals/atsc/51/9/1520-0469_1994_051_1206_ttbftp_2_0_co_2.xml.

Costa-Surós, M., O. Sourdeval, C. Acquistapace, H. Baars, C. Carbajal Henken, C. Genz, J. Hesemann, C. Jimenez, M. König, J. Kretzschmar, N. Madenach, C. I. Meyer, R. Schrödner, P. Seifert,

F. Senf, M. Brueck, G. Cioni, J. F. Engels, K. Fieg, K. Gorges, R. Heinze, P. K. Siligam, U. Burkhardt, S. Crewell, C. Hoose, A. Seifert, I. Tegen, and J. Quaas, 2020: Detection and attribution of aerosol–cloud interactions in large-domain large-eddy simulations with the ICOsahedral Non-hydrostatic model. *Atmospheric Chemistry and Physics*, **20 (9)**, 5657–5678, https://acp.copernicus.org/articles/20/5657/2020/.

Danilov, S., Q. Wang, R. Timmermann, N. Iakovlev, D. Sidorenko, M. Kimmritz, T. Jung, and J. Schröter, 2015: Finite-Element Sea Ice Model (FESIM), version 2. *Geoscientific Model Development*, **8 (6)**, 1747–1761, https://gmd.copernicus.org/articles/8/1747/2015/.

de Boer, G., H. Morrison, M. D. Shupe, and R. Hildner, 2011: Evidence of liquid dependent ice nucleation in high-latitude stratiform clouds from surface remote sensors. *Geophysical Research Letters*, **38 (1)**, https://agupubs.onlinelibrary.wiley.com/doi/abs/10.1029/2010GL046016.

Delanoë, J. and R. J. Hogan, 2008: A variational scheme for retrieving ice cloud properties from combined radar, lidar, and infrared radiometer. *Journal of Geophysical Research: Atmospheres*, **113 (D7)**, https://agupubs.onlinelibrary.wiley.com/doi/abs/10.1029/2007JD009000.

———, 2010: Combined CloudSat-CALIPSO-MODIS retrievals of the properties of ice clouds. *Journal of Geophysical Research: Atmospheres*, **115 (D4)**, https://agupubs.onlinelibrary.wiley.com/doi/abs/10.1029/2009JD012346.

Desai, N., M. Diao, Y. Shi, X. Liu, and I. Silber, 2023: Ship-Based Observations and Climate Model Simulations of Cloud Phase Over the Southern Ocean. *Journal of Geophysical Research: Atmospheres*, **128 (11)**, e2023JD038 581, https://onlinelibrary.wiley.com/doi/abs/10.1029/2023JD038581.

Després, V. R., J. A. Huffman, S. M. Burrows, C. Hoose, A. S. Safatov, G. Buryak, J. Fröhlich-Nowoisky, W. Elbert, M. O. Andreae, U. Pöschl, and R. Jaenicke, 2012: Primary biological aerosol particles in the atmosphere: A review. **64 (1)**, 15 598, https://b.tellusjournals.se/articles/10.3402/tellusb.v64i0.15598.

Diansky, N. A., V. V. Bagatinskaya, A. V. Gusev, and E. G. Morozov, 2021: Geostrophic and Wind-Driven Components of the Antarctic Circumpolar Current. *Antarctic Peninsula Region of the Southern Ocean: Oceanography and Ecology*, Morozov, E. G., M. V. Flint, and V. A. Spiridonov, Eds., Springer International Publishing, Cham, Advances in Polar Ecology, 3–20, https://doi.org/10.1007/978-3-030-78927-5_1.

Dietel, B., O. Sourdeval, and C. Hoose, 2023: Characterisation of low-base and mid-base clouds and their thermodynamic phase over the Southern and Arctic Ocean. *EGUsphere [preprint]*, 1–38, https://egusphere.copernicus.org/preprints/2023/egusphere-2023-2281/.

Doms, G., J. Förstner, E. Heise, T. Reinhardt, B. Ritter, and R. Schrodin, 2021: A Description of the Nonhydrostatic Regional COSMO-Model. *Deutscher Wetterdienst*.

Fleishauer, R. P., V. E. Larson, and T. H. Vonder Haar, 2002: Observed Microphysical Structure of Midlevel, Mixed-Phase Clouds. *Journal of the Atmospheric Sciences*, **59 (11)**, 1779–1804, https://journals.ametsoc.org/jas/article/59/11/1779/25097/Observed-Microphysical-Structure-of-Midlevel-Mixed.

Forbes, R. M. and M. Ahlgrimm, 2014: On the Representation of High-Latitude Boundary Layer Mixed-Phase Cloud in the ECMWF Global Model. *Monthly Weather Review*, **142 (9)**, 3425–3445, https://journals.ametsoc.org/mwr/article/142/9/3425/103686/On-the-Representation-of-High-Latitude-Boundary.

Forster, P., T. Storelvmo, K. Armour, W. Collins, J.-L. Dufresne, D. Frame, D. J. Lunt, T. Mauritsen, M. D. Palmer, M. Watanabe, M. Wild, and H. Zhang, 2021: The Earth's Energy Budget, Climate Feedbacks and Climate Sensitivity. *Climate Change 2021 – The Physical Science Basis: Contribution of Working Group I to the Sixth Assessment Report of the Intergovernmental Panel on Climate Change*, Masson-Delmotte, V., P. Zhai, A. Pirani, S. Connors, C. Péan, S. Berger, N. Caud, Y. Chen, L. Goldfarb, M. Gomis, M. Huang, K. Leitzell, E. Lonnoy, J. Matthews, T. Maycock, T. Waterfield, O. Yelekçi, R. Yu, and B. Zhou, Eds., Cambridge University Press, Cambridge, United Kingdom and New York, NY, USA, 923–1054, https://www.cambridge.org/core/books/climate-change-2021-the-physical-science-basis/earths-energy-budget-climate-feedbacks-and-climate-sensitivity/AE57C97E588FF3060C7C7E47DD4F3C6E.

Fukuta, N. and T. Takahashi, 1999: The Growth of Atmospheric Ice Crystals: A Summary of Findings in Vertical Supercooled Cloud Tunnel Studies. *Journal of the Atmospheric Sciences*, **56 (12)**, 1963–1979, https://journals.ametsoc.org/view/journals/atsc/56/12/1520-0469_1999_056_1963_tgoaic_2.0.co_2.xml.

Ginoux, P., M. Chin, I. Tegen, J. Prospero, B. Holben, O. Dubovik, and S.-J. Lin, 2001: Sources and distributions of dust aerosols simulated with the GOCART model. *Journal of Geophysical Research*, **106**, 20 255–20 274.

Griesche, H. J., K. Ohneiser, P. Seifert, M. Radenz, R. Engelmann, and A. Ansmann, 2021: Contrasting ice formation in Arctic clouds: Surface-coupled vs. surface-decoupled clouds. *Atmospheric Chemistry and Physics*, **21 (13)**, 10 357–10 374, https://acp.copernicus.org/articles/21/10357/2021/.

Ham, S.-H., S. Kato, F. G. Rose, D. Winker, T. L'Ecuyer, G. G. Mace, D. Painemal, S. Sun-Mack, Y. Chen, and W. F. Miller, 2017: Cloud occurrences and cloud radiative effects (CREs) from CERES-

CALIPSO-CloudSat-MODIS (CCCM) and CloudSat radar-lidar (RL) products. *Journal of Geophysical Research: Atmospheres*, **122 (16)**, 8852–8884, https://onlinelibrary.wiley.com/doi/abs/10.1002/2017JD026725.

Hanke, M., R. Redler, T. Holfeld, and M. Yastremsky, 2016: YAC 1.2.0: New aspects for coupling software in Earth system modelling. *Geoscientific Model Development*, **9 (8)**, 2755–2769, https://gmd.copernicus.org/articles/9/2755/2016/.

Hartmann, M., K. Adachi, O. Eppers, C. Haas, A. Herber, R. Holzinger, A. Hünerbein, E. Jäkel, C. Jentzsch, M. van Pinxteren, H. Wex, S. Willmes, and F. Stratmann, 2020: Wintertime Airborne Measurements of Ice Nucleating Particles in the High Arctic: A Hint to a Marine, Biogenic Source for Ice Nucleating Particles. *Geophysical Research Letters*, **47 (13)**, e2020GL087 770, https://onlinelibrary.wiley.com/doi/abs/10.1029/2020GL087770.

Henderson, D. S., T. L'Ecuyer, G. Stephens, P. Partain, and M. Sekiguchi, 2013: A Multisensor Perspective on the Radiative Impacts of Clouds and Aerosols. *Journal of Applied Meteorology and Climatology*, **52 (4)**, 853–871, https://journals.ametsoc.org/view/journals/apme/52/4/jamc-d-12-025.1.xml.

Hersbach, H., B. Bell, P. Berrisford, G. Biavati, A. Horányi, J. Muñoz-Sabater, J. Nicolas, C. Peubey, R. Radu, I. Rozum, D. Schepers, A. Simmons, C. Soci, D. Dee, and J.-N. Thépaut, 2023a: ERA5 hourly data on single levels from 1940 to present. *Copernicus Climate Change Service (C3S) Climate Data Store (CDS)*.

———, 2023b: ERA5 monthly averaged data on single levels from 1940 to present. *Copernicus Climate Change Service (C3S) Climate Data Store (CDS)*.

Hogan, R. J., P. N. Francis, H. Flentje, A. J. Illingworth, M. Quante, and J. Pelon, 2003: Characteristics of mixed-phase clouds. I: Lidar, radar and aircraft observations from CLARE'98. *Quarterly Journal of the Royal Meteorological Society*, **129 (592)**, 2089–2116, https://onlinelibrary.wiley.com/doi/abs/10.1256/rj.01.208.

Hohenegger, C., P. Korn, L. Linardakis, R. Redler, R. Schnur, P. Adamidis, J. Bao, S. Bastin, M. Behravesh, M. Bergemann, J. Biercamp, H. Bockelmann, R. Brokopf, N. Brüggemann, L. Casaroli, F. Chegini, G. Datseris, M. Esch, G. George, M. Giorgetta, O. Gutjahr, H. Haak, M. Hanke, T. Ilyina, T. Jahns, J. Jungclaus, M. Kern, D. Klocke, L. Kluft, T. Kölling, L. Kornblueh, S. Kosukhin, C. Kroll, J. Lee, T. Mauritsen, C. Mehlmann, T. Mieslinger, A. K. Naumann, L. Paccini, A. Peinado, D. S. Praturi, D. Putrasahan, S. Rast, T. Riddick, N. Roeber, H. Schmidt, U. Schulzweida, F. Schütte, H. Segura, R. Shevchenko, V. Singh, M. Specht, C. C. Stephan, J.-S. von Storch, R. Vogel, C. Wengel, M. Winkler, F. Ziemen, J. Marotzke, and B. Stevens, 2023: ICON-Sapphire: Simulating the components

of the Earth system and their interactions at kilometer and subkilometer scales. *Geoscientific Model Development*, **16 (2)**, 779–811, https://gmd.copernicus.org/articles/16/779/2023/.

Hoose, C. and O. Möhler, 2012: Heterogeneous ice nucleation on atmospheric aerosols: A review of results from laboratory experiments. *Atmospheric Chemistry and Physics*, **12 (20)**, 9817–9854, https://acp.copernicus.org/articles/12/9817/2012/.

Houze, R. A., 2014: *Cloud Dynamics*, International Geophysis, Vol. 104. 2d ed., Elsevier Science.

Houze Jr., R. A. and R. A. Houze Jr., 1994: *Cloud Dynamics*. Elsevier Science & Technology, San Diego, UNITED STATES, http://ebookcentral.proquest.com/lib/karlsruhetech/detail.action?docID=428643.

Hu, Y., S. Rodier, K.-m. Xu, W. Sun, J. Huang, B. Lin, P. Zhai, and D. Josset, 2010: Occurrence, liquid water content, and fraction of supercooled water clouds from combined CALIOP/IIR/MODIS measurements. *Journal of Geophysical Research: Atmospheres*, **115 (D4)**, https://agupubs.onlinelibrary.wiley.com/doi/abs/10.1029/2009JD012384.

Hu, Y.-X., D. Winker, P. Yang, B. Baum, L. Poole, and L. Vann, 2001: Identification of cloud phase from PICASSO-CENA lidar depolarization: A multiple scattering sensitivity study. *Journal of Quantitative Spectroscopy and Radiative Transfer*, **70 (4)**, 569–579, https://www.sciencedirect.com/science/article/pii/S0022407301000309.

Huang, S., W. Hu, J. Chen, Z. Wu, D. Zhang, and P. Fu, 2021: Overview of biological ice nucleating particles in the atmosphere. *Environment International*, **146**, 106 197, https://www.sciencedirect.com/science/article/pii/S0160412020321528.

Huang, Y., A. Protat, S. T. Siems, and M. J. Manton, 2015: A-Train Observations of Maritime Midlatitude Storm-Track Cloud Systems: Comparing the Southern Ocean against the North Atlantic. *Journal of Climate*, **28 (5)**, 1920–1939, https://journals.ametsoc.org/jcli/article/28/5/1920/35207/A-Train-Observations-of-Maritime-Midlatitude-Storm.

Huang, Y., S. T. Siems, M. J. Manton, A. Protat, and J. Delanoë, 2012: A study on the low-altitude clouds over the Southern Ocean using the DARDAR-MASK. *Journal of Geophysical Research: Atmospheres*, **117 (D18)**, https://agupubs.onlinelibrary.wiley.com/doi/abs/10.1029/2012JD017800.

Ickes, L., G. C. E. Porter, R. Wagner, M. P. Adams, S. Bierbauer, A. K. Bertram, M. Bilde, S. Christiansen, A. M. L. Ekman, E. Gorokhova, K. Höhler, A. A. Kiselev, C. Leck, O. Möhler, B. J. Murray, T. Schiebel, R. Ullrich, and M. E. Salter, 2020: The ice-nucleating activity of Arctic sea surface microlayer samples and marine algal cultures. *Atmospheric Chemistry and Physics*, **20 (18)**, 11 089–11 117, https://acp.copernicus.org/articles/20/11089/2020/.

Ilyina, T., K. D. Six, J. Segschneider, E. Maier-Reimer, H. Li, and I. Núñez-Riboni, 2013: Global ocean biogeochemistry model HAMOCC: Model architecture and performance as component of the MPI-Earth system model in different CMIP5 experimental realizations. *Journal of Advances in Modeling Earth Systems*, **5 (2)**, 287–315, https://onlinelibrary.wiley.com/doi/abs/10.1029/2012MS000178.

Inness, A., M. Ades, A. Agustí-Panareda, J. Barré, A. Benedictow, A.-M. Blechschmidt, J. J. Dominguez, R. Engelen, H. Eskes, J. Flemming, V. Huijnen, L. Jones, Z. Kipling, S. Massart, M. Parrington, V.-H. Peuch, M. Razinger, S. Remy, M. Schulz, and M. Suttie, 2019: The CAMS reanalysis of atmospheric composition. *Atmospheric Chemistry and Physics*, **19 (6)**, 3515–3556, https://acp.copernicus.org/articles/19/3515/2019/.

Inoue, J., Y. Tobo, F. Taketani, and K. Sato, 2021: Oceanic Supply of Ice-Nucleating Particles and Its Effect on Ice Cloud Formation: A Case Study in the Arctic Ocean During a Cold-Air Outbreak in Early Winter. *Geophysical Research Letters*, **48 (16)**, e2021GL094 646, https://onlinelibrary.wiley.com/doi/abs/10.1029/2021GL094646.

Intrieri, J. M., M. D. Shupe, T. Uttal, and B. J. McCarty, 2002: An annual cycle of Arctic cloud characteristics observed by radar and lidar at SHEBA. *Journal of Geophysical Research: Oceans*, **107 (C10)**, SHE 5–1–SHE 5–15, https://onlinelibrary.wiley.com/doi/abs/10.1029/2000JC000423.

IPCC, 2013: *Climate Change 2013: The Physical Science Basis. Contribution of Working Group I to the Fifth Assessment Report of the Intergovernmental Panel on Climate Change*. Cambridge University Press, Cambridge, United Kingdom and New York, NY, USA, 1535 pp., www.climatechange2013.org.

Irish, V. E., S. J. Hanna, M. D. Willis, S. China, J. L. Thomas, J. J. B. Wentzell, A. Cirisan, M. Si, W. R. Leaitch, J. G. Murphy, J. P. D. Abbatt, A. Laskin, E. Girard, and A. K. Bertram, 2019a: Ice nucleating particles in the marine boundary layer in the Canadian Arctic during summer 2014. *Atmospheric Chemistry and Physics*, **19 (2)**, 1027–1039, https://acp.copernicus.org/articles/19/1027/2019/.

Irish, V. E., S. J. Hanna, Y. Xi, M. Boyer, E. Polishchuk, M. Ahmed, J. Chen, J. P. D. Abbatt, M. Gosselin, R. Chang, L. A. Miller, and A. K. Bertram, 2019b: Revisiting properties and concentrations of ice-nucleating particles in the sea surface microlayer and bulk seawater in the Canadian Arctic during summer. *Atmospheric Chemistry and Physics*, **19 (11)**, 7775–7787, https://acp.copernicus.org/articles/19/7775/2019/.

JCOMM Expert Team on Sea Ice, 2009: WMO Sea-ice Nomenclature, WMO / OMM / BMO - No.259 Suppl.No.5. Linguistic equivalents. https://repository.oceanbestpractices.org/handle/11329/113.

Kalesse, H., G. de Boer, A. Solomon, M. Oue, M. Ahlgrimm, D. Zhang, M. D. Shupe, E. Luke, and A. Protat, 2016: Understanding Rapid Changes in Phase Partitioning between Cloud Liquid and Ice in Stratiform Mixed-Phase Clouds: An Arctic Case Study. *Monthly Weather Review*, **144 (12)**, 4805–4826, https://journals.ametsoc.org/view/journals/mwre/144/12/mwr-d-16-0155.1.xml.

Kanji, Z. A., L. A. Ladino, H. Wex, Y. Boose, M. Burkert-Kohn, D. J. Cziczo, and M. Krämer, 2017: Overview of Ice Nucleating Particles. *Meteorological Monographs*, **58 (1)**, 1.1–1.33, https://journals.ametsoc.org/view/journals/amsm/58/1/amsmonographs-d-16-0006.1.xml.

Kawai, K., H. Matsui, and Y. Tobo, 2023: Dominant Role of Arctic Dust With High Ice Nucleating Ability in the Arctic Lower Troposphere. *Geophysical Research Letters*, **50 (8)**, e2022GL102 470, https://onlinelibrary.wiley.com/doi/abs/10.1029/2022GL102470.

Kay, J. E., L. Bourdages, N. B. Miller, A. Morrison, V. Yettella, H. Chepfer, and B. Eaton, 2016a: Evaluating and improving cloud phase in the Community Atmosphere Model version 5 using spaceborne lidar observations. *Journal of Geophysical Research: Atmospheres*, **121 (8)**, 4162–4176, https://onlinelibrary.wiley.com/doi/abs/10.1002/2015JD024699.

Kay, J. E., T. L'Ecuyer, H. Chepfer, N. Loeb, A. Morrison, and G. Cesana, 2016b: Recent Advances in Arctic Cloud and Climate Research. *Current Climate Change Reports*, **2 (4)**, 159–169, https://doi.org/10.1007/s40641-016-0051-9.

Kayetha, V. K. and R. L. Collins, 2016: Optically thin midlevel ice clouds derived from Cloud Aerosol Lidar and Infrared Pathfinder Satellite Observations. *Journal of Applied Remote Sensing*, **10 (4)**, 046 007, https://www.spiedigitallibrary.org/journals/journal-of-applied-remote-sensing/volume-10/issue-4/046007/Optically-thin-midlevel-ice-clouds-derived-from-Cloud-Aerosol-Lidar/10.1117/1.JRS.10.046007.full.

King, M. D., S. Platnick, W. P. Menzel, S. A. Ackerman, and P. A. Hubanks, 2013: Spatial and Temporal Distribution of Clouds Observed by MODIS Onboard the Terra and Aqua Satellites. *IEEE Transactions on Geoscience and Remote Sensing*, **51 (7)**, 3826–3852, https://ieeexplore.ieee.org/document/6422379.

Klein, S. A., R. B. McCoy, H. Morrison, A. S. Ackerman, A. Avramov, G. de Boer, M. Chen, J. N. S. Cole, A. D. Del Genio, M. Falk, M. J. Foster, A. Fridlind, J.-C. Golaz, T. Hashino, J. Y. Harrington, C. Hoose, M. F. Khairoutdinov, V. E. Larson, X. Liu, Y. Luo, G. M. McFarquhar, S. Menon, R. A. J. Neggers, S. Park, M. R. Poellot, J. M. Schmidt, I. Sednev, B. J. Shipway, M. D. Shupe, D. A. Spangenberg, Y. C. Sud, D. D. Turner, D. E. Veron, K. von Salzen, G. K. Walker, Z. Wang,

A. B. Wolf, S. Xie, K.-M. Xu, F. Yang, and G. Zhang, 2009: Intercomparison of model simulations of mixed-phase clouds observed during the ARM Mixed-Phase Arctic Cloud Experiment. I: Single-layer cloud. *Quarterly Journal of the Royal Meteorological Society*, **135 (641)**, 979–1002, https://onlinelibrary.wiley.com/doi/abs/10.1002/qj.416.

Köhler, H., 1936: The nucleus in and the growth of hygroscopic droplets. *Transactions of the Faraday Society*, **32 (0)**, 1152–1161, https://pubs.rsc.org/en/content/articlelanding/1936/tf/tf9363201152.

Kolstad, E. W., 2011: A global climatology of favourable conditions for polar lows. *Quarterly Journal of the Royal Meteorological Society*, **137 (660)**, 1749–1761, https://onlinelibrary.wiley.com/doi/abs/10.1002/qj.888.

Korn, P., 2018: A structure-preserving discretization of ocean parametrizations on unstructured grids. *Ocean Modelling*, **132**, 73–90, https://www.sciencedirect.com/science/article/pii/S1463500318301859.

Korn, P., N. Brüggemann, J. H. Jungclaus, S. J. Lorenz, O. Gutjahr, H. Haak, L. Linardakis, C. Mehlmann, U. Mikolajewicz, D. Notz, D. A. Putrasahan, V. Singh, J.-S. von Storch, X. Zhu, and J. Marotzke, 2022: ICON-O: The Ocean Component of the ICON Earth System Model—Global Simulation Characteristics and Local Telescoping Capability. *Journal of Advances in Modeling Earth Systems*, **14 (10)**, e2021MS002 952, https://onlinelibrary.wiley.com/doi/abs/10.1029/2021MS002952.

Korolev, A. and T. Leisner, 2020: Review of experimental studies of secondary ice production. *Atmospheric Chemistry and Physics*, **20 (20)**, 11 767–11 797, https://acp.copernicus.org/articles/20/11767/2020/.

Lamb, D. and J. Verlinde, 2011: *Physics and Chemistry of Clouds*. Online-ausg. ed., Cambridge University Press, Cambridge, https://ebookcentral.proquest.com/lib/kxp/detail.action?docID=807307.

Landwehr, S., M. Volpi, F. A. Haumann, C. M. Robinson, I. Thurnherr, V. Ferracci, A. Baccarini, J. Thomas, I. Gorodetskaya, C. Tatzelt, S. Henning, R. L. Modini, H. J. Forrer, Y. Lin, N. Cassar, R. Simó, C. Hassler, A. Moallemi, S. E. Fawcett, N. Harris, R. Airs, M. H. Derkani, A. Alberello, A. Toffoli, G. Chen, P. Rodríguez-Ros, M. Zamanillo, P. Cortés-Greus, L. Xue, C. G. Bolas, K. C. Leonard, F. Perez-Cruz, D. Walton, and J. Schmale, 2021: Exploring the coupled ocean and atmosphere system with a data science approach applied to observations from the Antarctic Circumnavigation Expedition. *Earth System Dynamics*, **12 (4)**, 1295–1369, https://esd.copernicus.org/articles/12/1295/2021/.

Lapere, R., J. L. Thomas, L. Marelle, A. M. L. Ekman, M. M. Frey, M. T. Lund, R. Makkonen, A. Ranjithkumar, M. E. Salter, B. H. Samset, M. Schulz, L. Sogacheva, X. Yang, and P. Zieger, 2023: The Representation of Sea Salt Aerosols and Their Role in Polar Climate Within CMIP6. *Journal of Geophysical Research: Atmospheres*, **128 (6)**, e2022JD038 235, https://onlinelibrary.wiley.com/doi/abs/10.1029/2022JD038235.

L'Ecuyer, T. S., N. B. Wood, T. Haladay, G. L. Stephens, and P. W. Stackhouse, 2008: Impact of clouds on atmospheric heating based on the R04 CloudSat fluxes and heating rates data set. *Journal of Geophysical Research: Atmospheres*, **113 (D8)**.

Libbrecht, K. G., 2005: The physics of snow crystals. *Reports on Progress in Physics*, **68 (4)**, 855–895, https://iopscience.iop.org/article/10.1088/0034-4885/68/4/R03.

Liggett, D., B. Storey, Y. Cook, and V. Meduna, 2015: *Exploring the Last Continent: An Introduction to Antarctica / Edited by Daniela Liggett, Bryan Storey, Yvonne Cook, Veronika Meduna.*

Lilly, D. K., 1962: On the numerical simulation of buoyant convection. *Tellus*, **14 (2)**, 148–172, https://onlinelibrary.wiley.com/doi/abs/10.1111/j.2153-3490.1962.tb00128.x.

Lin, P., R. Zhong, Q. Yang, K. R. Clem, and D. Chen, 2023: A Record-Breaking Cyclone Over the Southern Ocean in 2022. *Geophysical Research Letters*, **50 (14)**, e2023GL104 012, https://onlinelibrary.wiley.com/doi/abs/10.1029/2023GL104012.

Linke, O., J. Quaas, F. Baumer, S. Becker, J. Chylik, S. Dahlke, A. Ehrlich, D. Handorf, C. Jacobi, H. Kalesse-Los, L. Lelli, S. Mehrdad, R. A. J. Neggers, J. Riebold, P. Saavedra Garfias, N. Schnierstein, M. D. Shupe, C. Smith, G. Spreen, B. Verneuil, K. S. Vinjamuri, M. Vountas, and M. Wendisch, 2023: Constraints on simulated past Arctic amplification and lapse rate feedback from observations. *Atmospheric Chemistry and Physics*, **23 (17)**, 9963–9992, https://acp.copernicus.org/articles/23/9963/2023/.

Listowski, C., J. Delanoë, A. Kirchgaessner, T. Lachlan-Cope, and J. King, 2019: Antarctic clouds, supercooled liquid water and mixed-phase investigated with DARDAR: Geographical and seasonal variations. *Atmospheric Chemistry and Physics*, **19 (10)**, 6771–6808, https://www.atmos-chem-phys.net/19/6771/2019/.

Liu, X., T. He, L. Sun, X. Xiao, S. Liang, and S. Li, 2022: Analysis of Daytime Cloud Fraction Spatiotemporal Variation over the Arctic from 2000 to 2019 from Multiple Satellite Products. *Journal of Climate*, **35 (23)**, 7595–7623, https://journals.ametsoc.org/view/journals/clim/35/23/JCLI-D-22-0007.1.xml.

Liu, Y., 2022: Impacts of active satellite sensors' low-level cloud detection limitations on cloud radiative forcing in the Arctic. *Atmospheric Chemistry and Physics*, **22 (12)**, 8151–8173, https://acp.copernicus.org/articles/22/8151/2022/.

Liu, Y., J. R. Key, S. A. Ackerman, G. G. Mace, and Q. Zhang, 2012: Arctic cloud macrophysical characteristics from CloudSat and CALIPSO. *Remote Sensing of Environment*, **124**, 159–173, https://linkinghub.elsevier.com/retrieve/pii/S003442571200209X.

Lundberg, S. and S.-I. Lee, 2017: A Unified Approach to Interpreting Model Predictions. http://arxiv.org/abs/1705.07874, 1705.07874.

Lundberg, S. M., G. Erion, H. Chen, A. DeGrave, J. M. Prutkin, B. Nair, R. Katz, J. Himmelfarb, N. Bansal, and S.-I. Lee, 2020: From local explanations to global understanding with explainable AI for trees. *Nature Machine Intelligence*, **2 (1)**, 56–67, https://www.nature.com/articles/s42256-019-0138-9.

Mace, G. G., A. Protat, and S. Benson, 2021: Mixed-Phase Clouds Over the Southern Ocean as Observed From Satellite and Surface Based Lidar and Radar. *Journal of Geophysical Research: Atmospheres*, **126 (16)**, e2021JD034 569, https://onlinelibrary.wiley.com/doi/abs/10.1029/2021JD034569.

Mace, G. G. and Q. Zhang, 2014: The CloudSat radar-lidar geometrical profile product (RL-GeoProf): Updates, improvements, and selected results. *Journal of Geophysical Research: Atmospheres*, **119 (15)**, 9441–9462, https://onlinelibrary.wiley.com/doi/abs/10.1002/2013JD021374.

Mace, G. G., Q. Zhang, M. Vaughan, R. Marchand, G. Stephens, C. Trepte, and D. Winker, 2009: A description of hydrometeor layer occurrence statistics derived from the first year of merged Cloudsat and CALIPSO data. *Journal of Geophysical Research: Atmospheres*, **114 (D8)**, https://onlinelibrary.wiley.com/doi/abs/10.1029/2007JD009755.

Mason, S., C. Jakob, A. Protat, and J. Delanoë, 2014: Characterizing Observed Midtopped Cloud Regimes Associated with Southern Ocean Shortwave Radiation Biases. *Journal of Climate*, **27 (16)**, 6189–6203, https://journals.ametsoc.org/view/journals/clim/27/16/jcli-d-14-00139.1.xml.

Matus, A. V. and T. S. L'Ecuyer, 2017: The role of cloud phase in Earth's radiation budget. *Journal of Geophysical Research: Atmospheres*, **122 (5)**, 2559–2578, https://agupubs.onlinelibrary.wiley.com/doi/abs/10.1002/2016JD025951.

Mayer, J., F. Ewald, L. Bugliaro, and C. Voigt, 2023: Cloud Top Thermodynamic Phase from Synergistic Lidar-Radar Cloud Products from Polar Orbiting Satellites: Implications for Observations from

Geostationary Satellites. *Remote Sensing*, **15 (7)**, 1742, https://www.mdpi.com/2072-4292/15/7/1742.

McCluskey, C. S., P. J. DeMott, P.-L. Ma, and S. M. Burrows, 2019: Numerical Representations of Marine Ice-Nucleating Particles in Remote Marine Environments Evaluated Against Observations. *Geophysical Research Letters*, **46 (13)**, 7838–7847, https://onlinelibrary.wiley.com/doi/abs/10.1029/2018GL081861.

McCluskey, C. S., T. C. J. Hill, R. S. Humphries, A. M. Rauker, S. Moreau, P. G. Strutton, S. D. Chambers, A. G. Williams, I. McRobert, J. Ward, M. D. Keywood, J. Harnwell, W. Ponsonby, Z. M. Loh, P. B. Krummel, A. Protat, S. M. Kreidenweis, and P. J. DeMott, 2018: Observations of Ice Nucleating Particles Over Southern Ocean Waters. *Geophysical Research Letters*, **45 (21)**, 11,989–11,997, https://onlinelibrary.wiley.com/doi/abs/10.1029/2018GL079981.

McCoy, D. T., I. Tan, D. L. Hartmann, M. D. Zelinka, and T. Storelvmo, 2016: On the relationships among cloud cover, mixed-phase partitioning, and planetary albedo in GCMs. *Journal of Advances in Modeling Earth Systems*, **8 (2)**, 650–668.

McCusker, G. Y., J. Vüllers, P. Achtert, P. Field, J. J. Day, R. Forbes, R. Price, E. O'Connor, M. Tjernström, J. Prytherch, R. Neely III, and I. M. Brooks, 2023: Evaluating Arctic clouds modelled with the Unified Model and Integrated Forecasting System. *Atmospheric Chemistry and Physics*, **23 (8)**, 4819–4847, https://acp.copernicus.org/articles/23/4819/2023/.

McFarquhar, G. M., C. S. Bretherton, R. Marchand, A. Protat, P. J. DeMott, S. P. Alexander, G. C. Roberts, C. H. Twohy, D. Toohey, S. Siems, Y. Huang, R. Wood, R. M. Rauber, S. Lasher-Trapp, J. Jensen, J. L. Stith, J. Mace, J. Um, E. Järvinen, M. Schnaiter, A. Gettelman, K. J. Sanchez, C. S. McCluskey, L. M. Russell, I. L. McCoy, R. L. Atlas, C. G. Bardeen, K. A. Moore, T. C. J. Hill, R. S. Humphries, M. D. Keywood, Z. Ristovski, L. Cravigan, R. Schofield, C. Fairall, M. D. Mallet, S. M. Kreidenweis, B. Rainwater, J. D'Alessandro, Y. Wang, W. Wu, G. Saliba, E. J. T. Levin, S. Ding, F. Lang, S. C. H. Truong, C. Wolff, J. Haggerty, M. J. Harvey, A. R. Klekociuk, and A. McDonald, 2021: Observations of Clouds, Aerosols, Precipitation, and Surface Radiation over the Southern Ocean: An Overview of CAPRICORN, MARCUS, MICRE, and SOCRATES. *Bulletin of the American Meteorological Society*, **102 (4)**, E894–E928, https://journals.ametsoc.org/view/journals/bams/102/4/BAMS-D-20-0132.1.xml.

Meredith, M., M. Sommerkorn, S. Cassota, C. Derksen, A. Ekaykin, A. Hollowed, G. Kofinas, A. Mackintosh, J. Melbourne-Thomas, M. M. Muelbert, G. Ottersen, and E. Schuur, 2019: Polar regions, IPCC Special Report on the Ocean and Cryosphere in a Changing Climate. IPCC Special Report on the Ocean and Cryosphere in a Changing Climate, Cambridge University Press, Cambridge, United Kingdom and New York, NY, USA, https://doi.org/10.1017/9781009157964.005.

Mignani, C., J. M. Creamean, L. Zimmermann, C. Alewell, and F. Conen, 2019: New type of evidence for secondary ice formation at around -15 °C in mixed-phase clouds. *Atmospheric Chemistry and Physics*, **19 (2)**, 877–886, https://acp.copernicus.org/articles/19/877/2019/.

Monahan, E. C., D. E. Spiel, and K. L. Davidson, 1986: A Model of Marine Aerosol Generation Via Whitecaps and Wave Disruption. *Oceanic Whitecaps: And Their Role in Air-Sea Exchange Processes*, Monahan, E. C. and G. M. Niocaill, Eds., Springer Netherlands, Dordrecht, Oceanographic Sciences Library, 167–174, https://doi.org/10.1007/978-94-009-4668-2_16.

Morrison, H., G. de Boer, G. Feingold, J. Harrington, M. D. Shupe, and K. Sulia, 2012: Resilience of persistent Arctic mixed-phase clouds. *Nature Geoscience*, **5 (1)**, 11–17, https://www.nature.com/articles/ngeo1332.

Mülmenstädt, J., O. Sourdeval, J. Delanoë, and J. Quaas, 2015: Frequency of occurrence of rain from liquid-, mixed-, and ice-phase clouds derived from A-Train satellite retrievals. *Geophysical Research Letters*, **42 (15)**, 6502–6509, https://agupubs.onlinelibrary.wiley.com/doi/abs/10.1002/2015GL064604.

Nagao, T. M. and K. Suzuki, 2022: Characterizing Vertical Stratification of the Cloud Thermodynamic Phase With a Combined Use of CALIPSO Lidar and MODIS SWIR Measurements. *Journal of Geophysical Research: Atmospheres*, **127 (21)**, e2022JD036 826, https://onlinelibrary.wiley.com/doi/abs/10.1029/2022JD036826.

Oreopoulos, L., N. Cho, and D. Lee, 2017: New insights about cloud vertical structure from CloudSat and CALIPSO observations. *Journal of Geophysical Research: Atmospheres*, **122 (17)**, 9280–9300, https://agupubs.onlinelibrary.wiley.com/doi/abs/10.1002/2017JD026629.

Papakonstantinou-Presvelou, I., O. Sourdeval, and J. Quaas, 2022: Strong Ocean/Sea-Ice Contrasts Observed in Satellite-Derived Ice Crystal Number Concentrations in Arctic Ice Boundary-Layer Clouds. *Geophysical Research Letters*, **49 (13)**, e2022GL098 207, https://onlinelibrary.wiley.com/doi/abs/10.1029/2022GL098207.

Papritz, L., S. Pfahl, H. Sodemann, and H. Wernli, 2015: A Climatology of Cold Air Outbreaks and Their Impact on Air–Sea Heat Fluxes in the High-Latitude South Pacific. *Journal of Climate*, **28 (1)**, 342–364, https://journals.ametsoc.org/view/journals/clim/28/1/jcli-d-14-00482.1.xml.

Paratoni, S., 2023: Wintertime Arctic Cloud Phase Distribution over Sea Ice and Ocean. Bachelor Thesis, Karlsruhe Institute of Technology, Karlsruhe.

Pedregosa, F., G. Varoquaux, A. Gramfort, V. Michel, B. Thirion, O. Grisel, M. Blondel, P. Prettenhofer, R. Weiss, V. Dubourg, J. Vanderplas, A. Passos, D. Cournapeau, M. Brucher, M. Perrot, and E. Duch-

esnay, 2011: Scikit-learn: Machine learning in Python. *Journal of Machine Learning Research*, **12**, 2825–2830.

Petty, G. W., 2006: *A First Course in Atmospheric Radiation*. 2d ed., Sundog Pub, Madison, Wis.

Pincus, R., E. J. Mlawer, and J. S. Delamere, 2019: Balancing Accuracy, Efficiency, and Flexibility in Radiation Calculations for Dynamical Models. *Journal of Advances in Modeling Earth Systems*, **11 (10)**, 3074–3089, https://onlinelibrary.wiley.com/doi/abs/10.1029/2019MS001621.

Pinto, J. O., 1998: Autumnal Mixed-Phase Cloudy Boundary Layers in the Arctic. *Journal of the Atmospheric Sciences*, **55 (11)**, 2016–2038, https://journals.ametsoc.org/view/journals/atsc/55/11/1520-0469_1998_055_2016_ampcbl_2.0.co_2.xml.

Porter, G. C. E., M. P. Adams, I. M. Brooks, L. Ickes, L. Karlsson, C. Leck, M. E. Salter, J. Schmale, K. Siegel, S. N. F. Sikora, M. D. Tarn, J. Vüllers, H. Wernli, P. Zieger, J. Zinke, and B. J. Murray, 2022: Highly Active Ice-Nucleating Particles at the Summer North Pole. *Journal of Geophysical Research: Atmospheres*, **127 (6)**, e2021JD036 059, https://onlinelibrary.wiley.com/doi/abs/10.1029/2021JD036059.

Previdi, M., K. L. Smith, and L. M. Polvani, 2021: Arctic amplification of climate change: A review of underlying mechanisms. *Environmental Research Letters*, **16 (9)**, 093 003, https://dx.doi.org/10.1088/1748-9326/ac1c29.

Radenz, M., J. Bühl, P. Seifert, H. Baars, R. Engelmann, B. Barja González, R.-E. Mamouri, F. Zamorano, and A. Ansmann, 2021: Hemispheric contrasts in ice formation in stratiform mixed-phase clouds: Disentangling the role of aerosol and dynamics with ground-based remote sensing. *Atmospheric Chemistry and Physics Discussions*, 1–34, https://acp.copernicus.org/preprints/acp-2021-360/.

Rantanen, M., A. Y. Karpechko, A. Lipponen, K. Nordling, O. Hyvärinen, K. Ruosteenoja, T. Vihma, and A. Laaksonen, 2022: The Arctic has warmed nearly four times faster than the globe since 1979. *Communications Earth & Environment*, **3 (1)**, 1–10, https://www.nature.com/articles/s43247-022-00498-3.

Raoult, F.-M., 1887: Loi générale des tensions de vapeur des dissolvants. *CR Hebd. Seances Acad. Sci*, **104**, 1430–1433.

———, 1889: Recherches expérimentales sur les tensions de vapeur des dissolutions. *Journal de Physique Théorique et Appliquée*, **8 (1)**, 5–20, http://dx.doi.org/10.1051/jphystap:0188900800500.

Rauber, R. M. and S. W. Nesbitt, 2018: *"Radar Meteorology: A First Course"*. First edition ed., Advancing Weather and Climate Science Series, Wiley-Blackwell, United States,

http://www.redi-bw.de/db/ebsco.php/search.ebscohost.com/login.aspx%3fdirect%3dtrue%26db%3dnlebk%26AN%3d1726690%26site%3dehost-live.

Reick, C. H., V. Gayler, D. Goll, S. Hagemann, M. Heidkamp, J. E. M. S. Nabel, T. Raddatz, E. Roeckner, R. Schnur, and S. Wilkenskjeld, 2021: JSBACH 3 - The land component of the MPI Earth System Model: Documentation of version 3.2. *Berichte zur Erdsystemforschung*, **(240)**, https://pure.mpg.de/pubman/faces/ViewItemOverviewPage.jsp?itemId=item_3279802.

Riley, E. M. and B. E. Mapes, 2009: Unexpected peak near -15°C in CloudSat echo top climatology. *Geophysical Research Letters*, **36 (9)**, https://onlinelibrary.wiley.com/doi/abs/10.1029/2009GL037558.

Sassen, K. and Z. Wang, 2008: Classifying clouds around the globe with the CloudSat radar: 1-year of results. *Geophysical Research Letters*, **35 (4)**, https://agupubs.onlinelibrary.wiley.com/doi/abs/10.1029/2007GL032591.

———, 2012: The Clouds of the Middle Troposphere: Composition, Radiative Impact, and Global Distribution. *Surveys in Geophysics*, **33 (3)**, 677–691, https://doi.org/10.1007/s10712-011-9163-x.

Schima, J., G. McFarquhar, U. Romatschke, J. Vivekanandan, J. D'Alessandro, J. Haggerty, C. Wolff, E. Schaefer, E. Järvinen, and M. Schnaiter, 2022: Characterization of Southern Ocean Boundary Layer Clouds Using Airborne Radar, Lidar, and In Situ Cloud Data: Results From SOCRATES. *Journal of Geophysical Research: Atmospheres*, **127 (21)**, e2022JD037 277, https://onlinelibrary.wiley.com/doi/abs/10.1029/2022JD037277.

Schotland, R. M., K. Sassen, and R. Stone, 1971: Observations by Lidar of Linear Depolarization Ratios for Hydrometeors. *Journal of Applied Meteorology and Climatology*, **10 (5)**, 1011–1017, https://journals.ametsoc.org/view/journals/apme/10/5/1520-0450_1971_010_1011_oblold_2_0_co_2.xml.

Schuddeboom, A. J. and A. J. McDonald, 2021: The Southern Ocean Radiative Bias, Cloud Compensating Errors, and Equilibrium Climate Sensitivity in CMIP6 Models. *Journal of Geophysical Research: Atmospheres*, **126 (22)**, e2021JD035 310, https://onlinelibrary.wiley.com/doi/abs/10.1029/2021JD035310.

Screen, J. A., T. J. Bracegirdle, and I. Simmonds, 2018: Polar Climate Change as Manifest in Atmospheric Circulation. *Current Climate Change Reports*, **4 (4)**, 383–395, https://doi.org/10.1007/s40641-018-0111-4.

Seifert, A., 2008: A Revised Cloud Microphysical Parameterization for COSMO-LME. **(7)**.

Semtner, A. J., 1976: A Model for the Thermodynamic Growth of Sea Ice in Numerical Investigations of Climate. *Journal of Physical Oceanography*, **6 (3)**, 379–389, https://journals.ametsoc.org/view/journals/phoc/6/3/1520-0485_1976_006_0379_amfttg_2_0_co_2.xml.

Serreze, M. C. and R. G. Barry, 2011: Processes and impacts of Arctic amplification: A research synthesis. *Global and Planetary Change*, **77 (1)**, 85–96, https://www.sciencedirect.com/science/article/pii/S0921818111000397.

———, 2014: *The Arctic Climate System / Mark C. Serreze (University of Colorado at Boulder), Roger G. Barry (University of Colorado at Boulder)*.

Shi, J., J. Yan, S. Wang, S. Zhao, M. Zhang, S. Xu, Q. Lin, H. Yang, and S. Dai, 2023: Cyclones enhance the transport of sea spray aerosols to the high atmosphere in the Southern Ocean. *Atmospheric Chemistry and Physics*, **23 (18)**, 10 349–10 359, https://acp.copernicus.org/articles/23/10349/2023/.

Shupe, M. D., 2011: Clouds at Arctic Atmospheric Observatories. Part II: Thermodynamic Phase Characteristics. *Journal of Applied Meteorology and Climatology*, **50 (3)**, 645–661, https://journals.ametsoc.org/view/journals/apme/50/3/2010jamc2468.1.xml.

Shupe, M. D., M. Rex, B. Blomquist, P. O. G. Persson, J. Schmale, T. Uttal, D. Althausen, H. Angot, S. Archer, L. Bariteau, I. Beck, J. Bilberry, S. Bucci, C. Buck, M. Boyer, Z. Brasseur, I. M. Brooks, R. Calmer, J. Cassano, V. Castro, D. Chu, D. Costa, C. J. Cox, J. Creamean, S. Crewell, S. Dahlke, E. Damm, G. de Boer, H. Deckelmann, K. Dethloff, M. Dütsch, K. Ebell, A. Ehrlich, J. Ellis, R. Engelmann, A. A. Fong, M. M. Frey, M. R. Gallagher, L. Ganzeveld, R. Gradinger, J. Graeser, V. Greenamyer, H. Griesche, S. Griffiths, J. Hamilton, G. Heinemann, D. Helmig, A. Herber, C. Heuzé, J. Hofer, T. Houchens, D. Howard, J. Inoue, H.-W. Jacobi, R. Jaiser, T. Jokinen, O. Jourdan, G. Jozef, W. King, A. Kirchgaessner, M. Klingebiel, M. Krassovski, T. Krumpen, A. Lampert, W. Landing, T. Laurila, D. Lawrence, M. Lonardi, B. Loose, C. Lüpkes, M. Maahn, A. Macke, W. Maslowski, C. Marsay, M. Maturilli, M. Mech, S. Morris, M. Moser, M. Nicolaus, P. Ortega, J. Osborn, F. Pätzold, D. K. Perovich, T. Petäjä, C. Pilz, R. Pirazzini, K. Posman, H. Powers, K. A. Pratt, A. Preußer, L. Quéléver, M. Radenz, B. Rabe, A. Rinke, T. Sachs, A. Schulz, H. Siebert, T. Silva, A. Solomon, A. Sommerfeld, G. Spreen, M. Stephens, A. Stohl, G. Svensson, J. Uin, J. Viegas, C. Voigt, P. von der Gathen, B. Wehner, J. M. Welker, M. Wendisch, M. Werner, Z. Xie, and F. Yue, 2022: Overview of the MOSAiC expedition: Atmosphere. *Elementa: Science of the Anthropocene*, **10 (1)**, 00 060, https://doi.org/10.1525/elementa.2021.00060.

Si, M., E. Evoy, J. Yun, Y. Xi, S. J. Hanna, A. Chivulescu, K. Rawlings, D. Veber, A. Platt, D. Kunkel, P. Hoor, S. Sharma, W. R. Leaitch, and A. K. Bertram, 2019: Concentrations, composition, and sources of ice-nucleating particles in the Canadian High Arctic during spring 2016. *Atmospheric Chemistry and Physics*, **19 (5)**, 3007–3024, https://acp.copernicus.org/articles/19/3007/2019/.

Siebesma, P., S. Bony, C. Jakob, and B. Stevens, 2020: *Clouds and Climate: Climate Science's Greatest Challenge / Edited by A. Pier Siebesma (Delft University of Technology), Sandrine Bony (Laboratoire de Meteorologie Dynamique), Christian Jakob (Monash University), Bjorn Stevens (Max-Planck-Institut Für Meteorologie)*.

Silber, I., P. S. McGlynn, J. Y. Harrington, and J. Verlinde, 2021: Habit-Dependent Vapor Growth Modulates Arctic Supercooled Water Occurrence. *Geophysical Research Letters*, **48 (10)**, e2021GL092 767, https://onlinelibrary.wiley.com/doi/abs/10.1029/2021GL092767.

Smagorinsky, J., 1963: GENERAL CIRCULATION EXPERIMENTS WITH THE PRIMITIVE EQUATIONS: I. THE BASIC EXPERIMENT. *Monthly Weather Review*, **91 (3)**, 99–164, https://journals.ametsoc.org/view/journals/mwre/91/3/1520-0493_1963_091_0099_gcewtp_2_3_co_2.xml.

Smith, A. J., V. E. Larson, J. Niu, J. A. Kankiewicz, and L. D. Carey, 2009: Processes that generate and deplete liquid water and snow in thin midlevel mixed-phase clouds. *Journal of Geophysical Research: Atmospheres*, **114 (D12)**, https://agupubs.onlinelibrary.wiley.com/doi/abs/10.1029/2008JD011531.

Solomon, A., M. D. Shupe, G. Svensson, N. P. Barton, Y. Batrak, E. Bazile, J. J. Day, J. D. Doyle, H. P. Frank, S. Keeley, T. Remes, and M. Tolstykh, 2023: The winter central Arctic surface energy budget: A model evaluation using observations from the MOSAiC campaign. *Elementa: Science of the Anthropocene*, **11 (1)**, 00 104, https://doi.org/10.1525/elementa.2022.00104.

Sourdeval, O., E. Gryspeerdt, M. Krämer, T. Goren, J. Delanoë, A. Afchine, F. Hemmer, and J. Quaas, 2018: Ice crystal number concentration estimates from lidar–radar satellite remote sensing – Part 1: Method and evaluation. *Atmospheric Chemistry and Physics*, **18 (19)**, 14 327–14 350, https://acp.copernicus.org/articles/18/14327/2018/.

Spada, M., O. Jorba, C. Pérez García-Pando, Z. Janjic, and J. M. Baldasano, 2013: Modeling and evaluation of the global sea-salt aerosol distribution: Sensitivity to size-resolved and sea-surface temperature dependent emission schemes. *Atmospheric Chemistry and Physics*, **13 (23)**, 11 735–11 755, https://acp.copernicus.org/articles/13/11735/2013/.

Stephens, G. L., D. G. Vane, R. J. Boain, G. G. Mace, K. Sassen, Z. Wang, A. J. Illingworth, E. J. O'connor, W. B. Rossow, S. L. Durden, S. D. Miller, R. T. Austin, A. Benedetti, and C. Mitrescu, 2002: The cloudsat mission and the a-train. *Bulletin of the American Meteorological Society*, **83 (12)**, 1771–1790.

Stephens, G. L., D. G. Vane, S. Tanelli, E. Im, S. Durden, M. Rokey, D. Reinke, P. Partain, G. G. Mace, R. Austin, T. L'Ecuyer, J. Haynes, M. Lebsock, K. Suzuki, D. Waliser, D. Wu, J. Kay, A. Gettelman,

Z. Wang, and R. Marchand, 2008: CloudSat mission: Performance and early science after the first year of operation. *Journal of Geophysical Research: Atmospheres*, **113 (D8)**.

Stevens, B., M. Satoh, L. Auger, J. Biercamp, C. S. Bretherton, X. Chen, P. Düben, F. Judt, M. Khairoutdinov, D. Klocke, C. Kodama, L. Kornblueh, S.-J. Lin, P. Neumann, W. M. Putman, N. Röber, R. Shibuya, B. Vanniere, P. L. Vidale, N. Wedi, and L. Zhou, 2019: DYAMOND: The DYnamics of the Atmospheric general circulation Modeled On Non-hydrostatic Domains. *Progress in Earth and Planetary Science*, **6 (1)**, 61, https://doi.org/10.1186/s40645-019-0304-z.

Sullivan, S. C., C. Hoose, A. Kiselev, T. Leisner, and A. Nenes, 2018: Initiation of secondary ice production in clouds. *Atmospheric Chemistry and Physics*, **18 (3)**, 1593–1610, https://acp.copernicus.org/articles/18/1593/2018/.

Sze, K. C. H., H. Wex, M. Hartmann, H. Skov, A. Massling, D. Villanueva, and F. Stratmann, 2023: Ice-nucleating particles in northern Greenland: Annual cycles, biological contribution and parameterizations. *Atmospheric Chemistry and Physics*, **23 (8)**, 4741–4761, https://acp.copernicus.org/articles/23/4741/2023/.

Takahashi, T., 2014: Influence of Liquid Water Content and Temperature on the Form and Growth of Branched Planar Snow Crystals in a Cloud. *Journal of the Atmospheric Sciences*, **71 (11)**, 4127–4142, https://journals.ametsoc.org/view/journals/atsc/71/11/jas-d-14-0043.1.xml.

Takahashi, T., T. Endoh, G. Wakahama, and N. Fukuta, 1991: Vapor Diffusional Growth of Free-Falling Snow Crystals between -3 and -23°C. *Journal of the Meteorological Society of Japan. Ser. II*, **69 (1)**, 15–30.

Takahashi, T., Y. Nagao, and Y. Kushiyama, 1995: Possible High Ice Particle Production during Graupel–Graupel Collisions. *Journal of the Atmospheric Sciences*, **52 (24)**, 4523–4527, https://journals.ametsoc.org/view/journals/atsc/52/24/1520-0469_1995_052_4523_phippd_2_0_co_2.xml.

Tamim Kashifi, M. and I. Ahmad, 2022: Efficient Histogram-Based Gradient Boosting Approach for Accident Severity Prediction With Multisource Data. *Transportation Research Record*, **2676 (6)**, 236–258, https://doi.org/10.1177/03611981221074370.

Taylor, K. E., R. J. Stouffer, and G. A. Meehl, 2012: An Overview of CMIP5 and the Experiment Design. *Bulletin of the American Meteorological Society*, **93 (4)**, 485–498, https://journals.ametsoc.org/view/journals/bams/93/4/bams-d-11-00094.1.xml.

Taylor, P. C., R. C. Boeke, Y. Li, and D. W. J. Thompson, 2019: Arctic cloud annual cycle biases in climate models. *Atmospheric Chemistry and Physics*, **19 (13)**, 8759–8782, https://acp.copernicus.org/articles/19/8759/2019/.

Thomson, W., 1871: LX. On the equilibrium of vapour at a curved surface of liquid. *The London, Edinburgh, and Dublin Philosophical Magazine and Journal of Science*, **42 (282)**, 448–452, https://doi.org/10.1080/14786447108640606.

Tjernström, M. and R. G. Graversen, 2009: The vertical structure of the lower Arctic troposphere analysed from observations and the ERA-40 reanalysis. *Quarterly Journal of the Royal Meteorological Society*, **135 (639)**, 431–443, https://onlinelibrary.wiley.com/doi/abs/10.1002/qj.380.

Tjernström, M., G. Svensson, L. Magnusson, I. M. Brooks, J. Prytherch, J. Vüllers, and G. Young, 2021: Central Arctic weather forecasting: Confronting the ECMWF IFS with observations from the Arctic Ocean 2018 expedition. *Quarterly Journal of the Royal Meteorological Society*, **147 (735)**, 1278–1299, https://onlinelibrary.wiley.com/doi/abs/10.1002/qj.3971.

Tremblay, L. B., M. M. Holland, I. V. Gorodetskaya, and G. A. Schmidt, 2007: An Ice-Free Arctic? Opportunities for Computational Science. *Computing in Science & Engineering*, **9 (3)**, 65–74, https://ieeexplore.ieee.org/document/4160261/figures.

Turner, J., R. Bindschadler, P. Convey, G. Di Prisco, E. Fahrbach, J. Gutt, D. Hodgson, P. A. Mayewski, and C. P. Summerhayes, (Eds.) , 2009: *Antarctic Climate Change and the Environment: A Contribution to the International Polar Year 2007 - 2008*. Scientific Committee on Antarctic Research, Cambridge.

Twohy, C. H., P. J. DeMott, L. M. Russell, D. W. Toohey, B. Rainwater, R. Geiss, K. J. Sanchez, S. Lewis, G. C. Roberts, R. S. Humphries, C. S. McCluskey, K. A. Moore, P. W. Selleck, M. D. Keywood, J. P. Ward, and I. M. McRobert, 2021: Cloud-Nucleating Particles Over the Southern Ocean in a Changing Climate. *Earth's Future*, **9 (3)**, e2020EF001 673, https://onlinelibrary.wiley.com/doi/abs/10.1029/2020EF001673.

Vergara-Temprado, J., A. K. Miltenberger, K. Furtado, D. P. Grosvenor, B. J. Shipway, A. A. Hill, J. M. Wilkinson, P. R. Field, B. J. Murray, and K. S. Carslaw, 2018: Strong control of Southern Ocean cloud reflectivity by ice-nucleating particles. *Proceedings of the National Academy of Sciences*, **115 (11)**, 2687–2692, http://www.pnas.org/lookup/doi/10.1073/pnas.1721627115.

von Terzi, L., J. Dias Neto, D. Ori, A. Myagkov, and S. Kneifel, 2022: Ice microphysical processes in the dendritic growth layer: A statistical analysis combining multi-frequency and polarimetric Doppler cloud radar observations. *Atmospheric Chemistry and Physics*, **22 (17)**, 11 795–11 821, https://acp.copernicus.org/articles/22/11795/2022/.

Vonder Haar, T. H., S. K. Cox, G. L. Stephens, J. M. Davis, T. L. Schneider, W. A. Peterson, A. C. Huffman, K. E. Eis, D. L. Reinke, and J. M. Forsythe, 1997: Overview and objectives of the DOD Center for Geosciences sponsored "Complex Layered-Cloud Experiment','paper presented at Cloud Impacts on DOD Operations and Systems Conference. *Philips Lab, Newport*.

Wang, X., J. Liu, H. Liu, and B. Yang, 2022: Characteristics of Arctic Summer Inversion and Its Correlation with Extreme Sea Ice Anomalies. *Atmosphere*, **13 (2)**, 316, https://www.mdpi.com/2073-4433/13/2/316.

Wehr, T., T. Kubota, G. Tzeremes, K. Wallace, H. Nakatsuka, Y. Ohno, R. Koopman, S. Rusli, M. Kikuchi, M. Eisinger, T. Tanaka, M. Taga, P. Deghaye, E. Tomita, and D. Bernaerts, 2023: The EarthCARE mission – science and system overview. *Atmospheric Measurement Techniques*, **16 (15)**, 3581–3608, https://amt.copernicus.org/articles/16/3581/2023/.

Wei, J., Z. Wang, M. Gu, J.-J. Luo, and Y. Wang, 2021: An evaluation of the Arctic clouds and surface radiative fluxes in CMIP6 models. *Acta Oceanologica Sinica*, **40 (1)**, 85–102, https://doi.org/10.1007/s13131-021-1705-6.

Welti, A., E. K. Bigg, P. J. DeMott, X. Gong, M. Hartmann, M. Harvey, S. Henning, P. Herenz, T. C. J. Hill, B. Hornblow, C. Leck, M. Löffler, C. S. McCluskey, A. M. Rauker, J. Schmale, C. Tatzelt, M. van Pinxteren, and F. Stratmann, 2020: Ship-based measurements of ice nuclei concentrations over the Arctic, Atlantic, Pacific and Southern oceans. *Atmospheric Chemistry and Physics*, **20 (23)**, 15 191–15 206, https://acp.copernicus.org/articles/20/15191/2020/.

Wex, H., L. Huang, W. Zhang, H. Hung, R. Traversi, S. Becagli, R. J. Sheesley, C. E. Moffett, T. E. Barrett, R. Bossi, H. Skov, A. Hünerbein, J. Lubitz, M. Löffler, O. Linke, M. Hartmann, P. Herenz, and F. Stratmann, 2019: Annual variability of ice-nucleating particle concentrations at different Arctic locations. *Atmospheric Chemistry and Physics*, **19 (7)**, 5293–5311, https://acp.copernicus.org/articles/19/5293/2019/.

Wiegner, M., F. Madonna, I. Binietoglou, R. Forkel, J. Gasteiger, A. Geiß, G. Pappalardo, K. Schäfer, and W. Thomas, 2014: What is the benefit of ceilometers for aerosol remote sensing? An answer from EARLINET. *Atmospheric Measurement Techniques*, **7 (7)**, 1979–1997, https://amt.copernicus.org/articles/7/1979/2014/.

Williams, M. J. M., 2015: The Southern Ocean. *Exploring the Last Continent: An Introduction to Antarctica*, Liggett, D., B. Storey, Y. Cook, and V. Meduna, Eds., Springer International Publishing, Cham, 115–127, https://doi.org/10.1007/978-3-319-18947-5_7.

Wilson, T. W., L. A. Ladino, P. A. Alpert, M. N. Breckels, I. M. Brooks, J. Browse, S. M. Burrows, K. S. Carslaw, J. A. Huffman, C. Judd, W. P. Kilthau, R. H. Mason, G. McFiggans, L. A. Miller, J. J. Nájera, E. Polishchuk, S. Rae, C. L. Schiller, M. Si, J. V. Temprado, T. F. Whale, J. P. S. Wong, O. Wurl, J. D. Yakobi-Hancock, J. P. D. Abbatt, J. Y. Aller, A. K. Bertram, D. A. Knopf, and B. J. Murray, 2015: A marine biogenic source of atmospheric ice-nucleating particles. *Nature*, **525 (7568)**, 234–238, http://www.nature.com/articles/nature14986.

Winker, D. M., J. Pelon, J. A. Coakley, S. A. Ackerman, R. J. Charlson, P. R. Colarco, P. Flamant, Q. Fu, R. M. Hoff, C. Kittaka, T. L. Kubar, H. L. Treut, M. P. Mccormick, G. Mégie, L. Poole, K. Powell, C. Trepte, M. A. Vaughan, and B. A. Wielicki, 2010: The CALIPSO Mission: A Global 3D View of Aerosols and Clouds. *Bulletin of the American Meteorological Society*, **91 (9)**, 1211–1230, https://journals.ametsoc.org/view/journals/bams/91/9/2010bams3009_1.xml, https://doi.org/10.1175/2010BAMS3009.1.

Winker, D. M., M. A. Vaughan, A. Omar, Y. Hu, K. A. Powell, Z. Liu, W. H. Hunt, and S. A. Young, 2009: Overview of the CALIPSO Mission and CALIOP Data Processing Algorithms. *Journal of Atmospheric and Oceanic Technology*, **26 (11)**, 2310–2323, https://journals.ametsoc.org/view/journals/atot/26/11/2009jtecha1281_1.xml.

World Meteorological Organization, 2017: Definitions of clouds. https://cloudatlas.wmo.int/clouds-definitions.html.

Xi, B., X. Dong, X. Zheng, and P. Wu, 2022: Cloud phase and macrophysical properties over the Southern Ocean during the MARCUS field campaign. *Atmospheric Measurement Techniques*, **15 (12)**, 3761–3777, https://amt.copernicus.org/articles/15/3761/2022/.

Zängl, G., D. Reinert, P. Rípodas, and M. Baldauf, 2015: The ICON (ICOsahedral Non-hydrostatic) modelling framework of DWD and MPI-M: Description of the non-hydrostatic dynamical core. *Quarterly Journal of the Royal Meteorological Society*, **141 (687)**, 563–579, https://onlinelibrary.wiley.com/doi/abs/10.1002/qj.2378.

Zaremba, T. J., R. M. Rauber, G. M. McFarquhar, M. Hayman, J. A. Finlon, and D. M. Stechman, 2020: Phase Characterization of Cold Sector Southern Ocean Cloud Tops: Results From SOCRATES. *Journal of Geophysical Research: Atmospheres*, **125 (24)**, e2020JD033 673, https://onlinelibrary.wiley.com/doi/abs/10.1029/2020JD033673.

Zelinka, M. D., T. A. Myers, D. T. McCoy, S. Po-Chedley, P. M. Caldwell, P. Ceppi, S. A. Klein, and K. E. Taylor, 2020: Causes of Higher Climate Sensitivity in CMIP6 Models. *Geophysical Research Letters*, **47 (1)**, e2019GL085 782, https://onlinelibrary.wiley.com/doi/abs/10.1029/2019GL085782.

Zhang, D., T. Luo, D. Liu, and Z. Wang, 2014: Spatial scales of altocumulus clouds observed with collocated CALIPSO and CloudSat measurements. *Atmospheric Research*, **149**, 58–69, http://www.sciencedirect.com/science/article/pii/S0169809514002324.

Zhang, D., A. Vogelmann, P. Kollias, E. Luke, F. Yang, D. Lubin, and Z. Wang, 2019: Comparison of Antarctic and Arctic Single-Layer Stratiform Mixed-Phase Cloud Properties Using Ground-Based Remote Sensing Measurements. *Journal of Geophysical Research: Atmospheres*, **124 (17-18)**, 10 186–10 204, https://onlinelibrary.wiley.com/doi/abs/10.1029/2019JD030673.

Zhang, D., Z. Wang, and D. Liu, 2010: A global view of midlevel liquid-layer topped stratiform cloud distribution and phase partition from CALIPSO and CloudSat measurements. *Journal of Geophysical Research: Atmospheres*, **115 (D4)**, https://agupubs.onlinelibrary.wiley.com/doi/abs/10.1029/2009JD012143.

Zhang, D., Z. Wang, T. Luo, Y. Yin, and C. Flynn, 2017: The occurrence of ice production in slightly supercooled Arctic stratiform clouds as observed by ground-based remote sensors at the ARM NSA site. *Journal of Geophysical Research: Atmospheres*, **122 (5)**, 2867–2877, https://agupubs.onlinelibrary.wiley.com/doi/abs/10.1002/2016JD026226.

Zygmuntowska, M., T. Mauritsen, J. Quaas, and L. Kaleschke, 2012: Arctic Clouds and Surface Radiation – a critical comparison of satellite retrievals and the ERA-Interim reanalysis. *Atmospheric Chemistry and Physics*, **12 (14)**, 6667–6677, https://acp.copernicus.org/articles/12/6667/2012/acp-12-6667-2012-discussion.html.

C. List of Figures

2.1 Schematic of homogeneous and heterogeneous freezing from Hoose and Möhler (2012). 7
2.2 Summary of INP concentrations taken from studies of field measurements conducted globally from Kanji et al. (2017). 8
2.3 Phase diagram of water adapted from Lamb and Verlinde (2011). 10
2.4 Scattering as function of the radius and the wavelength adapted from Petty (2006). . . . 11
2.5 Sea ice concentration in March and September averaged for 2007 and 2008 to illustrate sea ice cover over the Southern Ocean and the Arctic Ocean. Data are from Cavalieri et al. (1996) (version 1) provided by the National Snow and Ice Data Centre (NSIDC). . 14
2.6 Conceptual illustration of selected Southern Ocean processes from Landwehr et al. (2021). 15
2.7 Arctic Ocean surface circulation from Tremblay et al. (2007). 16
2.8 Sea-spray aerosol particles enriched in organic material are generated when bubbles burst at the air–sea interface. Figure and caption with permission from Wilson et al. (2015). . . 18
2.9 The global latitude variation of daytime cloud fraction from 2003 to 2016. The bottom solid line represent the standard deviation of all products. Adapted figure from Liu et al. (2022). © American Meteorological Society. Used with permission. 19
2.10 Annual cycles of total- and low-level cloud fraction from 2006 to 2009 for the Arctic Ocean from Zygmuntowska et al. (2012). 20
2.11 Relationship between cloud fraction (CF) profiles and shortwave cloud radiative effect at the top of the atmosphere (SWCRETOA) from Cesana et al. (2022). 23

3.1 Maps of the investigated regions 27
3.2 Number of DARDAR profile observations per day from 1 January 2007 until 31 December 2008. 28
3.3 Track of the sun-synchronous orbit of the A-Train, which the CloudSat and CALIPSO satellite are part of. 29
3.4 Overview of the DARDAR algorithm to categorize cloud phase. 31

4.1 Schematic of the different cloud types classified by their top and base heights. 37
4.2 Zonal mean temperature over the Southern Ocean (a) and the Arctic Ocean (b). 38
4.3 Schematic illustration of the three different ways to calculate the liquid fraction. 41

4.4 Mean absolute error in trainings and validation datset. 44
4.5 Histogram of the cloud top temperature (CTT) in gray (corresponding to the right y-axis). The lines show the mean absolute error (MAE) as a function of CTT (corresponding to the left y-axis). 46
4.6 Example to illustrate the information of SHAP values. 47

5.1 Frequency of different cloud type occurrence. 51
5.2 Annual cycle of the frequency of different cloud type occurrence. 51
5.3 Stacked bars of the relative frequency of different cloud types only considering single-layer clouds as a function of cloud top temperatures (CTTs). 52
5.4 Cloud phase distributions of various cloud types (columns) over the Southern Ocean (lower row) and the Arctic Ocean (upper row). 53
5.5 2-dimensional histogram of clouds with different phases regarding their horizontal and vertical extent. 56
5.6 Mean liquid fraction of profiles of different cloud types as a function of the cloud top temperatures (CTT). 57
5.7 Mean liquid fraction based on the phase of all cloudy pixels and their temperature comparing the results considering all profiles and considering only profiles in which the lidar signal is not fully extinguished. 58
5.8 Phase fraction at normalized cloud heights for mixed-phase clouds. 60
5.9 Difference between the mean liquid fraction of clouds over ocean and the mean liquid fraction of clouds over sea ice as a function of the cloud top temperature. 61
5.10 Vertically averaged aerosol mixing ratios (MR) within the heights of a cloud column for different aerosol types. 62
5.11 Difference of the mean liquid fraction of clouds collocated with high mixing ratio of an aerosol type, larger than the 75th percentile, and the mean liquid fraction of a cloud having a low aerosol mixing ratio, lower than the 25th percentile. 63
5.12 Pearson's correlation coefficient of the mean mixing ratios of different aerosol categories within a cloud. 64
5.13 Cloud radiative effects of different cloud types and with different cloud phases. 66
5.14 Mean SWCRE and LWCRE of clouds over ocean and over sea ice for the Southern Ocean (left panel) and the Arctic Ocean (right panel). 67
5.15 Mean SWCRE of cloud types over ocean as function of the latitude for the Southern Ocean and for the Arctic Ocean. 68
5.16 Contribution of different cloud types to the total cloud radiative effects over 2 years at the top of the atmosphere over the Southern Ocean (SO) and the Arctic Ocean (AO) in percent. 70

6.1 Importance of different features for the prediction of the liquid fraction for different cloud types over the Southern Ocean (SO) and the Arctic Ocean (AO). 74
6.2 Distribution of SHAP values of different features and the colors correspond to the feature value. 76
6.3 Map of the averaged liquid fraction in the different cloud types over the Arctic Ocean and the Southern Ocean. 77
6.4 2D-histograms of the SHAP values for dust as a function of the dust mixing ratio. 78
6.5 Map of the averaged SHAP value for dust. 78
6.6 Map of the averaged dust mixing ratio. 79
6.7 2D-histogram of the SHAP values for sea salt as a function of the sea salt mixing ratio. . 80
6.8 Map of the averaged SHAP value of sea salt. 81
6.9 Map of the averaged sea salt mixing ratio. 81
6.10 Map of the averaged SHAP values of the sea ice concentration. 83
6.11 Difference between normalized 2D-histograms once considering only cloud profiles over ocean and once considering only cloud profiles over sea ice. 84

7.1 Relative frequency of different cloud types in percent as fraction of the total number of observations of the summer period (10 August to 10 September) and of the winter period (30 January to 1 March). 86
7.2 Stacked frequency of occurrence of single-layer cloud types as a function of the cloud top temperature from 10 August to 10 September on the left hand side and from 30 January to 1 March on the right hand side. 88
7.3 Frequency of the cloud phase for the different cloud types (columns) over the Arctic Ocean (upper two rows) and the Southern Ocean (lower two rows) comparing results from DARDAR (upper row respectively) and DYAMOND (lower row respectively). . . . 89
7.4 Same as Fig. 7.3, but for the period from 30 January to 1 March using the DYAMOND winter datast. 89
7.5 Mean liquid fraction over the Arctic Ocean (top row) and the Southern Ocean (bottom row) for different cloud types in the DARDAR observations and the DYAMOND simulations for the August/September period and the February period. 90
7.6 Difference between the mean liquid fraction in clouds in the DYAMOND simulations and the mean liquid fraction in clouds in DARDAR observations over the Arctic Ocean (top row) and the Southern Ocean (bottom row) for different cloud types for the August/September period and the February period. 91
7.7 Mean liquid fraction over ocean (light colors) and over sea ice (dark colors) from DARDAR observations (dots) and in ICON-SAP simulations (triangle) as a function of the cloud top temperature. 93

7.8 Difference between the monthly averaged ERA-5 2-meter temperature (Hersbach et al., 2023b) of the corresponding year of the used DYAMOND dataset and the years of the used DARDAR dataset. 95

8.1 Summary schematic of some possibly relevant aspects influencing the phase of low-level and mid-level clouds over the Arctic Ocean and the Southern Ocean. 102

A.1 Comparison of the mean liquid fraction for different cloud top temperatures (CTT) between an analysis considering all profiles, and an analysis considering only profiles in which the lidar signal is not fully extinguished. 106
A.2 Mean cloud top liquid fraction based on the phase of all cloud top pixels and cloud top temperature comparing the results considering all profiles and considering only profiles in which the lidar signal is not fully extinguished. 106
A.3 Histogram of the cloud top temperatures for different cloud types considering all profiles and considering only profiles in which the lidar signal is not fully extinguished. 107
A.4 Annual cycle of the frequency of different cloud type occurrences for the same latitudes in the Arctic and the Southern Ocean, namely 60 °S/N to 62 °S/N. 107
A.5 Annual cycle of the relative frequency of different single-layer cloud type occurrence with respect to the total number of single-layer clouds for the same latitudes in the Arctic and the Southern Ocean, namely 60 °S/N to 62 °S/N. 108
A.6 Mean absolute error of the liquid fraction during the grid search over different combinations of hyperparameters sorted from the worst fit to the best fit. 110
A.7 Mean absolute error as a function of the maximal iterations (x-axis), the learning rate (y-axis), and the minimum number of samples per leaf (marker) for the training dataset. . 111
A.8 Same as in Fig. A.7 but for the test dataset of the cross validation. 112
A.9 Histogram of the predicted liquid fraction and the observed liquid fraction from the training dataset. 113
A.10 Histogram of the predicted liquid fraction and the observed liquid fraction from the validation dataset. 114
A.11 Histogram of the sea ice concentration (SIC) in gray (corresponding to the right y-axis). The lines show the mean absolute error (MAE) as a function of the SIC (corresponding to the left y-axis). 115
A.12 Histogram of the dust mixing ratio (MR_{Dust}) in gray (corresponding to the right y-axis). The lines show the mean absolute error (MAE) as a function of dust mixing ratio (corresponding to the left y-axis). 116
A.13 Histogram of the sea salt mixing ratio (MR_{Seasalt}) in gray (corresponding to the right y-axis). The lines show the mean absolute error (MAE) as a function of sea salt mixing ratio (corresponding to the left y-axis). 117

A.14 Map of the averaged dust mixing ratio with different range of the color bar. 118
A.15 Map of the averaged sea salt mixing ratio with different range of the color bar. 118
A.16 Map of the averaged cloud top temperature (CTT) of the different cloud types over the Arctic Ocean and the Southern Ocean. 119
A.17 Map of the SHAP value for the cloud top temperature. 119
A.18 Comparison of the cloud type frequencies in the DYAMOND Summer dataset including the 00:00:00 output time step in panel (a) and (c), and excluding the 00:00:00 output time step in the panel (b) and (c). 120
A.19 Comparison of the frequencies of the cloud phases in the different cloud types for the DYAMOND Summer dataset, once excluding the 00:00:00 output time step, and once including the 00:00:00 output time step. 121
A.20 Comparison of the mean mass liquid fraction in the DYAMOND summer dataset with once including the 00:00:00 output time step, and once excluding the 00:00:00 output time step. 121
A.21 Cloud type frequencies with respect to the number of single-layer clouds comparing DARDAR and DYAMOND results. 122
A.22 Histograms of the total number of cloud type profiles as function of cloud top temperature. 122

D. List of Tables

3.1 Overview of the analyzed DYAMOND ICON simulations 35

4.1 DARDAR-MASK categories and how they are considered for the cloud phase analysis in this study 39
4.2 Sample size of the two-year dataset 43
4.3 Sample size to train the machine learning models and to validate the model by the same number of different samples. 43
4.4 Hyperparamter grid used to tune the model with grid search. 43
4.5 Mean absolute error between the predicted liquid fraction and the observed liquid fraction. 44
4.6 Pearson correlation coefficient between the predicted liquid fraction and the observed liquid fraction 44
4.7 Conditions for the distinction between cloud phases based on the liquid fraction (f_{DYAMOND}). 48

A.1 Cloud radiative effect summed up over two years and normalized by the total number of observed cloud profiles. 108

Acknowledgments

First of all, I would like to express my gratitude to Prof. Dr. Corinna Hoose for her great supervision, her helpful advice, and her constant support throughout the whole time of my PhD. I am also very grateful to her for giving me the opportunity to exchange and extend my knowledge at international conferences, project meetings, and workshops. I have also enjoyed our meetings in a nice, friendly, inspiring, and motivating atmosphere. Many thanks to you!

I would also like to express my sincere gratitude to my second supervisor, Prof. Dr. Jan Cermak for accepting to be the second referee. Moreover, I want to thank him for taking time for meetings offering his helpful views and suggestions providing a different perspective.

I also want to thank Prof. Dr. Philip Stier and his group for giving me the opportunity to spend a three months research stay at Oxford University. The exchange really helped me getting an overview of many different machine learning approaches and different perspectives on cloud physics research. Besides the scientific work, I also found new friends and enjoyed exploring the country. I also thank the Graduate School for Climate and Environment (GRACE) for the funding this research stay.

Furthermore, I would like to thank all the members of the cloud physics group for the nice working atmosphere, the fruitful exchanges, and all the individual discussions about science, but also about everyday life. I especially thank my office mates for the nice conversations and the enjoyable atmosphere in our office.

I would also like to extend my sincere thanks to all my colleagues on the 13th floor of the physics building for the nice and cheerful lunch breaks, coffee breaks, but also the evening activities.

Additionally, this endeavor would not have been possible without the funding of the two projects, the European Research Council (ERC) under the European Union's Horizon 2020 research and innovation programme under grant agreement No 714062 (ERC Starting Grant "C2Phase"), and the FORCeS project under grant agreement No 821205.

I also thank all my friends who accompanied me during the journey of my PhD and contributed in many different ways to my achievements so far, but also for all the parts besides the PhD.

I would also like to express my deep appreciation to my family for their support and for believing in me, as well as providing me the opportunity to study and, thereby, lay the foundation of having the doing a PhD.

Finally, I deeply thank you, Dominik, for always being there for me, for your endless support, and for your love.